The evolution of the oceanic redox state through Precambrian times

Dissertation

der Mathematisch-Naturwissenschaftlichen Fakultät

der Eberhard Karls Universität Tübingen

zur Erlangung des Doktorgrades

der Naturwissenschaften

(Dr. rer. nat.)

vorgelegt von

M. Sc. Florian Kurzweil

aus Göttingen

Tübingen

2015

Gedruckt mit Genehmigung der Mathematisch-Naturwissenschaftlichen Fakultät der Eberhard Karls Universität Tübingen

Tag der mündlichen Qualifikation	27.11.2015
Dekan:	Prof. Dr. Wolfgang Rosenstiel
1. Gutachter	Prof. Dr. Ronny Schönberg
2. Gutachter	Prof. Dr. Andreas Kappler

Ich erkläre hiermit, dass ich die zur Promotion eingereichte Arbeit mit dem Titel “The evolution of the oceanic redox state through Precambrian times” selbstständig verfasst, nur die angegebenen Quellen und Hilfsmittel benutzt und wörtlich oder inhaltlich übernommene Stellen (alternativ: Zitate) als solche gekennzeichnet habe. Ich erkläre, dass die Richtlinien zur Sicherung guter wissenschaftlicher Praxis der Universität Tübingen (Beschluss des Senats vom 25.05.2000) beachtet wurden. Ich versichere an Eides statt, dass diese Angaben wahr sind und dass ich nichts verschwiegen habe. Mir ist bekannt, dass die falsche Angabe einer Versicherung an Eides statt mit Freiheitsstrafe bis zu drei Jahren oder mit Geldstrafe bestraft wird.

Ort, Datum Unterschrift

ABSTRACT

The oceanic redox state distinctly changed during the Precambrian Eon. Entirely anoxic oceans in earliest Earth history initially became mildly oxygenated in some shallow marine areas. The first appearance of such 'oxygen oases' remains controversial, but their areal extension in late Archean and early Proterozoic times possibly triggered atmospheric oxygenation during the Great Oxidation Event around 2.4 billion years ago. The timing of complete ocean oxygenation (including the deep ocean) is likewise debated in the scientific community, but may be linked to a second oxygenation event almost 2 billion years later during the final stages of the Precambrian Eon (Ediacaran Period).

In this cumulative dissertation periods of major environmental redox changes were investigated using the isotope proxies of redox sensitive elements such as iron (Fe) and molybdenum (Mo). The transitional period before the Great Oxidation Event was examined by a Mo isotope study of late Archean black shales and iron formations of the Hamersley Basin, Australia (CHAPTER I). Both types of sediments show a gradual increase towards heavy Mo isotopic ratios between 2.6 and 2.5 billion years ago. This increase requires a contemporaneously upcoming sink of isotopically light Mo, such as Manganese oxides (MnO_2), which may have formed in shallow marine 'oxygen oases'. To further verify this interpretation, 2.48 billion years old Mn-rich iron formations from the Griqualand West Basin, South Africa, were analyzed for the Mo and Fe isotopic composition (CHAPTER II). The observed negative correlation between Mn concentration and Mo isotopic ratios confirms that the adsorption of (isotopically light) molybdate onto Mn oxides represented an important Mo burial pathway. Importantly, also Fe isotopic ratios show a negative correlation with Mn concentrations. Considering modern redox stratified lake equivalents, this trend most likely arise from the depletion of heavy Fe isotopes in the uppermost water column along the chemocline due to iron oxidation by Mn oxides. Thus, multiple isotopic evidence confirms local Mn oxide formation in oxygen-rich shallow marine waters before atmospheric oxygenation during the Great Oxidation Event.

The assumed oxygenation of the deep ocean during the Ediacaran Period would have further extended the depositional area of Mn oxides, thus also increasing the sink of isotopically light Mo. As a consequence, the seawater Mo isotopic ratio is expected to have been risen to modern-like high ratios. However, the geochemical study of Teplá Barrandian black shales from this time period draws a different picture (CHAPTER III). The sulfur isotopic composition and the ratio of molybdenum concentrations to total organic carbon indicate the temporal restriction of the local depositional basin and accompanied depletion of dissolved sulfate and molybdate. The Mo isotopic composition of black shales deposited in such restricted and euxinic basins mirrors the contemporaneous global seawater Mo isotopic signature (like in the modern Black Sea). Constantly low Mo isotopic ratios in respective sediments suggest the lack of Mn oxide formation in contemporaneous deep sea settings due to continuously anoxic deep water conditions at the end of the Precambrian eon.

ZUSAMMENFASSUNG

Der Redoxzustand der Ozeane erlebte signifikante Veränderungen während des Präkambrischen Äons. Ausgehend von vollständig anoxischen Bedingungen während der frühesten Erdgeschichte entwickelten sich zunächst in lokalen Flachwasserbereichen leicht oxische Bedingungen. Das früheste Auftreten solcher ‚Sauerstoffoasen' bleibt umstritten, doch ihre Ausbreitung könnte die Oxidation der Atmosphäre während des Great Oxidation Events vor etwa 2,4 Milliarden Jahren ausgelöst haben. Die vollständige Oxidation der Ozeane, inklusive des tiefen Ozeans, fand hingegen vermutlich erst etwa 2 Milliarden Jahre später während eines zweiten Oxidationsereignisses am Ende des Präkambrischen Äons statt (Ediacara Periode).

In dieser kumulativen Dissertation wurden wesentliche Zeiträume, die geprägt waren durch Veränderungen des marinen Redoxzustandes, anhand von Isotopenmessungen redox-sensitiver Elemente, wie zum Beispiel Molybdän (Mo) und Eisen (Fe), genauer untersucht. Die Übergangsphase vor dem Great Oxidation Event wurde mithilfe von Mo-Isotopenmessungen an spät-archaischen Schwarzschiefern und Eisenformationen des Hamersley-Beckens, Australien, detailliert eruiert (CHAPTER I). Beide Sedimenttypen zeigen einen kontinuierlichen Anstieg zu schwereren Isotopenverhältnissen, welcher die regionale oder globale Ausweitung der Senke für isotopisch leichtes Mo impliziert. Manganoxide (MnO_2), die in oxischen Flachwasserregionen gebildet wurden, stellen eine solche Senke dar. Um diese Interpretation weiter zu verifizieren, wurden 2,48 Milliarden Jahre alte Mn-reiche Eisenformationen aus dem Griqualand West-Becken, Südafrika, auf die Mo- und Fe-Isotopie hin untersucht (CHAPTER II). Die hier festgestellte negative Korrelation von Mn-Konzentrationen und Mo-Isotopenverhältnissen bestätigt, dass die Adsorption von isotopisch leichtem Molybdat an Mn-Oxiden einen wichtigen Ablagerungsmechanismus darstellte. Die Fe-Isotopenverhältnisse zeigen ebenfalls eine negative Korrelation mit Mn-Konzentrationen. Im Hinblick auf rezente, redox-stratifizierte Seen weist dieser Trend auf die Oxidation von gelöstem Eisen durch Mn-Oxide entlang der Redoxkline hin. Zusammenfassend lässt sich also feststellen, dass mehrere isotopische Evidenzen die lokale Mn-Oxidation in oxischen Flachwasserregionen noch vor der Oxidation der Atmosphäre während des Great Oxidation Event bestätigen.

Die angenommene Oxidation des tiefen Ozeans während der Ediacara Periode hätte die weitere Ausbreitung von Mn-Oxid-Ablagerungen zur Folge gehabt und somit auch die Senke von isotopisch leichtem Molybdän vergrößert. Damit einhergehend wäre ein Anstieg des Meerwasser-Mo-Isotopenverhältnisses zu rezent hohen Werten zu erwarten. Die geochemische Studie an Schwarzschiefern vom Teplá Barrandium zeichnet allerdings ein anderes Bild (CHAPTER III). Die Messungen von Schwefel-Isotopenverhältnissen sowie den Verhältnissen von Mo-Konzentrationen zum gesamten organischen Kohlenstoff deuten auf temporäre Restriktion des lokalen Beckens hin, was mit der Abreicherung von Sulfat und Molybdat in der lokalen Wassersäule einherging. Die Mo-Isotopenverhältnisse von Schwarzschiefern aus solch restriktiven und euxinischen Becken spiegeln die zeitgleiche globale Meerwasserisotopie wider (vgl. heutiges Schwarzes Meer). Konstant niedrige Mo-Isotopenverhältnisse in diesen Schwarzschiefern deuten allerdings nicht auf erhöhte Mn-Oxid-Ablagerungen hin, sondern implizieren vielmehr kontinuierlich anoxische Tiefwasserbedingungen am Ende des Präkambriums.

LIST OF PUBLICATIONS AND AUTHOR CONTRIBUTIONS

CHAPTER I **Published paper**

Title ..... Continuously increasing δ^{98}Mo values in Neoarchean black shales and iron formations from the Hamersley Basin

Authors ..... Florian Kurzweil, Martin Wille, Ronny Schoenberg, Heinrich Taubald, Martin J. Van Kranendonk

Status ..... published 2015 (Geochimica et Cosmochimica Acta 164, 523-542)

Declaration	contribution by author
Position in list of authors	1
Scientific ideas	50%
Data generation	85%
Analysis and interpretation	85%
Writing	90%

CHAPTER II **In preparation for submission**

Title ..... Coupled Iron and Molybdenum isotopes from a 2.4 billion years old oxygen oasis

Authors ..... Florian Kurzweil, Martin Wille, Philip Nel, Niklas Gantert, Nicolas J. Beukes, Ronny Schoenberg

Status ..... In preparation for submission to Geology

Declaration	contribution by author
Position in list of authors	1
Scientific ideas	75%
Data generation	100%
Analysis and interpretation	90%
Writing	95%

CHAPTER III Published paper

Title ..... Coupled sulfur, iron and molybdenum isotope data from black shales of the Teplá-Barrandian unit argue against deep ocean oxygenation during the Ediacaran

Authors ..... Florian Kurzweil, Kerstin Drost, Jan Pašava, Martin Wille, Heinrich Taubald, Daniel Schoeckle, Ronny Schoenberg

Status ..... published 2015 (Geochimica et Cosmochimica Acta 171, 121-142)

Declaration	contribution by author
Position in list of authors	1
Scientific ideas	50%
Data generation	60%
Analysis and interpretation	80%
Writing	80%

TABLE OF CONTENTS

CHAPTER III Coupled sulfur, iron and molybdenum isotope data from black shales of the Teplá-Barrandian unit argue against deep ocean oxygenation during the Ediacaran

APPENDIX

Supplements of CHAPTER III

Introduction

1. The Precambrian evolution of environmental redox conditions

The evolution of the chemical composition of the atmosphere and the oceans represents a major task in geochemical research. It is generally assumed that anoxic conditions prevailed during the Hadean and Archean era until the so-called Great Oxidation Event (GOE) in the early Proterozoic. The 'smoking gun' for this view is the preservation of mass independent sulfur isotope fractionations (MIF) in Archean sediments, which requires an anoxic atmosphere with oxygen levels lower than 10^{-5} of present atmospheric level (Farquhar et al., 2000; Pavlov and Kasting, 2002). The loss of these MIF signals in Paleoproterozoic sediments between 2.45 and 2.32 Ga ago (Bekker et al., 2004; Guo et al., 2009; Hannah et al., 2004) provides strong evidence for increasing atmospheric oxygen levels above this threshold (Fig. 1). Consistent with this geochemical indication, geological observations such as the first appearance of paleosoils with oxidized iron ('red beds') and the disappearance of detrital pyrite and uranite in marine sediments younger than the GOE provide further compelling evidence for more oxidizing conditions (Canfield, 2005; Holland, 2006).

The availability of free oxygen is a question of the balance of oxygen sinks and sources. Some authors suggested that the GOE was triggered by decreasing oxygen sinks, for example due to the loss of hydrogen

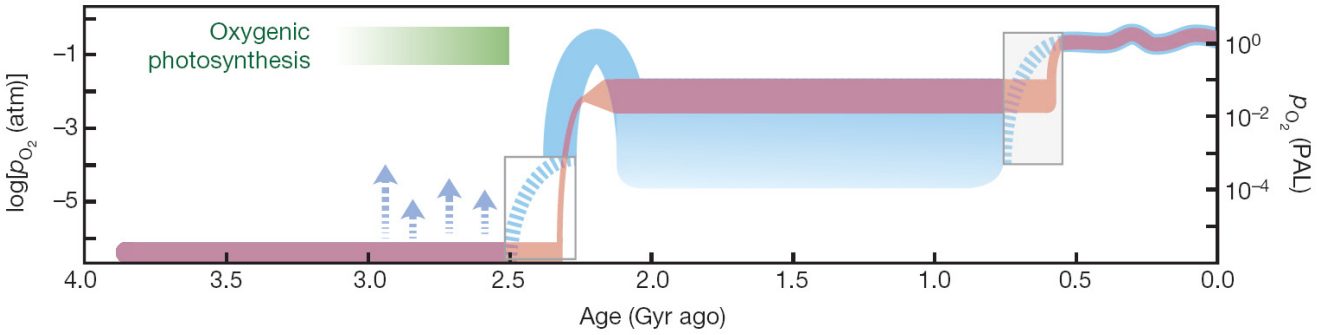

FIGURE 1: (from Lyons et al., 2014) The evolution of the atmospheric redox-state. Right axis: p_{O2} relative to the present atmospheric level (PAL). The red line marks the classical view of atmospheric oxygenation (Kump, 2008). The blue curve was established in more recent years. The arrows between 3.0 and 2.5 Ga indicate the transmission of oxygen from local marine oxygen oases to the atmosphere. During the GOE around 2.4 Ga ago atmospheric oxygen levels increased significantly and possibly 'overshot' during the subsequent Lumagundi-Jatuli event (2.3 to 2.1 Ga). The mid-Proterozoic time period was characterized by lower oxygen levels again. During a second major oxygenation event at the end of the Neoproterozoic the deep ocean may have become oxygenated and atmospheric oxygen levels reached modern-like values.

to space (Catling et al., 2001) or changes in the chemical composition of volcanic gases (Gaillard et al., 2011; Kump and Barley, 2007). Alternatively, bacterial oxygen production by oxygenic photosynthesis increased (Holland, 2006). Coupled with the burial of reduced carbon (organic matter), oxygenic photosynthesis represents a net source of oxygen. The evolution of oxygenic photosynthesis is still poorly understood but probably predates the GOE by several hundreds of million years (Eigenbrode and Freeman, 2006; Kurzweil et al., 2013; Planavsky et al., 2014). The local production of oxygen in shallow marine habitats during this transitional period could have oxygenated some surface areas of the ocean (Fig. 1). In these regions a stratified water column developed, with anoxic deep waters and oxic surface waters divided by a chemocline (Kendall et al., 2010; Planavsky et al., 2014; Riding et al., 2014). Oxygen exchange between local 'oxygen oases' and the atmosphere might have caused short-term fluctuations in atmospheric oxygen concentrations (Frei et al., 2009) and 'whiffs' of oxygen (Anbar et al., 2007). Higher rates of oxidative weathering of sulfides thereby increased the supply of associated metals (such as molybdenum) to the ocean, which may explain their enrichment in pre-GOE sediments (Anbar et al., 2007). However, persistent accumulation of oxygen in the atmosphere before the GOE was probably inhibited by the outbalancing capacity of reduced components of the continental crust and the ocean-atmosphere system.

Some authors suggested a short-lived ‚oxygen overshoot' In the aftermath of the GOE (Fig. 1) (Bekker and Holland, 2012). During the Lomagundi-Jatuli event between 2.3 and 2.1 Ga ago strong positive shifts in the carbonate carbon isotopic record indicate the increased burial of isotopically light organic carbon, a net source of oxygen (Karhu and Holland, 1996). Inconsistently with this claim, however, contemporaneous organic-rich sedimentary deposits are missing, but were only deposited during the subsequent Shunga Event. The precise interrelation of both events and their implications for the history of oxygenation are

still poorly understood and remain a matter of debate in the scientific community (Lyons et al., 2014). It is, however, well constrained that oxygen levels remained relatively low during the following period between 1.8 and 0.8 Ga ago (Holland, 2006; Lyons et al., 2014). Due to the invariability of several geochemical proxies this mid-Proterozoic time period was termed the 'boring billion' (Holland, 2006). The start of the boring billion also marks the disappearance of large iron-rich chemical sediments, so-called iron formation (IF), which developed by the local oxidation of dissolved Fe^{2+} to insoluble Fe^{3+} and subsequent precipitation of Fe^{3+}-minerals (see further explanation in 1.2). Their disappearance was initially interpreted to be a consequence of Fe^{2+} limitation in an oxic (Holland, 2005) or sulfidic ocean (Canfield, 1998). More recent studies, however, demonstrated that the deep ocean remained ferruginous beyond the GOE and during most of the Proterozoic era (Planavsky et al., 2011). Following these authors, the termination of BIF deposition is rather related to lower release of hydrothermal iron during volcanically more quite periods in mid-Proterozoic times.

Although controversial, first deep ocean oxygenation might have occurred in the course of a second major oxygenation event during the late Neoproterozoic (Canfield et al., 2007; Chen et al., 2015; Och and Shields-Zhou, 2012). This time period is also marked by major biologic innovations such as the evolution of multi-cellular life (Love et al., 2009), tectonic modifications such as the break-up of the supercontinent Rodinia (Hoffman, 1991) as well as climate changes, which caused the global Marinoan and Sturtian glaciations (Hoffman et al., 1998). A causal link between these environmental, biologic and tectonic changes seems manifest, although the primery trigger remains controversial (Butterfield, 2009; Fike et al., 2006; Lenton et al., 2014; Och and Shields-Zhou, 2012). But independent of the triggering mechanism higher and possibly modern-like oxygen concentrations in the ocean-atmosphere system are assumed for the first time during this second major oxygenation event at the end of the Precambrian (Och and Shields-Zhou, 2012).

2. The principles of the molybdenum and the iron isotope proxy

2.1 Mass-dependent isotope fractionation

During the last years the isotopic composition of transition metals became an important tool to better constrain the history of the Earth's redox-evolution (Arnold et al., 2004; Asael et al., 2013; Kendall et al., 2015; Rouxel et al., 2005; Wille et al., 2007). The use of these isotope proxy signals relies on fundamentals of mass dependent isotope fractionation, which arise from quantum chemical effects (Bigeleisen, 1965; Urey, 1947). The zero point energy of a molecule, which is the difference between its lowest allowed potential energy level and the minimum of the potential well, depends on the masses of the single atoms (Fig. 2). Molecules with heavier isotopes have relatively lower zero-point-energies and form stronger chemical bonds. The dissociation energy of these molecules is larger, which causes slower reaction rates and kinetic isotope fractionations during chemical reactions (Sharp, 2007). Furthermore, the lower potential and vibrational energy of heavy-isotope-molecules results in lower translational velocities (i.e. during diffusion) and lower contact probability (i.e. during adsorption), which can also cause isotope fractionations.

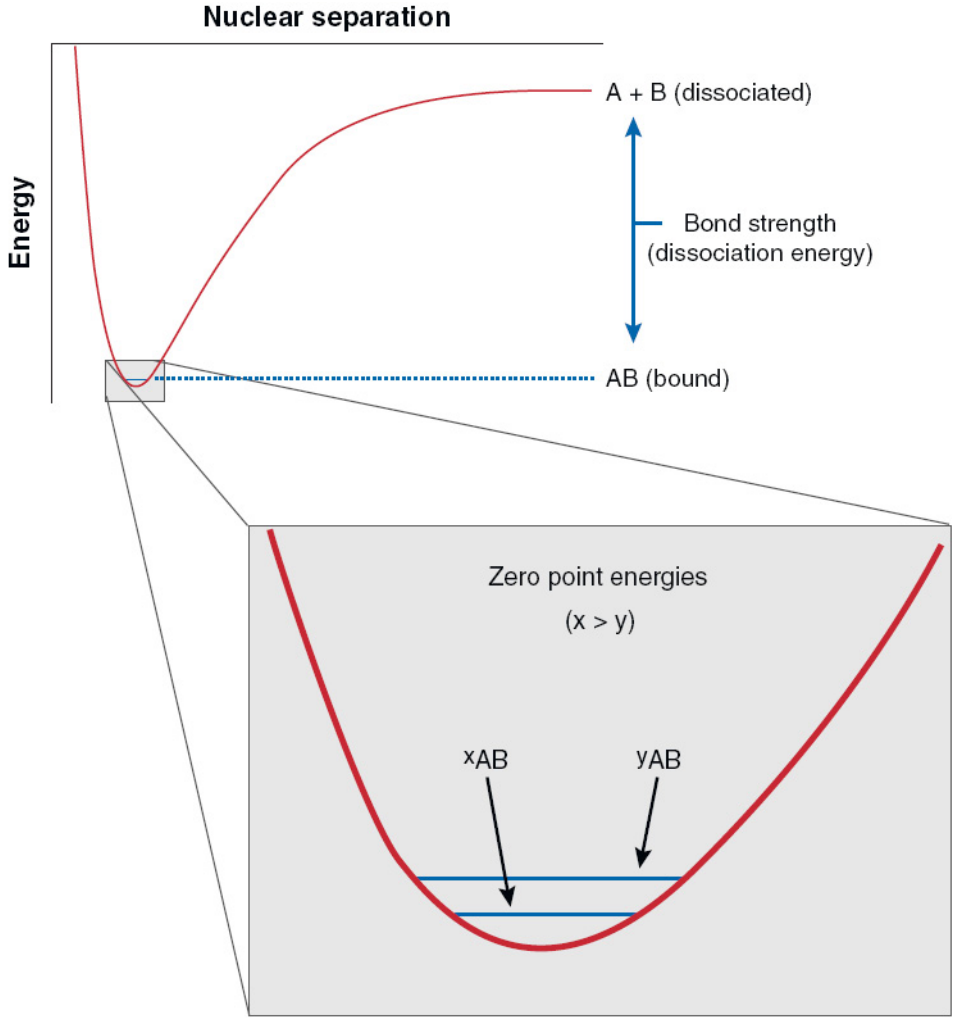

FIGURE 2: (from Anbar and Rouxel, 2007) Schematic illustration, which demonstrates the context of zero-point-energies and molecular bond-strength. The molecule AB with the heavy isotope of ^{x}A has a relatively lower zero-point-energy and forms stronger chemical bonds.

The relevant fractionation processes for the application of molybdenum (Mo) and iron (Fe) isotopes as a paleo-redox proxy are briefly described in the following and in more detail in chapters I to III. The Mo- and Fe isotopic composition of a sample is generally shown in the δ-notation, which relates the isotopic ratio of the sample to a certified standard material:

$$\delta^{R} = \left(\frac{R_{Sample}}{R_{Standard}} - 1\right) x\ 1000$$

where R represents the ratio of the abundance of the heavy to the light isotope.

2.2 Iron isotopes

Iron has four naturally occurring stable isotopes (Table 1) and a relative abundance in the Earth's crust of ~5 % (Taylor and McLennan, 1985). Nevertheless, the modern oxic ocean is strongly depleted and heterogeneously distributed with respect to iron (Gordon et al., 1982), which arise from the insolubility of oxidized Fe^{3+}. Figure 3 summarizes the modern in- and outfluxes of iron and their respective (strongly variable) isotopic compositions.

In reducing marine environments, however, iron is very soluble as Fe^{2+}. Therefore, it is expected that the anoxic Archean ocean was enriched and homogeneously distributed in Fe^{2+} (Johnson et al., 2008). Such a ferruginous ocean was a prerequisite for the deposition of proximal (Superior Type) iron formations, which resulted from local oxidation of Fe^{2+} and subsequent formation and precipitation of Fe^{3+}-minerals on the continental shelf (Isley and Abbott, 1999). The precise oxidation mechanism remains a matter of debate in the scientific community. The abiotic oxidation of Fe^{2+} by UV light (Cairns-Smith, 1978) was recently shown to be an unlikely mechanism (Konhauser et al., 2007). However, iron oxidation can proceed abiotically by oxidants such as O_2, which would suggest the local availability of oxygen (and possibly oxygenic photosynthesis) in the upper water column (Cloud, 1973). Alternatively, iron was oxidized biotically by anoxygenic phototrophic bacteria, which use Fe^{2+} as an electron donor (Kappler et al., 2005).

The abiotic as well as the biotic oxidation of iron is accompanied by large isotope fractionations, thereby enriching the heavy isotopes in the more oxidized species (Beard and Johnson, 2004; Croal et al., 2004; Welch et al., 2003). The transition from a homogeneous ferruginous ocean towards more oxidized conditions may change the seawater and sedimentary Fe isotopic composition (i.e. the Fe isotopic composition of contemporaneous IFs, Rouxel et al., 2005; Anbar and Rouxel, 2007). It is, however, difficult to distinguish between both mechanisms by the use of Fe isotopes. Furthermore, other processes

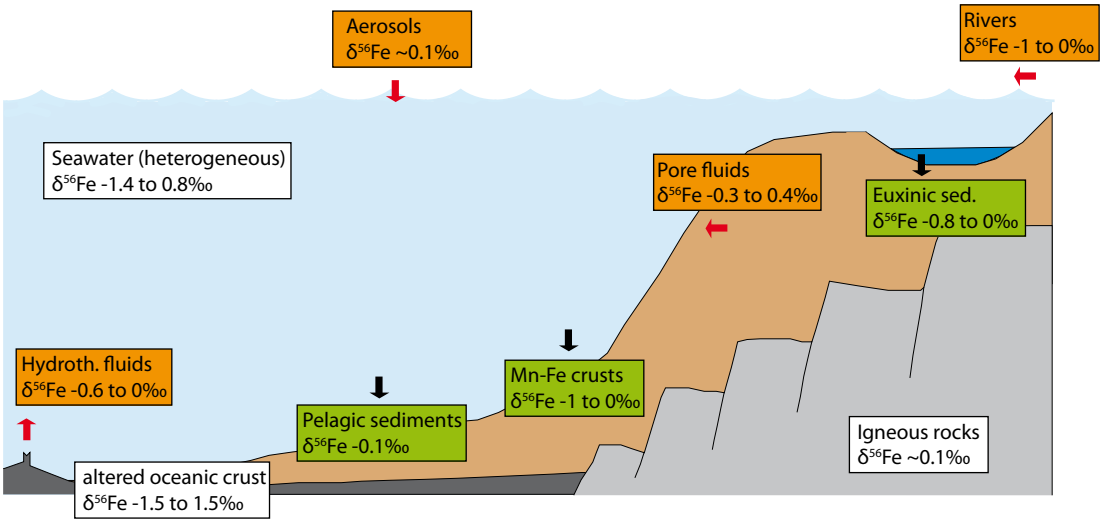

FIGURE 3: Schematic illustration of the Fe isotopic composition of the most relevant fluxes and reservoirs in the modern marine environment. In-fluxes are shown in orange boxes, out-fluxes in green boxes, respectively. The Fe isotopic composition of reservoirs is indicated in white boxes (Anbar and Rouxel, 2007, and references therein). The large variability as well as the similarity in the isotopic composition of most fluxes is striking. Importantly, the seawater Fe isotopic composition is heterogeneous in the modern ocean because of the insolubility of iron in oxic aquatic systems (Conway and John, 2014).

Table 1: Iron and molybdenum isotope abundances

Iron		**Molybdenum**	
Isotope	abundance (%)	Isotope	abundance (%)
^{54}Fe	5.8	^{92}Mo	14.84
^{56}Fe	91.72	^{94}Mo	9.25
^{57}Fe	2.2	^{95}Mo	15.92
^{58}Fe	0.28	^{96}Mo	16.68
		^{97}Mo	9.55
		^{98}Mo	24.13
		^{100}Mo	9.63

* after de Laeter et al. (2003)

apart from changes in the oxidation state are also accompanied by Fe isotopic fractionation, i.e. mineral formation processes (Beard and Johnson, 2004; Guilbaud et al., 2011; Guilbaud et al., 2010; Wiesli et al., 2004). Also, the bacterial reduction of iron cause significant Fe isotope fractionations (Johnson et al., 2005). Depending on the depositional history of the analyzed sediments and the abundant mineral species, all these fractionation processes need to be taken into account, when reconstructing ancient redox conditions by the use of Fe isotopes (see chapters II to III for more detailed explanations).

2.3 Molybdenum isotopes

Molybdenum has seven naturally occurring stable isotopes (Table 1). The abundance of molybdenum in the Earth's crust is relatively low (1ppm) (Taylor and McLennan, 1985). In contrast to Fe, Mo forms very unreactive molybdate ions (MoO_4^{2-}) in oxic oceans. It therefore represents the most abundant transition metal in the modern ocean (105 nM) with a residence time of ~440 ka (Miller et al., 2011), which implies a globally homogeneous distribution in respect of concentration and isotopic composition (Fig. 4). The modern sources and sinks of marine Mo and their respective Mo isotopic compositions are summarized in Fig. 4. Most importantly, the adsorption onto Mn oxides represents the main outflux of Mo in oxic settings, thereby preferentially adsorbing isotopically light Mo (Barling and Anbar, 2004). As a consequence, the remaining modern marine Mo reservoir is isotopically heavy. In sulfidic marine settings, molybdate transforms to thiomolybdate, which is efficiently removed from solution by adsorption onto organic matter or the precipitation of Mo-Fe-sulfides (Helz et al., 1996; Helz et al., 2011; Tribovillard et al., 2004). The near quantitative removal of Mo in such settings might preserve the Mo isotope signal in such sediments (i.e. organic-rich black shales). The Mo isotopic composition of global seawater (and euxinic sediments such as organic-rich black shales) may, thus, depend on the areal extension of oxic relative to sulfidic conditions. For example, an increase in the seawater $\delta^{98}Mo$ value (and the $\delta^{98}Mo$ value of euxinic black shales) is expected in the course of global ocean oxygenation (Arnold et al., 2004).

However, the application of Mo isotopes as a 'global paleo-redox proxy' is complicated by several aspects. First, the input was significantly lower during Archean times because of limited sulfide oxidation

in a predominantly anoxic environment. As a consequence, the seawater Mo reservoir was probably significantly smaller and possibly heterogeneously distributed (Scott et al., 2008). Furthermore, the assumption of quantitative Mo removal in euxinic environments is very simplified, particularly when considering environments with relatively low H_2S_{aq} concentrations. In respective settings large isotope fractionations can occur, which has implications on the local sedimentary as well as the seawater Mo isotopic composition. It is therefore critical to consider the Mo isotope data in a broader context, particularly regarding the local depositional environment (see chapters I for more detailed explanations).

In summary, isotope analyses of redox sensitive elements such as Mo and Fe in appropriate sediments have the potential to trace changes of ancient environmental redox states. The combination of Mo- and Fe isotopes is particularly promising because of their complementary behavior during redox-changes. However, several other parameters apart from redox changes (i.e. biologic activity and the availability of H_2S_{aq}) also have large implications for the sedimentary isotopic composition. A detailed understanding of the local depositional environment and the operating processes during sedimentation and diagenesis are therefore essential.

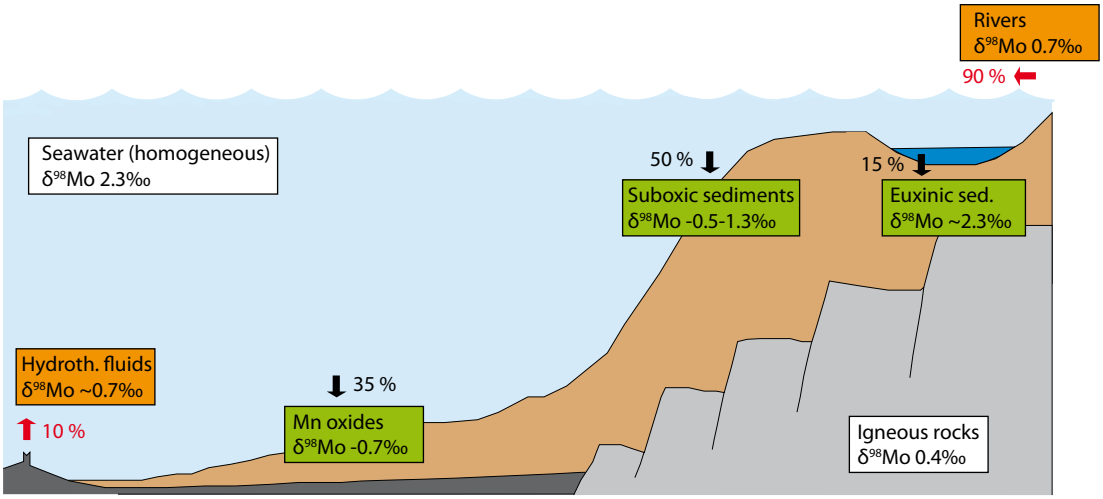

FIGURE 4: Schematic illustration of the Mo isotopic composition of the most relevant fluxes and reservoirs in the modern marine environment. In-fluxes are shown in orange boxes (Archer and Vance, 2008; McManus et al., 2006), out-fluxes in green boxes, respectively (Poulson et al., 2006, and references therein). The Mo isotopic composition of reservoirs is indicated in white boxes (Siebert et al., 2003; Voegelin et al., 2014). Numbers indicate the relative contribution of the flux (Scott et al., 2008). The seawater Mo reservoir is homogeneously distributed due to the stability of molybdate ions in oxic seawater. Isotope fractionations during adsorption onto Mn oxides cause the enrichment of light isotopes in respective sediments, leaving behind an isotopically heavy ocean. This seawater Mo isotope signal may be preserved in euxinic sediments, where the transformation of molybdate to particle reactive thiomolybdate causes near quantitative removal of Mo. As a consequence of the very efficient Mo removal, respective settings account for 15 % of the global Mo sink, although the areal extension of euxinic conditions is less than 1 % of the global ocean (Scott et al., 2008).

3. Overview of the cumulative dissertation

In the following three chapters of this cumulative dissertation various sediments from very different depositional settings were geochemically analyzed. By the use of 'non-traditional' stable isotope data of redox-sensitive elements (Fe, Mo) and the further complementation by major element and 'traditional' stable isotope data (C, O, S) the marine environmental conditions, which prevailed during deposition, are reconstructed. Thereby, the necessity to consider the isotopic proxy signals in the context of the local depositional environment is highlighted. The age of the analyzed sediments ranges from late Archean (Chapter I) to early Paleoproterozoic (Chapter II) to late Neoproterozoic (Chapter III), thus, covering time periods of major environmental changes (Fig. 1).

In CHAPTER I alternations of organic-rich black shales and siderite-rich iron formations from the Hamersley Group, Western Australia, were analyzed for the molybdenum, carbon and oxygen isotopic composition. The consideration of organic-rich black shales as well as siderite-rich iron formations helps to better understand the Mo burial pathway in each depositional environment and the consequential implications for the sedimentary and seawater Mo isotopic composition. The observed temporal trends in the sedimentary Mo isotopic composition combined with a Mo-flux box-model suggest regional/global changes in the oceanic redox-state with time. The depositional age of these sediments is bracketed between 2.6 and 2.5 Ga. This transitional time period before the GOE may denote the first local formation of near surface oxygen oases and so-called 'whiffs' of oxygen.

The marine redox evolution during the time period immediately before the GOE is considered in CHAPTER II. The analyzed iron formations from the Koegas Subgroup, Transvaal Supergroup, South Africa, were deposited around 2.48 Ga ago (Kendall et al., 2013). The combination of Mo and Fe isotope data from these sediments provides important constraints on the behavior of the respective redox sensitive elements in such settings and highlights the need to distinguish between their local and global implications. Comparing the results with isotopic data from a modern anoxic lake equivalent and other Precambrian sediments, the coupled Mo and Fe isotope data suggest the deposition along an anoxic-oxic chemocline in the vicinity of a local oxygen oasis. The expansion of oxygenic photosynthetic activity and the coupled dispersion of such near shore oxygen oases may have initiated the subsequent GOE.

The study in CHAPTER III deals with the question of the timing and the extent of deep ocean oxygenation, which may have represented the last major redox change towards a modern-like well-oxygenated world. Several studies link deep ocean oxygenation to the second major oxygenation event, which in turn may be linked to major biological evolutions during the late Neoproterozoic and Precambrian-Cambrian transition (Canfield et al., 2007; Chen et al., 2015; Fike et al., 2006). New S, Fe, and Mo isotopic data and precise U-Pb zircon dating of late Neoproterozoic black shales from the Teplá-Barrandian Unit, Czech Republic, are presented in this chapter. The results create a detailed picture of the local depositional setting and its variation with time. Coupled with this knowledge, the molybdenum isotope data strongly challenge the general view of deep ocean oxygenation close to the Precambrian-Cambrian boundary.

4. References

Anbar, A.D., Duan, Y., Lyons, T.W., Arnold, G.L., Kendall, B., Creaser, R.A., Kaufman, A.J., Gordon, G.W., Scott, C., Garvin, J., Buick, R., 2007. A Whiff of Oxygen Before the Great Oxidation Event? Science 317, 1903-1906.

Anbar, A.D., Rouxel, O., 2007. Metal stable isotopes in paleoceanography. Annu. Rev. Earth Planet. Sci. 35, 717-746.

Archer, C., Vance, D., 2008. The isotopic signature of the global riverine molybdenum flux and anoxia in the ancient oceans. Nature Geoscience 1, 597-600.

Arnold, G.L., Anbar, A., Barling, J., Lyons, T., 2004. Molybdenum isotope evidence for widespread anoxia in mid-Proterozoic oceans. Science 304, 87-90.

Asael, D., Tissot, F.L., Reinhard, C.T., Rouxel, O., Dauphas, N., Lyons, T.W., Ponzevera, E., Liorzou, C., Chéron, S., 2013. Coupled molybdenum, iron and uranium stable isotopes as oceanic paleoredox proxies during the Paleoproterozoic Shunga Event. Chemical Geology 362, 193-210.

Barling, J., Anbar, A., 2004. Molybdenum isotope fractionation during adsorption by manganese oxides. Earth and Planetary Science Letters 217, 315-329.

Beard, B.L., Johnson, C.M., 2004. Fe isotope variations in the modern and ancient earth and other planetary bodies. Reviews in Mineralogy and Geochemistry 55, 319-357.

Bekker, A., Holland, H., 2012. Oxygen overshoot and recovery during the early Paleoproterozoic. Earth and Planetary Science Letters 317, 295-304.

Bekker, A., Holland, H., Wang, P.-L., Rumble, D., Stein, H., Hannah, J., Coetzee, L., Beukes, N., 2004. Dating the rise of atmospheric oxygen. Nature 427, 117-120.

Bigeleisen, J., 1965. Chemistry of Isotopes Isotope chemistry has opened new areas of chemical physics, geochemistry, and molecular biology. Science 147, 463-471.

Butterfield, N., 2009. Oxygen, animals and oceanic ventilation: an alternative view. Geobiology 7, 1-7.

Cairns-Smith, A., 1978. Precambrian solution photochemistry, inverse segregation, and banded iron formations. Nature 276, 807-808.

Canfield, D., 1998. A new model for Proterozoic ocean chemistry. Nature 396, 450-453.

Canfield, D.E., 2005. The early history of atmospheric oxygen: homage to Robert M. Garrels. Annu. Rev. Earth Planet. Sci. 33, 1-36.

Canfield, D.E., Poulton, S.W., Narbonne, G.M., 2007. Late-Neoproterozoic deep-ocean oxygenation and the rise of animal life. Science 315, 92-95.

Catling, D.C., Zahnle, K.J., McKay, C.P., 2001. Biogenic methane, hydrogen escape, and the irreversible oxidation of early Earth. Science 293, 839-843.

Chen, X., Ling, H.-F., Vance, D., Shields-Zhou, G.A., Zhu, M., Poulton, S.W., Och, L.M., Jiang, S.-Y., Li, D., Cremonese, L., 2015. Rise to modern levels of ocean oxygenation coincided with the Cambrian radiation of animals. Nature communications 6.

Cloud, P., 1973. Paleoecological significance of the banded iron-formation. Economic Geology 68, 1135-1143.

Conway, T.M., John, S.G., 2014. Quantification of dissolved iron sources to the North Atlantic Ocean. Nature 511, 212-215.

Croal, L.R., Johnson, C.M., Beard, B.L., Newman, D.K., 2004. Iron isotope fractionation by Fe (II)-oxidizing photoautotrophic bacteria. Geochimica et cosmochimica acta 68, 1227-1242.

Eigenbrode, J.L., Freeman, K.H., 2006. Late Archean rise of aerobic microbial ecosystems. Proceedings of the National Academy of Sciences 103, 15759-15764.

Farquhar, J., Bao, H., Thiemens, M., 2000. Atmospheric influence of Earth's earliest sulfur cycle. Science 289, 756-758.

Fike, D., Grotzinger, J., Pratt, L., Summons, R., 2006. Oxidation of the Ediacaran ocean. Nature 444, 744-747.

Frei, R., Gaucher, C., Poulton, S.W., Canfield, D.E., 2009. Fluctuations in Precambrian atmospheric

oxygenation recorded by chromium isotopes. Nature 461, 250-253.

Gaillard, F., Scaillet, B., Arndt, N.T., 2011. Atmospheric oxygenation caused by a change in volcanic degassing pressure. Nature 478, 229-232.

Gordon, R., Martin, J., Knauer, G., 1982. Iron in north-east Pacific waters.

Guilbaud, R., Butler, I.B., Ellam, R.M., 2011. Abiotic pyrite formation produces a large Fe isotope fractionation. Science 332, 1548-1551.

Guilbaud, R., Butler, I.B., Ellam, R.M., Rickard, D., 2010. Fe isotope exchange between Fe (II) aq and nanoparticulate mackinawite (FeS m) during nanoparticle growth. Earth and Planetary Science Letters 300, 174-183.

Guo, Q., Strauss, H., Kaufman, A.J., Schröder, S., Gutzmer, J., Wing, B., Baker, M.A., Bekker, A., Jin, Q., Kim, S.-T., 2009. Reconstructing Earth's surface oxidation across the Archean-Proterozoic transition. Geology 37, 399-402.

Hannah, J.L., Bekker, A., Stein, H.J., Markey, R.J., Holland, H.D., 2004. Primitive Os and 2316 Ma age for marine shale: implications for Paleoproterozoic glacial events and the rise of atmospheric oxygen. Earth and Planetary Science Letters 225, 43-52.

Helz, G., Miller, C., Charnock, J., Mosselmans, J., Pattrick, R., Garner, C., Vaughan, D., 1996. Mechanism of molybdenum removal from the sea and its concentration in black shales: EXAFS evidence. Geochimica et Cosmochimica Acta 60, 3631-3642.

Helz, G.R., Bura-Nakić, E., Mikac, N., Ciglenečki, I., 2011. New model for molybdenum behavior in euxinic waters. Chemical Geology 284, 323-332.

Hoffman, P.F., 1991. Did the breakout of Laurentia turn Gondwanaland inside-out. Science 252, 1409-1412.

Hoffman, P.F., Kaufman, A.J., Halverson, G.P., Schrag, D.P., 1998. A Neoproterozoic snowball earth. Science 281, 1342-1346.

Holland, H.D., 2005. 100th anniversary special paper: sedimentary mineral deposits and the evolution of earth's near-surface environments. Economic Geology 100, 1489-1509.

Holland, H.D., 2006. The oxygenation of the atmosphere and oceans. Philosophical Transactions of the Royal Society B: Biological Sciences 361, 903-915.

Isley, A.E., Abbott, D.H., 1999. Plume-related mafic volcanism and the deposition of banded iron formation. Journal of Geophysical Research 104, 15461-15415,15477.

Johnson, C.M., Beard, B.L., Roden, E.E., 2008. The iron isotope fingerprints of redox and biogeochemical cycling in modern and ancient Earth. Annu. Rev. Earth Planet. Sci. 36, 457-493.

Johnson, C.M., Roden, E.E., Welch, S.A., Beard, B.L., 2005. Experimental constraints on Fe isotope fractionation during magnetite and Fe carbonate formation coupled to dissimilatory hydrous ferric oxide reduction. Geochimica et Cosmochimica Acta 69, 963-993.

Kappler, A., Pasquero, C., Konhauser, K.O., Newman, D.K., 2005. Deposition of banded iron formations by anoxygenic phototrophic Fe (II)-oxidizing bacteria. Geology 33, 865-868.

Karhu, J.A., Holland, H.D., 1996. Carbon isotopes and the rise of atmospheric oxygen. Geology 24, 867-870.

Kendall, B., Komiya, T., Lyons, T.W., Bates, S.M., Gordon, G.W., Romaniello, S.J., Jiang, G., Creaser, R.A., Xiao, S., McFadden, K., 2015. Uranium and molybdenum isotope evidence for an episode of widespread ocean oxygenation during the late Ediacaran Period. Geochimica et Cosmochimica Acta 156, 173-193.

Kendall, B., Reinhard, C.T., Lyons, T.W., Kaufman, A.J., Poulton, S.W., Anbar, A.D., 2010. Pervasive oxygenation along late Archaean ocean margins. Nature Geoscience 3, 647-652.

Kendall, B., van Acken, D., Creaser, R.A., 2013. Depositional age of the early Paleoproterozoic Klipputs Member, Nelani Formation (Ghaap Group, Transvaal Supergroup, South Africa) and implications for low-level Re–Os geochronology and Paleoproterozoic global correlations. Precambrian Research 237, 1-12.

Konhauser, K.O., Amskold, L., Lalonde, S.V., Posth, N.R., Kappler, A., Anbar, A., 2007. Decoupling photochemical Fe (II) oxidation from shallow-water BIF deposition. Earth and Planetary Science Letters 258, 87-100.

Kump, L.R., Barley, M.E., 2007. Increased subaerial volcanism and the rise of atmospheric oxygen 2.5

billion years ago. Nature 448, 1033-1036.

Kump, L.R., 2008. The rise of atmospheric oxygen. Nature 451, 277-278.

Kurzweil, F., Claire, M., Thomazo, C., Peters, M., Hannington, M., Strauss, H., 2013. Atmospheric sulfur rearrangement 2.7 billion years ago: Evidence for oxygenic photosynthesis. Earth and Planetary Science Letters 366, 17-26.

Lenton, T.M., Boyle, R.A., Poulton, S.W., Shields-Zhou, G.A., Butterfield, N.J., 2014. Co-evolution of eukaryotes and ocean oxygenation in the Neoproterozoic era. Nature Geoscience 7, 257-265.

Love, G.D., Grosjean, E., Stalvies, C., Fike, D.A., Grotzinger, J.P., Bradley, A.S., Kelly, A.E., Bhatia, M., Meredith, W., Snape, C.E., 2009. Fossil steroids record the appearance of Demospongiae during the Cryogenian period. Nature 457, 718-721.

Lyons, T.W., Reinhard, C.T., Planavsky, N.J., 2014. The rise of oxygen in Earth/'s early ocean and atmosphere. Nature 506, 307-315.

McManus, J., Berelson, W.M., Severmann, S., Poulson, R.L., Hammond, D.E., Klinkhammer, G.P., Holm, C., 2006. Molybdenum and uranium geochemistry in continental margin sediments: paleoproxy potential. Geochimica et Cosmochimica Acta 70, 4643-4662.

Miller, C.A., Peucker-Ehrenbrink, B., Walker, B.D., Marcantonio, F., 2011. Re-assessing the surface cycling of molybdenum and rhenium. Geochimica et Cosmochimica Acta 75, 7146-7179.

Och, L.M., Shields-Zhou, G.A., 2012. The Neoproterozoic oxygenation event: environmental perturbations and biogeochemical cycling. Earth-Science Reviews 110, 26-57.

Pavlov, A., Kasting, J., 2002. Mass-independent fractionation of sulfur isotopes in Archean sediments: strong evidence for an anoxic Archean atmosphere. Astrobiology 2, 27-41.

Planavsky, N.J., Asael, D., Hofmann, A., Reinhard, C.T., Lalonde, S.V., Knudsen, A., Wang, X., Ossa, F.O., Pecoits, E., Smith, A.J., 2014. Evidence for oxygenic photosynthesis half a billion years before the Great Oxidation Event. Nature geoscience.

Planavsky, N.J., McGoldrick, P., Scott, C.T., Li, C., Reinhard, C.T., Kelly, A.E., Chu, X., Bekker, A., Love, G.D., Lyons, T.W., 2011. Widespread iron-rich conditions in the mid-Proterozoic ocean. Nature 477, 448-451.

Poulson, R.L., Siebert, C., McManus, J., Berelson, W.M., 2006. Authigenic molybdenum isotope signatures in marine sediments. Geology 34, 617-620.

Riding, R., Fralick, P., Liang, L., 2014. Identification of an Archean marine oxygen oasis. Precambrian Research 251, 232-237.

Rouxel, O.J., Bekker, A., Edwards, K.J., 2005. Iron Isotope Constraints on the Archean and Paleoproterozoic Ocean Redox State. Science 307, 1088-1091.

Scott, C., Lyons, T., Bekker, A., Shen, Y., Poulton, S., Chu, X., Anbar, A., 2008. Tracing the stepwise oxygenation of the Proterozoic ocean. Nature 452, 456-459.

Sharp, Z., 2007. Principles of stable isotope geochemistry. Pearson Education Upper Saddle River, NJ.

Siebert, C., Nägler, T.F., von Blanckenburg, F., Kramers, J.D., 2003. Molybdenum isotope records as a potential new proxy for paleoceanography. Earth and Planetary Science Letters 211, 159-171.

Taylor, S.R., McLennan, S.M., 1985. The continental crust: its composition and evolution.

Tribovillard, N., Riboulleau, A., Lyons, T., Baudin, F., 2004. Enhanced trapping of molybdenum by sulfurized marine organic matter of marine origin in Mesozoic limestones and shales. Chemical Geology 213, 385-401.

Urey, H.C., 1947. The thermodynamic properties of isotopic substances. Journal of the Chemical Society (Resumed), 562-581.

Welch, S., Beard, B., Johnson, C., Braterman, P., 2003. Kinetic and equilibrium Fe isotope fractionation between aqueous Fe (II) and Fe (III). Geochimica et Cosmochimica Acta 67, 4231-4250.

Wiesli, R.A., Beard, B.L., Johnson, C.M., 2004. Experimental determination of Fe isotope fractionation between aqueous Fe (II), siderite and "green rust" in abiotic systems. Chemical Geology 211, 343-362.

Wille, M., Kramers, J., Nägler, T.F., Beukes, N., Schröder, S., Meisel, T., Lacassie, J., Voegelin, A., 2007. Evidence for a gradual rise of oxygen between 2.6 and 2.5 Ga from Mo isotopes and Re-PGE signatures in shales. Geochimica et Cosmochimica Acta 71, 2417-2435.

CHAPTER I

Continuously increasing δ^{98}Mo values in Neoarchean black shales and Iron formations from the Hamersley Basin

1. Abstract

We present Mo-, C- and O-isotope data from black shales, carbonate- and oxide facies iron formations from the Hamersley Group, Western Australia, that range in age from 2.6 to 2.5 billion years. The data show a continuous increase from near crustal δ^{98}Mo values of around 0.50 ‰ for the oldest Marra Mamba and Wittenoom formations towards higher values of up to 1.51 ‰ for the youngest sample of the Brockman Iron Formation. Thereby, the trend in increasing δ^{98}Mo values is portrayed by both, carbonate facies iron formations and black shales. Considering the positive correlation between Mo concentration and total organic carbon, we argue that this uniformity is best explained by molybdate adsorption onto organic matter in carbonate iron formations and scavenging of thiomolybdate onto sulfurized organic matter in black shales. A temporal increase in the seawater δ^{98}Mo over the period 2.6-2.5 Ga is observed assuming an overall low Mo isotope fractionation during both Mo removal processes. Oxide facies iron formations

show lowest Mo concentrations, lowest total organic carbon and slightly lower δ^{98}Mo compared to nearly contemporaneous black shales. This may indicate that in iron formation settings with very low organic matter burial rates, the preferential adsorption of light Mo isotopes onto Fe-(oxyhydr)oxides becomes more relevant.

A similar Mo-isotope pattern was previously found in contemporaneous black shales and carbonates of the Griqualand West Basin, South Africa. The consistent and concomitant increase in δ^{98}Mo after 2.54 billion years ago suggests a more homogenous distribution of seawater molybdate with uniform isotopic composition in various depositional settings within the Hamersley Basin and the Griqualand West Basin. The modeling of the oceanic Mo inventory in relation to the Mo in- and outflux suggests that the long-term build-up of an isotopically heavy seawater Mo reservoir requires a sedimentary sink for isotopically light Mo. The search for this sink (i.e. adsorption onto Mn-oxides in well oxygenated surface oceans and/or subaerial environments or incomplete thiomolybdate formation in weakly sulfidic settings) remains debated, but its relevance becomes more important closer to the Great Oxidation Event and is probably related to already weakly oxidizing conditions even prior to the 2.5 Ga “whiff of oxygen”.

2. Introduction

The exact timing and evolution of the oxygenation of Earth’s atmosphere and oceans still remain debated in the scientific community. The generally accepted model is of a Great Oxidation Event (GOE) between 2.45 and 2.32 Ga (Bekker et al., 2004; Hannah et al., 2004; Holland, 2006) when atmospheric oxygen levels rose above 10^{-5} of present atmospheric level (PAL) (Farquhar et al., 2000; Pavlov and Kasting, 2002). This view has been challenged by more recent studies that suggest at least locally a much earlier first appearance of free atmospheric oxygen, which were most likely subjected to strong fluctuations (Anbar et al., 2007; Crowe et al., 2013; Duan et al., 2010; Frei et al., 2009; Kurzweil et al., 2013; Planavsky et al., 2014; Reinhard et al., 2013; Voegelin et al., 2010; Wille et al., 2007). These (temporal) increases in atmospheric oxygen levels were tightly coupled with surface ocean oxygenation and the development of a stratified water column with anoxic deep waters (Kendall et al., 2010; Reinhard et al., 2009). However, the possible causes for environmental oxygenation during Meso- to Neoarchean are still a matter of debate, as described in detail by Catling (2014).

Due to their redox sensitive behavior, some transition metals (V, Cr, Fe, Mo, Re) and, particularly, their isotopic variations, can be used as proxies for environmental redox changes. Molybdenum, dissolved as molybdate (MoO_4^{2-}), is one of the most abundant transition metals in the modern oxygenated oceans. Its long residence time between 440 and 750 kyrs depending on fluxes and mass balance calculations (Miller et al., 2011; Morford and Emerson, 1999) results in a globally homogeneous modern seawater Mo-isotopic composition of 2.3 ‰ in δ^{98}Mo (Siebert et al., 2003). This seawater δ^{98}Mo value is in stark contrast with an average δ^{98}Mo value of 0.4 ‰ of the upper continental crust (Voegelin et al., 2014), the main source of oceanic Mo. The build-up of an isotopically heavy Mo oceanic reservoir is associated with Mo isotopic

fractionation during adsorption of MoO_4^{2-} onto mineral surfaces. Recent X-ray absorption spectroscopy studies (XANES and EXAFS) show that the coordination of tetrahedrally coordinated molybdate (MoO_4^{2-}) may change during adsorption (Wasylenky et al., 2008; Kashiwabara et al., 2011). With this, adsorbed Mo forms outer sphere complexes on ferrihydrite and Al-oxides that are partly tetrahedrally and partly octahedrally coordinated. By contrast, Mo forms inner sphere complexes on Mn- and Ti-oxides that are octahedrally coordinated (Kashiwabara et al., 2011). The Mo-coordination is of particular interest for Mo-isotope studies, as octahedrally bound Mo has longer and therefore weaker Mo-O bonds than tetrahedrally bound Mo. As a consequence, isotopically light Mo is preferentially incorporated into octahedral coordination sites. Therefore, adsorption onto Mn-oxides causes large differences in the Mo-isotopic composition ($\Delta^{98}Mo_{Mn\text{-}oxides\text{-}seawater} = \delta^{98}Mo_{Mn\text{-}oxides} - \delta^{98}Mo_{seawater}$ = -3 ‰; Barling et al., 2001), whereas the difference is somewhat smaller when molybdate adsorbs onto ferrihydrite ($\Delta^{98}Mo_{ferrihydrite\text{-}seawater} = \delta^{98}Mo_{ferrihydrite} - \delta^{98}Mo_{seawater}$ = -1.1 ‰; Goldberg et al., 2009). Under euxinic conditions with H_2S concentrations above 11 µmol L^{-1} (hereafter called as strongly euxinic conditions), molybdate is almost quantitatively transformed to thiomolybdate (MoS_4^{2-}) (Helz et al., 1996; Nägler et al., 2011), which is readily removed from solution either by adsorption onto organic matter (Dahl et al., 2010; McManus et al., 2006) or by the formation of authigenic Fe-Mo-sulfides (Helz et al., 2011). As a consequence, the $\delta^{98}Mo$ in black shales deposited below such a euxinic water column (hereafter called euxinic sediments) should reflect the isotopic composition of seawater molybdate. Modern euxinic sediments from the Black Sea exhibit the seawater isotopic composition of 2.3 ‰ (Nägler et al., 2011; Neubert et al., 2008), but are slightly depleted in the heavy isotopes compared to the directly overlying water column suggesting a small net fractionation between thiomolybdate and authigenic sedimentary Mo of $\Delta^{98}Mo_{thiomolybdate\text{-}black\ shale} = \delta^{98}Mo_{black\ shale\text{-}} \delta^{98}Mo_{thiomolybdate}$ = -0.5 ± 0.3 ‰ (Nägler et al., 2011). This indicates that the removal is only nearly-quantitative even at very high H_2S concentrations. In intermediate redox milieus (e.g., weakly euxinic environments, defined here as environments with low free H_2S concentrations below 11µmol L^{-1} and suboxic environments, where $H_2S_{(aq)}$ is only present in the pore-water) the incomplete transformation to thiomolybdate (and the formation of intermediate oxythiomolybdate species $MoO_XS_{4-X}^{2-}$) can cause more significant net Mo isotope fractionations. Accordingly, sediments from weakly euxinic depositional environments may reflect almost the full spectrum of observed Mo-isotope variations (Neubert et al., 2008; Poulson et al., 2006; Siebert et al., 2006).

The oxidation of Mo^{4+} to Mo^{6+} and the formation of soluble molybdate is a prerequisite for large subsequent isotope fractionation. In aqueous environments with Eh higher than -0.4 V (at a pH of 8), molybdate is the thermodynamically stable species. By contrast, abiotic oxidation of other redox sensitive metals such as iron (Fe^{2+} oxidation to Fe^{3+} at Eh of -0.1 V), chromium (Cr^{3+} oxidation to Cr^{6+} at Eh of 0.3 V) or manganese (Mn^{2+} oxidation to Mn^{4+} at Eh > 0.5 V), need much higher redox potentials (Takeno, 2005). This means that even under very reducing and ferruginous conditions, molybdate remains thermodynamically stable as dissolved phase in seawater.

The goal of this study is to investigate the onset and mode of Neoarchean redox changes in the ocean-atmosphere system. For this purpose we expand the Mo-isotope data of Hamersley Basin sedimentary rocks presented by Duan et al. (2010) back in time, turning our attention to the Mo-isotopic evolution

in different Archean sedimentary settings. The distinction between different depositional environments within the same basin throughout the same time interval may provide a more detailed picture of the Neoarchean Mo-cycle as well as the evolution of the oceanic redox state at different deposition depths. We present Mo-isotope data from black shales as well as from carbonate and oxide facies iron formations (IF) from the Neoarchean Hamersley Basin, spanning a depositional age range of 2.6 to 2.5 Ga.

3. Geological setting and sample description

The samples of this study are sedimentary rocks obtained from drill cores ABDP#9 and Millstream#9 from the Hamersley Basin of Western Australia (Fig. 1). Stratigraphically, samples from Millstream#9 represent the Marra Mamba Formation and the lower part of the Wittenoom Formation, which have an age of ~2597 ± 5 Ma (Fig. 1; Trendall et al., 1998). Samples from ABDP#9 are slightly younger, transitioning from the upper part of the Wittenoom Formation (spherule layer: ~2541 +18/-15 Ma; Woodhead et al., 1998) into the Mt. Sylvia Formation, the Mt. McRae Shale (~2501 ± 8 Ma; Anbar et al., 2007) and the Dales Gorge Member of the Brockman Iron Formation (2495 ± 16 and 2461 ± 6 Ma; Trendall et al., 2004).

The Hamersley Basin reflects a deep shelf/platform environment below wave base and above the calcite compensation depth (Morris, 1993). Its depositional setting has been described as an outer-shelf environment that was separated from the coast by a carbonate barrier, which inhibited large inputs of terrigenous detrital material (Morris and Horwitz, 1983). The Marra Mamba Iron Formation mainly consists of laminated ferruginous chert and oxide- and carbonate facies iron formation (Klein and Gole, 1981; Krapež et al., 2003) with intercalations of shaly, Fe-rich carbonates (Morris and Horwitz, 1983). The lower Paraburdoo Member of the conformably overlying Wittenoom Formation consists mainly of thinly bedded calcitic/dolomitic/sideritic carbonates. The upper Bee Gorge Member of the Wittenoom Formation represents alternating grey-black shales and limestones/dolostones (Simonson et al., 1993). A several meter thick chert layer, called the Lower Chert, marks the transition to the Mt. Sylvia Formation, which is mainly composed of shales, siliciclastics, and chert units and capped by a 5 m thick layer of banded iron formation, the so called Bruno's Band (Krapež et al., 2003). The Mt. McRae Shale consists of two black shale layers (S1 and S2) that are separated by a Fe-carbonate unit (Anbar et al., 2007). Conformably overlying this is the Dales Gorge Member of the Brockman Iron Formation, which predominantly consists of alternating layers of chert and banded iron formation (Krapež et al., 2003). The metamorphic grade of the Hamersley Basin is sub-greenschist facies (i.e. prehnite-pumpellyte; McConchie, 1984; Tyler and Thorne, 1990; Anbar et al., 2007).

The samples analyzed for this study include 1) organic rich, black shales, 2) grey-greenish and Fe-rich shaly carbonates, and 3) banded iron formations. Black shales (1) are fine-grained and finely laminated. They show strong enrichments in organic carbon and pyrite, the latter mainly appearing as early diagenetic nodules and disseminated grains. Black shale deposits represent the most proximal setting (Beukes and Gutzmer, 2008). Greenish shale units (2) are also finely laminated. These samples contain less organic

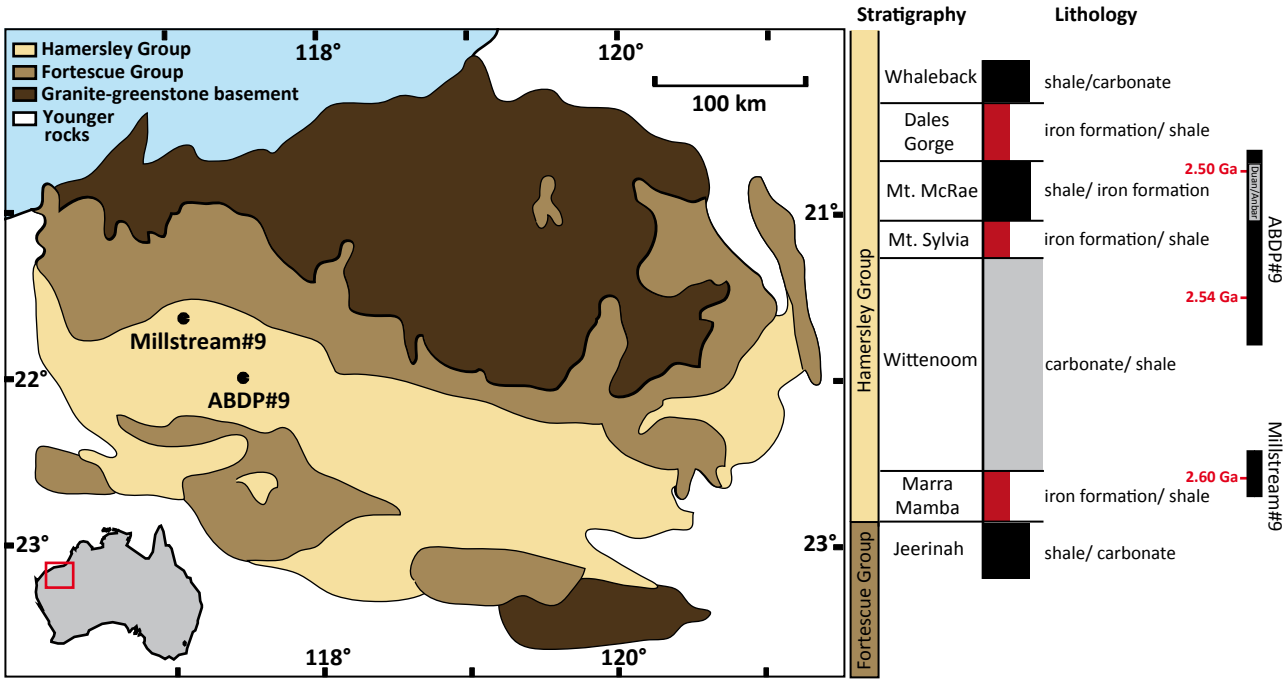

FIGURE 1: Geological map of the Pilbara Craton with drill core locations of ABDP#9 and Millstream#9. Also illustrated are the corresponding stratigraphic units and their predominant lithology. The bars on the far right site demonstrate which stratigraphic units are covered by both drill cores of this study and which parts of ABDP#9 were already analyzed by Anbar et al. (2007) and Duan et al. (2010). Also shown are a U-Pb zircon age (2.60 Ga; Trendall et al., 1998), a Pb-Pb age (2.54 Ga; Woodhead et al., 1998), and a Re-Os age (2.50 Ga; Anbar et al., 2007).

carbon and detrital material but are enriched in iron and carbonate. Most samples show disseminated Fe-carbonates in fine-grained chert matrices. Less common are later diagenetic coarse-grained rhombohedral carbonate grains. Beukes and Gutzmer (2008) argue that such samples represent relatively deep marine environments. Iron formations (3) have no detrital material and represent the most distal deep water facies (Beukes and Gutzmer, 2008). These samples show distinct bands of very fine grained chert alternating with bands of reddish hematite and coarse grained, idiomorphic magnetite crystals.

4. Methods

Major element concentrations were determined by X-ray fluorescence analyses (XRF) using the Bruker AXS Pioneer S4 at the University of Tuebingen. Glass beads were prepared by mixing 1.5 g of dried and powdered sample material with 7.5 g lithium tetraborate, which was fused at 1050 °C for 30 minutes. The loss of ignition was determined on a separate sample aliquot by the weight loss after 60 minutes of heating in a furnace at 1050 °C. For concentration measurements 32 standardized samples define

elemental calibration lines, with element specific analytical uncertainties is element specific (for Fe_2O_3 the 1σ standard error is 0.06 %).

To determine total organic carbon (TOC), powdered samples were decarbonized with 10 % HCl at room temperature and four-times rinsed with ultrapure H_2O (18.2 MΩ cm^{-1}). This procedure was repeated twice. The concentration of TOC (decarbonized samples) and total carbon (TC; of untreated bulk samples) were then measured by combustion with a Vario elemental analyzer. The total inorganic carbon component (TIC) was calculated as the difference between TC and TOC.

Carbonate carbon and oxygen isotope measurements were determined on bulk sample material that was treated with phosphoric acid (99 %) in a He-atmosphere at 90 °C for at least 150 minutes to fully assure complete dissolution of all carbonates including iron carbonates. Isotopic ratios of the evolving CO_2-gas were measured by continuous flow with a Gasbench II coupled to a Finnigan MAT 252 gas source mass spectrometer at the University of Tuebingen. Isotope ratios were calibrated with NBS18 (δ^{13}C of -5.00 ‰ and δ^{18}O of -22.96 ‰) and NBS19 (δ^{13}C of 1.95 ‰ and δ^{18}O of -2.20 ‰ relative to the Vienna Pee Dee Belemnite; V-PDB) and are reported in the δ-notation relative to the V-PDB standard:

$$\delta^{i}\mathrm{X} = \left(\frac{\left[\frac{^{i}X}{^{j}X}\right]\text{Sample}}{\left[\frac{^{i}X}{^{j}X}\right]\text{Standard}} - 1 \right)$$

where X is the respective element, i is the mass of the rare isotope, and j is the mass of the common isotope. δ-values are reported in ‰ by multiplication with a factor of 1000. The external reproducibility is 0.1 ‰ (2σ) for both, δ^{13}C and δ^{18}O.

For the determination of the carbon isotopic composition of the organic matter, a few milligrams of the dried and decarbonized sample material were flash combusted at 1050 °C. The evolving CO_2 gas was separated gas-chromatographically with a Carlo Erba NC 2500 elemental analyzer (EA). The EA was coupled to a Finnigan Delta^{+}XL for carbon isotope measurements using continuous flow mode. Results were calibrated to the in-house standard USGS 24 and are presented here in the δ-notation in per mill and relative to V-PDB.

Mo-isotope analyses follow the method described by Wille et al. (2013). Samples were ashed for 12 h at 600 °C to oxidize organic phases. An adequate amount of a ^{100}Mo-^{97}Mo double spike was added to 50-500 mg powdered sample material prior to sample digestion and Mo-purification. The double-spike method allows for the correction of the instrumental mass bias as well as mass fractionation that might be caused during chromatographic Mo-purification (Rudge et al., 2009). Samples were dissolved in Teflon beakers by sequential digestion steps using distilled HF, HNO_3 and HCl acids. Mo was purified using a combination of anion and cation exchange chromatography (i.e. using Dowex 1X8, 200-400 mesh and Dowex 50WX8 200-400 mesh resins, respectively) as described by Wille et al. (2013). Molybdenum isotopic ratios were measured on a multi-collector ICP-MS (ThermoFisher Scientific NeptunePlus) at the University of Tuebingen. Measurements of the in-house standard ZH-2, a Mo-rich sulfide that ran through

all chemical separation steps, yield a long-term reproducibility on δ^{98}Mo better than 0.09 ‰ (2σ). Results were calibrated using the Johnson Matthey ICP standard and are reported in the δ-notation relative to the NIST3134 standard (Goldberg et al., 2013), which was set to 0.25 ‰ following a proposal of Nägler et al. (2014):

$$\delta^{98}\mathrm{Mo} = \left(\frac{\left(\frac{^{98}Mo}{^{95}Mo}\right)_{\mathrm{Sample}}}{\left(\frac{^{98}Mo}{^{95}Mo}\right)_{\mathrm{NIST3134}}} - 1 \right) \mathrm{x}\ 1000$$

5. Results

In order to characterize the set of 23 samples we distinguish petrologically and chemically between black shales, and carbonate and oxide facies iron formations (Table 1). Black shales are rich in TOC, with values between 0.8 and 5.5 weight percent (wt%), have Fe_2O_3 below 15 wt% and Al_2O_3 above 10 wt%. In contrast, iron formations have Fe_2O_3 above 25 wt% and Al_2O_3 below 5 wt% (and most of them even below 1 wt%). We further distinguish between carbonate and oxide dominated iron formation facies, as well as mixtures of both (carb-IF, ox-IF and carb/ox-IF, respectively). To do so, we calculated the iron formation carbonate fraction assuming that all Ca and Mg are bound in carbonate. We further assumed that all remaining carbonate is ferrous carbonate. All samples with more than 70 % of the total iron bound in ferrous carbonate we refer to as carbonate facies iron formation, samples with less than 10 % we refer to as oxide facies iron formation, and intermediate samples we refer to as oxide/carbonate facies iron formation. This distinction is confirmed by petrological observations (Fig. 2).

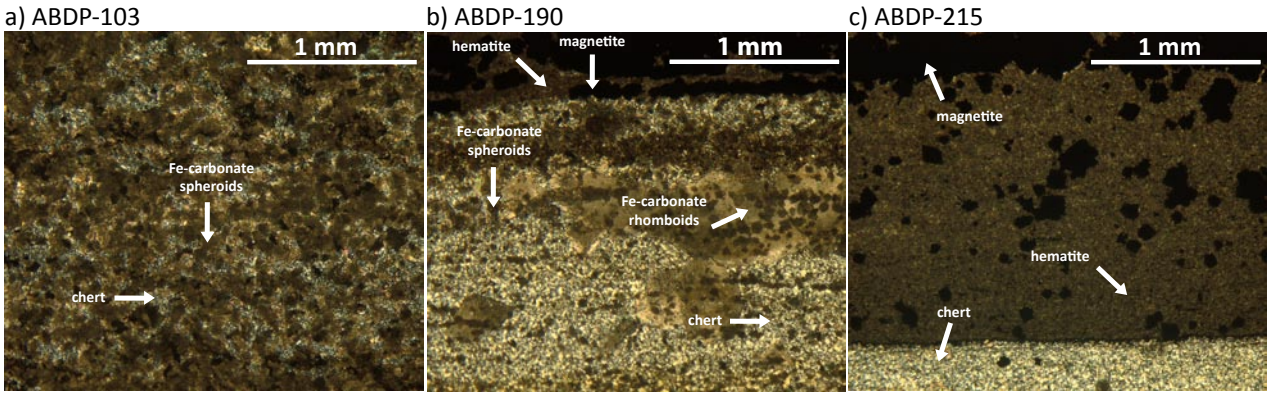

FIGURE 2: Reflected light microscopy images of samples ABDP-103 (a), ABDP-190 (b) and ABDP-215 (c). (a) shows iron carbonate spheroids in a fine grained chert matrix. Iron carbonate rhombs and iron carbonate spheroids within chert are observed in (b). A layer of fine grained hematite and large magnetite crystals marks a distinct boundary. (c) shows a fine chert matrix separated from a thick band of hematite filled with magnetite crystals.

Table 1: Main elements of drill cores ABDP#9 and Millstream#9

Sample	depth (m)	Formation	Lithology	SiO_2 (wt%)	Al_2O_3 (wt%)	TiO_2 (wt%)	Fe_2O_3 (wt%)	MnO (wt%)	MgO (wt%)	CaO (wt%)	Na_2O (wt%)	K_2O (wt%)	P_2O_5 (wt%)	LOI (wt%)	sum
ABDP-103	102.55	Dales Gorge	carb-IF	12.2	0.0	0.0	53.4	0.2	4.1	1.0	0.0	0.0	0.1	28.0	99.1
ABDP-114	114.4	Mt McRae	black shale	21.9	5.6	0.2	2.9	0.5	11.9	20.4	0.2	2.4	0.0	33.4	99.3
ABDP-133	132.7	Mt McRae	black shale	55.1	11.4	0.4	10.3	0.4	3.6	2.8	0.3	3.2	0.1	10.7	98.4
ABDP-164	163.5	Mt McRae	carb-IF	11.2	4.1	0.1	44.2	0.4	8.4	1.9	0.1	1.5	0.1	29.5	101.4
ABDP-177	176.7	Mt McRae	black shale	56.7	11.9	0.5	9.9	0.1	2.2	0.5	0.5	5.9	0.1	10.5	98.7
ABDP-180	179.8	Mt McRae	carb-IF	32.4	0.6	0.0	30.1	0.7	5.4	5.9	0.0	0.0	0.1	24.4	99.6
ABDP-190	190.2	Mt Sylvia	ox/carb-IF	12.9	0.0	0.0	65.7	0.3	2.7	2.8	0.1	0.0	0.1	15.1	99.6
ABDP-215	214.5	Mt Sylvia	ox-IF	16.4	0.3	0.0	76.3	0.0	2.4	2.1	0.1	0.0	0.1	1.9	99.6
ABDP-219	218.65	Mt Sylvia	black shale	52.0	12.8	0.5	13.3	0.1	3.5	1.3	0.1	6.1	0.1	9.2	98.9
ABDP-220	219.95	Mt Sylvia	ox-IF	58.5	0.0	0.0	37.6	0.0	0.7	1.1	0.1	0.0	0.0	1.0	98.9
ABDP-240	239.5	Wittenoom	black shale	64.8	12.7	0.5	6.8	0.1	3.0	1.3	0.8	3.2	0.0	6.2	99.3
ABDP-259	259.38	Wittenoom	black shale	64.9	10.8	0.4	10.2	0.1	3.4	1.4	0.6	1.4	0.1	5.8	99.3
ABDP-260	259.63	Wittenoom	limestone	9.0	0.1	0.0	1.5	0.6	0.8	48.3	0.1	0.0	0.0	38.6	99.0
ABDP-292	291.6	Wittenoom	carb-IF	22.0	3.6	0.2	28.5	0.4	6.9	11.5	0.1	0.3	0.0	26.2	99.6
ABDP-316	316	Wittenoom	black shale	59.3	16.1	0.6	5.5	0.1	4.2	1.4	3.5	3.6	0.1	4.7	99.2
ABDP-332	332	Wittenoom	limestone	0.9	0.1	0.0	0.8	0.2	0.6	54.8	0.1	0.0	0.0	43.0	100.6
ABDP-335	334.55	Wittenoom	carb-IF	8.6	0.8	0.1	29.3	0.5	6.8	19.3	0.1	0.0	0.1	34.4	99.9
ABDP-340	340	Wittenoom	black shale	57.1	15.9	0.7	6.9	0.2	4.5	2.1	1.3	3.1	0.1	7.5	99.3
ABDP-355	355.18	Wittenoom	limestone	10.7	3.1	0.1	1.7	0.9	1.0	44.4	0.6	0.6	0.0	36.0	99.0
Mill-205	205	Wittenoom	black shale	60.4	16.7	0.6	2.5	0.1	2.5	1.0	0.1	11.4	0.1	4.1	99.4
Mill-206	205.5	Wittenoom	black shale	58.3	13.5	0.7	1.8	0.1	4.1	3.7	0.1	8.2	0.1	8.7	99.3
Mill-217	217	Wittenoom	black shale	59.3	17.7	0.9	1.9	0.0	2.6	0.4	0.1	10.7	0.1	5.6	99.2
Mill-223	223	Marra Mamba	carb-IF	6.5	1.1	0.1	35.1	0.8	9.7	13.9	0.0	0.0	0.1	32.8	100.1
Mill-223.2	223.2	Marra Mamba	carb-IF	7.8	1.8	0.1	26.8	0.8	10.5	17.7	0.1	0.2	0.1	33.5	99.5
Mill-225	225	Marra Mamba	ox/carb-IF	12.3	1.1	0.1	40.5	0.6	6.9	15.1	0.2	0.4	0.1	22.4	99.6
Mill-229	229.3	Marra Mamba	black shale	45.8	11.0	0.5	2.6	0.3	7.6	9.2	0.1	6.0	0.1	16.3	99.5

Average concentrations of TIC follow the order ox-IFs (0.8 ± 0.3 wt%) < black shales (1.4 ± 2.2 wt%) < ox/carb IFs (5.9 ± 0.8 wt%) < carb IFs (8.5 ± 1.0 wt%). Corresponding $\delta^{13}C_{Carb}$ values vary strongly (between -17.0 and -0.1 ‰) with averages in the order of black shales (-3.8 ± 3.5 ‰) > carb IF (-5.6 ± 2.4 ‰) > ox/carb IFs (-6.9 ± 2.8 ‰) > ox IFs (-9.7 ± 2.1 ‰). The $\delta^{18}O_{Carb}$ pattern shows variable values only for black shales (-14.5 to -6.7 ‰) but is homogeneous for all iron formation (-11.1 to -9.1 ‰). For comparison, the oxygen and carbon isotopic composition of 3 limestones (ABDP-260; ABDP-332; ABDP-355) were measured. Both, $\delta^{13}C_{Carb}$ and $\delta^{18}O_{Carb}$ values span narrow ranges ($\delta^{13}C_{Carb}$ between -1.27 and -0.87 ‰ and $\delta^{18}O_{Carb}$ between -12.79 and -9.04 ‰). We observe no correlation between $\delta^{13}C_{Carb}$ and $\delta^{18}O_{Carb}$ (Fig. 3). Iron formations show strong variability in $\delta^{13}C_{Carb}$ (with values below limestone $\delta^{13}C_{Carb}$) at relatively constant $\delta^{18}O_{Carb}$.

Average TOC contents increase in the order ox-IFs (0.1 ± 0.0 wt%) = ox/carb-IFs (0.1 ± 0.1 wt%) < carb-IFs (0.7 ± 0.4 wt%) < black shales (2.4 ± 1.5 wt%). The corresponding $\delta^{13}C_{Org}$ values vary between -43.3 and -27.2 ‰ with averages of carb IFs (-35.9 ± 4.9 ‰), black shales (-33.6 ± 3.0 ‰), ox/carb-IFs (-32.5 ± 5.3 ‰) and ox-IFs (-30.1 ± 1.9 ‰) (Table 2). Considering only black shale samples, $\delta^{13}C_{Carb}$ and $\delta^{13}C_{Org}$ exhibit a positive linear correlation with an R^2 value of 0.86, whereas no correlation is observed in both types of

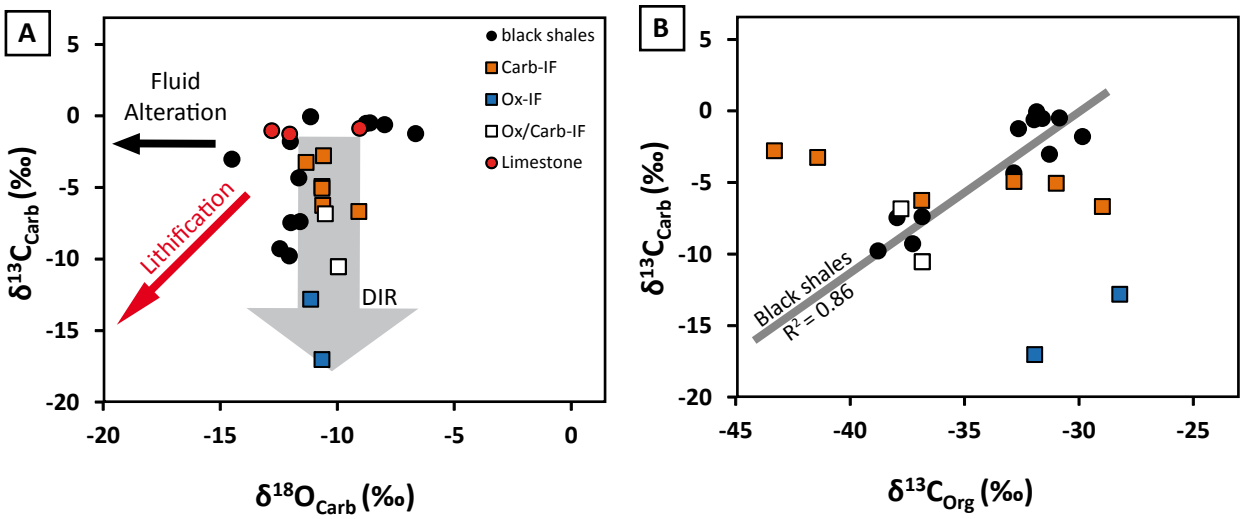

FIGURE 3: (a) Compilation of $\delta^{18}O$ and $\delta^{13}C$ of carbonates in bulk rock samples. Expected trends for fluid alteration or lithification during diagenesis (Knauth and Kennedy, 2009) are not observed. Iron formations have generally lower $\delta^{13}C_{Carb}$ but similar $\delta^{18}O_{Carb}$ as limestones (red circles), which is the result of iron carbonate formation during dissimilatory iron reduction (DIR). (b) illustrates $\delta^{13}C_{Org}$ vs. $\delta^{13}C_{Carb}$ showing a correlation only in black shale samples (black circles). Iron formations, displayed as squares (orange: carbonate facies IFs, white: oxide/carbonate facies IFs, blue: oxide facies IFs), exhibit no correlation.

iron formations (Fig. 3b). Accordingly, the difference in $\delta^{13}C_{Org}$ and $\delta^{13}C_{Carb}$ ($\Delta^{13}C_{Org\text{-}carb}$) is with -29.85 ± 1.36 ‰ very constant in black shales, but varies strongly in IFs (-26.15 ± 8.45 ‰).

For the determination of authigenic molybdenum concentrations we corrected all samples for a detrital component by normalizing on Al, assuming that all Al is detrital with a chemical composition of the Post Archean Australian Shale (PAAS) (Taylor and McLennan, 1985). Al concentrations in iron formations are very low and show only weak correlation with Mo concentrations (R^2 of 0.39; Fig. 4a), which clearly mismatches the range of Al/Mo ratios of average continental crust. The correction further indicates that more than 80 % of Mo in iron formations is non-detrital, but authigenic (see Table 2). Black shales have higher Al concentrations but are also enriched in Mo. The relative proportion of authigenic Mo is always above 77 % (mostly even above 85 %). Mo and Al show no correlation and suggest that Mo enrichment was decoupled from the detrital input.

Authigenic Mo concentrations vary between 0.3 and 13 ppm and averages increase in the order ox-IFs (0.4 ± 0.1 µg/g) = carb/ox-IFs (0.4 ± 0.1 µg/g) < carb-IFs (0.8 ± 0.4 µg/g) < black shales (7.1 ± 8.9 µg/g; Table 2). Considering only black shales, we observe average authigenic Mo concentrations of 2.2 µg/g in the Marra Mamba Formation (1 sample), 3.3 ± 1.2 µg/g in the Wittenoom Formation (7 samples), 3.8 µg/g in the Mt. Sylvia Formation (1 sample), 3.9 ± 1.3 µg/g in the S2 of the Mt. McRae Shale (19 samples; this study and Anbar et al., 2007) and 18.5 ± 9.4 µg/g in the S1 layer of the Mt. McRae Shale (46 samples; Anbar et al., 2007 and this study) revealing a concentration increase with time. Mo concentrations in all sedimentary rocks show no correlation with iron (Fig. 4b) but a positive correlation with TOC (Fig. 4c). Excluding the two black shale outliers with extremely high Mo and TOC, the linear trend between Mo and

TOC has an R^2 value of 0.51. Mo/TOC ratios of black shales are between 1.0 and 3.7 ppm/wt% and show no correlation with the molybdenum isotopic composition (δ^{98}Mo). The δ^{98}Mo values are between +0.51 and +1.51 ‰ (Fig. 5) and thus above the δ^{98}Mo composition of the continental crust. Black shales and carb-IFs of similar core depth have a similar Mo-isotopic composition (i.e. compare sample pairs ABDP-177 and ABDP-180, ABDP-335 and ABDP-340, and Mill-225 and Mill-229, respectively; Table 2). Oxide-IFs show more negative δ^{98}Mo values compared to black shales of similar core depth ($\Delta^{98}Mo_{ox\text{-}IF\text{-}black\ shale} = \delta^{98}Mo_{ox\text{-}IF} - \delta^{98}Mo_{black\ shale}$ = -0.4 ‰). Independent of the sediment type we observe a general increase in δ^{98}Mo of up to 1.51 ‰ passing up stratigraphy through the Mt. Sylvia Formation, Mt. McRae Shale and Brockman Iron Formation (Fig. 5). By contrast, older sedimentary rocks of the Marra Mamba and Wittenoom formations exhibit lower δ^{98}Mo, at a relatively constant level (mean of 0.66 ± 0.24 ‰ (2σ); excluding the outlier Millstream-223.2). Age constraints of a spherule layer within the Bee Gorge Member in drill core ABDP#9 (observed at a core depth of 295 m) define the onset of this increase in δ^{98}Mo to an age slightly younger than 2.54 Ga (Woodhead et al., 1998).

Table 2: Selected geochemical parameters of drill cores ABDP#9 and Millstream#9

Sample	depth (m)	Formation	Lithology	TOC (wt%)	TIC (wt%)	TC (wt%)	$\delta^{18}O_{Carb}$ ‰**	$\delta^{13}C_{Carb}$ ‰**	$\delta^{13}C_{Org}$ ‰	$\Delta^{13}C$ ‰	δ^{98}Mo ‰	2SE abs	Mo µg/g	Mo µg/g*	Mo/TOC (ppm/wt%)
ABDP-103	102.55	Dales Gorge	carb-IF	0.6	8.2	8.3	-9.07	-6.69	-28.98	-22.28	1.51	0.03	1.4	1.4	2.3
ABDP-114	114.4	Mt McRae	black shale	3.3	8.0	11.4	-6.65	-1.23	-32.64	-31.42	1.31	0.02	4.0	3.7	1.1
ABDP-133	132.7	Mt McRae	black shale	4.7	0.8	5.4	-12.45	-9.28	-37.27	-27.99	1.37	0.01	13.7	13.1	2.8
ABDP-164	163.5	Mt McRae	carb-IF	1.4	8.3	9.7	-10.62	-6.26	-36.87	-30.61	1.05	0.02	1.4	1.1	0.8
ABDP-177	176.7	Mt McRae	black shale	5.5	0.2	5.7	-12.05	-9.79	-38.78	-28.99	0.97	0.02	3.5	2.9	0.5
ABDP-180	179.8	Mt McRae	carb-IF	0.4	7.1	7.6	-9.95	-10.54	-36.84	-26.30	0.92	0.04	0.2	0.2	0.4
ABDP-190	190.2	Mt Sylvia	ox/carb-IF	0.0	5.1	5.1	-10.98	-12.52	-27.23	-14.70	0.90	0.05	0.5	0.5	12.5
ABDP-215	214.5	Mt Sylvia	ox-IF	0.1	1.1	1.2	-11.13	-12.81	-28.21	-15.40	0.83	0.04	0.3	0.3	4.5
ABDP-219	218.65	Mt Sylvia	black shale	3.6	0.6	4.2	-11.98	-7.46	-37.95	-30.49	1.10	0.02	4.5	3.8	1.0
ABDP-220	219.95	Mt Sylvia	ox-IF	0.1	0.6	0.6	-10.65	-17.03	-31.93	-14.90	0.64	0.05	0.4	0.4	6.9
ABDP-240	239.5	Wittenoom	black shale	1.4	0.4	1.8	-11.59	-7.37	-36.85	-29.48	0.58	0.03	2.1	1.4	1.0
ABDP-259	259.38	Wittenoom	black shale	1.1	0.5	1.6	-11.64	-4.32	-32.84	-28.53	0.89	0.03	2.5	1.9	1.8
ABDP-292	291.6	Wittenoom	carb-IF	0.5	7.1	7.6	-11.32	-4.94	-32.84	-27.90	0.72	0.03	1.2	1.0	2.1
ABDP-316	316	Wittenoom	black shale	1.0	0.3	1.3	-14.50	-3.02	-31.29	-28.27	0.61	0.02	4.4	3.6	3.7
ABDP-335	334.55	Wittenoom	carb-IF	0.2	9.9	10.1	-10.58	-5.05	-30.99	-25.94	0.57	0.12	0.6	0.5	2.9
ABDP-340	340	Wittenoom	black shale	2.0	0.5	2.5	-12.00	-1.78	-29.84	-28.06	0.62	0.02	3.8	2.9	1.5
Mill-205	205	Wittenoom	black shale	1.8	0.3	2.1	-7.98	-0.60	-31.96	-31.36	0.52	0.02	4.1	3.5	1.9
Mill-206	205.5	Wittenoom	black shale	1.7	1.4	3.1	-11.14	-0.05	-31.85	-31.80	0.84	0.01	4.9	4.2	2.5
Mill-217	217	Wittenoom	black shale	2.5	0.1	2.4	-8.60	-0.48	-30.85	-30.37	0.79	0.03	6.2	5.3	2.1
Mill-223	223	Marra Mamba	carb-IF	0.6	9.3	9.9	-9.82	-2.78	-43.31	-40.52	0.72	0.03	0.4	0.3	0.5
Mill-223.2	223.2	Marra Mamba	carb-IF	1.1	9.3	10.3	-10.07	-3.26	-41.41	-38.15	1.51	0.02	0.9	0.8	0.7
Mill-225	225	Marra Mamba	ox/carb-IF	0.2	6.8	6.9	-10.51	-6.85	-37.77	-30.92	0.51	0.03	0.4	0.3	2.0
Mill-229	229.3	Marra Mamba	black shale	0.8	3.8	4.6	-8.77	-0.53	-31.60	-31.08	0.59	0.02	2.8	2.2	2.9

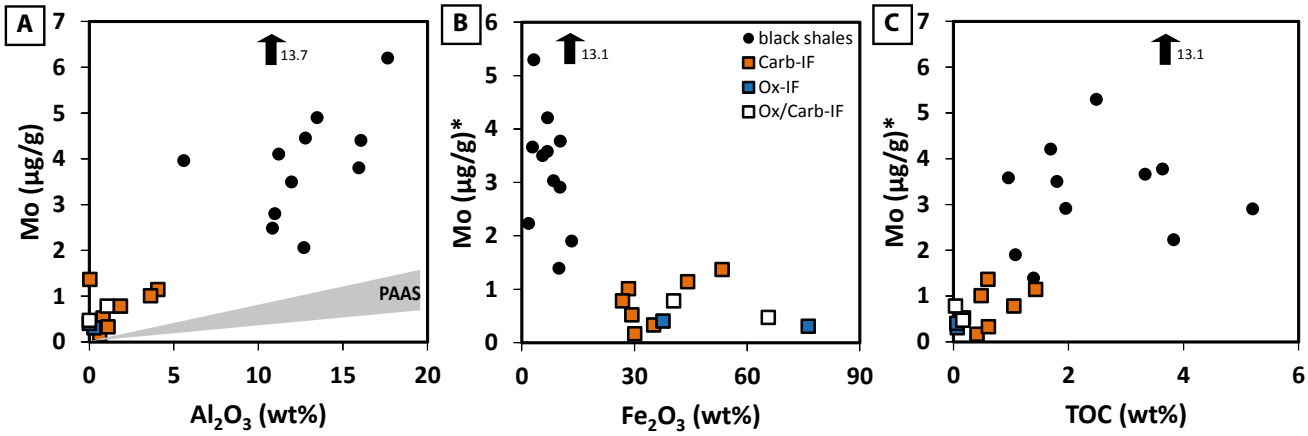

FIGURE 4: Molybdenum concentration versus Al_2O_3 (a), Fe_2O_3 (b) and TOC (c) concentrations, respectively. Note that authigenic molybdenum concentrations were plotted in (b) and (c) as indicated by *. Symbols are as in Figure 3. Grey shading indicates the expected range for samples with predominantly detrital Mo (PAAS: Post Archean Australian Shale) (Taylor and McLennan, 1985).

6. Discussion

The environmental conditions during sedimentation are critical for the removal mechanism of molybdate from the water column. As our samples span very different depositional settings across the continental shelf/slope, a more detailed analysis of prevailing environmental conditions is necessary.

6.1 Black shales

Black shales were deposited in a distal shelf environment, an area with relatively high primary microbial productivity and high detrital input. On average the detrital fraction accounts for 62 wt% of the black shales, assuming that all Al and Ti originate from detritus with a chemical composition of PAAS. However, less than 25 % of sedimentary Mo (usually even less than 15 %) is detrital, indicating strong authigenic Mo enrichment. High TOC contents up to 5.5 wt% are consistent with deposition in an anoxic environment. In more detail, we observe that black shales with high TOC (Mt. McRae Shale) have generally low $\delta^{13}C_{Org}$ (down to -38.8 ‰ in ABDP-177) as well as low $\delta^{13}C_{Carb}$ (down to -9.8 ‰ in ABDP-177; Fig. 3, 5). Nearly constant $\Delta^{13}C_{Org\text{-}Carb}$ values of -29.85 ± 1.36 ‰ mirror the expected range of fractionation during primary production in the Neoarchean (Eigenbrode and Freeman, 2006). The tight coupling of $\delta^{13}C_{Org}$ and $\delta^{13}C_{Carb}$ suggests one single carbon source for carbonates and organic matter, namely dissolved inorganic carbon (DIC) of the ambient seawater, which changed in its isotopic composition over time. This could indicate global trends with elevated $\delta^{13}C_{DIC}$, $\delta^{13}C_{Org}$ and $\delta^{13}C_{Carb}$ during periods of high organic matter burial rates. However, such a correlation was not observed in contemporaneous sedimentary rocks of the Griqualand West Basin, South Africa (Fischer et al., 2009). Considering the consistently higher $\delta^{13}C_{Carb}$ values of shallower water limestones (-1.27 to -0.87 ‰ in $\delta^{13}C_{Carb}$), a more plausible explanation for this feature is a local shelf environment that was characterized by a stratified water column with a large gradient (up to 9 ‰) in the $\delta^{13}C_{DIC}$ (Jiang et al., 2007). Periods of low $\delta^{13}C_{Org}$, low $\delta^{13}C_{Carb}$ and high TOC could reflect the upwelling of nutrient rich deep

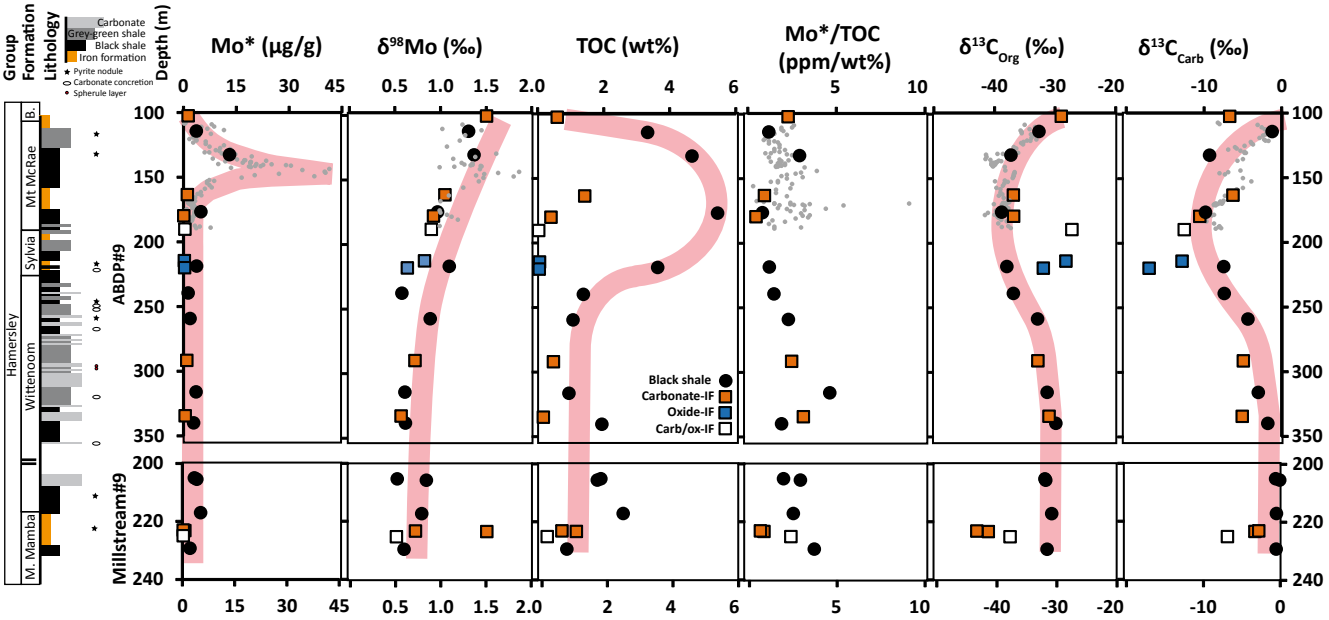

FIGURE 5: Geochemical parameters including authigenic Mo* concentration, δ^{98}Mo, TOC, Mo*/TOC, $\delta^{13}C_{Org}$ and $\delta^{13}C_{Carb}$ versus core depth of ABDP#9 and Millstream#9, respectively. Symbols are as in Figure 3. Small grey dots indicate higher resolution data from Anbar et al. (2007), Duan et al. (2010), and Kaufman et al. (2007). Red lines illustrate trends in black shale samples only, which are broadly confirmed by higher resolution data.

waters that were depleted in ^{13}C (Jiang et al., 2007; Kaufman et al., 1991). Such environmental conditions stimulate primary production (high TOC), as well as the activity of heterotrophic organisms. Productivity of methanogenic bacteria appears to be subordinate, as the expected difference in $\delta^{13}C_{Org}$ and $\delta^{13}C_{Carb}$ would be much larger. However, organisms that reduce sulfate and elemental sulfur within the sediment were very common throughout the Neoarchean Hamersley Group deposition (Partridge et al., 2008), as is also indicated by the abundance of diagenetic pyrite in our black shales. Locally formed euxinic conditions in the water column and/or the sediment would cause molybdate transformation to oxythiomolybdate ($MoO_xS_{4-x}^{2-}$) and/or thiomolybdate depending on the ambient concentration of dissolved $H_2S_{(aq)}$ (Helz et al., 1996; Nägler et al., 2011; Neubert et al., 2008). At $H_2S_{(aq)}$ concentrations above 11 µmol L^{-1}, thiomolybdate (MoS_4^{2-}) is the predominant species with a maximum abundance of 83 % (Erickson and Helz, 2000; Nägler et al., 2011) and with a constant Mo isotope fractionation between sediment and thiomolybdate of $\Delta^{98}Mo_{MoS4—sediment}$ = -0.5 ± 0.3 ‰ (Nägler et al., 2011). Assuming that the remaining 17 % represent the $MoOS_3^{2-}$ species with $\Delta^{98}Mo_{MoOS3-MoS4}$ of -1.75 ‰ (Nägler et al., 2011), the equilibrium fractionation between the sediment and euxinic seawater with $H_2S_{(aq)}$ above 11 µmol L^{-1} is $\Delta^{98}Mo_{euxinic\_seawater—sediment}$ = -0.7 ‰, consistent with observations in the Black Sea (Nägler et al., 2011; Neubert et al., 2008). Only if the removal is nearly quantitative (as in the deep Black Sea, where dissolved Mo-concentrations drop down to 8 nmol L^{-1} compared to 105 nmol L^{-1} in the open ocean; Algeo and Lyons, 2006) the isotopic composition of the sediment mirrors that of global seawater (Fig. 6). However, sedimentary δ^{98}Mo might be up to 0.7 ‰ lower compared to the δ^{98}Mo of global seawater, if the removal is non-quantitative (Fig. 6). In the case of the Cariaco Basin, Mo-removal from seawater is clearly non-quantitative, as indicated by only slightly lower concentrations of dissolved Mo (~80 nmol L^{-1}) compared to the global ocean (105 nmol L^{-1}) (Algeo

and Lyons, 2006). This might be due to lower $H_2S_{(aq)}$ concentrations, which are slightly below the switching point within the water column and unknown for the pore-water, and/or due to larger seawater exchange rates (Algeo and Lyons, 2006). The δ^{98}Mo value of sediments from the Cariaco Basin deposited around 13 ka ago (Lyons et al., 2003) is around 0.5 ‰ lower than the modern global seawater isotopic composition (Fig. 6) (Arnold et al., 2004). Although the environmental conditions might have changed during the last 13 ka (e.g. $H_2S_{(aq)}$ concentration and water renewal times), this may additionally indicate that basinal restriction is a key parameter that controls seawater Mo depletion and the preservation of the seawater Mo isotopic composition. If this model is correct, the deep water within the Cariaco Basin should show δ^{98}Mo slightly above the global seawater δ^{98}Mo. We therefore note that the δ^{98}Mo of ancient sediments only reflects the seawater δ^{98}Mo when $H_2S_{(aq)}$ concentrations of the seawater or pore-water were above 11 µmol L^{-1} (Erickson and Helz, 2000; Neubert et al., 2008) and when the marine depositional setting was connected to the open ocean but restricted enough to allow quantitative removal (Algeo and Lyons, 2006). If the removal of Mo is non-quantitative (like in the Cariaco Basin), sediments in euxinic settings are up to 0.7 ‰ lower in δ^{98}Mo than the ambient seawater.

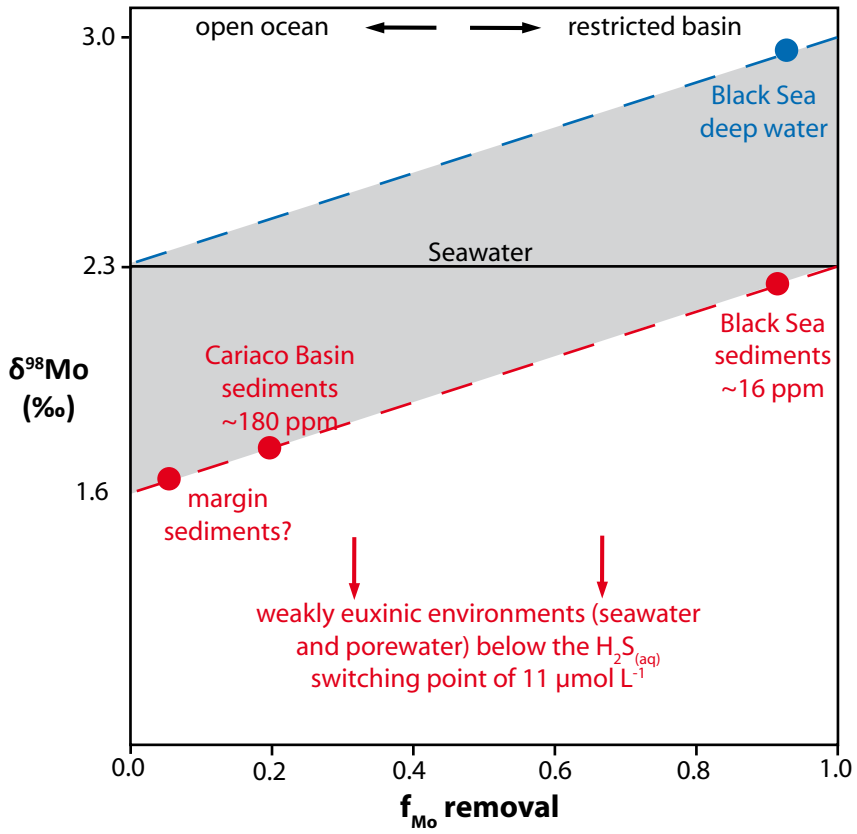

FIGURE 6: The hypothetical equilibrium isotope fractionation between euxinic seawater (Black Sea; Neubert et al., 2008) and possibly pore-water (e.g. Cariaco Basin; Arnold et al., 2004; and continental margins; Poulson et al., 2006; Poulson Brucker et al., 2009) with $H_2S_{(aq)}$ above 11 µmol L^{-1} (blue) and underlying sediments (red) in dependence of the Mo-fraction that is removed from seawater. We assume maximal thiomolybdate formation of 83 %, the rest being $MoOS_3^{2-}$(Erickson and Helz, 2000; Nägler et al., 2011), giving an equilibrium isotope fractionation of ~ -0.7 ‰ in δ^{98}Mo (Nägler et al., 2011). In weakly euxinic environments with $H_2S_{(aq)}$ below 11 µmol L^{-1}, when thiomolybdate formation is less predominant, significantly larger fractionations are possible.

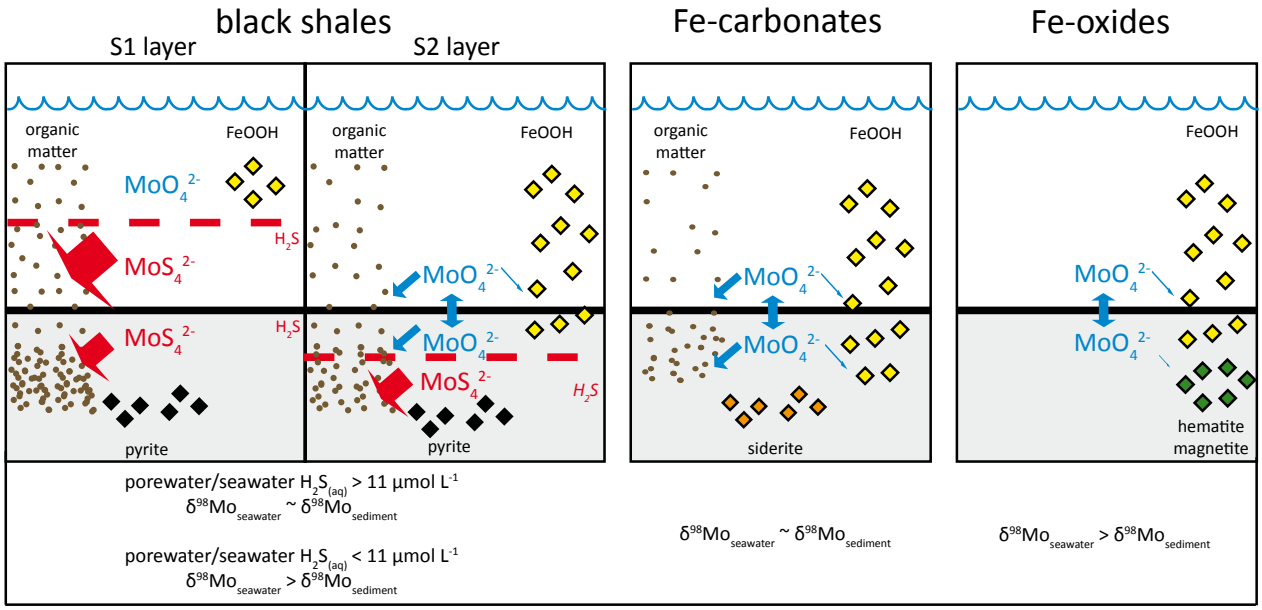

FIGURE 7: Simplified box model for Mo sequestration in black shale, Fe-carbonate and Fe-oxide settings. In black shale settings Mo is scavenged by sulfurized organic matter in a sulfidic zone in the water column (S1 layer) or within the sediment (S2 layer). In Fe-carbonate settings the adsorption of molybdate onto organic matter is the predominant Mo-removal pathway, whereas the adsorption onto Fe-oxyhydroxides is of minor importance. By contrast, in Fe-oxide settings where the supply of organic matter is largely missing, this adsorption mechanism becomes more important. Mo sequestration increases in the order Fe oxides < Fe-carbonates < "ferruginous" black shales (S2) < "euxinic" black shales (S1). Mo isotope fractionations in black shales are low, as long as $H_2S_{(aq)}$ concentrations within the water column and the sediment, respectively, are above the switching point of 11 µmol L^{-1}. Also the adsorption onto organic matter, the predominant Mo-removal pathway in Fe-carbonates is associated with low Mo isotope fractionations, so that the δ^{98}Mo of black shales and Fe-carbonates might be similarly close to the δ^{98}Mo of ancient seawater. In Fe-oxide settings isotopically light Mo is preferentially adsorbed onto Fe-oxyhydroxides and/or hematite/magnetite, which causes slightly lower δ^{98}Mo in Fe-oxides compared to nearly contemporaneous black shales.

In non-euxinic marine settings (e.g. suboxic settings with low bottom water O_2 and $H_2S_{(aq)}$ < 5 µmol L^{-1} and << 10 µmol L^{-1}, or ferruginous settings with no bottom water $H_2S_{(aq)}$ and O_2) the mechanisms of Mo-sequestration are different (Scott and Lyons, 2012). In these intermediate redox environments, Mo is scavenged from pore-water molybdate that can derive from seawater through diffusion, from reductive dissolution of Fe-Mn oxides in the uppermost layers of the sediment (Reitz et al., 2007; Scott and Lyons, 2012), or from decomposition of organic matter (Dellwig et al., 2007; Kowalski et al., 2013; Poulson Brucker et al., 2009). Mn-oxides, the predominant Mo-adsorbent in the modern oxic oceans, do not form inorganically below an Eh of 0.5 V at a marine pH of 8. Therefore, the role of Mn oxides might be subordinate in a largely anoxic Archean environment, although some studies point to local Mn oxide formation in iron formations already before the GOE (Planavsky et al., 2014; Crowe et al., 2013). We observe very low Mn concentrations and no correlation in Fe/Mn with δ^{98}Mo like Planavsky et al. (2014), which indicates that Mn oxide formation and re-dissolution within the sediment was unimportant in the black shale setting of the Hamersley Basin. Fe oxides were possibly present but probably more important in iron formation

settings (see 5.2 and 5.3). Relative Fe-depletion along with Mo enrichment in black shales excludes that the adsorption on Fe-oxyhydroxides was the predominant removal mechanism. In non-euxinic black shale settings, the diffusion of seawater molybdate into the sediments and the demineralisation of organic matter were probably the predominant sources of pore-water molybdate (Fig. 7).

Mo associated with organic matter is adsorbed onto organic aggregates or incorporated into the cells or both. The incorporation into cells can (but does not have to) cause a coordination change from tetrahedral to octahedral depending on the specific incorporation mechanism (see Liermann et al., 2005 for more details). Expected Mo-isotope fractionations during this coordination change were confirmed during experiments, although fractionation magnitudes are relatively low and range from $\Delta^{98}Mo_{organic\_cells-seawater} = \delta^{98}Mo_{organic\_cells} - \delta^{98}Mo_{seawater}$ = -0.2 to -1 ‰ (Liermann et al., 2005; Nägler et al., 2004; Zerkle et al., 2011). However, this effect might be subordinate, because the cells of nitrogen fixing cyanobacteria, which use Mo-rich enzymes, have only low Mo concentrations between 0.2 ppm and 2.4 ppm (Tuit et al., 2004). The relative contribution of cell related Mo to the total authigenic Mo fraction is very low (on average only 1.3 ± 0.6% in our black shale samples assuming the high-end cell-Mo concentration of 2.4 ppm). This might indicate that the adsorption of molybdate onto organic aggregates dominates, a process that is associated with low Mo-isotope fractionations (Kowalski et al., 2013). The pore-water molybdate in non-euxinic black shale settings therefore likely has a similar Mo-isotopic composition as seawater. It is transformed to oxythiomolybdate and/or thiomolybdate and scavenged by sulfurized organic matter, if a zone of sulfate reduction prevailed within the sediment (Fig. 7) (Helz et al., 1996; Poulson et al., 2006; Scott and Lyons, 2012; Tribovillard et al., 2004). Such a zone is indicated by the abundance of early diagenetic pyrite in our black shales. As described above, the magnitude of Mo-isotope fractionation during this process is mainly dependent on the ambient $H_2S_{(aq)}$ concentration within the sediment. In open marine settings with ferruginous bottom waters and high pore-water $H_2S_{(aq)}$ concentrations the Mo isotopic composition of the sediments is very uniform and close to the seawater Mo isotopic composition with $\Delta^{98}Mo_{ferruginous\_sediment-seawater} = \delta^{98}Mo_{ferruginous\_sediment} - \delta^{98}Mo_{seawater}$ = -0.7 ‰ (Poulson Brucker et al., 2009; Poulson et al., 2006). Interestingly, this fractionation magnitude is expected for an open marine setting with quantitative thiomolybdate formation assuming the equilibrium fractionation model (Fig. 6), but such an interpretation is speculative and requires further investigation. However, variability in the $\delta^{98}Mo$ of anoxic margin sediments is only expected if: (1) the seawater $\delta^{98}Mo$ changes, (2) the reductive dissolution of Fe-Mn oxides is relevant, or (3) thiomolybdate formation is non-quantitative ($H_2S_{(aq)}$ < 11µmol L^{-1}). For example, in suboxic settings where the reductive dissolution of Fe-Mn oxides is relevant, this additional source for pore-water molybdate can cause a larger range in the sedimentary Mo-isotopic composition of suboxic margin sediments (Siebert et al., 2006). The same would be true if thiomolybdate formation is incomplete, as occurs in weakly euxinic sedimentary environments.

Fe-speciation is commonly used to classify local redox conditions and to distinguish between euxinic and non-euxinic settings (Poulton et al., 2004; Raiswell and Canfield, 1998). However, we note that the distinction between weakly and strongly euxinic depositional environments of ancient sedimentary rocks is difficult, even with Fe speciation data. This proxy gives no exact indication about the quantitative H_2S concentration and hence whether the switching point of 11 µmol L^{-1} H_2S was reached and thiomolybdate

formation was nearly quantitative or not. Therefore, even black shales with iron speciation data indicating a euxinic depositional environment may not fully imprint the ambient seawater's Mo-isotopic composition. Moreover, the Fe speciation data refer to the water column redox state (Poulton et al., 2004). Efficient Mo-scavenging within the sulfate reduction zone of the sediment can still be the predominant removal pathway even if the overlying water column is ferruginous (e.g. see Poulson et al., 2006). Reinhard et al. (2009) showed that the ambient seawater during the deposition of the S2 layer of the Mt. McRae Shale was mainly ferruginous, whereas it was mainly euxinic during deposition of the younger S1 layer. We measured the Mo isotopic composition of two black shales from S1 (ABDP-114, ABDP-133) and one black shale from S2 (ABDP-177). Despite lower resolution, like Duan et al. (2010) we observe slightly lower δ^{98}Mo in the older and non-euxinic S2 layer and even lower values in black shales from older formations, an observation that can be explained by two different scenarios:

1) Consistent with the Fe-speciation data of Reinhard et al. (2009), the increase could indicate the preferential removal of light Mo isotopes in non-euxinic settings like the S2 layer, whereas the euxinic S1 layer might mimic the Neoarchean seawater Mo isotopic composition (Duan et al., 2010). Even if we exclude the reductive dissolution of Mn-oxides at our black shale depositional settings, weakly euxinic conditions in the pore-water of S2 with $H_2S_{(aq)}$ concentrations below the switching point of 11 µmol L^{-1} could have caused large Mo-isotope differences between seawater and sediment (Neubert et al., 2008). The continuous increase from low δ^{98}Mo during the Marra Mamba and Wittenoom black shales towards highest values in the S1 layer could indicate that Mo-isotope fractionations became less pronounced, possibly due to increasing pore-water $H_2S_{(aq)}$ concentrations. In this scenario the seawater Mo-isotopic composition could have remained relatively constant with δ^{98}Mo as high as those observed in the strongly euxinic S1 layer, which would give the best approximation for the ancient seawater δ^{98}Mo (Duan et al., 2010).

2) Alternatively, our data would indicate a temporal increase in seawater δ^{98}Mo, whereas authigenic molybdenum enrichment in the black shales remained quantitative and thus mirrored the changing seawater δ^{98}Mo (Duan et al., 2010). We prefer this scenario to the previous one for several reasons that will be discussed below, as well as in chapters 5.2 and 5.3. Considering the good correlation of Mo and TOC, Mo scavenging by sulfurized organic matter seems a reasonable removal pathway (Tribovillard et al., 2004) (Fig. 7). The large abundance of diagenetic pyrite indicates that H_2S and bacterial sulfate reduction prevailed within the sediment also during S2 deposition and deposition of older black shales (Reinhard et al., 2009). If thiomolybdate formation in this zone was nearly quantitative, all black shales (below a ferruginous and sulfidic water column) will show δ^{98}Mo that are similarly close to, and reflect minimum values of, the δ^{98}Mo of ancient seawater. We admit that the assumption of quantitative thiomolybdate formation remains hypothetical. However, we would expect large scatter in our δ^{98}Mo dataset if pore-water $H_2S_{(aq)}$ concentrations were relatively low and variable. Such scattering in δ^{98}Mo values is observed in contemporaneous black shales of the Griqualand West Basin, South Africa (Wille et al., 2007). Consistent with less efficient Mo-removal in weakly euxinic environments, Mo concentrations in the black shales of this location are also significantly lower (Wille et al., 2007). The lack of such pronounced scatter in our δ^{98}Mo dataset from the Hamersley Basin with continuously increasing values argues against strongly

variable authigenic enrichment factors under fluctuating low H_2S concentrations. We therefore suggest that the best modern analogue for our black shale settings are anoxic margin settings, where Mn-cycling is negligible, the seawater-sediment interface is ferruginous (and was only partly euxinic as during S1 deposition) and a sulfidic zone formed in the sulfate reduction zone within the sediment (Poulson Brucker et al., 2009; Poulson et al., 2006). These sediments, where pore-water molybdate was effectively scavenged by formation of oxythiomolybdate and organic matter deposition, exhibit relatively small Mo isotopic differences between seawater and sediments (Poulson et al., 2006; Scott and Lyons, 2012). The main difference to a hypothetical Neoarchean analogue was a significantly smaller seawater Mo-reservoir, as indicated by continuously low Mo/TOC (Scott et al., 2008). Quantitative Mo removal is easier achieved at such low seawater molybdate concentrations (Duan et al., 2010), such that Archean sediments may even more closely reflect the seawater δ^{98}Mo (Fig. 6). Mo enrichments will be highest when the bottom water was also euxinic, as during deposition of the S1 layer, but lower when the supply of molydbate is mainly dependent on the diffusional transport of seawater molybdate into the sediment. This might explain the extreme Mo enrichments in the black shales of S1 (Reinhard et al., 2009).

We conclude that during black shale deposition, the sediment and the sediment-water interface were anoxic and partly euxinic (S1, Mt. McRae Shale; Reinhard et al., 2009). The Mo-isotope data of authigenic Mo in these black shales reflect minimum values for ambient seawater (Wille et al., 2007). The continuous increase in black shale δ^{98}Mo from a mean value of 0.66 ‰ ± 0.22 (2σ) before 2.54 Ga up to 1.37 ‰ in the Mt. McRae Shale could therefore indicate decreasing net Mo scavenging in the youngest samples or (as preferred here) an increase in the Mo-isotopic composition of the ambient seawater.

6.2 Carbonate facies iron formation

Carb-IFs formed on the shelf/slope in more distal and deeper environments than black shales (Beukes and Gutzmer, 2008). The detrital influence during deposition of these units was negligible, as indicated by low Al and Ti concentrations (Table 1). Fe-carbonates precipitate when a solution is oversaturated in Fe^{2+} and HCO_3^- (Beukes et al., 1990; Winter and Knauth, 1992). Ohmoto et al. (2004) suggested that such oversaturation in Archean seawater was a consequence of extremely high atmospheric $p(CO_2)$. However, a more recent study of the ^{87}Rb-^{87}Sr radiogenic isotope system in iron carbonates points to an early diagenetic origin of Archean iron carbonates (Johnson et al., 2013). The oxidation of organic matter and coupled dissimilatory iron reduction during early diagenesis can also create an oversaturation of Fe^{2+} and HCO_3^- within the sediment's pore-water (Ellwood et al., 1988; Johnson et al., 2008) and the subsequent precipitation of iron carbonates before lithification (Johnson et al., 2013). This formation mechanism is consistent with lower $\delta^{13}C_{Carb}$ in carb-IFs compared to limestones, as it strongly indicates the integration of isotopically light carbon that was derived from organic matter remineralization within the sediment (Fig. 3a). Furthermore, the spheroidal shape of iron carbonate investigated in this study (Fig. 2a, b) was most likely caused by the reaction of ferrihydrite with organic matter during early diagenesis (Köhler et al., 2013). Ferrihydrite, which is the presumed precursor mineral for any iron formation, can form during iron oxidation by photoferrotrophic bacteria (Widdel et al., 1993) or inorganically by free oxygen in an oxic ocean surface layer (Cloud, 1965), whereas photo oxidation was ruled out as primary mechanism for

Fe-oxidation and subsequent BIF formation (Konhauser et al., 2007). The spheroidal and rhombohedral shape of iron carbonates might indicate that photoferrotrophic bacteria were the predominant primary producer (Köhler et al., 2013). The subsequent oxidation of organic matter by Fe^{3+} within the sediment requires the absence of energetically more efficient oxidants such as O_2. Furthermore, reduced iron would preferentially form iron sulfides if H_2S was available (Poulton et al., 2004). Consequently, iron carbonates formed in an anoxic and non-sulfidic pore-water environment overlain by a ferruginous water column (Holland, 2006; Kaufman et al., 2007; Poulton et al., 2004).

In an H_2S free pore-water/seawater environment, the formation and scavenging of thiomolybdate is excluded. Furthermore, the role of Mn-oxides and hence the adsorption of molybdate onto these minerals was probably of minor importance in an anoxic environment (see one exception in section 5.4). Still, Fe-carbonates are enriched in authigenic Mo, which make up more than 80 % of total Mo (Table 2). Considering the genesis of Fe-carbonates, molybdenum was either scavenged by organic matter or by Fe-oxyhydroxides. We would expect similar Mo enrichments in oxide and carbonate facies iron formations, if the adsorption onto Fe-oxyhydroxides was the predominant scavenging mechanism. However, authigenic Mo concentrations increase in the order oxide IF < carb/ox IF < carb IF. Thereby, authigenic Mo concentrations positively correlate with TOC. This rather suggests that Mo scavenging by organic matter was the predominant process (Fig. 7), a mechanism that was shown to be very efficient in the modern German Wadden Sea (Dellwig et al., 2007; Kowalski et al., 2013). It appears that only in settings with very low organic carbon burial rates does the adsorption of molybdate onto Fe-(oxyhydr)oxides significantly contribute to the sequestration of Mo into the sediments (Wichard et al., 2009).

The concentrations of Mo are lower in Fe carbonates compared to black shales, because a sulfidic zone and thiomolybdate formation was absent (Fig. 7). Independent of all these different Mo enrichment mechanisms, we observe very similar δ^{98}Mo values in black shale/carbonate IF sample pairs APDB-177/ APDB-180, APDB-335/APDB-340, and Mill-225/Mill-229, which are similar in depth and probably age (Table 2; Fig. 5). Furthermore, the δ^{98}Mo values of Fe carbonates generally follow the same trend as the δ^{98}Mo values of black shales with highest values in the youngest samples (excluding sample Mill-223.2, see section 5.4; Fig. 5). Considering the low Mo-isotope fractionations during Mo-scavenging by organic matter (Kowalski et al., 2013), the increase in δ^{98}Mo values of Fe-carbonates in the course of the Mt. Sylvia Formation, Mt. McRae Shale and Brockman Iron Formation indicates an increase in the seawater δ^{98}Mo. This in turn confirms our previous hypothesis that the magnitude of Mo scavenging in all black shale samples was similar and nearly quantitative, probably due to nearly quantitative thiomolybdate formation in H_2S rich sedimentary settings. Therefore, the most straightforward interpretation of the δ^{98}Mo record suggests similarly small Mo isotopic differences between seawater and black shales as well as carbonate facies iron formations, respectively, and an increase in the seawater δ^{98}Mo over the course of the deposition of the Mt. Sylvia Formation, Mt. McRae Shale and Brockman Iron Formation.

6.3 Oxide facies iron formation

According to Beukes and Gutzmer (2008), oxide-IFs represent the most distal deep-water facies in an anoxic environment. Correspondingly, the respective samples show no detrital component (undetectable concentrations of Al and Ti). Furthermore, TOC concentrations are extremely low (in the range of the analytical detection limit). Low TOC might limit the coupled reaction of iron (III) reduction and organic matter oxidation and hence the formation of iron carbonates. By contrast, the labile Fe-oxyhydroxide fraction formed layers of iron oxides such as hematite and magnetite during early diagenesis (Fig. 2b, c; Beukes and Gutzmer, 2008). Some samples show both, iron carbonates and iron oxides (Fig. 2b). The thin section in figure 2b clearly demonstrates the separation of iron carbonate and iron oxide layers, which suggests continuous sediment deposition under changing environmental conditions. The absence of pyrite in both types of iron formations indicates a ferruginous and non-sulfidic environment during deposition.

Oxide facies iron formations, as with carbonate facies iron formations, reveal a large authigenic Mo component. The H_2S free environment in these settings impedes the formation of particle reactive thiomolybdate and subsequent Mo sequestration as is the case for Fe carbonate settings. But, opposite to Fe carbonate settings, we suggest that the burial rate of organic matter was low enough so that Mo adsorption onto Fe-oxyhydroxides was the predominant authigenic Mo enrichment process in oxide facies iron formations (Fig. 7). This adsorption causes Mo-isotopic differences of $\Delta^{98}Mo_{ferrihydrite\text{-}seawater}$ = $\delta^{98}Mo_{ferrihydrite}$ - $\delta^{98}Mo_{seawater}$ of -1.1 ‰ (Goldberg et al., 2009). Consistent with our hypothesis the δ^{98}Mo of two pure oxide IFs (ABDP-215 and ABDP-220) are slightly lower than the δ^{98}Mo of the “contemporaneous” black shale (ABDP-219; $\Delta^{98}Mo_{ABDP215/220\text{-}ABDP219}$ = $\delta^{98}Mo_{ABDP215/220}$ - $\delta^{98}Mo_{ABDP219}$ = -0.4 ‰; Table 2). Low Mo concentrations in Fe oxides suggest that the efficiency of Mo removal at these settings was generally low, which could have been a question of competition for free adsorption sites. The Archean ocean was rich in Si (with concentrations more than 60 times higher than today; Siever, 1992), which has a higher affinity to ferric (oxyhydr)oxides than Mo (Balistrieri and Chao, 1990). During times of non-biological Si precipitation, mineral adsorption represented the main Si removal mechanism in the Archean ocean (Siever, 1992). Thus, the chemical composition of the Archean ocean (i.e. high Si concentrations), might have significantly hindered Mo-adsorption on ferric (oxyhydr)oxides.

6.4 The evolution of seawater δ^{98}Mo

The continental crust (and hence detrital Mo) has a relatively narrow range in δ^{98}Mo values between 0.0 and 0.6 ‰, with an average continental δ^{98}Mo value of ca. 0.3 - 0.4 ‰ (Greber et al., 2013; Siebert et al., 2003; Voegelin et al., 2014; Wille et al., 2013). Most early and middle Archean sedimentary rocks exhibit δ^{98}Mo values within this continental range (Siebert et al., 2005; Voegelin et al., 2014; Wille et al., 2013) along with low Mo/TOC ratios (Wille et al., 2013; Scott et al., 2008). Some higher δ^{98}Mo values in ~3.0 Ga old iron formations, which positively correlate with Fe/Mn ratios point to local Mo-isotope fractionations during adsorption onto Mn-oxides (Planavski et al., 2014). Altogether the current dataset suggests low seawater Mo concentrations (low Mo/TOC) along with global inhomogeneity of Archean seawater δ^{98}Mo, with temporal and spatial variability being dependent on the local Mo input as well as local fractionation processes (e.g. Planavsky et al., 2014).

The sedimentary rocks from the Neoarchean Marra Mamba and Wittenoom formations, Hamersley Basin, exhibit authigenic Mo enrichment, but still low Mo/TOC ratios. Most δ^{98}Mo values are only slightly above the average value of the continental crust and close to the majority of early and middle Archean δ^{98}Mo values, which indicates unchanged environmental conditions. One exception (Fe carbonate Mill-223.2) shows an anomalously high δ^{98}Mo value of 1.51 ‰ that is in stark contrast to significantly lower δ^{98}Mo values of all other samples of the Marra Mamba and Wittenoom formations. In addition, the carbonate IF (Mill-223), which is only 20 cm above this sample has a significantly lower δ^{98}Mo value of 0.72 ‰. The geochemical, petrological and mineralogical similarity of both Fe carbonates argues against a different Mo removal mechanism with variable Mo-isotope fractionations. Such short-term variability could result from the local formation of Mn-oxides. Mn-oxides represent an impermanent sink for isotopically light Mo (Scott and Lyons, 2012). During reductive dissolution of Mn-oxides within the sediment Mo is re-liberated and diffuses back into the water column as long as it is not fixed within a sulfidic zone of the sediment (Scott and Lyons, 2012). This means that isotopically light Mo is only temporary bound as long as Mn-oxides persist in the uppermost sediment layers and could temporary cause high δ^{98}Mo values of local seawater (i.e. during deposition of Mill-223.2). Theoretically, later instability of local Mn oxides in more reducing environments would re-liberate isotopically light Mo shifting the local seawater δ^{98}Mo back to lower values (i.e. during deposition of Mill-223). Such short scale temporal variability is only imaginable when the reservoir size of seawater molybdate is small and its residence time is short (consistent with low Mo/TOC ratios).

Alternatively, temporary high δ^{98}Mo values could also reflect a short-term increase of a homogeneous $\delta^{98}Mo_{sw}$ reservoir, which might also explain similarly high δ^{98}Mo values observed in nearly contemporaneous carbonates on the Kapvaal craton (Fig. 8) (Voegelin et al., 2010). Assuming such homogeneous distribution of Mo in seawater, we used the box-model described in Wille et al. (2008) to model the effect of an abruptly larger sink of isotopically light Mo on the seawater Mo isotopic composition (spike on the left in panel 2, Fig. 9a). Similarly, we modeled the effects of an abrupt short-term increase in the Mo-influx and the Mo removal efficiency, respectively, on the $\delta^{98}Mo_{sw}$ values (abrupt doubling for 100 ka at constant isotopic differences between seawater and sediment; spike on the left in panel 1, Fig. 9b and c, respectively). The seawater Mo inventory was set to 1 % of the modern inventory (Scott et al., 2008). Reduced oxidative weathering on the continents during the Archean are expected to cause a significantly lower Mo-influx, which we also set to 1 % of the modern influx (= outflux in steady state). Although Neoarchean Mo-fluxes are poorly constrained and the resulting modern-like residence time might be overvalued, we note that the perturbation of the Mo ocean inventory and its isotopic composition depend on changing the relative proportions of the two fluxes and the inventory as well as their isotopic compositions. The choice of these parameters assures homogenous seawater Mo distribution. The Mo-isotopic composition of the influx was kept constant at 0.4 ‰ in δ^{98}Mo throughout all models (Voegelin et al., 2014). For simplicity, we assume only two outfluxes. The euxinic outflux comprises 15 % of the total outflux (Scott et al., 2008) with a Mo-isotopic composition, which equals that of seawater. For the remaining 85 % of outflux in mainly reducing but not strongly euxinic environments an isotopic difference of $\Delta^{98}Mo_{sw\text{-}sed} = \delta^{98}Mo_{sw} - \delta^{98}Mo_{sed} = 0.9$ ‰ in steady state (Kendall et al., 2009) is assumed. We note that an increase in $\Delta^{98}Mo_{sw\text{-}sed}$ models the relative extension of weakly sulfidic as well as oxic environments, both of which will remove isotopically light Mo.

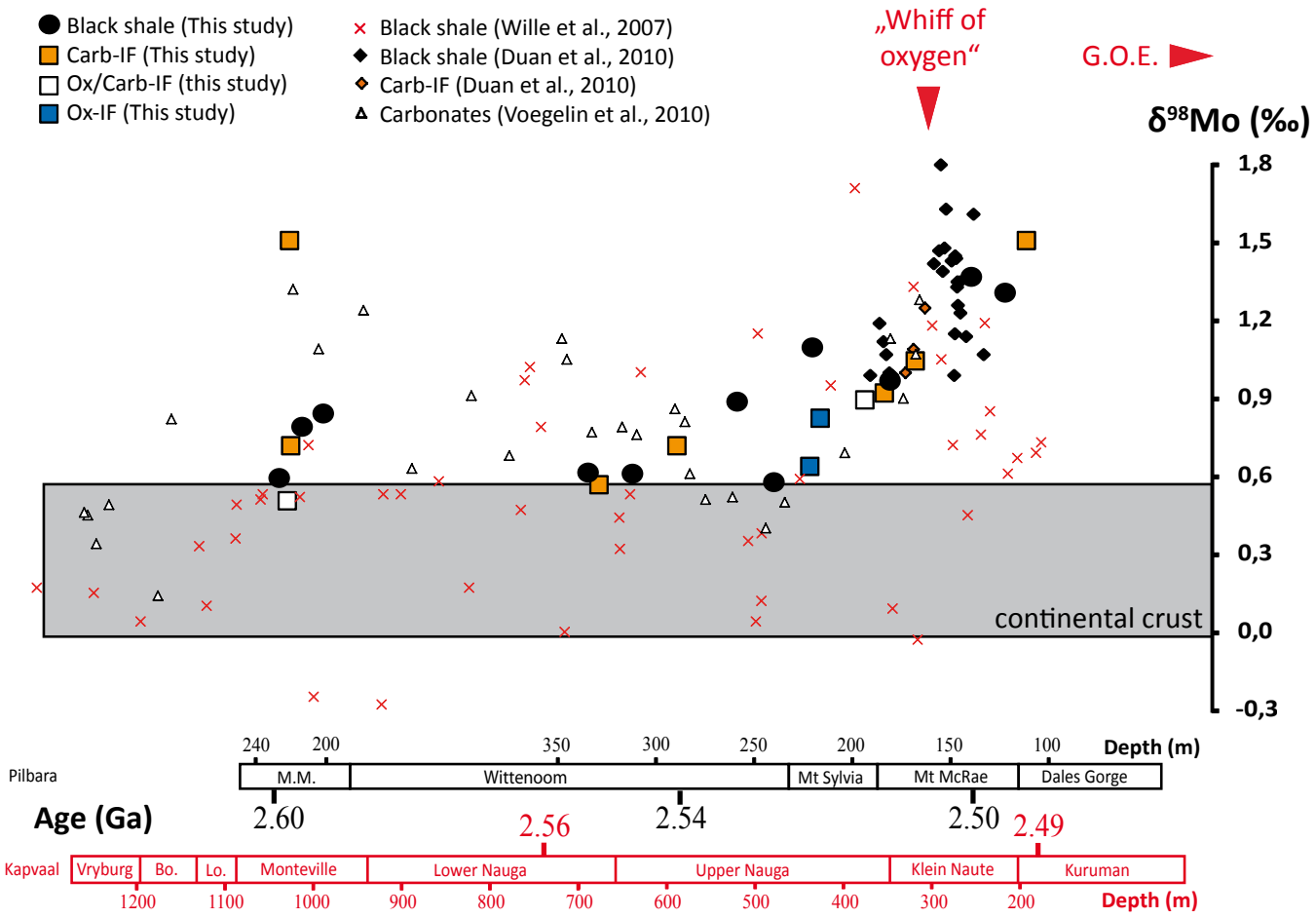

FIGURE 8: The evolution of δ^{98}Mo in black shales, carbonates and iron formations during the Neoarchean (Hamersley Basin: Duan et al., 2010 and this study; Griqualand West Basin: Wille et al., 2007; Voegelin et al., 2010). The δ^{98}Mo are plotted against sample depth of the Australian drill cores ABDP#9 and Millstream#9 (black: Duan et al., 2010; this study) and the Australian drill core GKP01 (red: Wille et al., 2007; Voegelin et al., 2010). All sample sets were time-correlated using spherule layers (Simonson et al., 2009), U-Pb zircon ages (2.60 Ga, Trendall et al., 1998), Pb-Pb ages (2.54 Ga; Woodhead et al., 1998) and a Re-Os shale age (2.50 Ga; Anbar et al., 2007). Our data show low δ^{98}Mo close to crustal values (grey area) before 2.54 Ga (Marra Mamba and Wittenoom formation) and a subsequent increase towards more positive values (Mt. Sylvia Formation, Mt. McRae Shale and Brockman Formation). Samples from the Griqualand West Basin, South Africa, (Wille et al., 2007) show larger variability but a qualitatively similar trend in maximum values. The increase is concomitant for black shales (black circles) and carbonate facies iron formation (orange squares). Ultimately, the increase is attributed to the build-up of a more homogeneous oceanic molybdate reservoir with a higher seawater δ^{98}Mo as a consequence of increasing redox-potentials before the G.O.E. and the “whiff” of oxygen.

The temporal increase of this value on the 10th to 100th ka timescale can explain short-term variability of seawater δ^{98}Mo (left side in panel 3, Fig. 9a) only if the period of perturbation gets closer to the range of the seawater residence time of Mo (~700 ka in the modern ocean and in the models). The short-term variability of $\delta^{98}Mo_{sw}$ is, however, amplified when combining higher $\Delta^{98}Mo_{sw\text{-}sed}$ with an abrupt increase in Mo removal efficiency (left side in panel 3, Fig. 9d). Such a combination is expected during increased Mo scavenging in more widespread weakly euxinic settings and better explains temporally high $\delta^{98}Mo_{sw}$

values as seen in the Marra Mamba Formation. However, during periods of strong Mo removal we would expect Mo enrichments and high - rather than low - Mo/TOC ratios during times of increased Mo removal efficiency (Wille et al., 2008). So far such enrichments are not observed in the global geological record. We therefore prefer the initial interpretation that the exceptional increase towards a high δ^{98}Mo value at 2.6 Ga (e.g. in Mill-223.2) is a local phenomenon, which is consistent with a seawater Mo-reservoir that was still heterogeneous and variable with respect to its isotopic composition.

In contrast to mainly low δ^{98}Mo values close to the crustal average in sediments of the Marra Mamba and Wittenoom formations with only one single excursion to higher values, we observe continuously increasing δ^{98}Mo values in the samples younger than 2.54 Ga, belonging to the Mt. Sylvia Formation, the Mt. McRae Shale and the Dales Gorge Member of the Brockman Iron Formation (ABDP-260 to -102; Fig. 8). The Neoarchean increase in δ^{98}Mo values of Hamersley Basin sedimentary rocks (up to 1.51 ‰ here and up to 1.86 ‰ for the S1 layer in the Mt. McRae Shale; Duan et al., 2010) was also observed in contemporaneous sedimentary rocks of the Griqualand West Basin, South Africa (Wille et al., 2007; Voegelin et al., 2010). The large scatter in black shales from the Griqualand West Basin (Wille et al., 2007) could be a consequence of Mo-isotope fractionations in weakly sulfidic settings or mixing of detrital and authigenic Mo (see 5.1). However, maximum values, which represent the best approximation for the ancient seawater δ^{98}Mo, show a broadly similar evolution (Fig. 8). These observations suggest that the seawater became isotopically heavier and more homogeneous with respect to Mo, at least regionally within the basin that straddled the South African and Australian regions.

Mo/TOC ratios remained relatively low also during deposition of the Mt. Sylvia Formation and the Mt. McRae Shale, which seems at odds with a larger and more homogeneous seawater Mo reservoir. However, the magnitude of Mo/TOC ratios is also dependent on local environmental conditions such as sedimentation rates and particularly sulfide levels (Algeo and Lyons, 2006; Dahl et al., 2013). Comparing the Mo/TOC ratios from the euxinic S1 interval of the Mt. McRae Shale ($Fe_{HR}/Fe_T > 0.38$ and $Fe_{Py}/Fe_{HR} > 0.8$; Reinhard et al., 2009) with Mo/TOC ratios from a euxinic interval of the 2.66 Ga old Jeerinah Formation of the conformably underlying Fortescue Group, Western Australia ($Fe_{HR}/Fe_T > 0.38$ and $Fe_{Py}/Fe_{HR} > 0.8$; Scott et al., 2011), the increase in Mo/TOC ratios from averaged 0.4 ± 0.2 in Jeerinah black shales (Scott et al., 2011) to averaged 2.0 ± 0.6 in Hamerslay Basin Mt. McRae black shales (Anbar et al., 2007) is significant. First strong enrichment of Mo in euxinic black shales of the Mt. McRae Shale, which led to the idea of a whiff of oxygen before the G.O.E. (Anbar et al., 2007) are therefore consistent with a larger and more homogeneous seawater Mo reservoir. These Mo enrichments required euxinic seawater conditions that could have been a consequence of local oceanographic changes (e.g. the upwelling of DIC and nutrient rich deep waters). Such local oceanographic changes in turn led to strong variations in the carbon isotope record but had little effects on the Mo-isotopic composition. The δ^{98}Mo still increases during the Dales Gorge Member, whereas the $\delta^{13}C_{org}$ and $\delta^{13}C_{carb}$ shift back to lower values (see red lines in Fig. 5). This pattern additionally suggests that the seawater molybdate reservoir was less affected by local changes but rather more homogeneous in its distribution and isotopic composition. Thus, the increase in the seawater molybdate reservoir apparently goes hand in hand with higher seawater δ^{98}Mo.

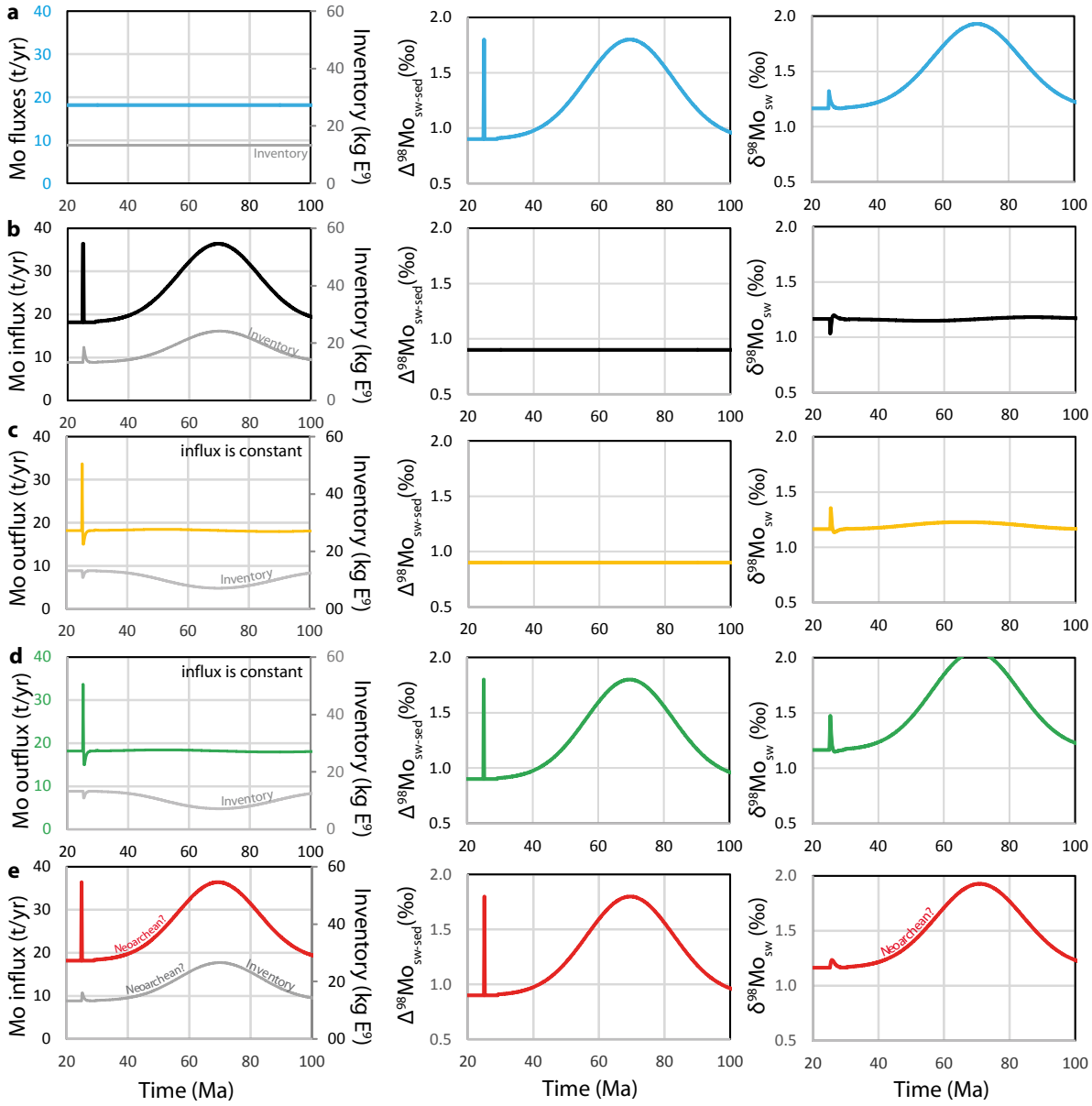

FIGURE 9: (a, blue) fluxes remain constant at 1 % of the modern influx with a seawater Mo reservoir that is also 1 % of the modern inventory (causing a modern-like residence time). The $\Delta^{98}Mo_{sw\text{-}sed} = \delta^{98}Mo_{sw} - \delta^{98}Mo_{sed}$ was changed by lowering the $^{98}Mo_{sed}$ (the output) abruptly on a short-term (100 ka, left side) and smoothly on a long-term (40 Ma, right side), respectively. We changed $\Delta^{98}Mo_{sw\text{-}sed}$ from 0.9 ‰ up to 1.8 ‰, whereby the subscript "sed" includes all but strongly euxinic sediments and modelled the effects on the $\delta^{98}Mo_{sw}$ value. (b, black) the effect of abrupt doubling of the Mo influx for 100 ka and a smooth doubling for 40 Ma, respectively, on the $\delta^{98}Mo_{sw}$ (keeping $\Delta^{98}Mo_{sw\text{-}sed}$ constant). (c, yellow) the effect of abrupt doubling of the Mo removal efficiency for 100 ka and a smooth doubling for 40 Ma, respectively, on the $\delta^{98}Mo_{sw}$ value. Note that the smooth long-term doubling of the Mo removal efficiency has little effects of the absolute outflux, because the outflux is correlated to the Mo inventory, which decreases with time (thus balancing higher Mo removal efficiency). (d, green) modelling of more widespread weakly euxinic environments, which would cause more efficient Mo removal of isotopically light Mo (thus a combination of a and c). We observe large effects on the $\delta^{98}Mo_{sw}$ value on a short-term and on a long term, but also a decline of the seawater Mo inventory. (e, red) modelling of environmental oxygenation. In this scenario higher rates of oxidative weathering (higher influx) come along with the preferential removal of isotopically light Mo during adsorption onto Mn oxides in well oxygenated shallow water habitats (higher $\Delta^{98}Mo_{sw\text{-}sed}$ combination of a and b). The modeled $\delta^{98}Mo_{sw}$ shows large variation only on the long-term. Coevally the model suggests the build-up of a larger Mo inventory, which is consistent with the Neoarchean geological record.

The possible causes for the build-up of a more homogeneous and isotopically heavier ocean are well discussed by Duan et al. (2010). These authors exclude a hydrothermal source of isotopically heavy Mo and highlight the need for an increasing sink of isotopically light Mo. Archean carbonate facies iron formations seem to fail as a sink for isotopically light Mo as they show similar positive δ^{98}Mo as black shales and Mo burial is associated with organic matter deposition rather than adsorption onto Fe-oxyhydroxides. The sequestration of isotopically light Mo in oxide facies iron formations with only slightly lower δ^{98}Mo values also appear to have been subordinate, considering the extremely low Mo concentrations of oxide IFs. Duan et al. (2010) conclude instead that the preferential removal of isotopically light Mo onto Mn oxides either during oxidative weathering on the continents or in well oxygenated marine coastal areas was a more probable cause. The generation of continental crust coupled with considerable relief-building increased remarkably during the Neoarchean (Flament et al., 2008; Rey and Coltice, 2008). Higher reliefs would have increased rates of physical weathering and the riverine and aeolian input of detrital material. In the course of increasing atmospheric oxygen concentrations (Anbar et al., 2007), higher rates of oxidative weathering are expected. Mn oxide formation and the involved retention of isotopically light Mo in well oxygenated surface ocean areas possibly caused higher seawater δ^{98}Mo values (Duan et al., 2010). This idea is confirmed by our modeling. The smooth long-term increase (over 40 Ma) of the Mo-influx by higher rates of oxidative weathering increases the Mo-inventory consistent with higher Mo concentrations and increasing Mo/TOC ratios in the Mt. McRae Shale. However, this increase alone cannot explain the shift towards higher seawater δ^{98}Mo (right side in panel 3, Fig. 9b). Also the long-term increase in Mo removal efficiency has little effects on the $\delta^{98}Mo_{sw}$ (right side in panel 3, Fig. 9c). However, by coupling a higher Mo-influx with higher $\Delta^{98}Mo_{sw\text{-}sed}$ (i.e. due to Mo-adsorption onto Mn-oxides), our model suggests a significant and long-term increase in the $\delta^{98}Mo_{sw}$ as well as the seawater Mo inventory consistent with the observed geological record (right side in panel 3, Fig. 9e). We therefore agree with Duan et al. (2010) that the increasing presence of Mn-oxides on well oxygenated shelf regions could have caused continuously higher δ^{98}Mo in black shales and siderites as long as the seawater Mo reservoir was at least regionally homogeneous.

Alternatively, light Mo was preferentially removed in weakly sulfidic environments, which would have similar effects on the $\delta^{98}Mo_{sw.}$ Coevally with increasing oxygenation in the course of the GOE, the weathering of sulfides on the continents led to elevated fluxes of sulfate and molybdenum to the oceans. On the one hand, this could have increased the ocean's Mo inventory and thus be a possible explanation for its more homogeneous distribution. On the other hand, higher sulfate concentrations stimulated bacterial sulfate reduction and hence the formation of sulfidic conditions (Reinhard et al., 2009). Thereby the build-up of a larger Mo inventory requires a Mo influx, which outbalances higher Mo removal rates in weakly euxinic settings. A larger inventory and more euxinic conditions enabled large Mo enrichments in black shales (Anbar et al., 2007). In the very beginning of environmental oxygenation before the GOE, the development of more weakly sulfidic rather than strongly conditions might be favored, which could have caused the gradual increase in the seawater δ^{98}Mo during the Neoarchean. For example, the predominant formation of MoO_3S^{2-} rather than MoS_4^{2-} in environments with $H_2S_{(aq)}$ concentrations lower than 5µmol L^{-1} cause large fractionations up to 3 ‰ in δ^{98}Mo (Neubert et al., 2008) and possibly the build-up of an isotopically heavy ocean. The subsequent areal expansion of sulfidic conditions during further oxygenation in the course

and after the GOE could have caused the development of more strongly sulfidic conditions with $H_2S_{(aq)}$ concentrations above 11 µmol L^{-1} and reduced net Mo-isotope fractionations (Duan et al., 2010). This could explain the leveling down of seawater δ^{98}Mo during the Proterozoic (Arnold et al., 2004; Duan et al., 2010; Kendall et al., 2009).

7. Conclusions

The molybdenum isotopic composition of black shales and carbonate facies iron formations exhibit authigenic Mo enrichment with near "crustal" δ^{98}Mo values in the Marra Mamba and Wittenoom formations (2.6 to 2.54 Ga) of the Hamersley Group, Western Australia, with only one single exception with significantly higher δ^{98}Mo. These results suggest a small and inhomogeneous seawater molybdate reservoir that was dominated by the unfractionated continental Mo input. Fractionation processes on Mn-oxides were temporally and spatially restricted causing locally high seawater δ^{98}Mo. Passing up section through the Mt. Sylvia Formation, Mt. McRae Shale and the Brockman Iron Formation δ^{98}Mo values continuously increase over time (2.54 to 2.50 Ga), by up to 1.5 ‰. We suggest that the uniform increase in δ^{98}Mo in Fe carbonates and black shales along with a good correlation of Mo concentration with total organic carbon, is best explained by two removal mechanisms that are associated with similarly low Mo-isotope fractionations, e.g. the adsorption of molybdate onto organic matter in Fe carbonate settings and thiomolybdate scavenging by the formation of sulfurized organic matter in the euxinic pore-water environments of black shale settings. Only in oxide iron formation settings does the adsorption of Mo onto Fe-oxyhydroxides seem relevant. Consistent with new modeling presented here, the concomitant increase in δ^{98}Mo within shelf sediments of the Hamersley Basin, Australia, and the Griqualand West Basin, South Africa, implies the build-up of a homogeneous and isotopically heavy Mo seawater reservoir after 2.54 Ga. The larger Mo reservoir size could have been a consequence of higher Mo-fluxes during oxidative weathering on the continents. The formation of Mn oxides during weathering or within well oxygenated coastal areas could have caused a seawater molybdate reservoir with high δ^{98}Mo. In contrast, iron formation appear to be unsuitable as an important sink for isotopically light Mo. Alternatively, the formation of weakly sulfidic conditions during early stages of environmental oxygenation could have amplified the sequestration of isotopically light Mo. Both explanations require mild oxygenation and sulfide weathering on the continents already before the GOE, so that our results and interpretations are in line with previous studies.

8. References

Algeo, T.J., Lyons, T.W., 2006. Mo–total organic carbon covariation in modern anoxic marine environments: Implications for analysis of paleoredox and paleohydrographic conditions. Paleoceanography 21.

Anbar, A.D., Duan, Y., Lyons, T.W., Arnold, G.L., Kendall, B., Creaser, R.A., Kaufman, A.J., Gordon, G.W., Scott, C., Garvin, J., Buick, R., 2007. A Whiff of Oxygen Before the Great Oxidation Event? Science 317, 1903-1906.

Arnold, G.L., Anbar, A., Barling, J., Lyons, T., 2004. Molybdenum isotope evidence for widespread anoxia in mid-Proterozoic oceans. Science 304, 87-90.

Balistrieri, L.S., Chao, T., 1990. Adsorption of selenium by amorphous iron oxyhydroxide and manganese dioxide. Geochimica et Cosmochimica Acta 54, 739-751.

Barling, J., Arnold, G.L., Anbar, A., 2001. Natural mass-dependent variations in the isotopic composition of molybdenum. Earth and Planetary Science Letters 193, 447-457.

Bekker, A., Holland, H., Wang, P.-L., Rumble, D., Stein, H., Hannah, J., Coetzee, L., Beukes, N., 2004. Dating the rise of atmospheric oxygen. Nature 427, 117-120.

Beukes, N.J., Gutzmer, J., 2008. Origin and paleoenvironmental significance of major iron formations at the Archean-Paleoproterozoic boundary. Reviews in Economic Geology 15, 5-47.

Beukes, N.J., Klein, C., Kaufman, A.J., Hayes, J., 1990. Carbonate petrography, kerogen distribution, and carbon and oxygen isotope variations in an early Proterozoic transition from limestone to iron-formation deposition, Transvaal Supergroup, South Africa. Economic geology and the bulletin of the Society of Economic Geologists 85, 663.

Catling, D.C., 2014. 6.7 - The Great Oxidation Event Transition, in: Holland, H.D., Turekian, K.K. (Eds.), Treatise on Geochemistry (Second Edition). Elsevier, Oxford, pp. 177-195.

Cloud, P.E., 1965. Significance of the Gunflint (Precambrian) Microflora Photosynthetic oxygen may have had important local effects before becoming a major atmospheric gas. Science 148, 27-35.

Crowe, S.A., Døssing, L.N., Beukes, N.J., Bau, M., Kruger, S.J., Frei, R., Canfield, D.E., 2013. Atmospheric oxygenation three billion years ago. Nature 501, 535-538.

Dahl, T.W., Anbar, A.D., Gordon, G.W., Rosing, M.T., Frei, R., Canfield, D.E., 2010. The behavior of molybdenum and its isotopes across the chemocline and in the sediments of sulfidic Lake Cadagno, Switzerland. Geochimica et Cosmochimica Acta 74, 144-163.

Dahl, T.W., Chappaz, A., Fitts, J.P., Lyons, T.W., 2013. Molybdenum reduction in a sulfidic lake: Evidence from X-ray absorption fine-structure spectroscopy and implications for the Mo paleoproxy. Geochimica et Cosmochimica Acta 103, 213-231.

Dellwig, O., Beck, M., Lemke, A., Lunau, M., Kolditz, K., Schnetger, B., Brumsack, H.-J., 2007. Non-conservative behaviour of molybdenum in coastal waters: Coupling geochemical, biological, and sedimentological processes. Geochimica et cosmochimica acta 71, 2745-2761.

Duan, Y., Anbar, A.D., Arnold, G.L., Lyons, T.W., Gordon, G.W., Kendall, B., 2010. Molybdenum isotope evidence for mild environmental oxygenation before the Great Oxidation Event. Geochimica et Cosmochimica Acta 74, 6655-6668.

Eigenbrode, J.L., Freeman, K.H., 2006. Late Archean rise of aerobic microbial ecosystems. Proceedings of the National Academy of Sciences 103, 15759-15764.

Ellwood, B.B., Chrzanowski, T.H., Hrouda, F., Long, G.J., Buhl, M.L., 1988. Siderite formation in anoxic deep-sea sediments: A synergetic bacteria controlled process with improtant implications in paleomagnetism. Geology 16, 980-982.

Erickson, B.E., Helz, G.R., 2000. Molybdenum (VI) speciation in sulfidic waters:: Stability and lability of thiomolybdates. Geochimica et Cosmochimica Acta 64, 1149-1158.

Farquhar, J., Bao, H., Thiemens, M., 2000. Atmospheric influence of Earth‘s earliest sulfur cycle. Science 289, 756-758.

Fischer, W., Schroeder, S., Lacassie, J., Beukes, N., Goldberg, T., Strauss, H., Horstmann, U., Schrag, D., Knoll, A., 2009. Isotopic constraints on the Late Archean carbon cycle from the Transvaal Supergroup along the western margin of the Kaapvaal Craton, South Africa. Precambrian Research 169, 15-27.

Flament, N., Coltice, N., Rey, P.F., 2008. A case for late-Archaean continental emergence from thermal evolution models and hypsometry. Earth and Planetary Science Letters 275, 326-336.

Frei, R., Gaucher, C., Poulton, S.W., Canfield, D.E., 2009. Fluctuations in Precambrian atmospheric oxygenation recorded by chromium isotopes. Nature 461, 250-253.

Goldberg, T., Archer, C., Vance, D., Poulton, S.W., 2009. Mo isotope fractionation during adsorption to Fe (oxyhydr) oxides. Geochimica et Cosmochimica Acta 73, 6502-6516.

Goldberg, T., Gordon, G., Izon, G., Archer, C., Pearce, C.R., McManus, J., Anbar, A.D., Rehkämper, M., 2013. Resolution of inter-laboratory discrepancies in Mo isotope data: an intercalibration. J. Anal. At. Spectrom. 28, 724-735.

Hannah, J.L., Bekker, A., Stein, H.J., Markey, R.J., Holland, H.D., 2004. Primitive Os and 2316 Ma age for marine shale: implications for Paleoproterozoic glacial events and the rise of atmospheric oxygen. Earth and Planetary Science Letters 225, 43-52.

Helz, G., Miller, C., Charnock, J., Mosselmans, J., Pattrick, R., Garner, C., Vaughan, D., 1996. Mechanism of molybdenum removal from the sea and its concentration in black shales: EXAFS evidence. Geochimica et Cosmochimica Acta 60, 3631-3642.

Helz, G.R., Bura-Nakić, E., Mikac, N., Ciglenečki, I., 2011. New model for molybdenum behavior in euxinic waters. Chemical Geology 284, 323-332.

Holland, H.D., 2006. The oxygenation of the atmosphere and oceans. Philosophical Transactions of the Royal Society B: Biological Sciences 361, 903-915.

Jiang, G., Kaufman, A.J., Christie-Blick, N., Zhang, S., Wu, H., 2007. Carbon isotope variability across the Ediacaran Yangtze platform in South China: Implications for a large surface-to-deep ocean< i> δ</i>< sup>

13</sup> C gradient. Earth and Planetary Science Letters 261, 303-320.

Johnson, C.M., Beard, B.L., Klein, C., Beukes, N.J., Roden, E.E., 2008. Iron isotopes constrain biologic and abiologic processes in banded iron formation genesis. Geochimica et Cosmochimica Acta 72, 151-169.

Johnson, C.M., Ludois, J.M., Beard, B.L., Beukes, N.J., Heimann, A., 2013. Iron formation carbonates: Paleoceanographic proxy or recorder of microbial diagenesis? Geology 41, 1147-1150.

Kashiwabara, T., Takahashi, Y., Tanimizu, M., Usui, A., 2011. Molecular-scale mechanisms of distribution and isotopic fractionation of molybdenum between seawater and ferromanganese oxides. Geochimica et Cosmochimica Acta 75, 5762-5784.

Kaufman, A.J., Hayes, J., Knoll, A.H., Germs, G.J., 1991. Isotopic compositions of carbonates and organic carbon from upper Proterozoic successions in Namibia: stratigraphic variation and the effects of diagenesis and metamorphism. Precambrian Research 49, 301-327.

Kaufman, A.J., Johnston, D.T., Farquhar, J., Masterson, A.L., Lyons, T.W., Bates, S., Anbar, A.D., Arnold, G.L., Garvin, J., Buick, R., 2007. Late Archean biospheric oxygenation and atmospheric evolution. Science 317, 1900-1903.

Kendall, B., Creaser, R.A., Gordon, G.W., Anbar, A.D., 2009. Re–Os and Mo isotope systematics of black shales from the Middle Proterozoic Velkerri and Wollogorang formations, McArthur Basin, northern Australia. Geochimica et Cosmochimica Acta 73, 2534-2558.

Kendall, B., Reinhard, C.T., Lyons, T.W., Kaufman, A.J., Poulton, S.W., Anbar, A.D., 2010. Pervasive oxygenation along late Archaean ocean margins. Nature Geoscience 3, 647-652.

Klein, C., Gole, M.J., 1981. Mineralogy and petrology of parts of the Marra Mamba Iron Formation, Hamersley Basin, Western Australia. American Mineralogist 66, 507-525.

Knauth, L.P., Kennedy, M.J., 2009. The late Precambrian greening of the Earth. Nature 460, 728-732.

Köhler, I., Konhauser, K.O., Papineau, D., Bekker, A., Kappler, A., 2013. Biological carbon precursor to diagenetic siderite with spherical structures in iron formations. Nature communications 4, 1741.

Konhauser, K.O., Amskold, L., Lalonde, S.V., Posth, N.R., Kappler, A., Anbar, A., 2007. Decoupling photochemical Fe (II) oxidation from shallow-water BIF deposition. Earth and Planetary Science Letters 258, 87-100.

Kowalski, N., Dellwig, O., Beck, M., Gräwe, U., Neubert, N., Nägler, T.F., Badewien, T.H., Brumsack, H.-J., van Beusekom, J.E., Böttcher, M.E., 2013. Pelagic molybdenum concentration anomalies and the impact of sediment resuspension on the molybdenum budget in two tidal systems of the North Sea. Geochimica et Cosmochimica Acta 119, 198-211.

Krapež, B., Barley, M.E., Pickard, A.L., 2003. Hydrothermal and resedimented origins of the precursor sediments to banded iron formation: sedimentological evidence from the Early Palaeoproterozoic Brockman Supersequence of Western Australia. Sedimentology 50, 979-1011.

Kurzweil, F., Claire, M., Thomazo, C., Peters, M., Hannington, M., Strauss, H., 2013. Atmospheric sulfur rearrangement 2.7 billion years ago: Evidence for oxygenic photosynthesis. Earth and Planetary Science

Letters 366, 17-26.

Liermann, L.J., Guynn, R.L., Anbar, A., Brantley, S.L., 2005. Production of a molybdophore during metal-targeted dissolution of silicates by soil bacteria. Chemical Geology 220, 285-302.

Lyons, T.W., Werne, J.P., Hollander, D.J., Murray, R., 2003. Contrasting sulfur geochemistry and Fe/Al and Mo/Al ratios across the last oxic-to-anoxic transition in the Cariaco Basin, Venezuela. Chemical Geology 195, 131-157.

McManus, J., Berelson, W.M., Severmann, S., Poulson, R.L., Hammond, D.E., Klinkhammer, G.P., Holm, C., 2006. Molybdenum and uranium geochemistry in continental margin sediments: paleoproxy potential. Geochimica et Cosmochimica Acta 70, 4643-4662.

Miller, C.A., Peucker-Ehrenbrink, B., Walker, B.D., Marcantonio, F., 2011. Re-assessing the surface cycling of molybdenum and rhenium. Geochimica et Cosmochimica Acta 75, 7146-7179.

Morford, J.L., Emerson, S., 1999. The geochemistry of redox sensitive trace metals in sediments. Geochimica et Cosmochimica Acta 63, 1735-1750.

Morris, R., 1993. Genetic modelling for banded iron-formation of the Hamersley Group, Pilbara Craton, Western Australia. Precambrian Research 60, 243-286.

Morris, R., Horwitz, R., 1983. The origin of the iron-formation-rich Hamersley Group of Western Australia—deposition on a platform. Precambrian Research 21, 273-297.

Nägler, T., Mills, M., Siebert, C., 2004. Biological fractionation of Mo isotopes during N-2 fixation by Trichodesmium sp. IMS 101. Geochimica et Cosmochimica Acta 68, A364.

Nägler, T., Neubert, N., Böttcher, M., Dellwig, O., Schnetger, B., 2011. Molybdenum isotope fractionation in pelagic euxinia: Evidence from the modern Black and Baltic Seas. Chemical Geology 289, 1-11.

Nägler, T.F., Anbar, A.D., Archer, C., Goldberg, T., Gordon, G.W., Greber, N.D., Siebert, C., Sohrin, Y., Vance, D., 2014. Proposal for an international molybdenum isotope measurement standard and data representation. Geostandards and Geoanalytical Research 38, 149-151.

Neubert, N., Nägler, T.F., Böttcher, M.E., 2008. Sulfidity controls molybdenum isotope fractionation into euxinic sediments: Evidence from the modern Black Sea. Geology 36, 775-778.

Ohmoto, H., Watanabe, Y., Kumazawa, K., 2004. Evidence from massive siderite beds for a CO2-rich atmosphere before ~ 1.8 billion years ago. Nature 429, 395-399.

Partridge, M.A., Golding, S.D., Baublys, K.A., Young, E., 2008. Pyrite paragenesis and multiple sulfur isotope distribution in late Archean and early Paleoproterozoic Hamersley Basin sediments. Earth and Planetary Science Letters 272, 41-49.

Pavlov, A., Kasting, J., 2002. Mass-independent fractionation of sulfur isotopes in Archean sediments: strong evidence for an anoxic Archean atmosphere. Astrobiology 2, 27-41.

Planavsky, N.J., Asael, D., Hofmann, A., Reinhard, C.T., Lalonde, S.V., Knudsen, A., Wang, X., Ossa, F.O., Pecoits, E., Smith, A.J., 2014. Evidence for oxygenic photosynthesis half a billion years before the Great Oxidation Event. Nature geoscience 7, 283-286.

Poulson Brucker, R.L., McManus, J., Severmann, S., Berelson, W.M., 2009. Molybdenum behavior during early diagenesis: Insights from Mo isotopes. Geochemistry, Geophysics, Geosystems 10.

Poulson, R.L., Siebert, C., McManus, J., Berelson, W.M., 2006. Authigenic molybdenum isotope signatures in marine sediments. Geology 34, 617-620.

Poulton, S.W., Krom, M.D., Raiswell, R., 2004. A revised scheme for the reactivity of iron (oxyhydr) oxide minerals towards dissolved sulfide. Geochimica et Cosmochimica Acta 68, 3703-3715.

Raiswell, R., Canfield, D.E., 1998. Sources of iron for pyrite formation in marine sediments. American Journal of Science 298, 219-245.

Reinhard, C.T., Planavsky, N.J., Lyons, T.W., 2013. Long-term sedimentary recycling of rare sulphur isotope anomalies. Nature 497, 100-103.

Reinhard, C.T., Raiswell, R., Scott, C., Anbar, A.D., Lyons, T.W., 2009. A late Archean sulfidic sea stimulated by early oxidative weathering of the continents. Science 326, 713-716.

Reitz, A., Wille, M., Nägler, T.F., de Lange, G.J., 2007. Atypical Mo isotope signatures in eastern Mediterranean sediments. Chemical Geology 245, 1-8.

Rey, P.F., Coltice, N., 2008. Neoarchean lithospheric strengthening and the coupling of Earth's geochemical reservoirs. Geology 36, 635-638.

Rudge, J.F., Reynolds, B.C., Bourdon, B., 2009. The double spike toolbox. Chemical Geology 265, 420-431.

Scott, C., Lyons, T., Bekker, A., Shen, Y., Poulton, S., Chu, X., Anbar, A., 2008. Tracing the stepwise oxygenation of the Proterozoic ocean. Nature 452, 456-459.

Scott, C., Lyons, T.W., 2012. Contrasting molybdenum cycling and isotopic properties in euxinic versus non-euxinic sediments and sedimentary rocks: Refining the paleoproxies. Chemical Geology 324, 19-27.

Scott, C.T., Bekker, A., Reinhard, C.T., Schnetger, B., Krapež, B., Rumble, D., Lyons, T.W., 2011. Late Archean euxinic conditions before the rise of atmospheric oxygen. Geology 39, 119-122.

Siebert, C., Kramers, J., Meisel, T., Morel, P., Nägler, T.F., 2005. PGE, Re-Os, and Mo isotope systematics in Archean and early Proterozoic sedimentary systems as proxies for redox conditions of the early Earth. Geochimica et Cosmochimica Acta 69, 1787-1801.

Siebert, C., McManus, J., Bice, A., Poulson, R., Berelson, W.M., 2006. Molybdenum isotope signatures in continental margin marine sediments. Earth and Planetary Science Letters 241, 723-733.

Siebert, C., Nägler, T.F., von Blanckenburg, F., Kramers, J.D., 2003. Molybdenum isotope records as a potential new proxy for paleoceanography. Earth and Planetary Science Letters 211, 159-171.

Siever, R., 1992. The silica cycle in the Precambrian. Geochimica et Cosmochimica Acta 56, 3265-3272.

Simonson, B.M., Schubel, K.A., Hassler, S.W., 1993. Carbonate sedimentology of the early Precambrian Hamersley Group of Western Australia. Precambrian Research 60, 287-335.

Takeno, N., 2005. Atlas of Eh-pH diagrams. Geological survey of Japan open file report, 102.

Taylor, S.R., McLennan, S.M., 1985. The continental crust: its composition and evolution.

Trendall, A., Compston, W., Nelson, D., De Laeter, J., Bennett, V., 2004. SHRIMP zircon ages constraining the depositional chronology of the Hamersley Group, Western Australia*. Australian Journal of Earth Sciences 51, 621-644.

Trendall, A.F., Nelson, D.R., De Laeter, J.R., Hassler, S.W., 1998. Precise zircon U-Pb ages from the Marra Mamba Iron Formation and Wittenoom Formation, Hamersley Group, Western Australia. Australian Journal of Earth Sciences 45, 137-142.

Tribovillard, N., Riboulleau, A., Lyons, T., Baudin, F., 2004. Enhanced trapping of molybdenum by sulfurized marine organic matter of marine origin in Mesozoic limestones and shales. Chemical Geology 213, 385-401.

Tuit, C., Waterbury, J., Ravizza, G., 2004. Diel variation of molybdenum and iron in marine diazotrophic cyanobacteria. Limnology and Oceanography 49, 978-990.

Voegelin, A.R., Nägler, T.F., Beukes, N.J., Lacassie, J.P., 2010. Molybdenum isotopes in late Archean carbonate rocks: implications for early Earth oxygenation. Precambrian Research 182, 70-82.

Voegelin, A.R., Pettke, T., Greber, N.D., von Niederhäusern, B., Nägler, T.F., 2014. Magma differentiation fractionates Mo isotope ratios: Evidence from the Kos Plateau Tuff (Aegean Arc). Lithos 190, 440-448.

Wasylenki, L.E., Rolfe, B.A., Weeks, C.L., Spiro, T.G., Anbar, A.D., 2008. Experimental investigation of the effects of temperature and ionic strength on Mo isotope fractionation during adsorption to manganese oxides. Geochimica et Cosmochimica Acta 72, 5997-6005.

Wichard, T., Mishra, B., Myneni, S.C.B., Bellenger, J.-P., Kraepiel, A.M.L., 2009. Storage and bioavailability of molybdenum in soils increased by organic matter complexation. Nature Geosci 2, 625-629.

Widdel, F., Schnell, S., Heising, S., Ehrenreich, A., Assmus, B., Schink, B., 1993. Ferrous iron oxidation by anoxygenic phototrophic bacteria. Nature 362, 834-836.

Wille, M., Kramers, J., Nägler, T.F., Beukes, N., Schröder, S., Meisel, T., Lacassie, J., Voegelin, A., 2007. Evidence for a gradual rise of oxygen between 2.6 and 2.5 Ga from Mo isotopes and Re-PGE signatures in shales. Geochimica et Cosmochimica Acta 71, 2417-2435.

Wille, M., Nägler, T.F., Lehmann, B., Schröder, S., Kramers, J.D., 2008. Hydrogen sulphide release to surface waters at the Precambrian/Cambrian boundary. Nature 453, 767-769.

Wille, M., Nebel, O., Van Kranendonk, M.J., Schoenberg, R., Kleinhanns, I.C., Ellwood, M.J., 2013. Mo–Cr isotope evidence for a reducing Archean atmosphere in 3.46–2.76 Ga black shales from the Pilbara, Western Australia. Chemical Geology 340, 68-76.

Winter, B.L., Knauth, L.P., 1992. Stable isotope geochemistry of cherts and carbonates from the 2.0 Ga Gunflint Iron Formation: implications for the depositional setting, and the effects of diagenesis and metamorphism. Precambrian research 59, 283-313.

Woodhead, J.D., Hergt, J.M., Simonson, B.M., 1998. Isotopic dating of an Archean bolide impact horizon, Hamersley basin, Western Australia. Geology 26, 47-50.

Zerkle, A., Scheiderich, K., Maresca, J., Liermann, L., Brantley, S., 2011. Molybdenum isotope fractionation by cyanobacterial assimilation during nitrate utilization and N2fixation. Geobiology 9, 94-106.

CHAPTER II

Coupled Iron and Molybdenum isotopes from a 2.4 billion years old oxygen oasis

1. Abstract

We provide new molybdenum and iron isotopic data from carbonate and silicate iron formations of the 2.48 Ga old Koegas Subgroup, South Africa, which were deposited below the anoxic-oxic redoxcline of a local oxygen oasis. The positive correlation of Fe/Mn ratios with both δ^{98}Mo and δ^{56}Fe values highlights the substantial role of Mn for the cycling of Mo and Fe. We suggest that pore water molybdate was recharged (1) by the diffusional transport of seawater molybdate with high δ^{98}Mo and (2) by the re-liberation of adsorbed molybdate with low δ^{98}Mo during Mn oxide dissolution. The relative contribution of isotopically light Mo is highest close to the Mn chemocline, where the flux of Mn oxides is largest, which causes the positive correlation of Fe/Mn ratios and δ^{98}Mo values in the Koegas sediments.

The relationship of $\delta^{56}Fe$ and Mn becomes apparent when considering modern depositional equivalents such as Lac Pavin. The $\delta^{56}Fe$ values of dissolved Fe^{2+} in Lac Pavin show a pronounced decrease along the Mn redox cline, which is attributed to the oxidation and precipitation of isotopically heavy Fe-hydroxides in this depth region (Busigny et al., 2014). The positive correlation of $\delta^{56}Fe$ values with Fe/Mn ratios in Koegas sediments therefore results from Mn oxide formation in the water depth region with lowest $\delta^{56}Fe$. Importantly, the Fe-isotope trends observed in Lac Pavin were not preserved in respective sediments. This might indicate that the gradient of the chemocline in early Proterozoic oxygen oases was smoother probably as a result of relatively low oxygen concentrations. We suggest that before the Great Oxidation Event the O_2-exchange of oxic surface waters with the still reducing atmosphere kept the local marine oxygen levels relatively low.

2. Introduction

The Great Oxidation Event (GOE) between 2.45 and 2.32 billion years (Ga) ago represents one of the major environmental changes in Earth history (Holland, 2006). During this time period atmospheric oxygen levels rose from below 10^{-5} up to 10^{-2} of Present Atmospheric Level (PAL) (Farquhar et al., 2000; Holland, 2006; Pavlov and Kasting, 2002). This jump in atmospheric oxygen concentration reflects a combination of increased primary production by oxygenic photosynthesis and organic carbon burial, a decrease in the O_2 buffer capacity or a combination of both (Catling et al., 2001; Gaillard et al., 2011; Holland, 2006; Kump and Barley, 2007; Lyons et al., 2014).

Some evidence points to photosynthetic activity by cyanobacteria several hundred million years earlier than the GOE (Canfield, 2005; Crowe et al., 2013; Kurzweil et al., 2013; Nisbet et al., 2007). However, the reducing power of the upper continental crust, the atmosphere and the deep ocean outbalanced oxygen production and prohibited the earlier accumulation of free oxygen. Separated from anoxic deep waters, only some shallow marine habitats became oxygenated (Planavsky et al., 2014; Reinhard et al., 2009), which caused the development of a locally stratified ocean margin (Kendall et al., 2010). The existence of such oxygen oasis were claimed as early as 3.0 Ga ago (Planavsky et al., 2014). However, their extension and the implications for the isotopic composition of different paleo-redox proxies remain poorly understood.

In this study we combine Fe and Mo isotopes from iron formations (IFs) of the Koegas Subgroup, South Africa, to reconstruct the local environment of the Griqualand West Basin more than 2.4 Ga ago. The deposition of such proximal iron formations is related to the local oxidation of very soluble Fe^{2+}, which was derived from a ferruginous deep ocean reservoir. Oxidized Fe^{3+} is poorly soluble and forms Fe-(oxy)hydroxide minerals, which may subsequently precipitate on the seafloor. This oxidation could be processed by anoxygenic phototrophic bacteria (Kappler et al., 2005). Alternatively, IFs of the Koegas Subgroup shortly before the GOE could indicate the local availability of oxygen in surface ocean areas (Cloud, 1973). We compare our results with isotopic data of modern anoxic lakes, which were claimed as modern ocean analogues (Busigny et al., 2014) as well as isotopic data of sediments from the oldest

known oxygen oasis (Planavsky et al., 2014). The combination of Mo and Fe isotopes provides important insights into the local marine environment with profound implications for the regional/global ocean redox state and the behavior of redox sensitive elements like Mo and Fe in such settings in general.

3. Geological setting and sample material

The Ghaap Group (Traansvaal Supergroup, South Africa) represents a continuous sedimentary succession, which was deposited in the Griqualand West Basin immediately before the GOE (Beukes and Gutzmer, 2008). The Koegas Subgroup forms the uppermost unit of the Ghaap Group, which represents the final stage of a long-term regressive period (Schröder et al., 2011). SHRIMP U-Pb zircon data of the subjacent Asbesheuwels Subgroup (Kuruman Formation) indicate a maximum depositional age of 2460 ± 5 Ma (Pickard, 2003). In contrast, Re-Os dating of shales from the Koegas Subgroup (Nelani Formation, Klipputs Member; GEC01 174-176) provide a depositional age of 2479 ± 22 Ma (Kendall et al., 2013), which may suggest a true depositional age at the lower end of this error range.

The sediments of the Koegas Subgroup represent periodical alternations of siliciclastic units during regressions (Pannetjie-, Naragas-, Heynskop Formation) and iron formations during transgressions (Doradale-, Rooinekke-, Nelani Formation) along a prograding delta or submarine fan system (Schröder et al., 2011). The terrigenous input was generally higher in the eastern parts of the basin, which argues for lateral basinal deepening from E to W (Schröder et al., 2011). The eastern drillcore GTF01 therefore represents the more proximal depositional setting (Fig. 1A). GTF01 samples of this study are from the Doradale Formation, which is associated with maximal sea level and the deposition of fine-grained and laminated IFs. The western GEC01 drillcore comprises sediments from deeper settings of the Rooinekke and Nelani formations. Beukes (1983) suggested a flooding surface at the base of the Nelani formation during the Klipputs Member (Fig. 1C). The subsequent regression during the Nelani Formation ends in granular carbonate iron formations (sample GEC 65.9), which represent deposition above wave base.

The petrological and mineralogical composition of our samples is described in detail by Nel (2013). This author mainly distinguishes between Fe-carbonate lutite and Fe-silicate lutite dominated samples, respectively, as well as a combination of both (Table 1, Fig 1C). In most samples dark green-black, very fine grained and massive Fe-silicate lutite layers alternate with lighter colored, greyish siderite lutite layers, which are coarser grained and can form a peloidal structure. This alternation results in fine laminations visible on the core material (http://general.uj.ac.za/agouron/). The abundance of Fe-oxides (mainly magnetite) is minor compared to Fe-silicates and Fe-carbonates. Few samples show minor abundance of Riebeckite (Table 1, 2), which point to low-grade metamorphism of the Koegas Subroup (Schröder et al., 2011). Pyrite is only abundant in detrital form in sandstone units of the Koegas Subgroup, which were not considered in this study (Johnson et al., 2013b). Very low concentrations of Al_2O_3 in our samples strongly suggest that the terrigenous input was generally reduced (Table 1).

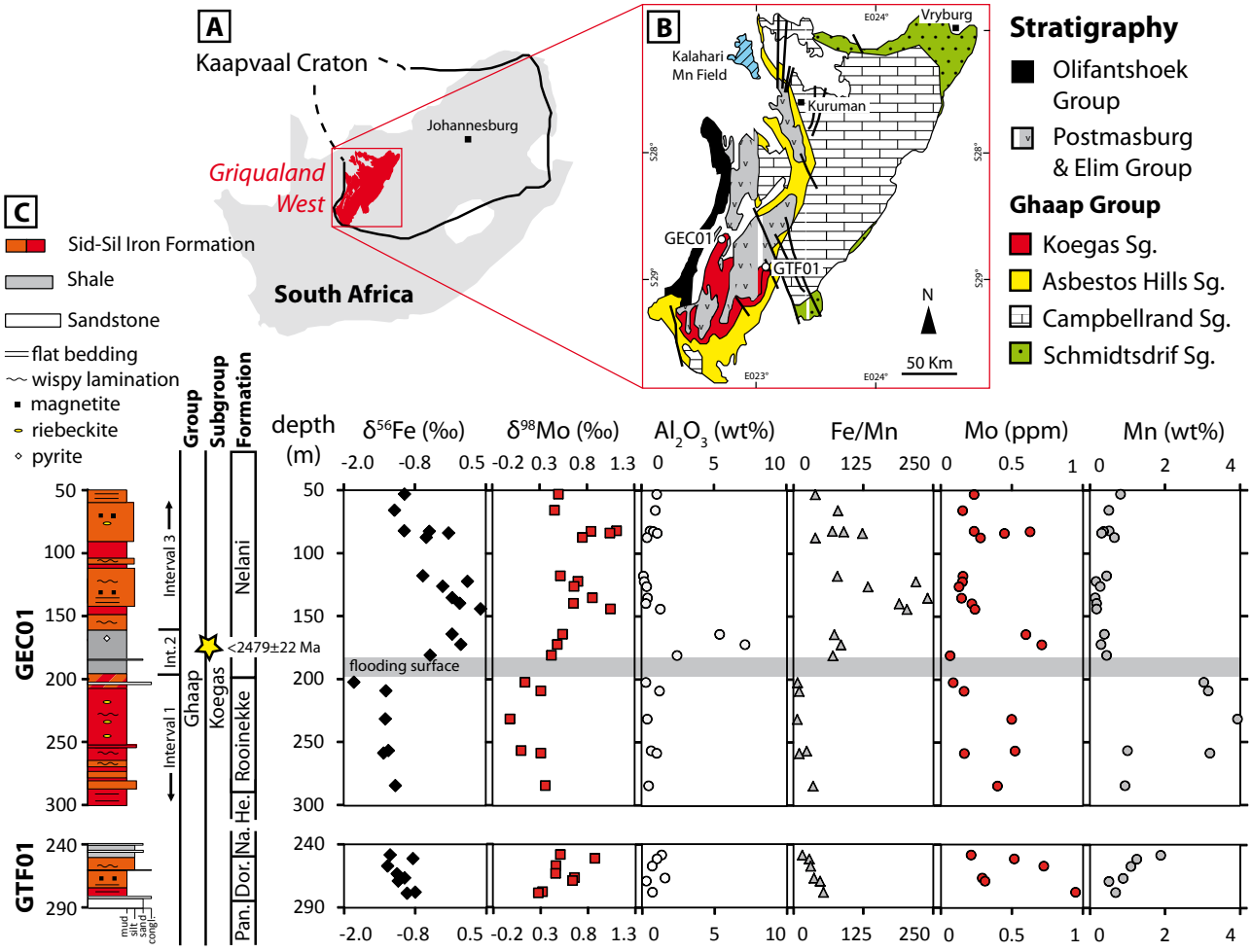

FIGURE 1: (A) Location of the Griqualand West Basin on the Kaapvaal Craton, South Africa (modified from Schroeder et al., 2011). (B) Geological map of the Griqualand West Basin and the drill core position of GEC01 and GTF01 (modified from Schroeder et al. , 2011). (C) Stratigraphic description of drill cores GEC01 and GTF01. Re-Os dating of shales deposited at the base of the Nelani Formation during the Klipputs Member provide a maximum depositional age of 2479 ± 22 Ma (Kendall et al., 2013). Selected geochemical parameters are shown against drill core depth. The concentrations of Al, Fe and Mn are from Nel (2013). Pan.: Pannetje; Dor.: Doradale; Na.: Naragas; He: Heynskop.

4. Methods

For Fe isotope measurements ~20 mg of powdered sample material were digested at 120°C for 48 hours using a 3:1 mixture of distilled HF and HNO_3 acids. Subsequently, dried samples were two times re-dissolved in distilled 6M HCl, which assured complete dissolution. An aliquot containing around 30 µg Fe was split for further purification of Fe. The separation of Fe by the use of an anion exchange resin (AG1-X8, 100-200 mesh) follows a procedure described by Schönberg and von Blacnkenburg (2005).

Table 1: major element composition, data from Nel, 2013

Formation	drillcore/ Depth	lithology	SiO2 wt%	Al_2O_3 wt%	Fe_2O_3 wt%	MgO wt%	CaO wt%	Na2O wt%	K_2O wt%	TiO_2 wt%	P_2O_5 wt%	MnO wt%	Fe/Mn	LOI wt%	Sum %
Nelani	**GEC 53.2**	sid	36.6	1.1	35.4	4.8	1.1	0.2	0.5	0.1	0.1	0.8	**39.0**	19.3	99.9
	GEC 65.9	sid (gr IF band)	20.7	1.0	45.0	5.8	1.2	0.2	0.5	0.1	0.1	0.5	**79.7**	24.9	99.8
	GEC 82.2	sid-sil	38.8	0.6	40.2	4.3	0.8	0.1	0.3	0.0	0.1	0.5	**69.9**	14.2	99.9
	GEC 82.8	sil-sid	39.1	0.9	36.9	4.5	2.6	0.2	0.4	0.0	0.1	0.4	**90.2**	14.7	99.8
	GEC 84	sid-sil	30.5	1.1	43.8	5.9	0.7	0.2	0.6	0.1	0.1	0.3	**123.8**	16.7	99.9
	GEC 87.5	mag sid-sil	48.7	0.4	28.8	3.1	5.1	0.3	0.2	0.0	0.0	0.7	**39.4**	12.6	99.9
	GEC 118	sid (some riebeckite)	30.2	0.2	39.3	5.3	1.0	0.3	0.1	0.0	0.1	0.5	**78.8**	22.9	99.9
	GEC 120	sid	21.7	0.0	40.0	4.9	2.2	0.1	0.0	0.0	0.0	0.8	**43.0**	26.5	96.4
	GEC 122.5	sid	38.2	0.2	41.2	3.8	1.3	0.1	0.1	0.0	0.1	0.2	**219.2**	14.6	99.9
	GEC 126.5	sid (minor sil)	41.2	0.4	41.4	4.8	0.8	0.1	0.2	0.0	0.1	0.3	**133.6**	10.6	99.9
	GEC 135.5	sid (minor rieb)	47.7	0.4	39.9	4.7	0.4	0.1	0.2	0.0	0.1	0.2	**240.2**	6.3	99.9
	GEC 140	sid (minor sil)	50.6	0.3	37.8	2.9	0.9	0.2	0.2	0.0	0.1	0.2	**189.6**	6.9	100.0
	GEC 144.3	sil	42.0	1.3	40.5	4.3	0.4	0.4	0.7	0.1	0.1	0.2	**203.3**	9.9	99.9
	GEC 164.5	sil	39.5	5.4	31.6	4.1	0.5	0.3	3.9	0.3	0.1	0.4	**73.3**	13.7	99.8
	GEC 172.5	sid-sil	44.6	7.2	28.3	3.6	0.2	0.3	4.9	0.3	0.1	0.3	**85.3**	10.0	99.8
	GEC 181.1	sid-sil	36.9	2.5	35.3	4.1	2.6	0.3	1.1	0.2	0.1	0.5	**70.9**	16.5	99.9
Rooinekke	**GEC 202.5**	sid-sil	46.8	0.3	24.1	3.1	4.9	0.4	0.2	<0.01	0.0	3.0	**7.2**	17.1	99.9
	GEC 209.4	sil	36.3	1.3	35.6	5.3	1.0	0.9	1.0	0.1	0.1	3.2	**10.2**	15.2	99.9
	GEC 231.7	sid-sil	42.8	0.4	30.2	3.4	3.7	0.4	0.3	0.0	0.1	3.9	**6.9**	14.8	100.0
	GEC 257	sil sid and rieb	59.9	0.7	26.6	2.2	1.3	2.0	0.3	0.0	0.1	1.0	**23.8**	5.9	99.9
	GEC 259	sid-sil	29.5	1.1	37.5	4.6	2.9	0.2	0.5	0.1	0.1	3.2	**10.6**	20.3	99.9
	GEC 284.7	sid-sil	37.3	0.5	36.8	3.6	6.8	0.2	0.2	0.0	0.1	0.9	**35.4**	13.4	99.9
Doradale	**GTF-248.5**	sid-sil	35.9	1.4	33.0	3.7	3.8	0.1	0.6	0.1	0.1	1.9	**15.8**	19.3	99.8
	GTF-251.5	sid-sil	34.6	1.0	38.9	3.8	1.2	0.1	0.5	0.1	0.1	1.3	**28.1**	18.3	99.9
	GTF-257.3	sid-sil	38.4	0.7	37.7	4.0	1.1	0.1	0.4	0.1	0.1	1.1	**31.0**	16.3	99.9
	GTF-263.4	sil-sid	42.5	0.6	36.5	3.7	0.6	0.1	0.2	0.1	0.1	0.8	**40.4**	11.7	96.8
	GTF-266.8	sil-sid	42.6	1.6	36.2	4.9	0.5	0.1	1.1	0.1	0.1	0.9	**36.7**	11.9	99.9
	GTF-269.2	sid-sil	60.6	0.3	26.9	2.8	1.1	0.0	0.1	0.0	0.0	0.5	**47.6**	7.6	100.0
	GTF-278	sil-sid	39.2	0.7	41.1	3.3	4.1	0.1	0.3	0.0	0.1	0.7	**53.8**	10.3	99.9
	GTF 278.8	sil-sid	47.0	1.0	38.0	4.3	0.7	0.1	0.2	0.1	0.0	0.5	**65.0**	7.8	99.7

Purified samples were dissolved in 0.3M HNO_3 and introduced into a multi collector ICP-MS (Thermo Scientific Neptune; University of Tuebingen) using a Stable Sample Introduction (SSI) spray dual chamber system with a PFA pneumatic nebulizer. Isotopic ratios were measured at high resolution, which assured the resolution of polyatomic interferences such as $^{40}Ar^{16}O^+$ on $^{56}Fe^+$ and $^{40}Ar^{14}N^+$ on $^{54}Fe^+$ (Weyer and Schwieters, 2003). The Isobaric interferences of $^{54}Cr^+$ and $^{58}Ni^+$ were corrected for by simultaneous measurements of $^{52}Cr^+$ and $^{60}Ni^+$, respectively, and the use of published relative isotope abundance data (de Laeter et al., 2003) assuming the same instrumental mass bias for Cr and Ni as determined for Fe. Fe isotopic ratios were measured by using the standard bracketing method (Schoenberg and von Blanckenburg, 2005). Each sample measurement was bracketed by IRMM-014 reference solution measurements (Institute of Reference Material and Measurements, Geel, Belgium). A measurement always included one block of 20 cycles, each having an integration time of 8.4 s. The correction of the instrumental mass bias follows a scheme of Schoenberg and von Blanckenburg (2005). Fe isotopic ratios are presented in the δ-notation and relative to the reference solution of IRMM-014 and are expressed in ‰:

$$\delta^{56}\mathrm{Fe} = \left(\frac{\left(\frac{^{56}Fe}{^{54}Fe}\right)_{\mathrm{Sample}}}{\left(\frac{^{56}Fe}{^{54}Fe}\right)_{\mathrm{IRM014}}} - 1 \right) \mathrm{x}\ 1000$$

All samples were measured twice and average isotopic values are presented in this study (Table 2). The long-term reproducibility of the HAN standard is 0.29 ± 0.05 ‰ (2SD; n = 145). The in-house standard HAN measured during the course of this study showed average δ^{56}Fe values of 0.294 ± 0.039 ‰ (2SD, n = 11), which is consistent with published values (Moeller et al., 2014). The IF-G reference material, which ran through all purification steps in the course of this study shows a δ^{56}Fe value of 0.644 ‰, which is also in agreement with literature values (Dauphas and Rouxel, 2006). Total Fe blanks were ~4 ng, contributing less than 0.1 % to the extracted Fe signal, which assures negligible contamination during the analytical procedure.

For Mo isotope measurements 100-300 mg of powdered and ashed (12h at 600°C) sample material, which is equivalent to ~50 ng Mo, was spiked in the ratio 1:1 (97Mo-100Mo double spike) and digested using the dissolution steps described above. The double spike method allows the correction for mass dependent isotope fractionations during the purification and measurement procedure. Chemical purification of Mo was achieved using a combination of anion and cation exchange resins (Eichrom AG1-X8, 200-400 mesh; Eichrom 50WX8, 200-400 mesh).

Mo isotopic ratios were measured in low resolution mode with a multi collector ICP-MS Thermo Scientific Neptune at the University of Tuebingen. To improve the signal intensity (the signal on 95Mo was always above 250 mV), samples were introduced using a CETAC Aridus IITM desolvating nebulizer system. The Isobaric interferences of $^{96}Ru^+$, $^{98}Ru^+$, and $^{100}Ru^+$ were corrected for by simultaneous measurements of $^{99}Ru^+$ and the use of published relative isotope abundance data (de Laeter et al., 2003) assuming the same instrumental mass bias for Ru as determined for Mo. Acid blank analyses, which bracketed each sample and standard measurement, were used for an on-peak-zero baseline subtraction. Samples and standards were measured for 100 cycles, each having an integration time of 8.4 s. The correction for instrumental

mass bias follows a scheme of Siebert et al. (2001). The Mo isotopic data are reported in the δ-notation relative to NIST 3134 and expressed in ‰:

$$\delta^{98}\mathrm{Mo} = \left(\frac{\left(\frac{^{98}Mo}{^{95}Mo}\right)_{\mathrm{Sample}}}{\left(\frac{^{98}Mo}{^{95}Mo}\right)_{\mathrm{NIST3134}}} - 1 \right) \mathrm{x}\ 1000$$

We follow the proposal of Nägler et al. (2013) and set NIST 3134 to 0.25 ‰ in δ^{98}Mo. The repeated cross-calibration of NIST 3134 with our in-house standard Johnson Matthey ICP during the measurement sequence of this study showed an isotopic difference of $\Delta^{98}Mo_{NIST3134\text{-}JM}$ = 0.286 ± 0.030 ‰ (2SD; n = 4), which is in agreement with the long term average $\Delta^{98}Mo_{NIST3134\text{-}JM}$ value of 0.273 ± 0.031 ‰ (2SD, n = 32) as well as with literature values (Goldberg et al., 2013). A second in-house standard, ZH-2, which ran through all purification steps during the course of this study shows a δ^{98}Mo value of 1.001 ‰ and 0.097 ‰, respectively. These values are consistent with the long-term reproducibility of ZH-2, which is 0.995 ± 0.086 (2σ; n = 16) as well as with literature values (Lehmann et al., 2007). The total blank was below 0.2 ng, which assured negligible contamination of sample measurements.

5. Iron isotopes

Iron isotopes can potentially be used to reconstruct the ancient marine redox-state (Rouxel et al., 2005) because the redox dependent speciation of iron is accompanied by fractionation processes. Dissolved $Fe_{(aq)}^{2+}$ and poorly soluble $Fe_{(aq)}^{3+}$ isotopically equilibrate within minutes with a large isotopic difference of $\Delta^{56}Fe_{Fe2+\text{ - }Fe3+} = \delta^{56}Fe_{Fe2+} - \delta^{56}Fe_{Fe3+}$ = -3 ‰ (Welch et al., 2003). The subsequent precipitation of $Fe_{(aq)}^{3+}$ as Fe-oxyhydroxide minerals causes a kinetic isotope fractionation in opposite direction, the magnitude being mainly dependent on the mineral species and temperature. For zero age ferrihydrite the isotopic difference is $\Delta^{56}Fe_{Fe3+\text{ - }FeOOH} = \delta^{56}Fe_{Fe3+} - \delta^{56}Fe_{FeOOH}$ = +2 ‰ (Beard and Johnson, 2004; Johnson et al., 2008). Altogether the oxidation and precipitation of Fe^{3+} minerals cause the relative depletion of heavy Fe isotopes in the remaining $Fe_{(aq)}^{2+}$ reservoir. The separation of anoxic $Fe_{(aq)}^{2+}$-rich deep waters and an oxic surface layer, where $Fe_{(aq)}^{2+}$ is oxidized therefore causes large isotopic gradients along the chemocline (Busigny et al., 2014). The Fe isotopic composition of sediments along this chemocline thus potentially records an ancient local oxygen oasis.

The Fe isotopic composition of the Koegas Subgroup sediments shows distinct trends along the stratigraphic column (Fig. 1C). During the Doradale Formation and the Rooinekke Formation δ^{56}Fe values remain below -0.75 ‰ and down to -1.82 ‰ (Interval 1; GTF01 + GEC01 250–195 m). Up in stratigraphy, we observe a sharp increase in δ^{56}Fe values at the base of the Nelani Formation (Klipput-Member, Interval 2; GEC01 195–160 m) followed by a continuous and smooth decrease in the course of the Nelani Formation (Interval 3 GEC 160-50 m; Fig. 1C). Low δ^{56}Fe values during the IF dominated interval 1 are accompanied by relatively high Mn concentrations as well as low Fe/Mn ratios. The continuous sharp increase during interval 2 reflects a change in lithology from pure iron formations towards alternations of shaly sediments

Table 2: Fe and Mo isotopic composition

Formation	Drillcore/ Depth	Depth	Lithology		$\delta^{56/54}$Fe (‰)	2σ	$\delta^{57/54}$Fe (‰)	2σ	$\delta^{58/54}$Fe (‰)	2σ	$\delta^{57/56}$Fe (‰)	2σ	Mo µg/g	δ^{98}Mo (‰)	Mo µg/g	*replicates* δ^{98} *Mo* (‰)	*Mo* µg/g
Nelani	**GEC 53.2**	53.2	sid	0.50	**-0.93**	0.08	-1.36	0.11	-1.94	0.42	-0.43	0.03	0.24	**0.48**	**0.20**	*0.48*	*0.21*
	GEC 65.9	65.9	sid (gr IF)	0.46	**-1.11**	0.03	-1.64	0.05	-1.73	0.37	-0.53	0.05	0.16	**0.46**	**0.16**		
	GEC 82.2	82.2	sid-sil	1.11	**-0.93**	0.03	-1.37	0.08	-1.89	0.02	-0.44	0.05	0.24	**0.96**	**0.27**	*1.09*	*0.24*
	GEC 82.8	82.8	sil-sid	0.85	**-0.49**	0.03	-0.74	0.08	-1.16	0.13	-0.25	0.05	0.63	**0.91**	**0.59**	*0.82*	*0.63*
	GEC 84	84	sid-sil	1.04	**-0.16**	0.03	-0.27	0.06	-0.24	0.44	-0.12	0.06	0.45	**1.03**	**0.46**	*1.02*	*0.45*
	GEC 87.5	87.5	mag sid-sil	0.75	**-0.55**	0.03	-0.81	0.07	-0.98	0.39	-0.27	0.06	0.28	**0.77**	**0.30**	*0.73*	*0.28*
	GEC 118	118	sid (some rieb)	0.52	**-0.60**	0.03	-0.90	0.09	-1.09	0.13	-0.29	0.06	0.16	**0.52**	**0.16**		
	GEC 120	120		0.44	**-1.34**	0.01	-1.97	0.01	-2.56	0.03	-0.63	0.00	0.09	**0.44**	**0.09**		
	GEC 122.5	122.5	sid	0.71	**0.18**	0.02	0.25	0.00	0.32	0.08	0.07	0.02	0.15	**0.71**	**0.15**		
	GEC 126.5	126.5	sid (minor sil)	0.67	**-0.26**	0.03	-0.38	0.12	-0.38	0.08	-0.12	0.08	0.13	**0.67**	**0.13**		
	GEC 135.5	135.5	sid (minor rieb)	0.86	**-0.09**	0.04	-0.09	0.04	-0.22	0.11	0.00	0.00	0.15	**0.86**	**0.15**		
	GEC 140	140	sid (minor sil)	0.66	**0.04**	0.04	0.06	0.06	0.09	0.30	0.02	0.01	0.22	**0.66**	**0.22**		
	GEC 144.3	144.3	sil	1.05	**0.41**	0.04	0.57	0.03	0.78	0.07	0.16	0.01	0.24	**1.03**	**0.23**	*1.03*	*0.24*
	GEC 164.5	164.5	sil	0.55	**-0.09**	0.02	-0.14	0.00	-0.02	0.01	-0.05	0.02	0.60	**0.53**	**0.66**	*0.52*	*0.60*
	GEC 172.5	172.5	sid-sil	0.49	**0.06**	0.03	0.09	0.06	0.16	0.29	0.03	0.04	0.71	**0.50**	**0.85**	*0.47*	*0.71*
	GEC 181.1	181.1	sid-sil	0.43	**-0.48**	0.01	-0.71	0.05	-0.47	0.23	-0.23	0.06	0.07	**0.43**	**0.07**		
Rooinekke	**GEC 202.5**	202.5	sid-sil	0.15	**-1.82**	0.00	-2.67	0.03	-3.52	0.21	-0.86	0.03	0.09	**0.45**	**0.09**		
	GEC 209.4	209.4	sil	0.32	**-1.26**	0.02	-1.89	0.04	-2.23	0.29	-0.63	0.05	0.17	**0.32**	**0.17**	*0.29*	*0.17*
	GEC 231.7	231.7	sid-sil	-0.01	**-1.27**	0.03	-1.88	0.03	-2.33	0.02	-0.61	0.00	0.50	**-0.01**	**0.50**		
	GEC 257	257	sil sid and rieb	0.11	**-1.21**	0.03	-1.80	0.04	-2.31	0.19	-0.59	0.01	0.53	**0.11**	**0.53**	*0.09*	*0.52*
	GEC 259	259	sid-sil	0.32	**-1.30**	0.00	-1.92	0.01	-2.52	0.03	-0.62	0.01	0.17	**0.32**	**0.16**		
	GEC 284.7	284.7	sid-sil	0.36	**-1.09**	0.02	-1.63	0.10	-2.21	0.01	-0.54	0.08	0.40	**0.36**	**0.41**	*0.34*	*0.40*
Doradale	**GTF-248.5**	248.5	sid-sil	0.51	**-1.19**	0.02	-1.77	0.03	-2.24	0.25	-0.58	0.05	0.22	**0.48**	**0.22**	*0.49*	*0.22*
	GTF-251.5	251.5	sid-sil	0.88	**-0.79**	0.01	-1.18	0.02	-1.47	0.23	-0.39	0.03	0.52	**0.88**	**0.52**		
	GTF-257.3	257.3	sid-sil	0.46	**-1.23**	0.00	-1.83	0.01	-2.23	0.00	-0.60	0.01	0.73	**0.46**	**0.73**		
	GTF-263.4	263.4	sil-sid	0.46	**-1.07**	0.10	-1.58	0.13	-1.78	0.07	-0.51	0.03	0.39	**0.46**	**0.39**		
	GTF-266.8	266.8	sil-sid	0.66	**-0.94**	0.03	-1.34	0.08	-1.46	0.33	-0.40	0.06	0.29	**0.68**	**0.27**	*0.64*	*0.28*
	GTF-269.2	269.2	sid-sil	0.64	**-1.05**	0.01	-1.55	0.02	-1.73	0.02	-0.51	0.03	0.31	**0.51**	**0.21**	*0.62*	*0.31*
	GTF-278	278	sil-sid	0.32	**-0.75**	0.00	-1.14	0.02	-1.95	1.00	-0.39	0.01	0.95	**0.36**	**0.96**	*0.30*	*0.95*
	GTF 278.8	278.8	sil-sid	0.28	**-0.89**	0.03	-1.34	0.01	-1.75	0.02	-0.45	0.03	0.28	**0.25**	**0.29**	*0.26*	*0.28*

sil: Fe-silicate; sid: siderite; rieb: riebeckite; mag: magnetite; gr IF: granular iron formation

and silicate lutites. This change is also depicted by higher Al concentrations and near crustal $\delta^{56}Fe$ values in this interval (Beard et al., 2003; Poitrasson, 2006) (Fig. 1C). The IF dominated succession between 150 and 50 m shows low Al concentrations again. However, these IFs exhibit significantly lower Mn concentrations and higher Fe/Mn ratios compared to the lower IF section. All intervals together reflect a positive correlation of $\delta^{56}Fe$ values with Fe/Mn ratios (Fig. 2A).

This positive correlation of $\delta^{56}Fe$ values with Fe/Mn ratios suggests that Fe isotope fractionation was related to Mn oxide formation, an interrelation, which was also observed in Lac Pavin, a modern redox-stratified lake, which was claimed as a "Archean ocean analogue" (Busigny et al., 2014). Similar as Precambrian oxygen oases, Lac Pavin shows a well oxygenated upper surface layer divided from anoxic and ferruginous deep waters (Fig. 3). Along a Mn chemocline between these water bodies Mn^{2+} derived from anoxic deep waters is oxidized. Slightly below this chemocline, Fe^{2+} is oxidized either by the concomitant reduction of Mn oxides or by oxygen (Busigny et al., 2014; Hongve, 1997). Busigny et al. (2014) observed a sharp decline in $\delta^{56}Fe$ values of dissolved Fe^{2+} along the Mn oxidation reaction zone. This relation is attributed to the oxidation of Fe^{2+} to Fe^{3+} probably by the reduction of Mn oxides and the concomitant enrichment of heavy Fe isotopes in precipitated Fe^{3+} minerals, which leaves behind a $Fe_{(aq)}^{2+}$ reservoir with low $\delta^{56}Fe$ values (Tsikos et al., 2010) (Fig. 3).

Considering the mineralogy of GEC01 and GTF01 samples, Mn is exclusively bound in carbonate phases, which implies the quantitative reduction of Mn oxides within the water column and/or the sediment (Johnson et al., 2013b). The enrichment of Mn in carbonates during diagenesis is a question of Mn availability within the sediments, which in turn largely depends on the flux of Mn oxides to the sediment. The deeper the ferruginous water column, the more efficient is the reduction and re-dissolution of Mn oxides within the water column (Tsikos et al., 2010). This hinders the precipitation of Mn oxides in the deeper parts of the anoxic basin. Relative enrichment of Mn in carbonates of GEC01 and GTF01 samples is therefore expected in sediments directly beneath the chemocline, and along the water depth region with low $\delta^{56}Fe$ values in dissolved Fe^{2+} (Fig. 3). We suggest that this association causes the most negative $\delta^{56}Fe$ values in sediments with high Mn concentrations and low Fe/Mn ratios (Fig. 2A).

Importantly, the trends in the $\delta^{56}Fe$ value of dissolved Fe^{2+}, observed along the chemocline by Busigny et al. (2014), are not preserved in the associated bulk rocks of the lake. One reason could be that bulk rock Fe isotope measurements from Lac Pavin were masked by detrital Fe. Most negative $\delta^{56}Fe_{Fe2+}$ values in Lac Pavin were measured in water samples with very low $Fe_{(aq)}^{2+}$ concentration. Mass balance constraints therefore indicate that their impact on the sedimentary $\delta^{56}Fe$ value might be relatively low. In contrast, the near absence of detrital components in the chemical sediments from intervals 1 and 3 might allow the better preservation of water column isotope signals. Additionally, we suggest that the surface waters of the Griqualand West Basin were lower concentrated in O_2 compared to Lac Pavin. This would have lowered $Mn_{(aq)}^{2+}$ and $Fe_{(aq)}^{2+}$ oxidation rates, because their half-life mainly depends on pH and the oxygen concentration in seawater (Field and Sherrell, 2000). Lower $Mn_{(aq)}^{2+}$ and $Fe_{(aq)}^{2+}$ oxidation rates in turn could have developed a rather smooth Mn chemocline with more smoothly declining $Fe_{(aq)}^{2+}$ concentrations and $\delta^{56}Fe$ values. If the chemocline extended over several and maybe tens of meters, the development

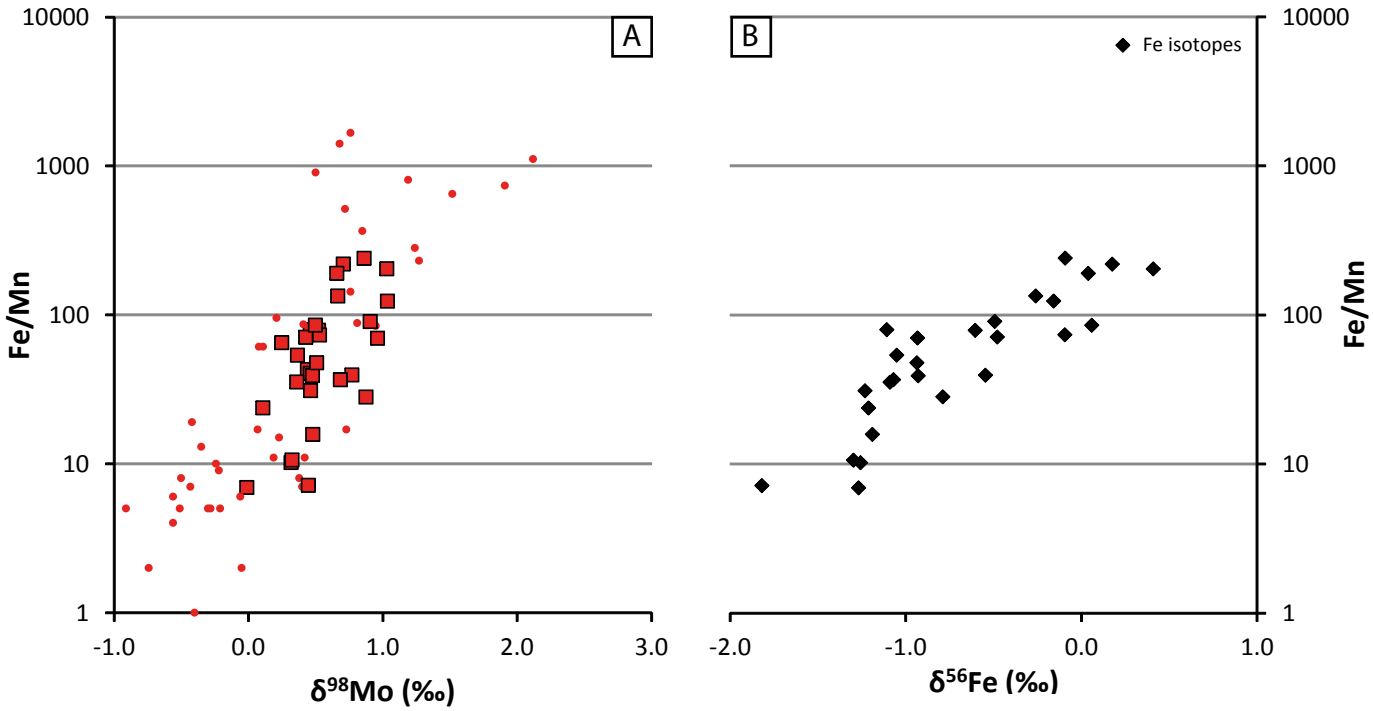

FIGURE 2: (A) The positive correlation of δ^{98}Mo values and Fe/Mn ratios in 3.0 Ga old banded iron formations from the Sinqeni Formation, Pongola Supergroup, South Africa (red dots; Planavsky et al., 2014) is also observed in banded iron formations from the 2.4 Ga old Koegas Subgroup, Transvaal Supergroup, South Africa (although the spread is somewhat smaller). This trend was attributed to the preferential adsorption of isotopically light Mo onto Mn oxides in a well oxygenated near shore environments (Planavsky et al., 2014) B) Similarly, δ^{56}Fe values show a positive correlation with Fe/Mn ratios. The oxidation of Fe^{2+} by Mn oxides and the precipitation of Fe oxyhydroxides with high δ^{56}Fe causes low $\delta^{56}Fe_{Fe2+}$ values in the uppermost water column (Busigny et al., 2014). As a consequence, relatively lower δ^{56}Fe values in sediments below the most oxidized near surface environment are expected. Both trends thus reflect a redox stratified water column with anoxic deep waters and a well oxygenated surface layer.

of higher concentrated $Fe_{(aq)}^{2+}$ with low δ^{56}Fe values might more significantly contribute to the low bulk sedimentary δ^{56}Fe values.

The preservation of distinct and primary trends in our dataset might benefit from the missing of Fe sulfides in the IFs of the Koegas Subgroup (Nel, 2013), which strongly suggest that dissolved H_2S was poorly available during the deposition of the Koegas Formation. This precludes iron isotope fractionations during pyrite formation. Johnson et al. (2013a) argue that siderite is unsuitable for the reconstruction of the redox structure of the water column, because of large Fe isotope fractionations during the (bacterial) dissimilatory iron reduction within the sediment. The differentiation between Fe isotope fractionations within the water column and within the sediment, respectively, are therefore extremely difficult (Johnson et al., 2013a). However, the appearance of Fe oxides in our samples is subordinated compared to Fe carbonates and Fe silicates (Nel, 2013). This might indicate near quantitative reduction of primary Fe (oxy)hydroxides within the sediment, which would assure negligible net Fe isotope fractionations during dissimilatory iron reduction (DIR), and the preservation of primary seawater Fe isotope signals.

6. Molybdenum isotopes

In contrast to Fe, Mo is poorly reactive in oxic as well as in anoxic-ferruginous waters. In the modern predominantly oxic ocean dissolved molybdate (MoO_4^{2-}) is therefore homogeneously distributed in concentration as well as in its isotopic composition with a residence time of around 440 ka (Miller et al., 2011). Only if free sulfide is available, molybdate transforms to particle reactive (oxy)thiomolybdates species ($MoO_xS_{4-x}^{2-}$), which are probably scavenged by sulfurized organic matter (Helz et al., 1996; Tribovillard et al., 2004). As mentioned above, the missing of Fe sulfides strongly suggest that dissolved H_2S was poorly available during the deposition of the Koegas Formation. This argues against (oxy)thiomolybdate formation in our sediments. Large fractionations associated with this transformation (Tossell, 2005), as well as the efficient scavenging of (oxy)thiomolybdate by sulfurized organic matter (Tribovillard et al., 2004) can therefore be excluded.

The adsorption of molybdate onto Mn-oxides represents the probably most important Mo-sink in oxic marine settings (Bertine and Turekian, 1973; Scott and Lyons, 2012). This adsorption is associated with large equilibrium Mo isotopic fractionation, thereby preferentially adsorbing light Mo isotopes ($\Delta^{98}Mo_{sw\text{-}MnO2}$ = $\delta^{98}Mo_{sw}$ - $\delta^{98}Mo_{MnO2}$ = 3 ‰) (Barling and Anbar, 2004). The formation of Mn oxides requires free oxygen and the catalyzing effect of Mn oxidizing bacteria (Diem and Stumm, 1984; Morgan, 2005; Tebo et al., 2005), which are expected in most proximal, well oxygenated surface ocean areas during the Proterozoic.

The $\delta^{98}Mo$ values of our sample set follow similar trends as $\delta^{56}Fe$ values, although the magnitude of variation is somewhat smaller (Fig. 1C). We observe relatively low $\delta^{98}Mo$ values down to -0.01 ‰ during interval 1. The shaly succession of interval 2 shows $\delta^{98}Mo$ values around 0.4 ‰, which is in the expected range of the detrital Mo isotopic composition (Voegelin et al., 2014). The uppermost interval 3 shows highest $\delta^{98}Mo$ values up to 1.11 ‰. Like $\delta^{56}Fe$ values, also $\delta^{98}Mo$ values positively correlate with Fe/Mn ratios (Fig. 2B), a correlation, which was also observed in other 1.8 to 3.0 Ga old iron formations (Planavsky et al., 2014). Planavsky et al. (2014) suggested that low $\delta^{98}Mo$ values reflect the local formation of Mn oxides and the subsequent preferential adsorption of isotopically light Mo. Accordingly, Mn enriched samples with low Fe/Mn ratios should show lowest $\delta^{98}Mo$ values. Higher $\delta^{98}Mo$ values in Mn-poor samples require an additional Mo source with relatively heavier Mo isotopic composition. In search for this additional Mo source, the more detailed consideration of the Mo burial pathway is necessary. As mentioned above, Mn oxides were quantitatively reduced within the sediment (Johnson et al., 2013b), which also causes the re-liberation of adsorbed Mo (Scott and Lyons, 2012). We suggest that the pore water molybdate reservoir is recharged by this dissolution of Mn oxides (low $\delta^{98}Mo$) as well as the diffusional transport of seawater molybdate (high $\delta^{98}Mo$) into the sediment. The higher the flux of Mn oxides to the sediments, the more relevant is the isotopically light component of adsorbed Mo for the pore water molybdate reservoir.

The exact burial pathway of pore water molybdate into the sediment remains difficult to reconstruct. We observe no correlation of Mo and Mn concentrations (Fig. 4), which might indicate the decoupling of burial pathways. Mn is exclusively incorporated into carbonates (Johnson et al., 2013b), whereas Mo might also adsorb onto organic compounds. The Mo isotope data seems more robust against this decoupling,

possibly because of low Mo isotope fractionations during Mo adsorption onto organic matter (Kowalski et al., 2013).

The local formation of Mn oxides within the water column of the Griqualand West Basin is consistent with our Fe isotope results as well as mineralogical observations (Johnson et al., 2013b). The positive correlation of δ^{98}Mo values and Fe/Mn ratios in our sample set therefore confirms the interpretation of Planavsky et al. (2014). But the question arises, if the adsorption of isotopically light Mo has, like Fe, effects of the Mo isotopic composition of the remaining seawater Mo reservoir. Assuming a similar depletion of dissolved molybdate along the Mn chemocline due to efficient Mo drawdown by adsorption onto Mn oxides, we would expect strong enrichment of heavy Mo isotopes in this remaining reservoir. If so, high δ^{98}Mo values should correlate with low Fe/Mn ratios and low δ^{56}Fe values, which is not the case. This indicates that the removal of Mo by adsorption onto Mn oxides has negligible effects on the concentration and the isotopic composition of the local seawater molybdate reservoir (Fig. 3). It rather suggests an at least regionally homogeneous seawater Mo isotopic composition and a significant Mo seawater reservoir in the oxic surface layer and beyond the deeper ferruginous ocean (Fig. 3). It remains however unclear, if the seawater Mo reservoir was already homogeneous on a global scale.

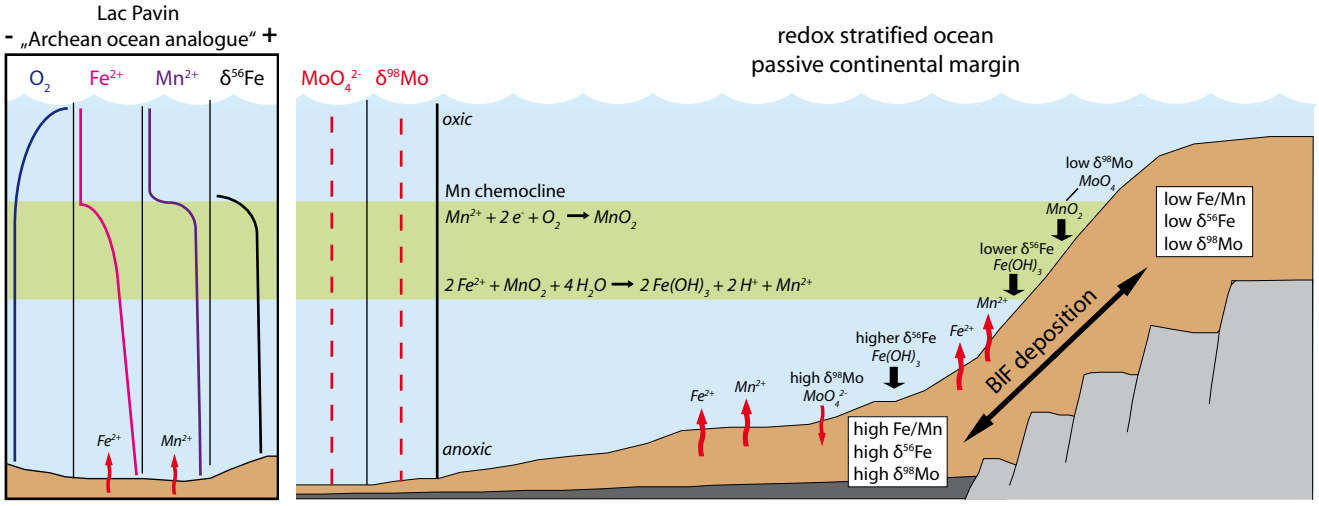

FIGURE 3: The modelled environment during BIF depoisition of the Koegas subgroup in comparism to Lac Pavin, an „Archean ocean analogue“ (Busigny et al., 2014). A chemocline devides anoxic deep waters from a well oxygenated surface layer. The oxidation of Fe^{2+} and Mn^{2+} and the precipitation of Fe and Mn oxides, respectively (black straight arrows), cause strong concentration gradients near the oxic surface layer. The gradient is particularly sharp and slightly shallower for Mn^{2+}, which might indicate that Fe^{2+} is oxidized in deeper regions by sinking Mn oxides formed above (Busigny et al., 2014). As a consequence of this oxidation reaction, the δ^{56}Fe values of remaining Fe^{2+} strongly decrease at the Mn chemocline. Applied to the Koegas environment, the deposition of Fe oxides formed in shallower settings should show relatively lower δ^{56}Fe values. In respective settings the flux of Mn oxides is higher, which causes higher Mn^{2+} concentrations in the porewater (and carbonates). Bulk sediments, thus, show relatively low Fe/Mn ratios. The preferential adsorption of isotopically light Mo onto these Mn oxides will cause lower δ^{98}Mo values in sediments from most proximal settings (Planavsky et al., 2014), where the Mn oxide flux is highest. In more distal setting the diffusional transport of seawater Mo with higher δ^{98}Mo may be the predominant Mo source.

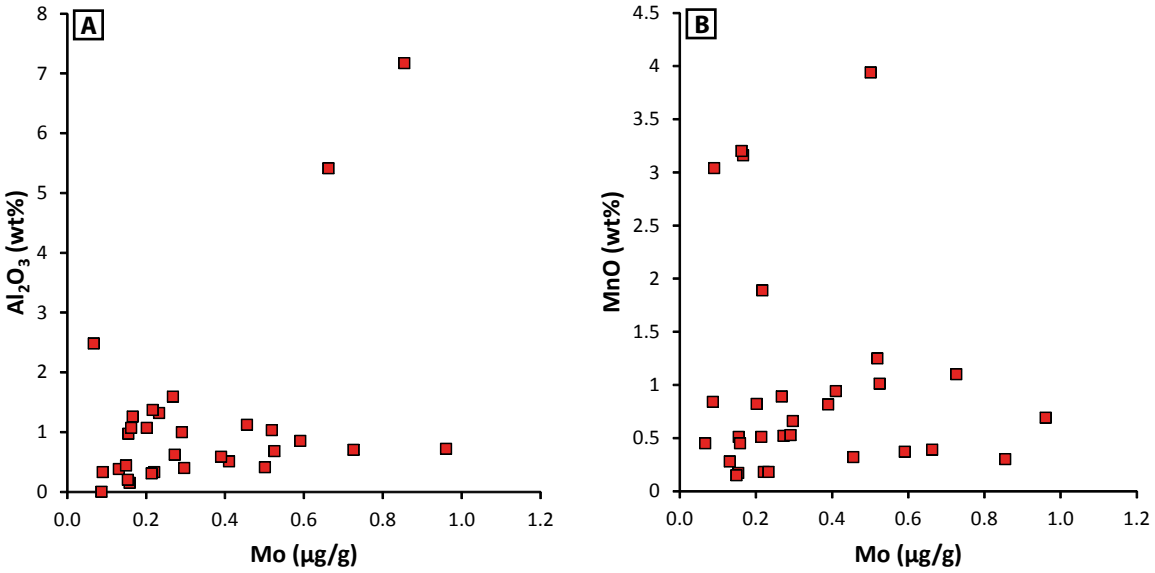

FIGURE 4: (A) Compilation of Mo and Al concentration data, which shows no correlation. This indicates that Mo enrichment is not associated with the supply of detrital material. (B) Similarly, there is no correlation between Mo and Mn concentrations. Despite the linked flux of Mn oxides and adsorbed molybdate to the sediments, the final burial of Mo and Mn after dissolution of Mn oxides within the sediment might be decoupled.

7. Summary and Implications for the pre-GOE environment

Our data strongly indicates a stratified water column in the Griqualand West Basin shortly before the GOE around 2.48 Ga ago. We find no evidence for a euxinic water body at intermediate depth. Our data rather suggest the continuous development of a chemocline between oxic surface waters and ferruginous deep waters. IFs of the Koegas Subgroup were deposited close to this chemocline in relatively shallow water environments. The development of the chemocline with depth was rather smooth, probably because of significantly lower oxygen concentrations in the oxic surface layer compared to modern lake equivalents. The precise quantification of oxygen concentrations in the surface water layer by our data seems, however, impossible.

The local burial pathways of Fe and Mo within such an oxygen oasis are different but both related to the formation of Mn oxides along the redox boundary. The removal of isotopically light Mo during adsorption onto Mn oxides has negligible effects on the seawater δ^{98}Mo value, because of reservoir effects discussed above. In contrast the more efficient removal of Fe during oxidation along the Mn redox-cline cause a local shift in the δ^{56}Fe value of the local water column like in modern redox stratified lakes. Therefore, Mo isotopes have the general potential to trace regional or even global redox changes, whereas Fe isotopes are more dependent on local fractionation processes. However, the possibility of large Mo isotope fractionations during adsorption onto Mn oxides in the discussed Griqualand West Basin make IF sediments an inadequate sedimentary deposit to reconstruct the seawater Mo isotopic composition and

its variation with time (in contrast to black shales). For the use of Fe isotopes, in contrast, the negligible dilution with detrital material and the near missing of Fe bound in oxides and sulfides may allow the preservation of local seawater Fe isotope fluctuations in the here studied IF sediments.

If δ^{56}Fe values, δ^{98}Mo values and Fe/Mn ratios depend on the closeness to the oxic-anoxic redox boundary, their temporal variation is a consequence of sea level fluctuations. Relatively high δ^{56}Fe values, high δ^{98}Mo values and high Fe/Mn ratios reflect a high stand of sea level. Consistent with this hypothesis, a transgressive event at the base of the Nelani Formation (Beukes, 1983) coincides with an increase in δ^{98}Mo values, δ^{56}Fe values and Fe/Mn ratios. The subsequent regression during the Nelani Formation is accompanied by decreasing δ^{56}Fe values and Fe/Mn ratios. The δ^{56}Fe values during transgressive periods might constrain the Fe isotopic composition of the ancient ferruginous deep ocean. Considering highest δ^{56}Fe values along the flooding surface of the Nelani Formation, the deep water Fe isotopic composition might have been close to the average continental crust δ^{56}Fe value around 0 ‰.

8. References

Barling, J., Anbar, A., 2004. Molybdenum isotope fractionation during adsorption by manganese oxides. Earth and Planetary Science Letters 217, 315-329.

Beard, B.L., Johnson, C.M., 2004. Fe isotope variations in the modern and ancient earth and other planetary bodies. Reviews in Mineralogy and Geochemistry 55, 319-357.

Beard, B.L., Johnson, C.M., Skulan, J.L., Nealson, K.H., Cox, L., Sun, H., 2003. Application of Fe isotopes to tracing the geochemical and biological cycling of Fe. Chemical Geology 195, 87-117.

Bertine, K.K., Turekian, K.K., 1973. Molybdenum in marine deposits. Geochimica et Cosmochimica Acta 37, 1415-1434.

Beukes, N., 1983. Palaeoenvironmental setting of iron-formations in the depositional basin of the Transvaal Supergroup, South Africa. Developments in Precambrian Geology 6, 131-198.

Beukes, N.J., Gutzmer, J., 2008. Origin and paleoenvironmental significance of major iron formations at the Archean-Paleoproterozoic boundary. Reviews in Economic Geology 15, 5-47.

Busigny, V., Planavsky, N.J., Jézéquel, D., Crowe, S., Louvat, P., Moureau, J., Viollier, E., Lyons, T.W., 2014. Iron isotopes in an Archean ocean analogue. Geochimica et Cosmochimica Acta 133, 443-462.

Canfield, D.E., 2005. The early history of atmospheric oxygen: homage to Robert M. Garrels. Annu. Rev. Earth Planet. Sci. 33, 1-36.

Catling, D.C., Zahnle, K.J., McKay, C.P., 2001. Biogenic methane, hydrogen escape, and the irreversible oxidation of early Earth. Science 293, 839-843.

Cloud, P., 1973. Paleoecological significance of the banded iron-formation. Economic Geology 68, 1135-

1143.

Crowe, S.A., Døssing, L.N., Beukes, N.J., Bau, M., Kruger, S.J., Frei, R., Canfield, D.E., 2013. Atmospheric oxygenation three billion years ago. Nature 501, 535-538.

Dauphas, N., Rouxel, O., 2006. Mass spectrometry and natural variations of iron isotopes. Mass Spectrometry Reviews 25, 515-550.

de Laeter, J.R., Böhlke, J.K., De Bièvre, P., Hidaka, H., Peiser, H., Rosman, K., Taylor, P., 2003. Atomic weights of the elements. Review 2000 (IUPAC Technical Report). Pure and Applied Chemistry 75, 683-800.

Diem, D., Stumm, W., 1984. Is dissolved Mn 2+ being oxidized by O 2 in absence of Mn-bacteria or surface catalysts? Geochimica et Cosmochimica Acta 48, 1571-1573.

Farquhar, J., Bao, H., Thiemens, M., 2000. Atmospheric influence of Earth‘s earliest sulfur cycle. Science 289, 756-758.

Gaillard, F., Scaillet, B., Arndt, N.T., 2011. Atmospheric oxygenation caused by a change in volcanic degassing pressure. Nature 478, 229-232.

Goldberg, T., Gordon, G., Izon, G., Archer, C., Pearce, C.R., McManus, J., Anbar, A.D., Rehkämper, M., 2013. Resolution of inter-laboratory discrepancies in Mo isotope data: an intercalibration. J. Anal. At. Spectrom. 28, 724-735.

Helz, G., Miller, C., Charnock, J., Mosselmans, J., Pattrick, R., Garner, C., Vaughan, D., 1996. Mechanism of molybdenum removal from the sea and its concentration in black shales: EXAFS evidence. Geochimica et Cosmochimica Acta 60, 3631-3642.

Holland, H.D., 2006. The oxygenation of the atmosphere and oceans. Philosophical Transactions of the Royal Society B: Biological Sciences 361, 903-915.

Hongve, D., 1997. Cycling of iron, manganese, and phosphate in a meromictic lake. Limnology and Oceanography 42, 635-647.

Johnson, C.M., Beard, B.L., Roden, E.E., 2008. The iron isotope fingerprints of redox and biogeochemical cycling in modern and ancient Earth. Annu. Rev. Earth Planet. Sci. 36, 457-493.

Johnson, C.M., Ludois, J.M., Beard, B.L., Beukes, N.J., Heimann, A., 2013a. Iron formation carbonates: Paleoceanographic proxy or recorder of microbial diagenesis? Geology 41, 1147-1150.

Johnson, J.E., Webb, S.M., Thomas, K., Ono, S., Kirschvink, J.L., Fischer, W.W., 2013b. Manganese-oxidizing photosynthesis before the rise of cyanobacteria. Proceedings of the National Academy of Sciences 110, 11238-11243.

Kappler, A., Pasquero, C., Konhauser, K.O., Newman, D.K., 2005. Deposition of banded iron formations by anoxygenic phototrophic Fe (II)-oxidizing bacteria. Geology 33, 865-868.

Kendall, B., Reinhard, C.T., Lyons, T.W., Kaufman, A.J., Poulton, S.W., Anbar, A.D., 2010. Pervasive oxygenation along late Archaean ocean margins. Nature Geoscience 3, 647-652.

Kendall, B., van Acken, D., Creaser, R.A., 2013. Depositional age of the early Paleoproterozoic Klipputs

Member, Nelani Formation (Ghaap Group, Transvaal Supergroup, South Africa) and implications for low-level Re–Os geochronology and Paleoproterozoic global correlations. Precambrian Research 237, 1-12.

Kowalski, N., Dellwig, O., Beck, M., Gräwe, U., Neubert, N., Nägler, T.F., Badewien, T.H., Brumsack, H.-J., van Beusekom, J.E., Böttcher, M.E., 2013. Pelagic molybdenum concentration anomalies and the impact of sediment resuspension on the molybdenum budget in two tidal systems of the North Sea. Geochimica et Cosmochimica Acta.

Kump, L.R., Barley, M.E., 2007. Increased subaerial volcanism and the rise of atmospheric oxygen 2.5 billion years ago. Nature 448, 1033-1036.

Kurzweil, F., Claire, M., Thomazo, C., Peters, M., Hannington, M., Strauss, H., 2013. Atmospheric sulfur rearrangement 2.7 billion years ago: Evidence for oxygenic photosynthesis. Earth and Planetary Science Letters 366, 17-26.

Lehmann, B., Nägler, T.F., Holland, H.D., Wille, M., Mao, J., Pan, J., Ma, D., Dulski, P., 2007. Highly metalliferous carbonaceous shale and Early Cambrian seawater. Geology 35, 403-406.

Lyons, T.W., Reinhard, C.T., Planavsky, N.J., 2014. The rise of oxygen in Earth/'s early ocean and atmosphere. Nature 506, 307-315.

Miller, C.A., Peucker-Ehrenbrink, B., Walker, B.D., Marcantonio, F., 2011. Re-assessing the surface cycling of molybdenum and rhenium. Geochimica et Cosmochimica Acta 75, 7146-7179.

Moeller, K., Schoenberg, R., Grenne, T., Thorseth, I.H., Drost, K., Pedersen, R.B., 2014. Comparison of iron isotope variations in modern and Ordovician siliceous Fe oxyhydroxide deposits. Geochimica et Cosmochimica Acta 126, 422-440.

Morgan, J.J., 2005. Kinetics of reaction between O 2 and Mn (II) species in aqueous solutions. Geochimica et Cosmochimica Acta 69, 35-48.

Nel, B.P., 2013. Petrography and geochemistry of iron formations of the Paleoproterozoic Koegas Subgroup, Transvaal Supergroup, Griqualand West, South Africa.

Nisbet, E., Grassineau, N., Howe, C.J., Abell, P., Regelous, M., Nisbet, R., 2007. The age of Rubisco: the evolution of oxygenic photosynthesis. Geobiology 5, 311-335.

Pavlov, A., Kasting, J., 2002. Mass-independent fractionation of sulfur isotopes in Archean sediments: strong evidence for an anoxic Archean atmosphere. Astrobiology 2, 27-41.

Pickard, A., 2003. SHRIMP U–Pb zircon ages for the Palaeoproterozoic Kuruman Iron Formation, Northern Cape Province, South Africa: evidence for simultaneous BIF deposition on Kaapvaal and Pilbara Cratons. Precambrian Research 125, 275-315.

Planavsky, N.J., Asael, D., Hofmann, A., Reinhard, C.T., Lalonde, S.V., Knudsen, A., Wang, X., Ossa, F.O., Pecoits, E., Smith, A.J., 2014. Evidence for oxygenic photosynthesis half a billion years before the Great Oxidation Event. Nature geoscience.

Poitrasson, F., 2006. On the iron isotope homogeneity level of the continental crust. Chemical Geology 235, 195-200.

Reinhard, C.T., Raiswell, R., Scott, C., Anbar, A.D., Lyons, T.W., 2009. A late Archean sulfidic sea stimulated by early oxidative weathering of the continents. Science 326, 713-716.

Rouxel, O.J., Bekker, A., Edwards, K.J., 2005. Iron Isotope Constraints on the Archean and Paleoproterozoic Ocean Redox State. Science 307, 1088-1091.

Schoenberg, R., von Blanckenburg, F., 2005. An assessment of the accuracy of stable Fe isotope ratio measurements on samples with organic and inorganic matrices by high-resolution multicollector ICP-MS. International Journal of Mass Spectrometry 242, 257-272.

Schröder, S., Bedorf, D., Beukes, N., Gutzmer, J., 2011. From BIF to red beds: Sedimentology and sequence stratigraphy of the Paleoproterozoic Koegas Subgroup (South Africa). Sedimentary Geology 236, 25-44.

Scott, C., Lyons, T.W., 2012. Contrasting molybdenum cycling and isotopic properties in euxinic versus non-euxinic sediments and sedimentary rocks: Refining the paleoproxies. Chemical Geology 324, 19-27.

Siebert, C., Nägler, T.F., Kramers, J.D., 2001. Determination of molybdenum isotope fractionation by double-spike multicollector inductively coupled plasma mass spectrometry. Geochemistry, Geophysics, Geosystems 2.

Tebo, B.M., Johnson, H.A., McCarthy, J.K., Templeton, A.S., 2005. Geomicrobiology of manganese (II) oxidation. TRENDS in Microbiology 13, 421-428.

Tossell, J., 2005. Calculating the partitioning of the isotopes of Mo between oxidic and sulfidic species in aqueous solution. Geochimica et Cosmochimica Acta 69, 2981-2993.

Tribovillard, N., Riboulleau, A., Lyons, T., Baudin, F., 2004. Enhanced trapping of molybdenum by sulfurized marine organic matter of marine origin in Mesozoic limestones and shales. Chemical Geology 213, 385-401.

Tsikos, H., Matthews, A., Erel, Y., Moore, J.M., 2010. Iron isotopes constrain biogeochemical redox cycling of iron and manganese in a Palaeoproterozoic stratified basin. Earth and Planetary Science Letters 298, 125-134.

Voegelin, A.R., Pettke, T., Greber, N.D., von Niederhäusern, B., Nägler, T.F., 2014. Magma differentiation fractionates Mo isotope ratios: Evidence from the Kos Plateau Tuff (Aegean Arc). Lithos 190, 440-448.

Welch, S., Beard, B., Johnson, C., Braterman, P., 2003. Kinetic and equilibrium Fe isotope fractionation between aqueous Fe (II) and Fe (III). Geochimica et Cosmochimica Acta 67, 4231-4250.

Weyer, S., Schwieters, J., 2003. High precision Fe isotope measurements with high mass resolution MC-ICPMS. International Journal of Mass Spectrometry 226, 355-368.

CHAPTER III

Coupled sulfur, iron and molybdenum isotope data from black shales of the Teplá-Barrandian unit argue against deep ocean oxygenation during the Ediacaran

1. Abstract

The Earth's atmosphere and hydrosphere changed from an Archean anoxic to a modern oxygenated world in two major steps, the Paleoproterozoic Great Oxidation Event (2.4-2.3 billion years ago) and the Neoproterozoic Oxidation Event (0.8 to 0.5 billion years ago). Both events had a strong influence on the availability of redox sensitive and bio-essential metals within the ocean and are, thus, strongly linked to fundamental biological innovations and diversification. Biological diversification during the Precambrian-Cambrian transition between 555 and 540 million years ago may have been driven by ocean-atmosphere oxygenation. The exact timing and the extent of (deep) ocean oxygenation within this time period remains unresolved though.

Here we present major and trace element compositions as well as Mo, S and Fe isotopic data of organic-rich black shales from the Teplá-Barrandian unit, Czech Republic. New in situ zircon U-Pb ages provide

a maximum depositional age of 559.8 ± 3.8 million years. Black shales with strong metal enrichment show low δ^{56}Fe values due to the dominance of authigenic pyrite-Fe with δ^{56}Fe values around -0.6 ‰ over detrital Fe with δ^{56}Fe values around 0.1 ‰. Samples with lower authigenic metal enrichment show relatively low Mo/TOC ratios and increasing δ^{34}S values, which is interpreted to reflect basinal restriction and longer seawater renewal times. In analogy to the modern Black Sea, the accompanied depletion of basinal Mo_{aq} due to near quantitative Mo removal might have led to the preservation of the seawater δ^{98}Mo in the respective black shales. Our best estimate for this seawater Mo isotopic composition <560 million years ago is +1.2 ‰ in δ^{98}Mo, which is nearly identical to seawater δ^{98}Mo values inferred from Mid-Proterozoic black shales. The lack of higher δ^{98}Mo values in black shales (and seawater) argues against contemporaneous Mn oxide formation in well oxygenated deep sea settings, which would preferentially adsorb isotopically light Mo leaving behind an isotopically heavy ocean. By contrast, the deep ocean might have remained ferruginous with the hydrothermal Fe still outbalancing surficial oxygen production. Our results therefore contribute to a growing data set, which suggests limited deep water oxygenation during major biological innovations in the late Ediacaran period.

2. Introduction

After the so-called boring billion between 1.8 and 0.8 billion years ago (Ga), an exciting period with major biologic innovations, tectonic and climatic modifications as well as environmental changes followed during late Neoproterozoic times between 0.8 and 0.54 Ga (Och and Shields-Zhou, 2012). The break-up of the supercontinent Rodinia between 825 Ma and 720 Ma (Hoffman, 1991; Li et al., 2008) was accompanied by continental drift from high towards equatorial latitudes (Hoffman et al., 1998). Glacial deposits on these low latitude continents suggest two global glaciation events, the Sturtian glaciation from 740 to 647 Ma and the Marinoan glaciation from 660 to 635 Ma (Hoffman et al., 1998; Kennedy et al., 1998). Contemporaneously, first Metazoan fossils indicate the evolution of multi-cellular life during this Cryogenian period (850 to 635 Ma) (Love et al., 2009; Yin et al., 2007). At the end of the subsequent Ediacaran period (635 to 541 Ma) the development of mobility and bioturbation around 555 Ma (Martin et al., 2000), of biological calcification around 550 Ma (Grotzinger et al., 2000) and predation around 549 Ma (Bengtson and Zhao, 1992) led to rapid biological diversification within the Ediacaran period. These major biologic inventions might have benefited from the amalgamation of the supercontinent Gondwana between 650 and 515 Ma, which led to high rates of tectonic uplift and an elevated erosion-related nutrient discharge (Kennedy et al., 2006). Higher sedimentation rates along with enhanced primary production increased the burial of organic matter and, therefore, represented a net source of free oxygen for the ocean-atmosphere system (Campbell and Squire, 2010; Kaufman et al., 1997). Several geochemical proxies such as C and S isotopes (Fike et al., 2006), Fe speciation data (Canfield et al., 2007), Mo isotopes (Kendall et al., 2015) and enrichments of redox sensitive trace metals such as V, Cr and Mo (Frei et al., 2009; Sahoo et al., 2012; Scott et al., 2008) confirm an increase in oxygen levels at the end of the Neoproterozoic era during the so-called Neoproterozoic Oxygenation Event (Och and Shields-Zhou, 2012).

A causal link between tectonic, biologic and environmental changes seems to manifest in the Neoproterozoic era, but the primery trigger remains elusive. Mills and Canfield (2014) highlight the need to distinguish between the first eukaryote evolution in the Cryogenian period (850 to 635 Ma) and its subsequent diversification during Ediacaran (Ediacaran Fauna from 585 to 541 Ma) and Cambrian times. Eukaryote evolution clearly preceded environmental oxygenation, whereas the later diversification seems more closely related to it. Some authors consider higher $p(O_2)$ a necessary precondition, because the evolution of large animals requires more significant amounts of oxygen (Berner et al., 2003; Falkowski et al., 2005; Knoll and Carroll, 1999). By contrast, Butterfield (2009) argues that biologic innovations proceeded independently from external features like the increase in atmospheric oxygen concentration. These authors favor the development of a well-mixed clear water system generated by suspension feeding eukaryotes, which enabled the evolution of larger animals in light-flooded surface ocean areas. Larger and faster sinking fecal pellets then enhanced the burial of organic matter and enabled oxygen enrichment in the ocean-atmosphere system. Both theories give, however, little explanation for diversification. Other ecological innovations such as predation might have increased selection pressure promoting further morphological innovations (Bengtson, 2002). However, arguments always steer towards the rise of atmospheric oxygen when considering that carnivores prefer high oxygen environments (Sperling et al., 2013). This again highlights the close relationship of oxygen concentrations in the oceans and animal diversification and the consequential challenge to resolve the triggering mechanisms (intrinsic vs. extrinsic) for the Ediacaran Fauna and the Cambrian “explosion of life”.

Mills and Canfield (2014) pointed out that a more detailed understanding of temporal and spatial changes of oxygen concentrations in the ocean-atmosphere system is one key question that needs to be better resolved. Mo isotopes represent a well-established proxy to reconstruct the oceanic redox-state (Arnold et al., 2004; Asael et al., 2013; Kendall et al., 2011; Kendall et al., 2015; Kendall et al., 2010; Neubert et al., 2008). The Mo input is considered to be temporally invariable with $\delta^{98}Mo$ values close to average continental crust (~0.4 ‰) (Greber et al., 2014; Voegelin et al., 2014) and the modern weathering input (~0.7 ‰ (Archer and Vance, 2008)). The predominant Mo species dissolved in well oxygenated seawater, the tetrahedrally coordinated molybdate (MoO_4^{2-}), is relatively unreactive and globally homogeneous with a mean ocean residence time of 440 to 750 ka (Miller et al., 2011; Morford and Emerson, 1999). Today, the main Mo sink in oxic marine settings is molybdate adsorption onto Mn oxides in the deep ocean. Thereby, the formation of octahedrally coordinated inner-sphere complexes causes the preferential adsorption of isotopically light Mo and a large isotopic difference of $\Delta^{98}Mo_{Mn\text{-}oxides\text{-}seawater} = \delta^{98}Mo_{Mn\text{-}oxides} - \delta^{98}Mo_{seawater} = -3$ ‰ (‚closed system‘ equilibrium exchange process; Barling and Anbar, 2004; Kashiwabara et al., 2011). In sulfidic environments the oxygen in molybdate molecules substitutes with sulfur and forms oxythiomolybdates ($MoO_xS_{4-x}^{2-}$; x = 0-4). This species change is also accompanied with isotopic fractionation, enriching the more sulfurized species in the light Mo isotopes (Tossell, 2005). The sulfurization is mainly dependent on the concentration of free H_2S_{aq}. At H_2S_{aq} above 11 µmol L^{-1}, thiomolybdate (MoS_4^{2-}) becomes the predominant species, which is very particle reactive and readily removed from solution either by adsorption onto sulfurized organic matter (Helz et al., 1996; Tribovillard et al., 2004) or by authigenic precipitation of Mo-Fe-S minerals (Helz et al., 2011). The nearly quantitative removal ensures the preservation of the seawater Mo isotopic signature in restricted sulfidic settings, i.e. black shales (Arnold et al., 2004; Neubert et al.,

2008). However, at lower H_2S_{aq} concentrations in weakly euxinic settings the formation and removal of thiomolybdate is incomplete and causes enrichment of light Mo isotopes in the respective sediments (Nägler et al., 2011; Poulson Brucker et al., 2009; Poulson et al., 2006; Siebert et al., 2006). Today, Mn crusts and weakly euxinic sediments represent the predominant sinks of isotopically light Mo, leaving behind a modern seawater molybdate reservoir that is strongly enriched in the heavy isotopes with a globally homogeneous δ^{98}Mo of 2.3 ‰ relative to NIST3134 (set to 0.25 ‰) (Archer and Vance, 2008; Barling et al., 2001; Siebert et al., 2003). In theory and despite Mo-isotope fractionation during incomplete thiomolybdate formation in weakly euxinic settings, the absence of Mn crusts in pelagic deep-sea settings and the concomitant lack of large Mo-isotope fractionations during Mo adsorption onto these Mn oxides would cause considerably lower seawater δ^{98}Mo values in Precambrian times. The oxygenation of the deep ocean during the Neoproterozoic Oxygenation Event should then be accompanied by a shift towards higher seawater δ^{98}Mo values, which would be preserved in contemporaneous sediments from restricted sulfidic settings (black shales).

Here, we provide new geochemical data (S-, Fe- and Mo-isotopes, main element concentrations) of metal-rich black shales from the Teplá-Barrandian unit (Czech Republic), which were deposited in an arc setting, likely influenced by hydrothermal activity. The combination of element ratios such as Mo/TOC and Fe/Al and the isotopic compositions of sulfur, iron and molybdenum allow the detailed reconstruction of the local depositional setting and the distinction of the different sources of S, Fe and Mo (hydrothermal vs. seawater vs. detrital) as well as their respective isotopic composition. This in turn provides a unique view on the marine environmental conditions that prevailed during late Neoproterozoic times. New U-Pb zircon age constraints allow the placement of our geochemical dataset in the stratigraphic context.

3. Geological background

The Teplá-Barrandian unit in the Center of the Bohemian Massif consists of a Neoproterozoic to earliest Cambrian basement that formed during Cadomian subduction and accretion processes at the NW-African periphery of Gondwana (e.g., Zulauf et al., 1999, and references therein). The overlying Cambrian to Mid-Devonian volcano-sedimentary successions indicate rifting, a passive margin stage, and incipient Variscan docking processes that preceded Variscan continental collision between Laurussia and Gondwana (e.g., Drost 2008 and references therein). Despite the Variscan overprint, the Cadomian basement of the Teplá-Barrandian unit is well preserved and consists of the Blovice accretionary complex in the NW, which formed during S-directed subduction beneath a magmatic arc or active continental margin in the SE (Fig. 1). According to the present understanding the sedimentary and volcanic rocks preserved in the Blovice complex were deposited in an intra-oceanic back-arc basin the closure of which led to the formation of the accretionary wedge and to arc magmatism in the SE (Drost et al., 2011; Hajná et al., 2014; Pin and Waldhausrová, 2007).

The accretionary wedge is composed of several fault-bounded coherent belts alternating with belts of mélanges (Hajná et al., 2014). The coherent belts consist of rhythmical alternations of graywackes, mudstones and shales, while the mélange belts display a block-in-matrix architecture and contain chiefly mafic volcanics derived from a depleted or enriched mantle source, respectively, as well as black shales, cherts and rare carbonates in graywacke and shale matrix.

The timing of the onset of the subduction processes is not well constrained. An imprecise whole-rock Sm-Nd isochron age for back-arc mid ocean ridge basalts within the Blovice accretionary complex indicates growth of the intra-oceanic back-arc basin at 605 ± 39 Ma (95 % conf.; Pin and Waldhausrová, 2007). Consumption of the intra-oceanic back arc basin by subduction may have started at ~620 Ma (age of trondjemite pebbles; Sláma et al. 2008a). Subduction beneath the magmatic arc/active continental margin in the SE appears to last until around the Precambrian-Cambrian boundary. This is indicated by ~540 Ma amphibolites with MORB signature in the Mariánské Lázně complex, which are thought to represent remnants of the subducting plate and must have formed before the termination of subduction (Timmermann et al., 2006; Timmermann et al., 2004). An age close to the Precambrian-Cambrian transition (541 Ma) for the termination of subduction is also in agreement with a recent study of Hajná et al. (2013), which provides evidence that mélange forming processes lasted until early Cambrian times.

4. Sample material

All samples are from two drill cores (HRM-3 and KA-5) in the northeast of Pilsen, Czech Republic (Fig. 1). Borehole HRM-3 (~300 m deep) was drilled NW of the village Hromnice and comprises black shale layers with a thickness of several tens of meters intercalated by layers of mafic volcanogenic products (Fig. 2a). Borehole KA-5 (~100 m deep) was drilled E of the village Kamenec and encountered a sequence of submarine metabasalts alternating with fine layers and lenses of black shales (Fig. 2b). Both drill cores are located in the Cadomian basement of the Teplá-Barrandian unit, namely in mélange belt 2 (sensu Hajná et al., 2014) of the Blovice accretionary complex. The rocks in this belt show a chaotic structure of several different lithologies such as terrigenous mass flows (graywackes), pillow (meta)basalts, deep water sediments (black shales) and rare carbonates pointing to a variety of depositional environments within the intra-oceanic back-arc basin. The black shale setting was described as a semi-isolated basin part with restricted seawater circulation and strong influence of submarine volcanic activity (Pašava et al., 1996). Large fluxes of metal-rich hydrothermal fluids created an area of high primary productivity and caused the enrichment of metals and organic matter in black shales (Pašava et al., 1993; Pašava et al., 1996). As large parts of the Blovice complex (including the sampling area) were only little affected by Variscan metamorphism (lower greenschist facies: chlorite facies in HRM-3 and prehnite-pumpellite facies in KA-5, respectively) syn- to early diagenetic mineral structures in the black shales from HRM-3 and KA-5 are still preserved (Pašava et al., 1996).

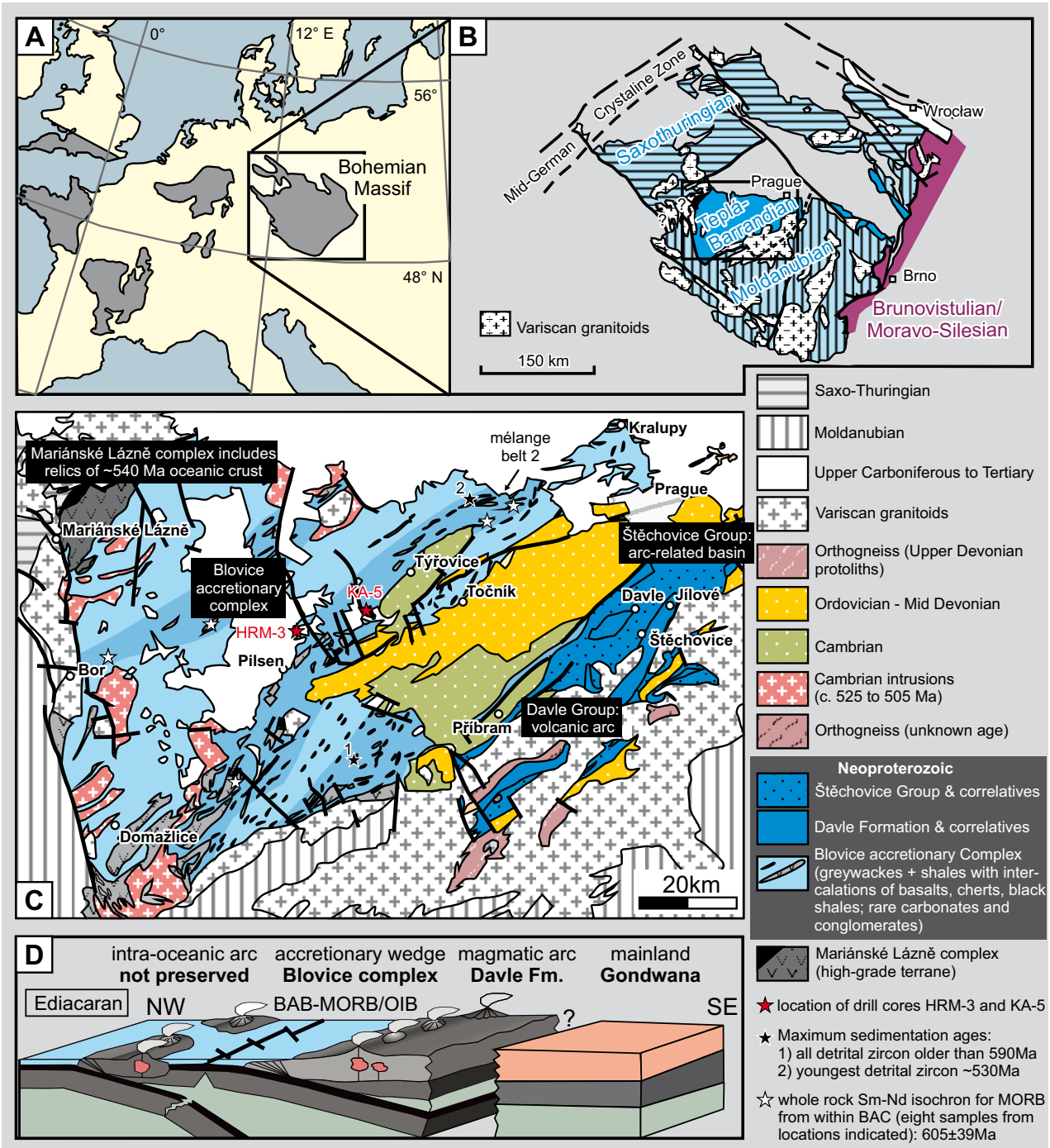

FIGURE 1 (A) Location of the Bohemian Massif. (B) Subdivision of the Bohemian Massif with the Teplá-Barrandian unit in its center (modified after Dallmeyer et al., 1995; Mazur et al., 2005). (C) Sketch map of the Teplá-Barrandian unit (modified after Kachlík in Linnemann et al., 2008; Hajná et al., 2014). Detrital zircon data from Drost et al. (2011) and Hajná et al. (2013). Sm-Nd date from Pin and Waldhausrová (2007). (D) Simplified geotectonic setting of the Teplá-Barrandian unit during Ediacaran times (after Zulauf et al., 1999; Drost et al., 2011; Hajná et al., 2014).

Constraints on the depositional age of the deposits in mélange belt 2 come from a detrital zircon study of Hajná et al. (2013) (Fig. 1). This study found two prominent peaks in the age distribution at ~560 and ~530 Ma, the latter representing the maximum age of mélange formation. However, the history of different lithologies in mélanges including their depositional age can differ significantly. The depositional age of organic-rich black shales within mélange belt 2 was previously thought to be distinctly older (635 ± 45 Ma, 1σ, whole rock Pb isochron, Pašava and Amov, 1993).

5. Methods

For the determination of major element concentrations glass beads of a homogenized mixture of 1.5 g dried and powdered sample material and 7.5 g lithium tetraborate were fused at 1050 °C for 30 minutes. Glass beads were then analyzed by wavelength dispersive X-ray fluorescence (XRF) using a Bruker AXS Pioneer S4 at the University of Tuebingen. Thirty-two standardized samples define a calibration line, the average analytical error of which is element specific and generally lower than 0.25 % for major element oxides (e.g. 0.06 % for Fe_2O_3). The loss on ignition (LOI) was determined externally and calculated by weight loss after 60 minutes heating of 1g dried and pulverized sample material at 1050 °C.

Around 1 g of powdered sample material was ashed for 12 hours at 600 °C prior to chemical purification of Mo and Fe to destroy organic compounds. The ashed sample material (20-50 mg) was weighed in pre-cleaned PFA beakers and dissolved using a mix of concentrated and distilled HF and HNO_3 at 120 °C for 72 hours. Upon drying down the solutions the samples were taken up in 6M HCl and re-dissolved in closed beakers at 130 °C for 48 hours. Visual inspection of this solution for residual solids was performed to ensure complete sample dissolution. Subsequently, aliquots were taken for further Mo and Fe purification, respectively.

An adequate amount of ^{100}Mo-^{97}Mo double spike was added to the samples to correct for any mass dependent isotope fractionation during the Mo purification procedure and Mo isotope measurements. The purification of Mo included anion exchange chromatographic methods (Dowex 1X8, 200-400 mesh) and cation exchange chromatographic methods (Dowex 50WX8 200-400 mesh), the latter assuring separation from Fe and other heavy metals. The Mo isotopic composition was measured on the ThermoFisher Scientific NeptunePlus multi-collector ICP-MS at the University of Tuebingen. To correct for background intensities we performed on-peak-zero (OPZ) measurements of the carrier solution (2% nitric acid) before and after each sample and standard measurement. Samples and standards were measured for 100 cycles each having an integration time of 8.4 s. Interferences of Ru (on $^{96}Mo^+$, $^{98}Mo^+$ and $^{100}Mo^+$) as well as Zr (on $^{92}Mo^+$ and $^{96}Mo^+$) were corrected for by simultaneous measurement of $^{99}Ru^+$ and $^{91}Zr^+$, respectively, and the use of published relative isotope abundance data (de Laeter et al., 2003) assuming an equal instrumental mass bias for Zr and Ru as determined for Mo. Isotopic data are reported in the δ-notation against NIST 3134 (Goldberg et al., 2013; Greber et al., 2012):

$$\delta^{98}\mathrm{Mo} = \left(\frac{\left(\frac{^{98}Mo}{^{95}Mo}\right)_{\mathrm{Sample}}}{\left(\frac{^{98}Mo}{^{95}Mo}\right)_{\mathrm{NIST3134}}} - 1 \right) \mathrm{x}\ 1000$$

Thereby, NIST3134 was set to 0.25 ‰ for better comparison with earlier published data (Nägler et al., 2014). Cross-calibration with an in-house Johnson Matthey ICP standard gave an isotopic difference of $\Delta^{98}Mo_{NIST3134\text{-}JM}$ = 0.27 ± 0.02 ‰ (2SD; n = 5), which is consistent with results of Goldberg et al. (2013). The long-term 2SD standard deviation of $\delta^{98}Mo_{NIST3134}$ measurements is better than 0.09 ‰ (n = 40). Two geological in-house standards (ZH-2 and ZH-5), which ran through all purification steps during the course of this study showed δ^{98}Mo values of 1.00 ‰ and 1.23 ‰, respectively, consistent with previously published estimates (Lehmann et al., 2007). The long-term reproducibility of ZH-2 and ZH-5 is 0.99 ± 0.09 ‰ (2SD; n = 16) and 1.24 ± 0.09 ‰ (2SD; n= 15), respectively.

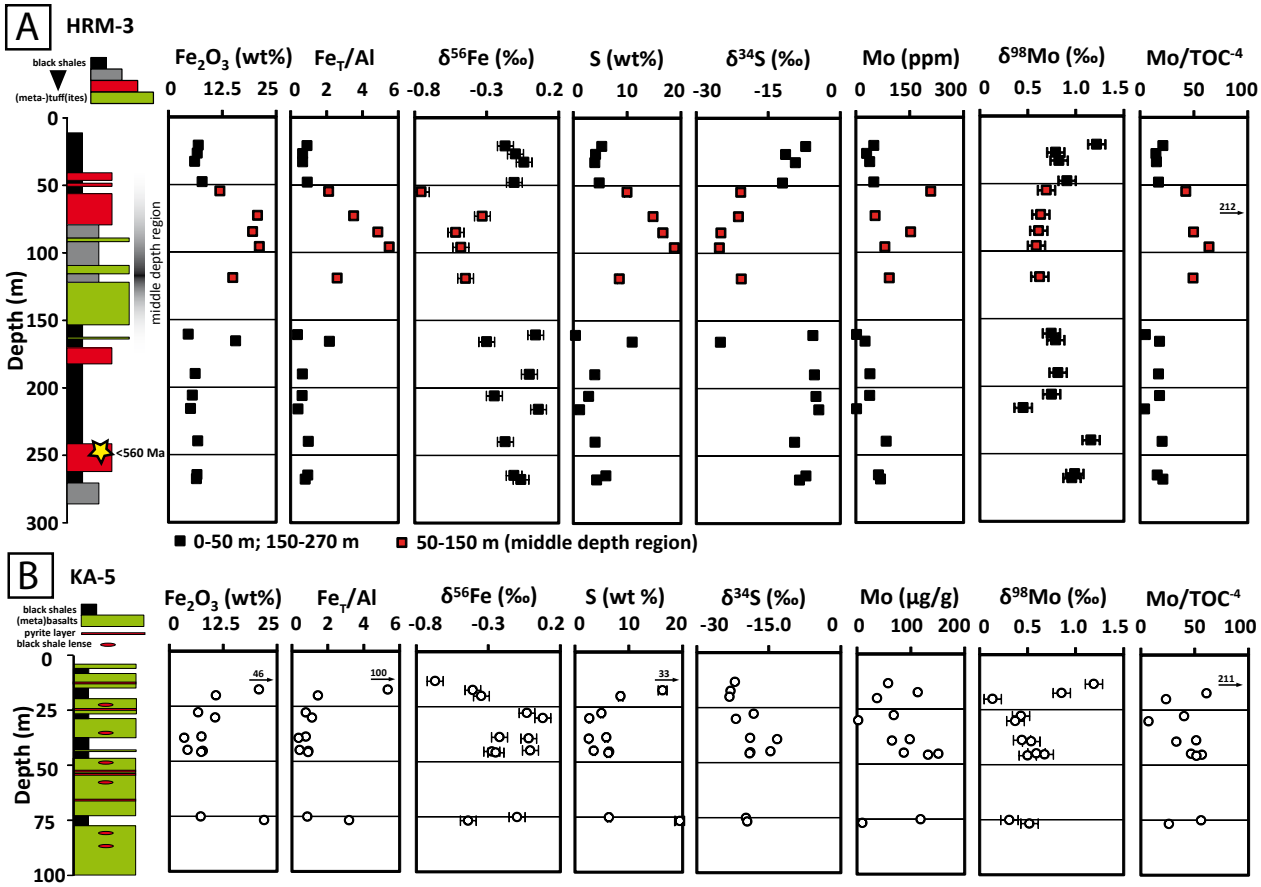

FIGURE 2: (A) Lithological composition and depth-resolved chemical parameters of the HRM-3 drill core. Between ~50 and ~150 m depth the rock record is dominated by volcanic products and also shows authigenic enrichments of S, Fe and Mo as well as low δ^{56}Fe and low δ^{34}S (red squares). Below and above, the lithology is dominated by several tens of meters of black shales that show significantly lower authigenic enrichments of S, Fe and Mo as well as higher δ^{56}Fe and higher δ^{34}S (black squares). Zircon U-Pb dating of a layer rich in volcanogenic detritus (250 m) provides a maximum depositional age of ~560 Ma. (B) Lithological and geochemical features of the KA-5 drill core (white circles). In contrast to borehole HRM-3, the entire lithology of KA-5 is dominated by metabasalts with intercalations of meter-thick black shale layers and lenses.

Purification of Fe follows a method described in Schoenberg and von Blackenburg (2005). Thereby, the Fe fraction was separated using an anion exchange resin (AG1-X8, 100-200 mesh). Samples were dissolved in 0.3M HNO_3 and isotopic ratios were measured by Multi-collector ICP-MS (ThermoFisher Scientific NeptunePlus) at the University of Tuebingen using the standard-sample bracketing method (SSB) described in Schoenberg and von Blackenburg (2005) or by the ^{57}Fe-^{58}Fe double spike method described in Swanner et al. (2015), respectively. The high resolution mode allowed the resolution of polyatomic interferences such as $^{40}Ar^{16}O^+$ on $^{56}Fe^+$ and $^{40}Ar^{14}N^+$ on $^{54}Fe^+$ (Weyer and Schwieters, 2003). Isobaric interferences of $^{54}Cr^+$ and $^{58}Ni^+$ were corrected for by simultaneous measurements of $^{52}Cr^+$ and $^{60}Ni^+$, respectively, and the use of published relative isotope abundance data (de Laeter et al., 2003) assuming the same instrumental mass bias for Cr and Ni as determined for Fe. For SSB samples were measured for 20 cycles with an integration time of 8.4 s each cycle. Instrumental mass bias correction was approached using the scheme of Schoenberg and von Blanckenburg (2005). For the double-spike method an adequate amount of ^{57}Fe-^{58}Fe double spike was added prior to Fe purification. We performed on-peak-zero (OPZ) measurements of the 0.3M nitric acid carrier solution before and after each sample and standard measurement to correct for background intensities. Samples were measured for 90 cycles with an integration time of 8.4 s each cycle. The correction of the instrumental mass bias was performed iteratively using a scheme described by Compston and Oversby (1969) with the assumption of an exponential fractionation law (Maréchal et al., 1999). Fe isotopic ratios are presented in the δ-notation relative to IRMM-014 (Institute of Reference Material and Measurements, Geel, Belgium):

$$\delta^{56}\mathrm{Fe} = \left(\frac{\left(\frac{^{56}Fe}{^{54}Fe}\right)_{\mathrm{Sample}}}{\left(\frac{^{56}Fe}{^{54}Fe}\right)_{\mathrm{IRM014}}} - 1 \right) \mathrm{x}\ 1000$$

For SSB the $\delta^{56}Fe$ of repeated measurements of our in-house standard HanFe during the course of this study was on average 0.28 ± 0.05 ‰ (2SD; n = 11), which agrees with the long-term reproducibility of 0.29 ± 0.05 ‰ (2SD; n = 145) and is also in excellent agreement with previously published values (Moeller et al., 2014). Every sample was measured twice, showing very good reproducibility (Table APPENDIX-III-1). For double-spike measurements the $\delta^{56}Fe$ of the in-house standard HanFe was also 0.28 ± 0.04 ‰ (2SD, n = 5). The reference material IF-G, an iron formation from Isua, Greenland, that run through all purification steps together with our samples during the course of this study, showed a $\delta^{56}Fe$ value of 0.63 ± 0.02 (2SE), which is consistent with literature values of 0.63 ± 0.02 (2σ) (Dauphas and Rouxel, 2006).

Between 0.5 and 5 mg bulk rock sample material was used for sulfur isotope and sulfur concentration analyses. Both were measured with a NC 2500 elemental analyzer coupled to a Thermo Quest Delta*XL mass spectrometer at the University of Tuebingen. Samples were calibrated to the $\delta^{34}S$ values of several in-house standards, such as the NBS 123 ($\delta^{34}S$ = 17.10 ‰), the NBS 127 ($\delta^{34}S$ = 20.31 ‰), the IAEA-S-1 ($\delta^{34}S$ = -0.30 ‰), and the IAEA-S-3 ($\delta^{34}S$ = 21.70 ‰), relative to the Vienna Canyon Diablo Troilite (V-CDT). S-isotope ratios are presented in the δ-notation relative to V-CDT. The long-term reproducibility is ± 0.3 ‰ (2SD) for $\delta^{34}S$ measurements and ± 5 % (2SD) for the sulfur concentration.

For U-Pb zircon dating heavy minerals were separated from the crushed rocks using heavy liquid (sodium polytungstate in water). Zircon crystals of all colors, shapes and sizes were hand-picked under the binocular microscope and set in epoxy mounts. After polishing and CL imaging with a LEO 1450 VP Scanning electron microscope (Oxford Instruments at the University of Tuebingen), the zircon mounts were sonicated in dilute HNO_3 to remove all surface contamination.

Zircon U-Pb dating was performed using a ThermoFisher Scientific iCAP Qc quadrupole ICP-MS and a Resonetics RESOlution M-50 eximer laser at the University of Tuebingen. Instrument settings and operating conditions are listed in Table APPENDIX-III-2. After 30 seconds of gas blank measurement, laser ablation data were collected for another 30 seconds. The data were processed offline in a spreadsheet-based program. Data reduction included correction for gas blank as well as for time-dependent, laser-induced and instrumental fractionation. Fractionation correction was done by bracketing the unknowns with GJ1 zircon standard (608 Ma, ~430 ppm U; Jackson et al., 2004) and applying the intercept method for the $^{206}Pb/^{238}U$ ratio. Reported uncertainties were propagated by quadratic addition of the within run precision of each analysis and the external reproducibility of the GJ1 standard (<1 % for $^{207}Pb/^{206}Pb$ and $^{206}Pb/^{238}U$, 1.5 to 4.9 % for $^{208}Pb/^{232}Th$ due to low Th concentration in GJ1; 1σ) during the analytical session. A common Pb correction using the 204 method (Košler and Sylvester, 2003) was applied when necessary. Reference zircons 91500 (1065 Ma, 81 ppm U; Wiedenbeck et al. 1995) and Plešovice (337 Ma, ~800 ppm U; Sláma et al. 2008b) were treated as unknowns and provided a quality control (Fig. APPENDIX-III-2, Table APPENDIX-III-4). Age calculations and plots were obtained using Isoplot (Ludwig, 2012). The concordia ages given in Table APPENDIX-III-3 were calculated from the analyses with >0.15 probability of concordance (Isoplot function; Ludwig, 2012). Maximum sedimentation ages were calculated using the criteria and suggestions by Dickinson and Gehrels (2009). Kernel density estimations were constructed using Density Plotter (Vermeesch, 2012).

6. Results

6.1 Depositional age

To better constrain the depositional age of the studied black shales we analyzed detrital zircon from two samples (Fig. 3, Table-APPENDIX-III-3). One sample is from HRM-3 drill core and represents the depths interval 249.5 to 250.1 m, i.e. comes from the lower part of the section analyzed for stable metal isotopes (Fig. 2). The youngest detrital zircon ages form a peak at ~560 Ma corresponding to a maximum depositional age for the lower part of HRM-3 drill core of 559.5 ± 3.5Ma (weighted mean ± 2σ, n = 11 concordia ages, MSWD = 0.76). The second sample is from a surface outcrop next to HRM-3 drill site. The youngest peak in this greywacke sample is ~535 Ma corresponding to a distinctly younger maximum sedimentation age of 534.8 ± 3.5 Ma (weighted mean ± 2σ, n = 11 concordia ages, MSWD = 0.50; Fig. 3, S1).

Generally, the constituents of mélanges can have a different origin and different depositional ages. Therefore, the maximum sedimentation age of the black shales in HRM-3 might not be constrained by

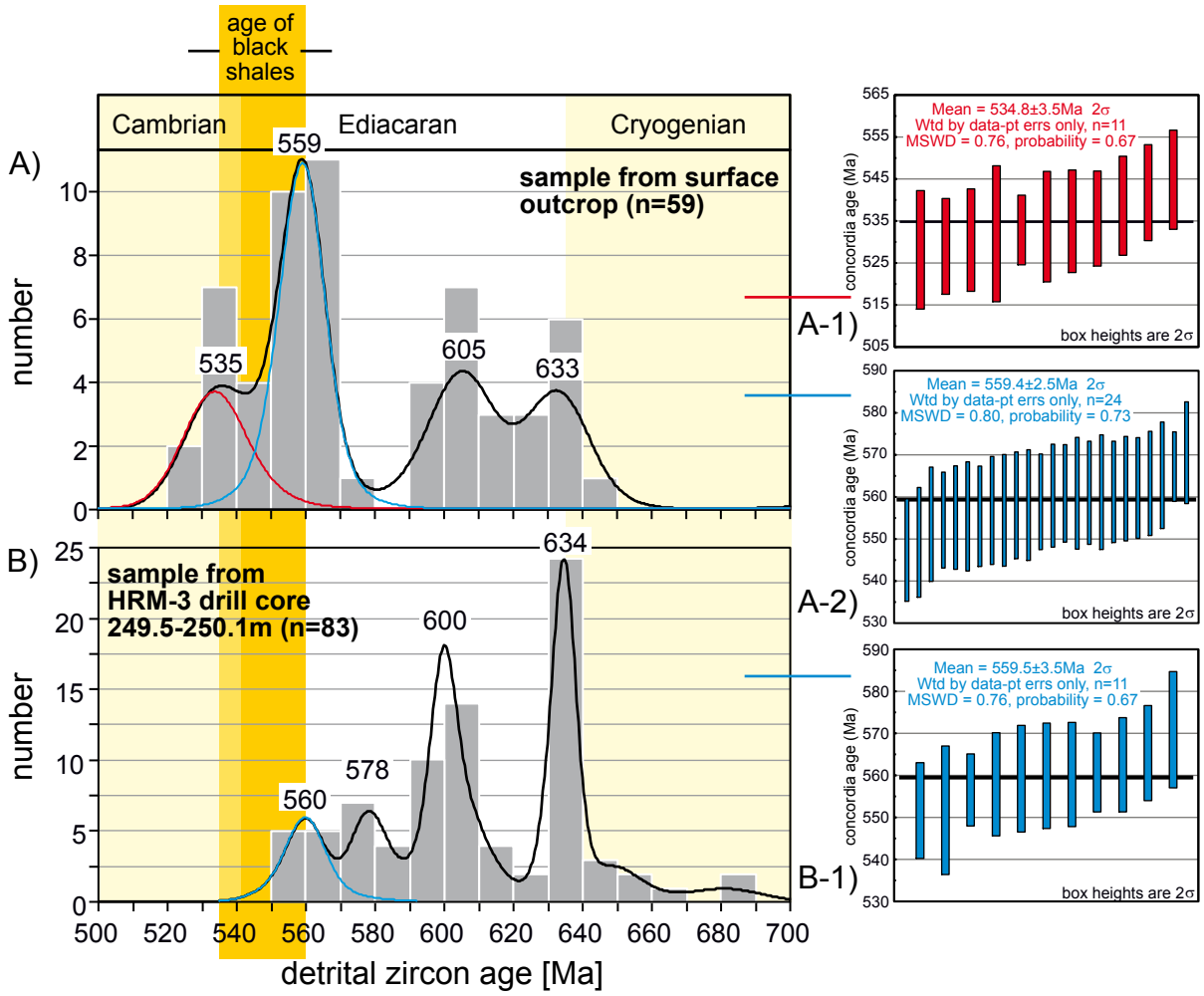

FIGURE 3: Kernel density estimation plots (Vermeesch, 2012) of detrital zircon ages between 500 and 700 Ma. The concordia ages of analyses with >0.15 probability of concordance were plotted. A) Graywacke sample from above black shale sequence showing four major detrital zircon age peaks and an Early Cambrian maximum sedimentation age. (A-1) and (A-2) Weighted means of the concordia ages constituting the peaks at 535 Ma and 559 Ma. (B) and (B-1) A sample from HRM-3 drill core taken in the lower part of the black shale sequence (cf. Fig. 2) gives a maximum sedimentation age of 559.5 ± 3.5 Ma. The concurrence of the ~560 Ma peaks in both samples and the absence of the ~535 Ma peak in the older rock suggest that the lower part of the black shale sequence is younger than ~560 Ma. Due to the early Cambrian maximum depositional age of the overlying graywackes the upper part of the section may even be early Cambrian in age.

the two samples. However, as one of the samples is from the lower part of the analyzed section and the second one from a surface outcrop above the drill core and both samples have similar peaks in the detrital zircon age distribution, i.e. the same provenance, we assume that the HRM-3 section represents a deformed but coherent stratigraphic interval rather than two (or more) tectonically juxtaposed rock assemblages of different origin. Thus, we consider the age of the HRM-3 black shales analyzed for stable metal isotopes to be younger than 559.5 ± 3.5 Ma. The upper part of the drill core may even be early Cambrian in age (<534.8 ± 3.5 Ma).

6.2 Geochemical composition

The black shales of both drill cores show large variations in transition metal concentrations such as V (35 – 2020 ppm), Ni (14 – 1200 ppm), Cu (15 – 1044 ppm) or Zn (16 – 4170 ppm) (Table 1). The concentrations of these metals fluctuate intensely over the depth range of KA-5 but vary more continuously in the HRM-3 drill core. HRM-3 black shales between 50 and 150 m, which are frequently intercalated by (meta-)tuffites, are significantly more enriched in trace metals compared to black shales from the depth region below and above (Table 1). Trace metal enriched samples are also more enriched in Fe but depleted in Al, thus showing remarkably high Fe_T/Al ratios (Fig, 2a). The black shales below and above show relatively lower Fe_T/Al ratios, reflecting the same range as sediments from the Black Sea, which is the largest modern anoxic ocean basin (Severmann et al., 2008).

The iron isotopic composition of pyritic black shales from both drill cores varies between -0.75 and +0.08 ‰ in δ^{56}Fe (Fig. 2; Fig. APPENDIX-III-1; Table 1). HRM-3 black shales with lower metal enrichment (0-50 m and 150-270 m) show relatively higher δ^{56}Fe values that are (similar as Fe_T/Al ratios) within the range of δ^{56}Fe values from modern Black Sea sediments (Severmann et al., 2008). In contrast, black shales, which are more enriched in iron, sulfur and trace metals show lower δ^{56}Fe values (Fig. 2a; Table 1, 2). A positive correlation between S (wt%) and Fe_T/Al ratios (R^2 = 0.85, excluding sample KA-5-13) is observed (Fig. 4a). Whole rock δ^{34}S values vary between -25.1 and -4.4 ‰ with more negative values in sulfur-rich

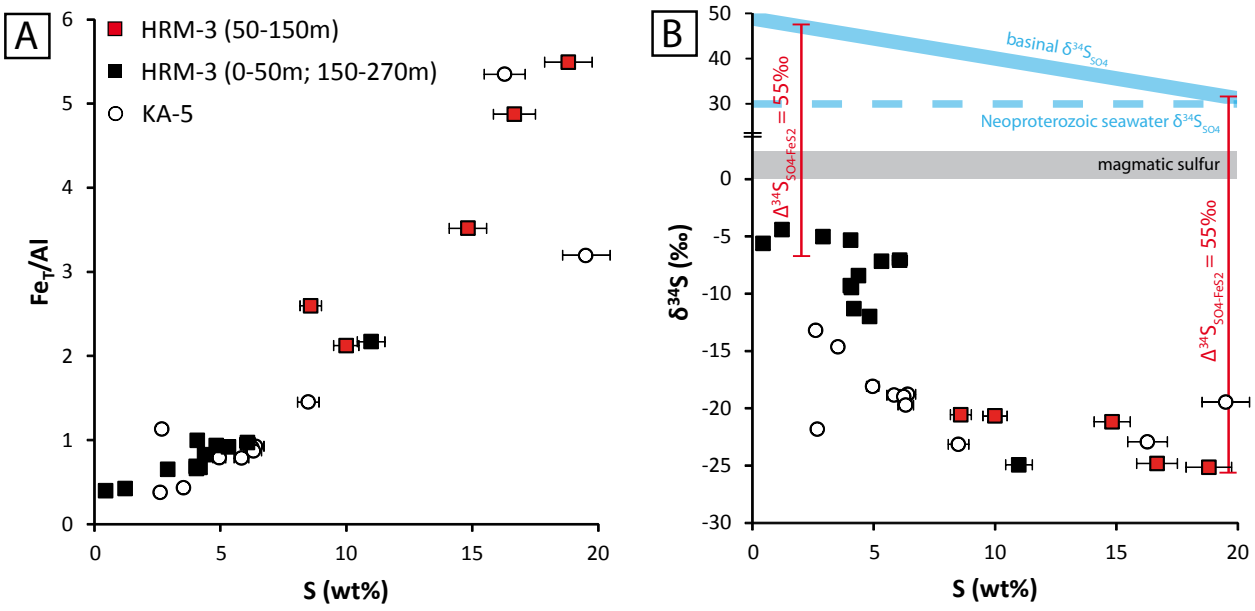

FIGURE 4: (A) Sulfur concentrations show a positive correlation with Fe_T/Al, which is attributed to authigenic pyrite enrichment. The latter is particularly pronounced in samples of the depth interval between 50 to 150 m in HRM-3 (red squares). (B) Sulfur concentration against δ^{34}S values. All δ^{34}S values are below the δ^{34}S of magmatic sulfur and imply S-isotope fractionations during sulfate reduction (displayed as $\Delta^{34}S_{SO4\text{-}FeS2}$). Samples with lower sulfur enrichment (and lower abundance of authigenic pyrite; e.g. black squares) show higher δ^{34}S values. Increasing δ^{34}S values are attributed to a repeatedly evolving basinal sulfate reservoir with increasing δ^{34}S values due to the continuous precipitation of ^{34}S depleted pyrite.

Table 1a. Fe, S and Mo isotopic composition and concentrations of selected elements of samples from drillcore HRM-3 (Hromnice)

sample	depth	δ^{56}Fe	2SD	δ^{56}Fe	2SE	δ^{98}Mo	δ^{34}S	Mo	TOC	Mo/TOC	Zn	Cu	Ni	V	S	Fe_T/Al
	m	(‰)[a]		(‰)[b]		(‰)[c]	(‰)[d]	µg/g	(wt%)	g*10^{-4}/g	µg/g	µg/g	µg/g	µg/g	wt%	
HRM-3-21	21	-0.17	0.04			1.20	-7.2	50.7	2.4	21.4	699	164	213	535	5.3	0.9
HRM-3-27	27	-0.10	0.04			0.77	-11.3	30.8	2.1	15.0	442	142	149	509	4.2	0.7
HRM-3-33	33	-0.04	0.04			0.80	-9.3	39.6	2.5	15.6	438	118	138	626	4.0	0.7
HRM-3-48	48	-0.11	0.04			0.89	-12.0	51.1	2.9	17.4	418	117	151	983	4.8	0.9
HRM-3-55	55	-0.75	0.03			0.67	-20.7	209.3	4.9	42.8	4170	862	1200	2020	10.0	2.1
HRM-3-73	73			-0.33	0.02	0.61	-21.2	54.7	0.3	212.0	613	130	116	348	14.8	3.5
HRM-3-85	85	-0.52	0.03			0.59	-24.8	153.6	3.1	49.9	3300	1044	860	1920	16.7	4.9
HRM-3-96	96	-0.47	0.04			0.57	-25.1	81.5	1.3	64.2	1365	161	367	1060	18.8	5.5
HRM-3-119	119	-0.41	0.04			0.60	-20.6	93.6	1.9	49.5	1636	370	738	895	8.6	2.6
HRM-3-161	161	0.04	0.04			0.72	-5.6	2.5	0.5	5.3	98	18	14	108	0.4	0.4
HRM-3-166	166	-0.30	0.04			0.77	-24.9	26.2	1.4	18.4	256	87	122	410	11.0	2.2
HRM-3-190	190			0.00	0.02	0.79	-5.3	39.7	2.3	17.4	287	101	70	587	4.1	0.7
HRM-3-206	206			-0.25	0.02	0.72	-5.0	39.6	2.2	18.4	293	87	78	618	2.9	0.7
HRM-3-216	216	0.06	0.03			0.43	-4.4	2.4	0.5	4.6	109	35	20	122	1.2	0.4
HRM-3-240	240	-0.17	0.04			1.14	-9.5	85.2	4.1	20.7	607	188	176	979	4.1	1.0
HRM-3-265	265	-0.11	0.03			0.97	-7.1	63.5	3.9	16.2	361	119	121	972	6.1	1.0
HRM-3-268	268			-0.06	0.02	0.94	-8.4	69.2	3.2	21.5	403	123	115	850	4.4	0.8

Table 1b. Fe, S and Mo isotopic composition and concentrations of selected elements of samples from drillcore KA-5 (Kamenec)

KA-5-13	13.4			-0.65	0.01	1.17	-22.0	58.1	0.3	211.1	16	15	16	35	33.0	100.9
KA-5-18	17.5			-0.44	0.02	0.83	-22.9	113.4	1.9	61.1	1212	232	746	1223	16.3	5.3
KA-5-20	20.2			-0.37	0.02	0.12	-23.1	37.9	1.6	23.6	493	194	177	768	8.5	1.5
KA-5-28	27.9			-0.06	0.02	0.41	-18.1	68.6	1.7	40.3	526	209	166	547	5.0	0.8
KA-5-30	30.2			0.10	0.02	0.35	-21.8	2.8	0.4	7.4	90	41	99	503	2.7	1.1
KA-5-39	38.9			-0.10	0.02	0.42	-18.9	98.6	1.9	51.6	787	269	274	690	5.8	0.8
KA-5-40	39.5			0.01	0.02	0.52	-13.2	65.3	2.0	33.3	382	131	91	331	2.6	0.4
KA-5-45	44.9			0.01	0.02	0.57	-14.6	87.6	1.9	46.9	553	173	121	471	3.5	0.4
KA-5-45.5	45.4			-0.23	0.02	0.66	-18.8	151.7	2.7	56.9	1273	379	449	974	6.4	0.9
KA-5-46	45.9			-0.20	0.02	0.48	-19.0	132.2	2.5	51.9	1211	352	449	929	6.2	0.9
KA-5-72	75.2			-0.10	0.02	0.29	-19.7	118.4	2.1	56.1	1115	331	355	896	6.3	0.9
KA-5-77	76.8			-0.25	0.01	0.50	-19.5	10.4	0.4	26.2	31	119	58	314	19.5	3.2

[a] average of two seperate SSB measurements (see supplements for individual results); long-term 2SD reproducibility of the HanFe standards and natural samples is 0.05 ‰ (Schoenberg and von Blankenburg, 2005)

[b] δ^{56}Fe values measured by the double-spike method, with a 2SD reproducibility of 0.04 ‰ (HanFe standards)

[c] the long term reproducibility of the $\delta^{98}Mo_{NIST3134}$, as well as the long term reproducibility of ZH-2 is better than 0.09 ‰ (2SD)

[d] the 2SD long-term reproducibility is 0.3 ‰

samples (Fig. 4b). Metal enriched samples of HRM-3 (50 to 150 m) also show strong sulfur enrichments and low $\delta^{34}S$ values being in stark contrast to lower S concentrations and higher $\delta^{34}S$ values in the depth region below and above. Most of the black shales from KA-5 plot in between, which results in a continuous negative trend (Fig. 4b).

The chemical heterogeneity in our sample set is also depicted in variable Mo abundances ranging from 2 to 209 ppm (Fig. 2, Table 1). In comparison with modern euxinic settings our Mo and TOC data show similar concentration ranges as well as similar correlations of Mo and TOC (Fig. 5). Samples from KA-5 indicate a relatively steep slope of 49 (units 10-4; $R^2 = 0.74$), which is also observed in sediment samples of the weakly restricted Saanich Inlet, an anoxic silled basin along the uplifted convergent margin of Vancouver Island, Canada (Algeo and Lyons, 2006). In the drill core HRM-3, the ratios of Mo/TOC vary with core depth. Samples with overall high metal concentrations (between 50 and 150 m) show a slope of 35 ($R^2 = 0.99$, red squares), whereas samples below and above have a slope of 21 ($R^2 = 0.95$, black squares). The latter is slightly lower than that observed in sediment samples from the Cariaco Basin, an anoxic silled basin at the convergent margin of the Venezuelan continental shelf (Algeo and Lyons, 2006).

The range in $\delta^{98}Mo$ values is similar in both drill cores (Fig. 2) with a minimum value of +0.12 ‰ and a maximum value of +1.20 ‰. HRM-3 samples with lower Mo/TOC ratios tend to have higher $\delta^{98}Mo$ (Table 1). Along the drill core depth of HRM-3 we observe high $\delta^{98}Mo$ values up to 1.1 ‰ at greater depth, a continuous decrease until metal-enriched samples from middle depth with constant $\delta^{98}Mo$ values around 0.7 ‰ and a subsequent re-increase towards higher values around 1.2 ‰ in the uppermost part of the drill core (Fig. 2).

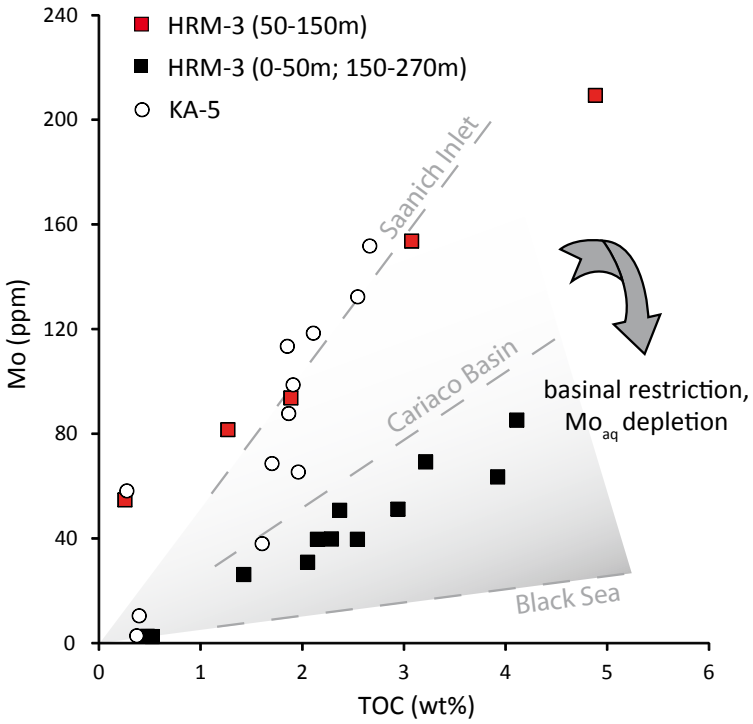

FIGURE 5: Compilation of Mo and total organic carbon concentrations. For comparism the Mo/TOC slopes of various modern euxinic settings with contrasting restrictions and water renewal times are plotted (Algeo and Lyons, 2006; note that the dashed lines only indicate the characteristic slope of respective settings and do not represent absolute values). The lower the slope the more depleted is the Mo_{aq} reservoir possibly due to restricted water circulation in the basin (Algeo and Lyons, 2006).

Table 2a. Major element data of drillcore HRM-3 (Hromnice)

sample	depth	SiO_2	TiO_2	Al_2O_3	Fe_2O_3	MnO	MgO	CaO	Na_2O	K_2O	P_2O_5	LOI	sum
	m	wt%	wt%	wt%	wt%	wt%	wt%	wt%	wt%	wt%	wt%	wt%	%
HRM-3-21	21	64.73	0.44	10.15	6.92	0.03	1.15	0.61	2.38	1.40	0.14	11.67	99.62
HRM-3-27	27	62.51	0.69	13.18	6.69	0.07	2.17	1.26	0.35	2.26	0.16	10.25	99.59
HRM-3-33	33	60.14	0.55	11.90	6.12	0.05	2.89	2.86	1.51	2.20	0.14	11.16	99.50
HRM-3-48	48	61.39	0.49	11.24	7.86	0.04	1.96	1.89	1.62	1.85	0.11	10.85	99.31
HRM-3-55	55	51.21	0.33	7.75	11.97	0.03	2.34	1.67	0.20	1.40	0.13	21.65	98.67
HRM-3-73	73	41.15	0.63	8.03	20.71	0.12	2.05	14.56	0.67	0.31	0.16	11.18	99.57
HRM-3-85	85	42.04	0.23	5.70	19.54	0.03	1.90	1.64	0.19	0.94	0.12	26.56	98.88
HRM-3-96	96	38.71	0.23	5.49	21.12	0.03	0.86	2.16	0.75	1.03	0.07	28.87	99.32
HRM-3-119	119	33.97	0.71	7.90	14.94	0.11	9.91	9.72	0.35	0.69	0.17	20.62	99.09
HRM-3-161	161	66.99	0.66	15.27	4.60	0.07	1.67	1.21	4.03	2.16	0.12	3.04	99.82
HRM-3-166	166	43.38	0.67	9.71	15.60	0.10	4.07	5.41	1.48	1.65	0.14	17.43	99.64
HRM-3-190	190	63.55	0.58	12.49	6.22	0.06	2.03	1.54	2.65	2.46	0.13	7.99	99.69
HRM-3-206	206	67.97	0.48	11.41	5.56	0.05	1.21	0.28	1.73	2.57	0.12	8.37	99.73
HRM-3-216	216	61.08	0.86	16.10	5.16	0.08	3.31	2.67	3.54	2.22	0.14	4.58	99.72
HRM-3-240	240	64.00	0.41	9.29	6.82	0.07	2.05	1.96	0.95	2.35	0.14	11.60	99.64
HRM-3-265	265	66.85	0.41	9.28	6.64	0.04	1.21	1.30	1.45	1.89	0.12	10.41	99.60
HRM-3-268	268	66.55	0.47	10.61	6.51	0.05	1.42	1.42	1.94	1.94	0.14	8.55	99.61

Table 2b. Major element data of drillcore KA-5 (Kamenec)

KA-5-13	13.4	10.57	0.12	0.60	46.16	0.08	0.30	6.86	0.06	0.02	0.02	35.07	99.88
KA-5-18	17.5	21.99	0.24	5.16	20.86	0.04	0.73	1.75	0.34	1.22	0.09	46.81	99.22
KA-5-20	20.2	52.35	0.21	9.89	10.86	0.05	0.79	2.36	2.43	1.51	0.07	18.13	98.64
KA-5-28	27.9	52.98	0.62	13.63	6.74	0.05	2.36	2.22	2.23	2.54	0.16	15.35	98.89
KA-5-30	30.2	47.23	2.13	12.29	10.69	0.17	4.92	8.34	3.16	0.12	0.18	7.22	96.45
KA-5-39	38.9	54.27	0.64	12.64	7.51	0.06	2.18	3.73	2.51	2.13	0.17	12.39	98.22
KA-5-40	39.5	66.36	0.36	12.38	3.54	0.05	1.46	2.50	2.72	2.20	0.08	7.16	98.82
KA-5-45	44.9	62.62	0.46	13.13	4.28	0.05	1.72	2.56	2.70	2.43	0.10	8.65	98.70
KA-5-45.5	45.4	53.50	0.50	11.86	7.85	0.05	2.09	2.83	1.63	2.51	0.14	15.45	98.41
KA-5-46	45.9	50.10	0.45	10.87	7.48	0.05	1.91	2.85	1.54	2.29	0.12	21.01	98.67
KA-5-72	75.2	51.88	0.46	11.14	7.34	0.04	1.84	2.01	1.93	2.18	0.12	19.82	98.75
KA-5-77	76.8	29.03	1.27	9.14	22.07	0.17	4.16	10.83	2.14	0.29	0.10	18.09	97.29

7. Discussion

7.1 The local depositional environment

The concentration of aluminum serves as a good proxy for quantifying the terrigeneous input due to overall low aqueous solubility of Al. The ratio of Fe_T/Al in sediment samples is therefore a measure for authigenic Fe enrichment vs. detrital input. The positive correlation of Fe_T/Alratios and S concentration in our samples strongly suggests that authigenic Fe enrichment was linked to pyrite formation (Fig. 4a). This is confirmed by several petrological and mineralogical studies of the KA-5 and HRM-3 drillcores, which pointed out that other authigenic Fe phases are limited to secondary quartz carbonate veinlets (e.g. siderite) or are completely absent (e.g. Fe oxides) (Pašava et al., 1993; Pašava et al., 1996). The predominance of authigenic Fe sulfide minerals and the concomitant lack of Fe carbonates and Fe oxides in primary black shale layers suggest a high degree of pyritization (DOP), although there is no Fe speciation data available to further confirm this hypothesis. This would indicate that the local depositional environment was euxinic (Raiswell et al., 1994).

In euxinic settings molybdenum forms particle reactive thiomolybdate species, which are efficiently trapped by sulfur-rich organic matter (Tribovillard et al., 2004). Accordingly, Mo is particularly enriched in the organic-sulfur-rich matrix of the samples (Pašava et al., 1993). Significant correlations of Mo with TOC are consistent with this observation (Fig. 5) and can be attributed to variable water renewal times as shown by Algeo and Lyons (2006). These authors demonstrate that flat Mo/TOC slopes are controlled by limitation of Mo_{aq} in more restricted euxinic basins. Mo and TOC concentrations of samples from the KA-5 drill core define a steep slope, which is similar to data from the modern Saanich Inlet. This modern analogue is a relatively well mixed anoxic silled basin with short water renewal times (Algeo and Lyons, 2006). In the HRM-3 drill core, the slope of Mo vs. TOC changes with core depth. High Mo/TOC ratios in samples from trace metal enriched core depth between 50 and 150 m indicate higher bottom water Mo concentrations in a more ventilated depositional setting with better access to the open ocean. In contrast, low Mo/TOC ratios of samples from deeper and higher sections of HRM-3 drill core are consistent with lower Mo_{aq} concentrations in the contemporaneous seawater and, thus, point to deposition in a temporarily more restricted basin. In principle, such temporal restriction could result from changes in the ocean circulation pattern and/or water column stratification with sporadic venting like in the Gotland deep of the Baltic Sea or the Saanich Inlet, Canada. Alternatively, physical changes in the sedimentary environment due to contemporary tectonic activity or temporal changes in the chemocline depth may have led to variations in ventilation and water exchange. A probable major difference of the Kamenec and Hromnice depositional settings compared to modern settings was the significantly higher H_2S_{aq} concentration, as indicated by the generally high abundance of authigenic pyrite.

The relative depletion of other metals such as Fe, Ni, Cu or Zn in HRM-3 samples with low Mo/TOC might similarly result from restricted supply during times of low water renewal rates. Low authigenic enrichments of these metals correlate with low sulfur concentrations. The relative depletion of sulfur in the uppermost and lowermost part of HRM-3 is accompanied by higher $\delta^{34}S$ values (Fig. 4b). These relatively high $\delta^{34}S$ values are still lower than the isotopic composition of modern mantle sulfur, which

shows homogeneous $\delta^{34}S$ values between 0 and 4 ‰ (Seal, 2006). Negative $\delta^{34}S$ values require fractionation processes during sulfate reduction, during which the light ^{32}S is enriched in the sulfide phase. Considering the S isotopic composition of contemporaneous seawater sulfate during late Neoproterozoic times with $\delta^{34}S$ values around 30 ‰ (Hurtgen et al., 2002; Strauss, 1993), the isotopic difference $\Delta^{34}S_{sulfate\text{-}FeS2}$ was up to 55 ‰. Such isotopic differences are relatively large but within the range observed in modern marine sulfides (Canfield and Teske, 1996; Canfield and Thamdrup, 1994; Jørgensen, 1990). Assuming similar S-isotopic differences between sulfate and pyrite in all black shales, the $\delta^{34}S$ value of the sulfate must have increased during more restricted periods (Fig. 4b). Such an increase could reflect a temporally evolving sulfate pool within times of increased basinal restriction, which gets isotopically heavier due to continuous pyrite burial (and the preferential removal of isotopically light S) in combination with limited replenishment from seawater sulfate. The sulfur isotope data are therefore consistent with the restriction vs. well-mixed scenario.

In line with changing sulfur concentrations and $\delta^{34}S$ values, the bulk iron isotopic composition changes with increasing authigenic pyrite enrichment. A linear positive correlation between $\delta^{56}Fe$ and Al/Fe_T (Fig. 6) indicates binary mixing between an Al-rich detrital source with high $\delta^{56}Fe$ around 0.1 ‰ (Beard et al., 2003; Schoenberg and von Blanckenburg, 2006) and high Al/Fe_T ratios around 2 (estimated from other sedimentary rocks and potential basaltic source rocks in the Blovice accretionary complex) (Drost et al., 2007; Pin and Waldhausrová, 2007) and a Fe-rich authigenic source with low $\delta^{56}Fe$ around -0.6 ‰ (Fig. 6; S2). The impact of the detrital Fe component increases during periods of increased basinal restriction.

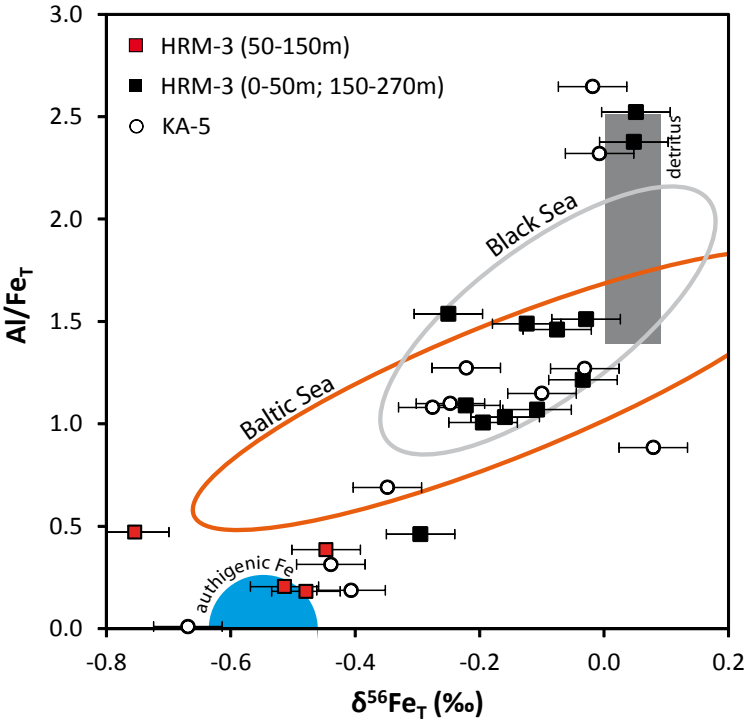

FIGURE 6: Compilation of $\delta^{56}Fe$ values against Al/Fe_T ratios. The gray shaded area displays the expected composition of detrital material with a $\delta^{56}Fe$ value between 0.0 and 0.1 ‰ (Beard et al., 2003) and a ratio of Al/Fe_T between 1.25 and 2.5 (see text for further explanation). The blue shaded area indicates the Fe isotopic composition of additional authigenic Fe enrichment with a $\delta^{56}Fe$ value around -0.6 ‰. Most samples plot within the binary mixing area of these components. Furthermore, most HRM-3 samples with relatively low authigenic Fe enrichment (black squares) resemble compositions of modern black shales from the Black Sea (Severmann et al., 2008) and the Baltic Sea (Fehr et al., 2010). Only one sample has a significantly lower $\delta^{56}Fe$ than expected from the binary mixing array, possibly indicating Fe isotope fractionation effects.

The preservation of the observed correlations in the δ^{56}Fe-Al/Fe_T plot and their explanation by a simple binary mixing model (Fig. 6) seem unexpected considering large kinetic Fe isotope fractionations during pyrite formation and the possible preferential uptake of isotopically light Fe (Guilbaud et al., 2011; see detailed explanation of pyrite formation processes and Fe isotope fractionation during pyrite formation in APPENDIX-III). Only one sample (HRM-3-55) deviates from the modeled mixing array showing a low δ^{56}Fe value of -0.75 ‰. We suggest that Fe isotope fractionation during rapid and non-quantitative mackinawite/ pyrite formation caused the enrichment of light Fe isotopes in this sample. Fast growing sulfide nuclei might have inhibited the equilibration of Fe_{aq} and FeS, which caused the preservation of a larger isotopic difference (Butler et al., 2005). The lack of other δ^{56}Fe values, which are significantly lower than proposed by the mixing area, suggests in turn that the net effect of Fe isotope fractionations during pyrite formation was low for all other samples. This strongly indicates that the removal of Fe was quantitative, thus preserving the original Fe isotope signal of the authigenic source in the sediment. Quantitative Fe removal implies that pyrite precipitation was limited by Fe_{aq} availability in an H_2S_{aq} supersaturated (e.g. euxinic) local environment, which is consistent with our argumentation for a euxinic setting.

In contrast to Fe, Mo concentration data indicate that variations in the detrital Mo-flux had little effect on the bulk Mo isotopic composition of most black shales. Only three samples, HRM-3-161, HRM-3-216 and KA-5-30 show Mo concentrations below 3 ppm, which is close to the value of the PAAS (1.0 ppm) (Taylor and McLennan, 1985). In these tuff-rich layers detrital Mo might dominate. However, assuming a detrital composition similar to PAAS (Taylor and McLennan, 1985) and that all Al_2O_3 in our samples is detrital, the terrigeneous Mo flux rate accounts on average for only 1.3 % of the total Mo in all other black shales, which highlights the predominance of authigenic Mo enrichment.

7.2 Authigenic metal enrichment from seawater- proposal 1

Changes in water renewal times and Mo_{aq} availability not only alter the ratio of Mo/TOC, but also have an impact on the sedimentary Mo isotope signal (Kurzweil et al., 2015). For example, in euxinic and strongly restricted basins like the modern Black Sea the δ^{98}Mo value of the sediments is slightly lower than the local deep water δ^{98}Mo (Nägler et al., 2011) but mirrors the open ocean δ^{98}Mo. This is because the deep water renewal time and therefore the Mo supply is significantly lower than Mo scavenging (Algeo and Lyons, 2006). The removal of Mo is extremely high in euxinic settings (Scott et al., 2008) and nearly quantitative in restricted settings like the Black Sea (Nägler et al., 2011; Neubert et al., 2008). In less restricted euxinic basins like the Cariaco Basin, where Mo depletion is less pronounced, sediments show δ^{98}Mo values ~0.6 ‰ lower compared to the open ocean (Arnold et al., 2004). Thus, the more restricted a euxinic basin, the more depleted is the basinal Mo_{aq} and the more converge the sedimentary δ^{98}Mo and the open ocean δ^{98}Mo (Kurzweil et al., 2015).

In such a scenario, our black shale samples with low Mo/TOC and high δ^{98}Mo values must have been deposited during one or several period(s) of relative depletion in Mo_{aq} resulting from restricted seawater circulation (Fig. 7a; black squares; HRM-3: 0-50 m, 150-270 m; excluding KA-5-13). Accordingly, the maximum δ^{98}Mo value of 1.2 ‰ in our dataset represents the best estimate of the contemporaneous seawater δ^{98}Mo value. The Mo/TOC ratios of the respective black shales follow a trend intermediate

between that of black shales from the modern Black Sea and the Cariaco Basin (Algeo and Lyons, 2006). In the case of sediments from the Black Sea δ^{98}Mo values mirror the global seawater δ^{98}Mo value (Neubert et al., 2008). We therefore argue that our highest δ^{98}Mo value of 1.2 ‰ is very close to the late Neoproterozoic seawater δ^{98}Mo value. We note that the δ^{98}Mo values during these restricted periods are not constantly high but show some variation towards lower values, although Mo/TOC ratios remain relatively invariant. Mo isotope fractionations under weakly sulfidic conditions could represent a possible explanation for this variation (Poulson Brucker et al., 2009; Poulson et al., 2006). Lowering the local H_2S_{aq} concentration below the switching point of 11 µmol L^{-1} causes an increase in the abundance of oxythiomolybdate relative to that of the thiomolybdate species (Neubert et al., 2008). Sediments below such weakly sulfidic water columns generally exhibit lower δ^{98}Mo values than the global ocean δ^{98}Mo value (Poulson Brucker et al., 2009; Poulson et al., 2006; Siebert et al., 2006). So far there is, however, no proxy established that allows to evaluate whether or not the switching point was reached. Even if Fe speciation data indicate sulfidic conditions, it is not clear whether or not H_2S_{aq} concentrations were high enough for near quantitative thiomolybdate formation. We note, however, that increasing δ^{98}Mo values in respective black shales correlate with increasing sulfur concentrations, which may indicate higher H_2S_{aq} and more efficient thiomolybdate formation during deposition of black shales with highest δ^{98}Mo values (Fig. 7b).

Samples from intermediate core depth of HRM-3 (50-150m) show high Mo/TOC at relatively constant δ^{98}Mo values of 0.63 ± 0.08 ‰ (2SD, Fig. 7). High sulfur concentrations in the respective samples may furthermore suggest particularly strong euxinic conditions. During these periods of minor basinal restriction the sedimentary δ^{98}Mo value is expected to be around 0.7 ‰ lower than the contemporaneous seawater δ^{98}Mo value (Kurzweil et al., 2015). The absence of significantly lower δ^{98}Mo values during well-mixed periods therefore represents an additional indication that the seawater δ^{98}Mo value was close to 1.2 ‰.

In contrast to δ^{98}Mo values, which remain constant independent of absolute Mo enrichment, we observe lower δ^{56}Fe values in samples with a larger authigenic Fe component. As suggested above, the supply from a Fe source with negative δ^{56}Fe values around -0.6 ‰ probably overwhelmed the contribution of detrital Fe during more ventilated periods. A ferruginous deep ocean could represent this source. Its Fe isotopic composition is poorly constrained, but might have been close to or slightly lower in the δ^{56}Fe than average continental crust (~0.05 ‰) (Beard et al., 2003; Johnson et al., 2008a). Temporal invariability in the δ^{56}Fe value of this source would be expected because of the long residence time of Fe in a Precambrian anoxic deep ocean (Johnson et al., 2008a).

A benthic Fe-shuttle from nearby shelf regions could represent an alternative and/or additional Fe source with negative δ^{56}Fe values. Interestingly, the Al/Fe_T-δ^{56}Fe relationship of the Kamenec-Hromnice black shales follow a similar trend as modern black shales from the Gotland Deep (Baltic Sea) and the Black Sea (Fig. 6; S2) (Fehr et al., 2008; Severmann et al., 2008) This modern trend was explained by the export of shelf Fe with low δ^{56}Fe values, which subsequently precipitated as pyrite in the euxinic sediments of the basin (Severmann et al., 2008). Our HRM-3 samples from more restricted periods, plot in the very same area of the Al/Fe_T-δ^{56}Fe plot as samples from the modern Black Sea and, therefore, may suggest a similar depositional environment (Fig. 6) (Severmann et al., 2008).

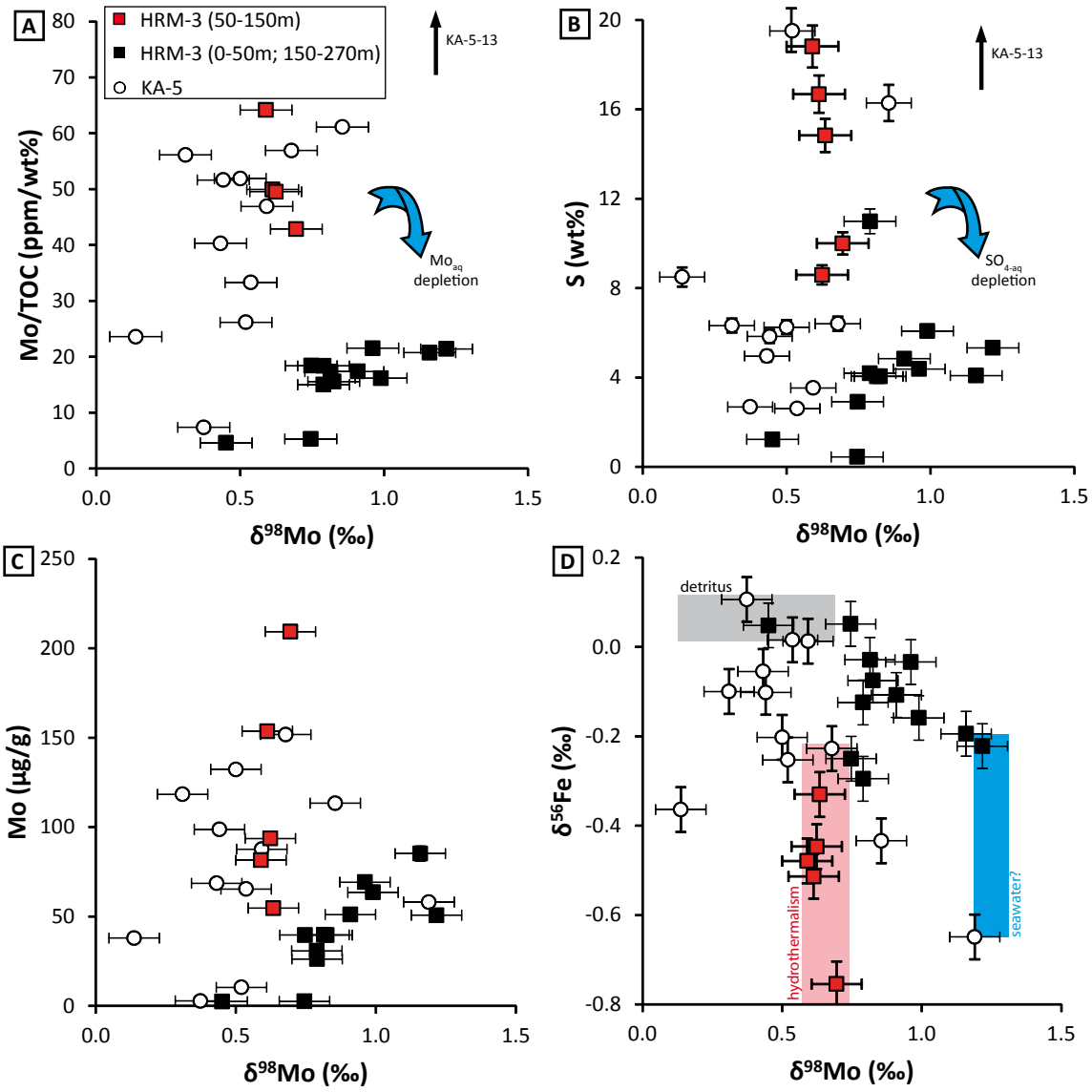

FIGURE 7: (A) Mo/TOC ratios against δ^{98}Mo values. Low Mo/TOC indicate Mo_{aq} depletion during more restricted periods (Algeo and Lyons, 2006). Near quantitative Mo_{aq} removal allowed the preservation of the seawater δ^{98}Mo within the sediment (1.2 ‰, proposal 1). During deposition of black shales with higher Mo/TOC, Mo_{aq} depletion was reduced and the sedimentary δ^{98}Mo value up to 0.7 ‰ lower than contemporaneous seawater (Kurzweil et al., 2015). Alternatively, the supply of hydrothermal Mo with a δ^{98}Mo value of around 0.7 ‰ was higher during more ventilated periods (proposal 2). (B) Sulfur concentrations against δ^{98}Mo values. The supply of sulfate from the open ocean was reduced during more restricted periods, which caused lower precipitation rates of authigenic sulfides. (C) Mo concentration against Mo isotopic composition. (D) δ^{98}Mo values against δ^{56}Fe values. The grey area marks the field of the modern detrital Fe- and Mo isotopic composition (Beard and Johnson, 2004; Dauphas and Rouxel, 2006; Siebert et al., 2003; Voegelin et al., 2014). The red area marks the Mo and Fe isotopic composition of modern hydrothermal fluids (Johnson et al., 2008b; McManus et al., 2006; Sharma et al., 2001). The blue area marks the suggested Mo and Fe isotopic composition of the late Neoproterozoic ocean. All data points fall within the mixing area of these components. However, we note again, that lower δ^{98}Mo values could reflect a stronger hydrothermal component (proposal 2) as well as larger differences in $\Delta^{98}Mo_{sediment\text{-}seawater}$ (up to 0.7 ‰) due to less circulation restriction and/or less Mo_{aq} depletion (proposal 1).

7.3 Hydrothermal metal enrichment – proposal 2

The documented local volcanogenic-hydrothermal input could represent an alternative or additional source for authigenic metal enrichment. The pattern of PGE's (platinum group elements) in Teplá Barrandian black shales indicates a hydrothermal source of these elements, although absolute enrichments of PGE's are significantly lower compared to high-temperature hydrothermal ore deposits (Pašava et al., 1996). Variability in PGE and other metal enrichment might indicate changes in the supply from a local low-temperature hydrothermal source. The δ^{56}Fe values of modern hydrothermal fluids are not globally uniform but tend to negative values down to -1 ‰, with an average of -0.4 ‰ (Beard et al., 2003; Johnson et al., 2008b; Moeller et al., 2014; Sharma et al., 2001). The binary mixing of detrital Fe with δ^{56}Fe values around 0.1 ‰ and a hydrothermal authigenic Fe source with δ^{56}Fe values around -0.6 ‰ is therefore also consistent with the proposal of hydrothermal metal enrichment (Fig. 6).

The S-isotope record is more difficult to explain by changes in the supply from a low-temperature hydrothermal vent system. In modern low-T hydrothermal settings sulfate, which is used for bacterial sulfate reduction and subsequent pyrite formation, is supplied from seawater on the one hand and diffusional transport from underlying basement formation waters on the other hand (Böttcher et al., 2006; Wheat et al., 2002). The latter brines are ultimately also recharged from the seawater reservoir, but are isotopically heavier due to subsurface pyrite precipitation (Böttcher et al., 2006). We therefore expect higher instead of lower δ^{34}S values during periods of high hydrothermal fluxes, when the impact of isotopically heavy brines is higher (Fig. 4b).

Alternatively, sulfate was additionally supplied from magmatic fluids (Fig. 4b) (Alt, 1995; Gamo et al., 1997; Herzig et al., 1998). Sulfate-rich hydrothermal fluids with even higher sulfate concentrations than seawater are observed in hydrothermal systems along back-arc basins (Gamo et al., 1997), which likely represent a modern analogue to the setting studied here (Pin and Waldhausrová, 2007). The addition of magmatic sulfate with lower δ^{34}S values compared to seawater sulfate could therefore explain lower δ^{34}S values and higher sulfur concentrations in metal enriched samples. During reduced hydrothermal activity seawater sulfate with higher δ^{34}S values could have represented the only or predominant sulfate source, resulting in higher δ^{34}S values (Fig. 4b).

For those samples of the HRM-3 drill core, which show low δ^{56}Fe and low δ^{34}S, Mo/TOC ratios are higher and the δ^{98}Mo values are relatively constant (+0.63 ± 0.08 ‰, 2SD), independent of the absolute authigenic Mo enrichment. High Mo/TOC ratios might indicate higher Mo_{aq} availability due to increased hydrothermal fluxes instead of better access to the open ocean (see section 5.2). The Mo isotopic composition agrees very well with the δ^{98}Mo value of modern low-temperature hydrothermal fluids (~+0.7 ‰ in δ^{98}Mo) (McManus et al., 2006) and provides a reasonable estimate of the Mo isotopic composition of the local hydrothermal input at Hromnice (Fig. 7c). Such constant δ^{98}Mo values of the hydrothermal flux would argue against temporal variability in the Mo isotopic composition due to fractionation processes within the hydrothermal system. Mo isotope fractionations during species changes and reduction of hydrothermal Mo(VI) in $HMoO^{4-}$ (Rempel et al., 2009) and the subsequent precipitation of molybdenite (MoS_2) as a co-phase of chalcopyrite ($CuFeS_2$) were therefore negligible. Such a scenario is supported by high Cu and Mo concentrations in the respective samples.

For HRM-3 black shales with high $\delta^{34}S$ values and lower Mo/TOC ratios, Mo enrichment is accompanied by increasing $\delta^{98}Mo$ values up to +1.20 ‰ (Fig. 7c), a correlation that requires further consideration. The observed trend in respective samples can be explained by a pure seawater signal, which was partly modified by fractionation processes during Mo sequestration in a weakly sulfidic environment (see section 5.2) or alternatively by a mixing trend of seawater Mo with hydrothermal Mo. The latter interpretation implies that the relative contribution of Mo from a hydrothermal source with $\delta^{98}Mo$ of ~+0.7 ‰ and from Neoproterozoic seawater with $\delta^{98}Mo$ of ~+1.2 ‰ was variable. However, such mixing processes should result in a positive rather than a negative correlation of $\delta^{98}Mo$ and $\delta^{56}Fe$ values (Fig. 7d), because the hydrothermal fluid would have been characterized by very low $\delta^{56}Fe$ and also lower $\delta^{98}Mo$ values. Furthermore, we expect higher rather than lower Mo concentrations in the respective samples (Fig. 7c). The positive trend between Mo concentration and $\delta^{98}Mo$ values (Fig. 7c) and the observed negative trend in the $\delta^{98}Mo$ vs. $\delta^{56}Fe$-plot (Fig. 7d) therefore argue against significant authigenic enrichment of Mo from a hydrothermal source in respective samples.

We note that even in modern settings it remains unclear if the hydrothermal input represents a net sink or source of marine Mo (Chester, 2009). Therefore, some metals such as PGE, which might have been depleted in seawater, could have been enriched from a local hydrothermal source (possibly also Fe, Ni, Cu and some other trace metals during some periods), whereas the source of Mo and also sulfate was probably mainly seawater (Fig. 8). Altogether, the geochemical and isotopic features exhibited by our black shale samples can be explained by intermittent variations in basin restriction and are, thus, consistent with proposal 1 (Fig. 8). Additionally, a temporally available hydrothermal component may have affected the composition of some black shales (Pašava et al., 1996).

7.4 Implication for the Neoproterozoic environment

Recent studies point to unchanged ferruginous seawater conditions far into the Paleozoic era (Feng et al., 2014; Goldberg et al., 2007; Wang et al., 2012; Wood et al., 2015), which seems inconsistent with several other geochemical studies that claim for deep ocean oxygenation at the Precambrian-Cambrian boundary or even before (Canfield et al., 2007; Fike et al., 2006; Kendall et al., 2015; Sahoo et al., 2012). In our view, the best explanation for this apparent inconsistency is a heterogeneous ocean with a spatially variable redox structure. For example, late Neoproterozoic Fe speciation data from Newfoundland (Canfield et al., 2007) describe a locally developed oxic water column. Similarly, strong authigenic enrichments of redox sensitive trace metals like V, Mo and U (Sahoo et al., 2012) are not only dependent on the global availabilities of these metals in more oxygenated environments but also on local factors such as the sedimentation rate, the local redox state and access of the basin to the open ocean (Algeo and Lyons, 2006; Noordmann et al., 2015). To overcome this problem of local vs. global tracers, the geochemical analysis of sediments from various depositional and geographical settings is necessary. Therefore, our new geochemical data from the Teplá Barrandian black shales represent an important supplement to the existing late Neoproterozoic – early Cambrian dataset. The lack of preservation of Neoproterozoic deep sea sediments, however, excludes conclusions on the deep sea redox-state by geochemical analyses of local proxies. Therefore, geochemical proxies representing global signals are required.

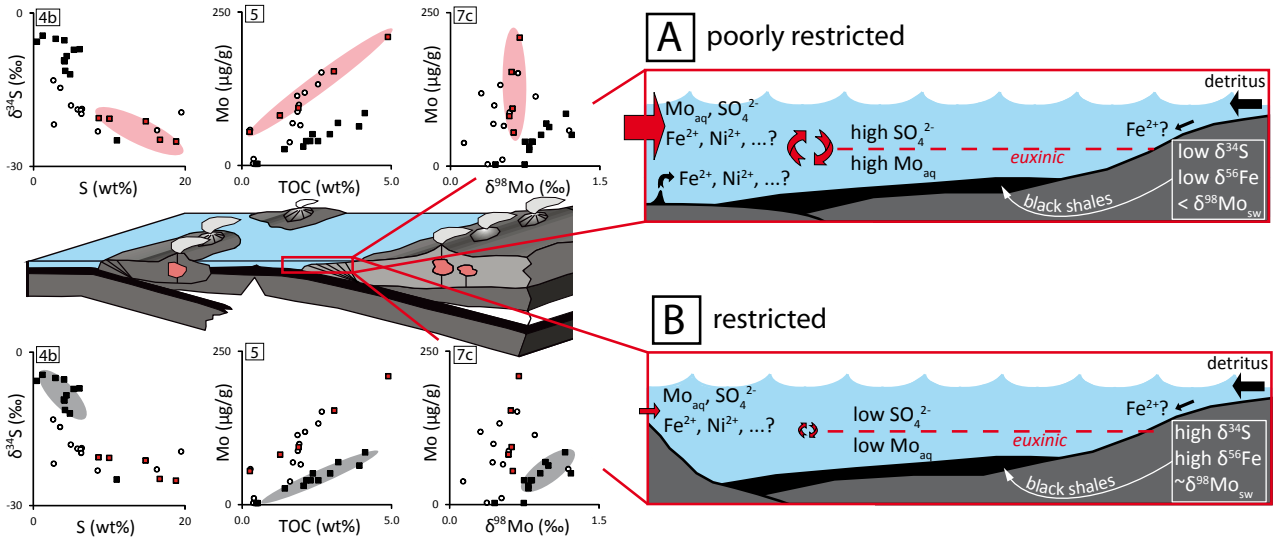

FIGURE 8: Predicted sedimentary setting during poorly restricted (A) and restricted (B) periods. The implications for several geochemical parameters are exemplary demonstrated by the shaded areas on the left side. Restriction could for example result from changes in the ocean circulation pattern and/or from physical changes in the sedimentary environment resulting from tectonic activity.

We agree with Sahoo et al. (2012), who observed modern-like authigenic enrichments of Mo in ~635 Ma old sediments of the Doushantou Formation, South China, that the presence of a significant seawater Mo reservoir is a precondition for strong authigenic enrichments (Sahoo et al., 2012). Such a reservoir involves a globally homogeneous Mo concentration and isotopic composition in seawater. The long mean ocean residence time of molybdenum along with redox-dependent fractionation processes particularly in oxic deep sea settings make Mo isotopes one of the most powerful proxies to trace changes in the global redox state. The formation of Mn-oxides in well oxygenated deep sea settings would cause the removal of isotopically light Mo leaving behind an isotoipically heavier ocean. The resulting increase in δ^{98}Mo values should be preserved in black shales like those analyzed here and in other studies (Arnold et al., 2004; Asael et al., 2013; Dahl et al., 2010; Gordon et al., 2009; Kendall et al., 2009). It has to be kept in mind that lower δ^{98}Mo values could result from fractionation processes, for example during non-quantitative thiomolybdate formation in weakly sulfidic settings. Therefore, maximum δ^{98}Mo values generally apply as the best approximates of the ancient global seawater Mo isotopic composition. Considering the evolution of δ^{98}Mo values from sediments of anoxic environments, the first increase to modern-like high δ^{98}Mo values is observed in sediments from the late Neoproterozoic Member IV of the Doushantuo Formation, South China, which show δ^{98}Mo values up to +2.3 ‰ around 560 Ma (Fig. 9) (Kendall et al., 2015). This value is in contrast to and significantly higher than the seawater δ^{98}Mo value inferred from approximately contemporaneous Teplá-Barrandian black shales presented in this study as well as maximum δ^{98}Mo values inferred from Mid-Proterozoic rocks (Arnold et al., 2004; Kendall et al., 2009).

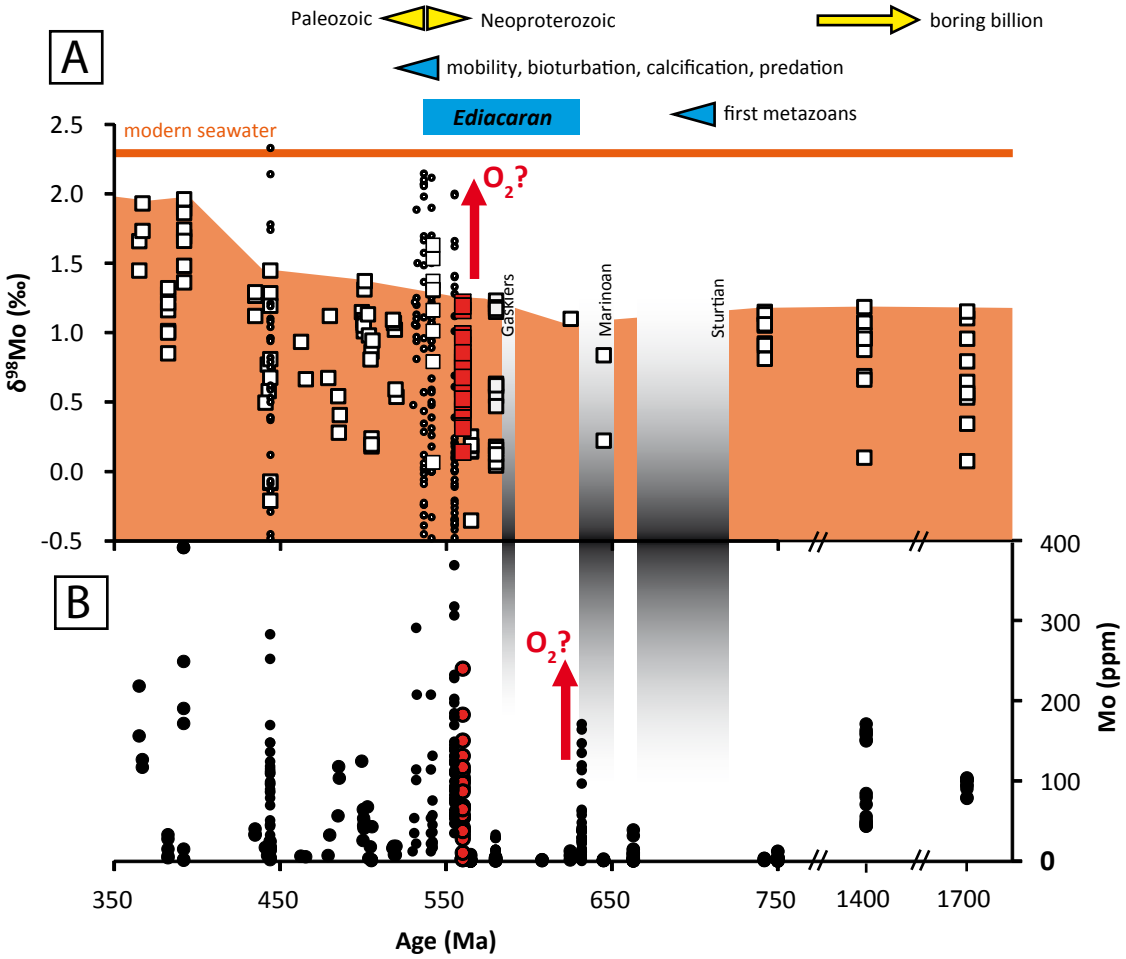

FIGURE 9: δ^{98}Mo values (a) and Mo concentration (b) from the literature (small white circles represent δ^{98}Mo data from Southern China, white squares δ^{98}Mo data from other regions and black circles concentration data, respectively; see Kendall et al., 2015 and references therein) and this study (red squares and red circles, respectively). Glaciations are highlighted by gray shading. Sahoo et al. (2012) proposed an increase in atmospheric O_2 shortly after the Marinoan glaciation based on metal enrichments in black shales, which contrasts with lower enrichments during the „boring billion" between 1.8 to 0.8 Ga. Kendall et al. (2015) argued that deep ocean oxygenation caused high and modern-like δ^{98}Mo values during the Ediacaran at 560 Ma. Interestingly, very high δ^{98}Mo values are mainly from continental margin sediments of Southern China (small white circles) and are closely related to carbon isotope excursions (I.e. Jiang et al., 2007). This could indicate local upwelling environments (Jiang et al., 2007), where the Mo isotope composition of anoxic sediments represents a transient signal (Wille et al., 2008). It is striking that very high δ^{98}Mo values correlate with very low δ^{98}Mo in the same succession, which would be consistent with the modeling of transient Mo isotope signals (Wille et al., 2008). As indicated by the orange area, which reflects maximum δ^{98}Mo values excluding those from sediments of Southern China, globally and modern-like δ^{98}Mo values might be first observed in Devonian sediments (Dahl et al., 2010). This may indicate a delayed deep water oxygenation long after the evolution and diversification of Metazoan life during the Ediacaran.

High Mo isotopic values (2.34 ‰ in δ^{98}Mo) in black shales of the upper Doushantuo Formation, Yangtze Platform, China (560 to 551 Ma) have been interpreted as transient episodes of extensive ocean oxygenation (Kendall et al., 2015). Another transient signal with high δ^{98}Mo values up to 2.15 ‰ were found in slightly younger black shales and phosporite deposits of the lower Niutitang Formation, Yangtze Platform, China (532 Ma) (Chen et al., 2015; Wen et al., 2011; Xu et al., 2012), which was interpreted as evidence for homeostasis of oxic deep oceanic redox conditions (Chen et al., 2015). These black shales (and sulfide ores) also show very high Mo concentrations up to 7.31 wt%, respectively (Xu et al., 2012). Differences in the δ^{13}C record between platform and slope to basinal sections within the Yangtze Platform during the Ediacaran period have been interpreted as evidence for sulfate reduction in anoxic deep oceans and long term deep ocean anoxia/euxinia (Jiang et al., 2007). Carbon isotope anomalies found in both black shale succession (Jiang et al., 2007) with associated transient heavy Mo isotope signals indicate a non-steady state dynamic of reactive DOC and DIC pools (Rothman et al., 2003) possibly triggered by upwelling of DOC rich anoxic/euxinic bottom waters (Jiang et al., 2007). Such an expansion of euxinic shelf settings can cause a transient Mo isotopic signal with temporary heavy isotopic composition (Wille et al., 2008). If transient heavy Mo isotope signals reflect short term changes in the global ocean circulation pattern associated with deep ocean ventilation and oxygenation or local/regional upwelling effects remains therefore elusive. Remarkably, all very high δ^{98}Mo values in pre-Devonian sediments come from Southern China (see small circles in Fig. 9). Moreover, very high δ^{98}Mo values are often in close stratigraphic relationship with very low and negative δ^{98}Mo values, a relation, which is expected during transient δ^{98}Mo excursions (Wille et al., 2008). We, thus, highlight that short term high δ^{98}Mo values do not necessarily represent extensive ocean oxygenation. A very cautious consideration of the local depositional environment is necessary before interpreting the Mo isotope data in black shales.

Again, we agree with Sahoo et al. (2012) that the seawater Mo reservoir established already during Neoproterozoic times but suggest that the main sink of isotopically light Mo in the modern ocean, the adsorption of molybdate on Mn oxides in deep sea settings, remained relatively unimportant. This may have caused the temporal decoupling of high Mo concentrations and long-term high δ^{98}Mo values (Fig. 9). Whereas molybdate is the stable Mo species already at relatively low redox-potentials, the oxidation of Mn^{2+} to Mn^{4+} and the subsequent formation of MnO_2 requires significantly higher redox potential (Takeno, 2005). We argue that such high redox potentials were not accomplished in late Neoproterozoic deep sea settings, as indicated by continuously low δ^{98}Mo values (Fig. 9). The lack of Mn oxide formation in these settings, thus, argues against deep ocean oxygenation as early as the Ediacaran period.

In case of a continuously anoxic deep ocean during Ediacaran times, the question about expected consequences for the biology arises. The modern deep ocean and the deep ocean seabed are characterized by relatively less diverse life forms and slow rates of microbial activity compared to shallow marine shelf settings. The bacterial biomass per square meter of the sea floor decreases exponentially with increasing seafloor depth (Jørgensen and Boetius, 2007; Rowe and Pariente, 2012). Furthermore, no eukaryotic live forms have been observed in modern deep sediment samples (Parkes et al., 2005). Lower biologic activity results from energy limitation (excluding special locations such as black smoker environments) and temperature depression (Jørgensen and Boetius, 2007) and is, thus, controlled by parameters, which

would barely change in a more oxygenated deep water setting. It therefore seems questionable, that deep ocean oxygenation significantly increased the habitable area.

The evolution and diversification of larger animals is rather related to shallow marine water habitats. Life in these areas might have suffered from the occasional upwelling of anoxic (and toxic) deep waters (Chen et al., 2015). Reducing the potential of such upwelling events by full ocean oxygenation could in turn optimize the conditions for life in shallower environments and possibly pave the way for enhanced biological activity (Chen et al., 2015). However, local extinction events can also create free habitable space area and, thus, stimulate new biological innovations.

The formation of larger organic pellets during Ediacaran times would prevent organic matter more efficiently from oxidation and, thus, decrease the oxygen demand in the upper water column (Butterfield, 2009; Lenton et al., 2014). The resulting increased net burial of organic matter then represents a net source for oxygen. Higher oxygen concentrations are a precondition for larger animals (Berner et al., 2003; Falkowski et al., 2005) and the evolution of carnivore life (Sperling et al., 2013). Carnivores might have increased the selection pressures, which further promoted diversification (Bengtson, 2002). Lowering the oxygen demand in surface ocean waters could potentially outcompete reducing marine chemical components and finally also oxygenate the deep ocean. However, we highlight that biologic inventions in surface ocean environments and the deep ocean redox-state are poorly syndetic but both linked to surface ocean oxygenation. The absence of evidence for deep ocean oxygenation during the Ediacaran does therefore not necessarily imply continuously low surface ocean oxygen concentrations. Limited exchange with the deep ocean may have inhibited its concomitant oxygenation. Therefore, it is also possible that the deep ocean oxygenation was decoupled from higher surface ocean redox potentials and major biological evolutions at the Precambrian-Cambrian boundary.

If the net flux of oxygen to the deep sea increased, we suggest that the redox-potential in deep sea settings during the Ediacaran was not high enough to allow pelagic Mn crust formation like in the modern ocean. The continuous increase towards non-transient high δ^{98}Mo values in Devonian black shales (Fig. 9) might then indicate the full oxygenation of the deep ocean (Dahl et al., 2010), possibly as a consequence of the dispersion and expansion of land plants. The higher resistance of land plants against oxygenation and the resulting increased organic matter burial rates may have caused a later pulse of deep water oxygenation (Dahl et al., 2010).

8. Conclusions

Late Neoproterozoic black shales from the Teplá-Barrandian unit, Czech Republic, which have a maximum depositional age of ~560 Ma, were analyzed for main and trace element concentrations as well as for their S, Fe and Mo isotopic composition. We observe temporal variations in the Mo/TOC ratio, which are attributed to changes in Mo_{aq} availability and water circulation restriction. Consistent with

this interpretation, $\delta^{34}S$ values increase from -25 ‰ to -4 ‰ and S concentrations decrease during more restricted periods due to the continuous burial of ^{34}S depleted pyrite in an evolving basin. Black shales deposited during more ventilated periods show strongest authigenic enrichments of metals like Fe, Ni, Cu or Zn. The predominant authigenic Fe phase is pyrite suggesting a euxinic depositional environment. The positive linear relationship of Al/Fe_T vs. $\delta^{56}Fe$ indicates binary mixing of this authigenic Fe in pyrite with low $\delta^{56}Fe$ values (~-0.6 ‰) and detrital Fe with high $\delta^{56}Fe$ values (~0.1 ‰). Anoxic deep seawater in combination with a temporally active local hydrothermal vent could represent the ultimate source for authigenic metal enrichment.

Samples deposited during well-mixed periods show relatively low and constant $\delta^{98}Mo$ values between 0.6 and 0.7 ‰. These values could reflect the Mo isotopic composition of the local hydrothermal source. Alternatively, the non-quantitative Mo removal from seawater in a less restricted basin might have caused slightly lower $\delta^{98}Mo$ values in the sediments compared to the open ocean. Higher $\delta^{98}Mo$ values of up to 1.2 ‰ are the result of near quantitative Mo removal during more restricted periods and represent our best estimate of the late Neoproterozoic seawater Mo isotopic composition. The value of 1.2 ‰ is in the range of $\delta^{98}Mo$ values of black shales from the middle Proterozoic. This invariance might indicate the continuous absence of (1) Mn oxide formation in deep sea settings, (2) the absence of large Mo isotope fractionations during adsorption onto Mn oxides and (3) the build-up of a heavier seawater Mo reservoir. In line with previous studies, the Mo isotopic composition of black shales from the Teplá-Barrandian unit consistently suggests that the deep ocean was still decoupled from oxygenation and remained largely anoxic, and ferruginous until at least ~560 Ma. These conditions may only have changed during another oxygenation event in Devonian times (Dahl et al., 2010).

9. References

Algeo, T.J., Lyons, T.W., 2006. Mo–total organic carbon covariation in modern anoxic marine environments: Implications for analysis of paleoredox and paleohydrographic conditions. Paleoceanography 21.

Alt, J.C., 1995. Sulfur isotopic profile through the oceanic crust: sulfur mobility and seawater-crustal sulfur exchange during hydrothermal alteration. Geology 23, 585-588.

Archer, C., Vance, D., 2008. The isotopic signature of the global riverine molybdenum flux and anoxia in the ancient oceans. Nature Geoscience 1, 597-600.

Arnold, G.L., Anbar, A., Barling, J., Lyons, T., 2004. Molybdenum isotope evidence for widespread anoxia in mid-Proterozoic oceans. Science 304, 87-90.

Asael, D., Tissot, F.L., Reinhard, C.T., Rouxel, O., Dauphas, N., Lyons, T.W., Ponzevera, E., Liorzou, C., Chéron, S., 2013. Coupled molybdenum, iron and uranium stable isotopes as oceanic paleoredox proxies during the Paleoproterozoic Shunga Event. Chemical Geology 362, 193-210.

Barling, J., Anbar, A., 2004. Molybdenum isotope fractionation during adsorption by manganese oxides. Earth and Planetary Science Letters 217, 315-329.

Barling, J., Arnold, G.L., Anbar, A., 2001. Natural mass-dependent variations in the isotopic composition of molybdenum. Earth and Planetary Science Letters 193, 447-457.

Beard, B.L., Johnson, C.M., 2004. Fe isotope variations in the modern and ancient earth and other planetary bodies. Reviews in Mineralogy and Geochemistry 55, 319-357.

Beard, B.L., Johnson, C.M., Von Damm, K.L., Poulson, R.L., 2003. Iron isotope constraints on Fe cycling and mass balance in oxygenated Earth oceans. Geology 31, 629-632.

Bengtson, S., 2002. Origins and early evolution of predation. Paleontological Society Papers 8, 289-318.

Bengtson, S., Zhao, Y., 1992. Predatorial borings in late Precambrian mineralized exoskeletons. Science 257, 367-369.

Berner, R.A., Beerling, D.J., Dudley, R., Robinson, J.M., Wildman Jr, R.A., 2003. Phanerozoic atmospheric oxygen. Annual Review of Earth and Planetary Sciences 31, 105-134.

Böttcher, M.E., Ferdelman, T.G., Jørgensen, B.B., Blake, R.E., Surkov, A.V., Claypool, G.E., 2006. Sulfur isotope fractionation by the deep biosphere within sediments of the eastern equatorial Pacific and Peru margin, Proceedings of the Ocean Drilling Program, Scientific Results, pp. 1-21.

Butler, I.B., Archer, C., Vance, D., Oldroyd, A., Rickard, D., 2005. Fe isotope fractionation on FeS formation in ambient aqueous solution. Earth and Planetary Science Letters 236, 430-442.

Butterfield, N., 2009. Oxygen, animals and oceanic ventilation: an alternative view. Geobiology 7, 1-7.

Campbell, I.H., Squire, R.J., 2010. The mountains that triggered the Late Neoproterozoic increase in oxygen: the Second Great Oxidation Event. Geochimica et Cosmochimica Acta 74, 4187-4206.

Canfield, D.E., Poulton, S.W., Narbonne, G.M., 2007. Late-Neoproterozoic deep-ocean oxygenation and the rise of animal life. Science 315, 92-95.

Canfield, D.E., Teske, A., 1996. Late Proterozoic rise in atmospheric oxygen concentration inferred from phylogenetic and sulphur-isotope studies. Nature 382, 127-132.

Canfield, D.E., Thamdrup, B., 1994. The production of 34S-depleted sulfide during bacterial disproportionation of elemental sulfur. Science 266, 1973-1975.

Chen, X., Ling, H.-F., Vance, D., Shields-Zhou, G.A., Zhu, M., Poulton, S.W., Och, L.M., Jiang, S.-Y., Li, D., Cremonese, L., 2015. Rise to modern levels of ocean oxygenation coincided with the Cambrian radiation of animals. Nature communications 6.

Chester, R., 2009. Marine geochemistry. John Wiley & Sons.

Compston, W., Oversby, V., 1969. Lead isotopic analysis using a double spike. Journal of Geophysical Research 74, 4338-4348.

Dahl, T.W., Hammarlund, E.U., Anbar, A.D., Bond, D.P., Gill, B.C., Gordon, G.W., Knoll, A.H., Nielsen, A.T., Schovsbo, N.H., Canfield, D.E., 2010. Devonian rise in atmospheric oxygen correlated to the radiations of terrestrial plants and large predatory fish. Proceedings of the National Academy of Sciences 107, 17911-17915.

Dallmeyer, R.D., Franke, W., Weber, K., 1995. Pre-Permian geology of central and eastern Europe. Springer.

Dauphas, N., Rouxel, O., 2006. Mass spectrometry and natural variations of iron isotopes. Mass Spectrometry Reviews 25, 515-550.

de Laeter, J.R., Böhlke, J.K., De Bièvre, P., Hidaka, H., Peiser, H., Rosman, K., Taylor, P., 2003. Atomic weights of the elements. Review 2000 (IUPAC Technical Report). Pure and Applied Chemistry 75, 683-800.

Dickinson, W.R., Gehrels, G.E., 2009. Use of U–Pb ages of detrital zircons to infer maximum depositional ages of strata: a test against a Colorado Plateau Mesozoic database. Earth and Planetary Science Letters 288, 115-125.

Drost, K., 2008. Sources and geotectonic setting of Late Neoproterozoic, Early Palaeozoic volcano-sedimentary successions of the Teplá-Barrandian unit (Bohemian Massif): evidence from petrographical, geochemical, and isotope analyses. Geologica saxonica 54, 1-165.

Drost, K., Gerdes, A., Jeffries, T., Linnemann, U., Storey, C., 2011. Provenance of Neoproterozoic and early Paleozoic siliciclastic rocks of the Teplá-Barrandian unit (Bohemian Massif): evidence from U–Pb detrital zircon ages. Gondwana Research 19, 213-231.

Drost, K., Romer, R.L., Linnemann, U., Fatka, O., Kraft, P., Marek, J., 2007. Nd-Sr-Pb isotopic signatures of Neoproterozoic–Early Paleozoic siliciclastic rocks in response to changing geotectonic regimes: A case study from the Barrandian area (Bohemian Massif, Czech Republic). Geological Society of America Special

Papers 423, 191-208.

Falkowski, P.G., Katz, M.E., Milligan, A.J., Fennel, K., Cramer, B.S., Aubry, M.P., Berner, R.A., Novacek, M.J., Zapol, W.M., 2005. The rise of oxygen over the past 205 million years and the evolution of large placental mammals. Science 309, 2202-2204.

Fehr, M.A., Andersson, P.S., Hålenius, U., Mörth, C.-M., 2008. Iron isotope variations in Holocene sediments of the Gotland Deep, Baltic Sea. Geochimica et Cosmochimica Acta 72, 807-826.

Feng, L., Li, C., Huang, J., Chang, H., Chu, X., 2014. A sulfate control on marine mid-depth euxinia on the early Cambrian (ca. 529–521Ma) Yangtze platform, South China. Precambrian Research 246, 123-133.

Fike, D., Grotzinger, J., Pratt, L., Summons, R., 2006. Oxidation of the Ediacaran ocean. Nature 444, 744-747.

Frei, R., Gaucher, C., Poulton, S.W., Canfield, D.E., 2009. Fluctuations in Precambrian atmospheric oxygenation recorded by chromium isotopes. Nature 461, 250-253.

Gamo, T., Okamura, K., Charlou, J.-L., Urabe, T., Auzende, J.-M., Ishibashi, J., Shitashima, K., Chiba, H., 1997. Acidic and sulfate-rich hydrothermal fluids from the Manus back-arc basin, Papua New Guinea. Geology 25, 139-142.

Goldberg, T., Gordon, G., Izon, G., Archer, C., Pearce, C.R., McManus, J., Anbar, A.D., Rehkämper, M., 2013. Resolution of inter-laboratory discrepancies in Mo isotope data: an intercalibration. J. Anal. At. Spectrom. 28, 724-735.

Goldberg, T., Strauss, H., Guo, Q., Liu, C., 2007. Reconstructing marine redox conditions for the Early Cambrian Yangtze Platform: evidence from biogenic sulphur and organic carbon isotopes. Palaeogeography, Palaeoclimatology, Palaeoecology 254, 175-193.

Gordon, G., Lyons, T., Arnold, G.L., Roe, J., Sageman, B., Anbar, A., 2009. When do black shales tell molybdenum isotope tales? Geology 37, 535-538.

Greber, N.D., Pettke, T., Nägler, T.F., 2014. Magmatic–hydrothermal molybdenum isotope fractionation and its relevance to the igneous crustal signature. Lithos 190, 104-110.

Greber, N.D., Siebert, C., Nägler, T.F., Pettke, T., 2012. δ98/95Mo values and molybdenum concentration data for NIST SRM 610, 612 and 3134: towards a common protocol for reporting Mo data. Geostandards and Geoanalytical Research 36, 291-300.

Grotzinger, J.P., Watters, W.A., Knoll, A.H., 2000. Calcified metazoans in thrombolite-stromatolite reefs of the terminal Proterozoic Nama Group, Namibia. Journal Information 26.

Guilbaud, R., Butler, I.B., Ellam, R.M., 2011. Abiotic pyrite formation produces a large Fe isotope fractionation. Science 332, 1548-1551.

Hajná, J., Žák, J., Kachlík, V., 2014. Growth of accretionary wedges and pulsed ophiolitic mélange formation by successive subduction of trench-parallel volcanic elevations. Terra Nova 26, 322-329.

Hajná, J., Žák, J., Kachlík, V., Dörr, W., Gerdes, A., 2013. Neoproterozoic to early Cambrian Franciscan-type mélanges in the Teplá–Barrandian unit, Bohemian Massif: Evidence of modern-style accretionary processes along the Cadomian active margin of Gondwana? Precambrian Research 224, 653-670.

Helz, G., Miller, C., Charnock, J., Mosselmans, J., Pattrick, R., Garner, C., Vaughan, D., 1996. Mechanism of molybdenum removal from the sea and its concentration in black shales: EXAFS evidence. Geochimica et Cosmochimica Acta 60, 3631-3642.

Helz, G.R., Bura-Nakić, E., Mikac, N., Ciglenečki, I., 2011. New model for molybdenum behavior in euxinic waters. Chemical Geology 284, 323-332.

Herzig, P., Hannington, M., Arribas Jr, A., 1998. Sulfur isotopic composition of hydrothermal precipitates from the Lau back-arc: implications for magmatic contributions to seafloor hydrothermal systems. Mineralium Deposita 33, 226-237.

Hoffman, P.F., 1991. Did the breakout of Laurentia turn Gondwanaland inside-out. Science 252, 1409-1412.

Hoffman, P.F., Kaufman, A.J., Halverson, G.P., Schrag, D.P., 1998. A Neoproterozoic snowball earth. Science 281, 1342-1346.

Hurtgen, M.T., Arthur, M.A., Suits, N.S., Kaufman, A.J., 2002. The sulfur isotopic composition of Neoproterozoic seawater sulfate: implications for a snowball Earth? Earth and Planetary Science Letters 203, 413-429.

Jackson, S.E., Pearson, N.J., Griffin, W.L., Belousova, E.A., 2004. The application of laser ablation-inductively coupled plasma-mass spectrometry to in situ U–Pb zircon geochronology. Chemical Geology 211, 47-69.

Jiang, G., Kaufman, A.J., Christie-Blick, N., Zhang, S., Wu, H., 2007. Carbon isotope variability across the Ediacaran Yangtze platform in South China: Implications for a large surface-to-deep ocean δ13C gradient. Earth and Planetary Science Letters 261, 303-320.

Johnson, C.M., Beard, B.L., Klein, C., Beukes, N.J., Roden, E.E., 2008a. Iron isotopes constrain biologic and abiologic processes in banded iron formation genesis. Geochimica et Cosmochimica Acta 72, 151-169.

Johnson, C.M., Beard, B.L., Roden, E.E., 2008b. The iron isotope fingerprints of redox and biogeochemical cycling in modern and ancient Earth. Annu. Rev. Earth Planet. Sci. 36, 457-493.

Jørgensen, B.B., 1990. A thiosulfate shunt in the sulfur cycle of marine sediments. Science 249, 152-154.

Jørgensen, B.B., Boetius, A., 2007. Feast and famine—microbial life in the deep-sea bed. Nature Reviews Microbiology 5, 770-781.

Kashiwabara, T., Takahashi, Y., Tanimizu, M., Usui, A., 2011. Molecular-scale mechanisms of distribution and isotopic fractionation of molybdenum between seawater and ferromanganese oxides. Geochimica et Cosmochimica Acta 75, 5762-5784.

Kaufman, A.J., Knoll, A.H., Narbonne, G.M., 1997. Isotopes, ice ages, and terminal Proterozoic earth history. Proceedings of the National Academy of Sciences 94, 6600-6605.

Kendall, B., Creaser, R.A., Gordon, G.W., Anbar, A.D., 2009. Re–Os and Mo isotope systematics of black shales from the Middle Proterozoic Velkerri and Wollogorang formations, McArthur Basin, northern Australia. Geochimica et Cosmochimica Acta 73, 2534-2558.

Kendall, B., Gordon, G.W., Poulton, S.W., Anbar, A.D., 2011. Molybdenum isotope constraints on the extent of late Paleoproterozoic ocean euxinia. Earth and Planetary Science Letters 307, 450-460.

Kendall, B., Komiya, T., Lyons, T.W., Bates, S.M., Gordon, G.W., Romaniello, S.J., Jiang, G., Creaser, R.A., Xiao, S., McFadden, K., 2015. Uranium and molybdenum isotope evidence for an episode of widespread ocean oxygenation during the late Ediacaran Period. Geochimica et Cosmochimica Acta 156, 173-193.

Kendall, B., Reinhard, C.T., Lyons, T.W., Kaufman, A.J., Poulton, S.W., Anbar, A.D., 2010. Pervasive oxygenation along late Archaean ocean margins. Nature Geoscience 3, 647-652.

Kennedy, M., Droser, M., Mayer, L.M., Pevear, D., Mrofka, D., 2006. Late Precambrian oxygenation; inception of the clay mineral factory. Science 311, 1446-1449.

Kennedy, M.J., Runnegar, B., Prave, A.R., Hoffmann, K.-H., Arthur, M.A., 1998. Two or four Neoproterozoic glaciations? Geology 26, 1059-1063.

Knoll, A.H., Carroll, S.B., 1999. Early animal evolution: emerging views from comparative biology and geology. Science 284, 2129-2137.

Košler, J., Sylvester, P.J., 2003. Present trends and the future of zircon in geochronology: laser ablation ICPMS. Reviews in mineralogy and geochemistry 53, 243-275.

Kurzweil, F., Wille, M., Schoenberg, R., Taubald, H., Van Kranendonk, M.J., 2015. Continuously increasing δ 98 Mo values in Neoarchean black shales and iron formations from the Hamersley Basin. Geochimica et Cosmochimica Acta.

Lehmann, B., Nägler, T.F., Holland, H.D., Wille, M., Mao, J., Pan, J., Ma, D., Dulski, P., 2007. Highly metalliferous carbonaceous shale and Early Cambrian seawater. Geology 35, 403-406.

Lenton, T.M., Boyle, R.A., Poulton, S.W., Shields-Zhou, G.A., Butterfield, N.J., 2014. Co-evolution of eukaryotes and ocean oxygenation in the Neoproterozoic era. Nature Geoscience 7, 257-265.

Li, Z.-X., Bogdanova, S., Collins, A.S., Davidson, A., De Waele, B., Ernst, R., Fitzsimons, I.C., Fuck, R., Gladkochub, D., Jacobs, J., 2008. Assembly, configuration, and break-up history of Rodinia: a synthesis. Precambrian Research 160, 179-210.

Linnemann, U., Romer, R., Pin, C., Aleksandrowski, P., Bula, Z., Geisler, T., Kachlik, V., Krzeminska, E.,

Mazur, S., Motuza, G., 2008. Precambrian, in: McCann, T. (Ed.), The geology of Central Europe Volume 1: Precambrian and Paleozoic, Geological Society, London, pp. 21-101.

Love, G.D., Grosjean, E., Stalvies, C., Fike, D.A., Grotzinger, J.P., Bradley, A.S., Kelly, A.E., Bhatia, M., Meredith, W., Snape, C.E., 2009. Fossil steroids record the appearance of Demospongiae during the Cryogenian period. Nature 457, 718-721.

Ludwig, 2012. User's manual for Isoplot 3.75. Berkeley Geochronology Center Special Publication 5, 1-75.

Maréchal, C.N., Télouk, P., Albarède, F., 1999. Precise analysis of copper and zinc isotopic compositions by plasma-source mass spectrometry. Chemical Geology 156, 251-273.

Martin, M., Grazhdankin, D., Bowring, S., Evans, D.A.D., Fedonkin, M., Kirschvink, J., 2000. Age of Neoproterozoic bilatarian body and trace fossils, White Sea, Russia: Implications for metazoan evolution. Science 288, 841-845.

Mazur, S., Aleksandrowski, P., Szczepański, J., 2005. The presumed Tepla-Barrandian/Moldanubian terrane boundary in the Orlica Mountains (Sudetes, Bohemian Massif): structural and petrological characteristics. Lithos 82, 85-112.

McManus, J., Berelson, W.M., Severmann, S., Poulson, R.L., Hammond, D.E., Klinkhammer, G.P., Holm, C., 2006. Molybdenum and uranium geochemistry in continental margin sediments: paleoproxy potential. Geochimica et Cosmochimica Acta 70, 4643-4662.

Miller, C.A., Peucker-Ehrenbrink, B., Walker, B.D., Marcantonio, F., 2011. Re-assessing the surface cycling of molybdenum and rhenium. Geochimica et Cosmochimica Acta 75, 7146-7179.

Mills, D.B., Canfield, D.E., 2014. Oxygen and animal evolution: Did a rise of atmospheric oxygen "trigger" the origin of animals? BioEssays 36, 1145-1155.

Moeller, K., Schoenberg, R., Grenne, T., Thorseth, I.H., Drost, K., Pedersen, R.B., 2014. Comparison of iron isotope variations in modern and Ordovician siliceous Fe oxyhydroxide deposits. Geochimica et Cosmochimica Acta 126, 422-440.

Morford, J.L., Emerson, S., 1999. The geochemistry of redox sensitive trace metals in sediments. Geochimica et Cosmochimica Acta 63, 1735-1750.

Nägler, T., Neubert, N., Böttcher, M., Dellwig, O., Schnetger, B., 2011. Molybdenum isotope fractionation in pelagic euxinia: Evidence from the modern Black and Baltic Seas. Chemical Geology 289, 1-11.

Nägler, T.F., Anbar, A.D., Archer, C., Goldberg, T., Gordon, G.W., Greber, N.D., Siebert, C., Sohrin, Y., Vance, D., 2014. Proposal for an international molybdenum isotope measurement standard and data representation. Geostandards and Geoanalytical Research 38, 149-151.

Neubert, N., Nägler, T.F., Böttcher, M.E., 2008. Sulfidity controls molybdenum isotope fractionation into euxinic sediments: Evidence from the modern Black Sea. Geology 36, 775-778.

Noordmann, J., Weyer, S., Montoya-Pino, C., Dellwig, O., Neubert, N., Eckert, S., Paetzel, M., Böttcher, M., 2015. Uranium and molybdenum isotope systematics in modern euxinic basins: Case studies from the central Baltic Sea and the Kyllaren fjord (Norway). Chemical Geology 396, 182-195.

Och, L.M., Shields-Zhou, G.A., 2012. The Neoproterozoic oxygenation event: environmental perturbations and biogeochemical cycling. Earth-Science Reviews 110, 26-57.

Parkes, R.J., Webster, G., Cragg, B.A., Weightman, A.J., Newberry, C.J., Ferdelman, T.G., Kallmeyer, J., Jørgensen, B.B., Aiello, I.W., Fry, J.C., 2005. Deep sub-seafloor prokaryotes stimulated at interfaces over geological time. Nature 436, 390-394.

Pašava, J., Amov, B., 1993. Isotopic composition of lead in Proterozoic anoxic metasedimentary and volcanogenic rocks from the Bohemian Massif (Czech Republic) with metallogenetic implications. Chemical geology 109, 293-304.

Pašava, J., Hladikova, J., Dobes, P., 1996. Origin of Proterozoic metal-rich black shales from the Bohemian Massif, Czech Republic. Economic Geology 91, 63-79.

Pašava, J., Sulovsky, P., Kovalova, M., 1993. Geochemistry and mineralogy of Proterozoic metal-rich black shales from the Bohemian Massif, Czech Republic, with a description of possible new molybdenum selenide and telluride phases. The Canadian Mineralogist 31, 745-754.

Pin, C., Waldhausrová, J., 2007. Sm-Nd isotope and trace element study of Late Proterozoic metabasalts ("spilites") from the Central Barrandian domain (Bohemian Massif, Czech Republic). Geological Society of America Special Papers 423, 231-247.

Poulson Brucker, R.L., McManus, J., Severmann, S., Berelson, W.M., 2009. Molybdenum behavior during early diagenesis: Insights from Mo isotopes. Geochemistry, Geophysics, Geosystems 10.

Poulson, R.L., Siebert, C., McManus, J., Berelson, W.M., 2006. Authigenic molybdenum isotope signatures in marine sediments. Geology 34, 617-620.

Raiswell, R., Canfield, D., Berner, R., 1994. A comparison of iron extraction methods for the determination of degree of pyritisation and the recognition of iron-limited pyrite formation. Chemical Geology 111, 101-110.

Rempel, K.U., Williams-Jones, A.E., Migdisov, A.A., 2009. The partitioning of molybdenum (VI) between aqueous liquid and vapour at temperatures up to 370 C. Geochimica et Cosmochimica Acta 73, 3381-3392.

Rothman, D.H., Hayes, J.M., Summons, R.E., 2003. Dynamics of the Neoproterozoic carbon cycle. Proceedings of the National Academy of Sciences 100, 8124-8129.

Rowe, G.T., Pariente, V., 2012. Deep-sea food chains and the global carbon cycle. Springer Science & Business Media.

Sahoo, S.K., Planavsky, N.J., Kendall, B., Wang, X., Shi, X., Scott, C., Anbar, A.D., Lyons, T.W., Jiang, G., 2012. Ocean oxygenation in the wake of the Marinoan glaciation. Nature 489, 546-549.

Schoenberg, R., von Blanckenburg, F., 2005. An assessment of the accuracy of stable Fe isotope ratio measurements on samples with organic and inorganic matrices by high-resolution multicollector ICP-MS. International Journal of Mass Spectrometry 242, 257-272.

Schoenberg, R., von Blanckenburg, F., 2006. Modes of planetary-scale Fe isotope fractionation. Earth and Planetary Science Letters 252, 342-359.

Scott, C., Lyons, T., Bekker, A., Shen, Y., Poulton, S., Chu, X., Anbar, A., 2008. Tracing the stepwise oxygenation of the Proterozoic ocean. Nature 452, 456-459.

Seal, R.R., 2006. Sulfur isotope geochemistry of sulfide minerals. Reviews in mineralogy and geochemistry 61, 633-677.

Severmann, S., Lyons, T.W., Anbar, A., McManus, J., Gordon, G., 2008. Modern iron isotope perspective on the benthic iron shuttle and the redox evolution of ancient oceans. Geology 36, 487-490.

Sharma, M., Polizzotto, M., Anbar, A., 2001. Iron isotopes in hot springs along the Juan de Fuca Ridge. Earth and Planetary Science Letters 194, 39-51.

Siebert, C., McManus, J., Bice, A., Poulson, R., Berelson, W.M., 2006. Molybdenum isotope signatures in continental margin marine sediments. Earth and Planetary Science Letters 241, 723-733.

Siebert, C., Nägler, T.F., von Blanckenburg, F., Kramers, J.D., 2003. Molybdenum isotope records as a potential new proxy for paleoceanography. Earth and Planetary Science Letters 211, 159-171.

Sláma, J., Dunkley, D.J., Kachlík, V., Kusiak, M.A., 2008a. Transition from island-arc to passive setting on the continental margin of Gondwana: U–Pb zircon dating of Neoproterozoic metaconglomerates from the SE margin of the Teplá–Barrandian Unit, Bohemian Massif. Tectonophysics 461, 44-59.

Sláma, J., Košler, J., Condon, D.J., Crowley, J.L., Gerdes, A., Hanchar, J.M., Horstwood, M.S., Morris, G.A., Nasdala, L., Norberg, N., 2008b. Plešovice zircon—a new natural reference material for U–Pb and Hf isotopic microanalysis. Chemical Geology 249, 1-35.

Sperling, E.A., Frieder, C.A., Raman, A.V., Girguis, P.R., Levin, L.A., Knoll, A.H., 2013. Oxygen, ecology, and the Cambrian radiation of animals. Proceedings of the National Academy of Sciences 110, 13446-13451.

Strauss, H., 1993. The sulfur isotopic record of Precambrian sulfates: new data and a critical evaluation of the existing record. Precambrian research 63, 225-246.

Swanner E.D., Wu W., Schoenberg R., Byrne J., Michel M.F., Pan Y., Kappler A., 2015. Fractionation of Fe isotopes during Fe(II) oxidation by marine photoferrotroph is controlled by the formation of organic Fe-complexes and colloidal Fe fractions. Geochimica et Cosmochimica Acta 165, 44-61.

Takeno, N., 2005. Atlas of Eh-pH diagrams. Geological survey of Japan open file report, 102.

Taylor, S.R., McLennan, S.M., 1985. The continental crust: its composition and evolution.

Timmermann, H., Dörr, W., Krenn, E., Finger, F., Zulauf, G., 2006. Conventional and in situ geochronology of the Teplá Crystalline unit, Bohemian Massif: implications for the processes involving monazite formation. International Journal of Earth Sciences 95, 629-647.

Timmermann, H., Štědrá, V., Gerdes, A., Noble, S., Parrish, R., Dörr, W., 2004. The problem of dating high-pressure metamorphism: a U–Pb isotope and geochemical study on eclogites and related rocks of the Mariánské Lázně Complex, Czech Republic. Journal of Petrology 45, 1311-1338.

Tossell, J., 2005. Calculating the partitioning of the isotopes of Mo between oxidic and sulfidic species in aqueous solution. Geochimica et Cosmochimica Acta 69, 2981-2993.

Tribovillard, N., Riboulleau, A., Lyons, T., Baudin, F., 2004. Enhanced trapping of molybdenum by sulfurized marine organic matter of marine origin in Mesozoic limestones and shales. Chemical Geology 213, 385-401.

Vermeesch, P., 2012. On the visualisation of detrital age distributions. Chemical Geology 312, 190-194.

Voegelin, A.R., Pettke, T., Greber, N.D., von Niederhäusern, B., Nägler, T.F., 2014. Magma differentiation fractionates Mo isotope ratios: Evidence from the Kos Plateau Tuff (Aegean Arc). Lithos 190, 440-448.

Wang, J., Chen, D., Yan, D., Wei, H., Xiang, L., 2012. Evolution from an anoxic to oxic deep ocean during the Ediacaran–Cambrian transition and implications for bioradiation. Chemical Geology 306, 129-138.

Wen, H., Carignan, J., Zhang, Y., Fan, H., Cloquet, C., Liu, S., 2011. Molybdenum isotopic records across the Precambrian-Cambrian boundary. Geology 39, 775-778.

Weyer, S., Schwieters, J., 2003. High precision Fe isotope measurements with high mass resolution MC-ICPMS. International Journal of Mass Spectrometry 226, 355-368.

Wheat, C.G., Mottl, M.J., Rudnicki, M., 2002. Trace element and REE composition of a low-temperature ridge-flank hydrothermal spring. Geochimica et Cosmochimica Acta 66, 3693-3705.

Wiedenbeck, M., Alle, P., Corfu, F., Griffin, W., Meier, M., Oberli, F., Quadt, A.v., Roddick, J., Spiegel, W., 1995. Three natural zircon standards for U-Th-Pb, Lu-Hf, trace element and REE analyses. Geostandards newsletter 19, 1-23.

Wille, M., Nägler, T.F., Lehmann, B., Schröder, S., Kramers, J.D., 2008. Hydrogen sulphide release to surface waters at the Precambrian/Cambrian boundary. Nature 453, 767-769.

Wood, R., Poulton, S., Prave, A., Hoffmann, K.-H., Clarkson, M., Guilbaud, R., Lyne, J., Tostevin, R., Bowyer, F., Penny, A., 2015. Dynamic redox conditions control late Ediacaran metazoan ecosystems in the Nama Group, Namibia. Precambrian Research 261, 252-271.

Xu, L., Lehmann, B., Mao, J., Nägler, T.F., Neubert, N., Böttcher, M.E., Escher, P., 2012. Mo isotope and trace element patterns of Lower Cambrian black shales in South China: Multi-proxy constraints on the paleoenvironment. Chemical Geology 318, 45-59.

Yin, L., Zhu, M., Knoll, A.H., Yuan, X., Zhang, J., Hu, J., 2007. Doushantuo embryos preserved inside diapause egg cysts. Nature 446, 661-663.

Zulauf, G., Schitter, F., Riegler, G., Finger, F., Fiala, J., Vejnar, Z., 1999. Age constraints on the Cadomian evolution of the Teplá Barrandian unit (Bohemian Massif) through electron microprobe dating of metamorphic monazite. Zeitschrift der deutschen geologischen Gesellschaft, 627-639.

Appendix

Supplements of CHAPTER III

1. Pyrite formation and Iron isotope systematics

Pyrite is the predominant authigenic Fe-mineral phase in the black shales of the Hromnice and Kamenec boreholes (Pašava et al., 1996). The hydrothermal and marine cycles of Fe, S and Mo are strongly linked to authigenic pyrite formation. Pyrite, therefore, represents a key mineral component in a S-Fe-Mo-isotope study and as such demands a detailed investigation of its formation mechanism and associated fractionation processes. In our samples pyrite appears as anhedral grains and in framboidal form (Pašava et al., 1996). The larger grains and grainy aggregates are associated with quartz-carbonate veinlets and have been interpreted as post-depositional recrystallization products of framboidal pyrite (Pašava et al., 1993). In contrast, the more abundant framboidal pyrite represents a syn- to early diagenetic mineral phase (Wilkin and Barnes, 1997). Its formation involves the rapid nucleation of tetragonal mackinawite (FeS) from an anoxic solution that is supersaturated in Fe^{2+} and H_2S (Butler and Rickard, 2000; Wilkin and Barnes, 1997). The subsequent contemporary diffusional growth may cause a raspberry like texture

of similar sized framboids. Mackinawite formation is accompanied by a kinetic Fe-isotope fractionation with $\Delta^{56}Fe_{Fe(II)\text{-}FeS}$ = 0.85 ± 0.3 ‰ for zero age FeS at pH 4 (Butler et al., 2005). During aging the isotopic difference becomes significantly smaller and might get close to equilibrium with $\Delta^{56}Fe_{Fe(II)\text{-}FeS}$ < -0.34 ‰ as a consequence of continuous isotope exchange between iron in solution and iron in the surface layer of mackinawite (e.g. Butler et al., 2005). Wu et al. (2012) concluded that at higher (near neutral) pH the diffusional growth of mackinawite is slow enough to generally allow Fe isotopic equilibration causing an isotopic difference of $\Delta^{56}Fe_{Fe(II)\text{-}FeS}$ = 0.32 ± 0.29 ‰. However, isotopic equilibration is not attained, if the diffusional growth of mackinawite is fast, which can cause a larger difference between the Fe isotopic composition of the mineral and the solution (Guilbaud et al., 2010).

In a subsequent step, pyrite may form via two different pathways from redissolved mackinawite.

(1) $FeS_{(aq)} + S_n^{2-} = FeS_2 + S_{2-n}^{-1}$; polysulfide pathway (i.e. Schoonen and Barnes, 1991)
(2) $FeS_{(aq)} + H_2S = FeS_2 + H_2$; H_2S pathway (i.e. Rickard and Luther III, 1997)

In sulfidic environments the latter reaction pathway is predominant due to higher abundance of H_2S relative to $S^{-2}_{(aq)}$ species (Rickard and Luther, 2007). The initial step of mackinawite dissolution probably causes negligible isotope fractionation as Fe remains in the same redox state as well as in tetrahedral coordination (Guilbaud et al., 2011). However, Fe in pyrite is octahedrally coordinated. According to quantum mechanical insights, lighter isotopes preferentially partition into higher coordination numbers (Bigeleisen and Mayer, 1947). This might explain the experimentally determined kinetic isotope fractionation factor of $\alpha Fe(II)\text{-}FeS_2$ = 1.0022 ±0.0007 at temperatures of 40-100 °C (Guilbaud et al., 2011), which would result in strong depletion of heavy Fe isotopes in pyrite. Conflicting with this observation, experiments at high temperatures (300-350 °C) and high pressures (500 bars) predict equilibrium Fe-isotope fractionations in opposite direction with a difference of $\Delta^{56}Fe_{Fe(II)\text{-}FeS2}$ = -0.99 ± 0.29 ‰ (Syverson et al., 2013). These experimental results are consistent with theoretical calculations and spectral data from Mössbauer spectroscopy and inelastic resonant X-ray scattering, which also predict enrichment of heavy Fe-isotopes in the sulfide phase (Polyakov et al., 2007; Schauble et al., 2001). The disputed results and predictions of Fe isotope fractionation during pyrite formation remain controversial and apparently vary under different environmental conditions. The pyrite fraction in modern anoxic sediments generally shows negative $\delta^{56}Fe$ values (Busigny et al., 2014; Severmann et al., 2006; Severmann et al., 2008) confirming the experimental results of Guilbaud et al. (2011). Similarly, in modern high temperature environments like hydrothermal deposits and massive sulfides pyrite also shows lower $\delta^{56}Fe$ values compared to the hydrothermal fluid (Rouxel et al., 2004; Rouxel et al., 2008). Such deposits seem most appropriate for comparison with the sulfide-rich black shales from the Teplá-Barrandian unit. Importantly, the effects of Fe isotope fractionations will only be preserved in the sedimentary record, if the removal of dissolved Fe(II) is incomplete with a remaining dissolved Fe reservoir. If pyrite formation is limited by $Fe(II)_{aq}$ availability in a H_2S_{aq} supersaturated environment, we expect little net Fe isotope fractionation effects.

2. Fe-mixing model

We calculated a two component Fe mixing model (Fig. APPENDIX-III-1) using the following parameters: (1) a detrital $\delta^{56}Fe$ of +0.05 ‰ as indicated by detritus dominated samples HRM-3-161 and HRM-3-216. Such a value is in line with $\delta^{56}Fe$ of the modern detrital input and terrestrial igneous rocks (Beard et al., 2003; Dauphas and Rouxel, 2006; Schoenberg and von Blanckenburg, 2006; Severmann et al., 2004; Sharma et al., 2001). (2) a variable detrital Fe_T/Al of 0.4 to 0.8, as the parameter depends on the weathered source rock type and may vary temporally. This range was derived from the most detritus dominated samples in our dataset (Fe_T/Al=0.4 in HRM-3-161 and HRM-3-216), the average Fe_T/Al ratio of other siliciclastic (meta-)sediments in the Blovice accretionary complex (0.49) (Drost, 2008; Drost et al., 2007; Pin and Waldhausrová, 2007) and the average Fe_T/Al ratio of potential basaltic source rocks in the area (average 0.8; data of Pin and Waldhausrová, 2007). The FeT/Al ratio of the average upper continental crust (0.48) (Rudnick and Gao, 2003) is well within this range. (3) a lower value for authigenic $\delta^{56}Fe$ of -0.6 ‰ as indicated by the x-axis intercept in the $\delta^{56}Fe$ vs. Al/Fe_T plot. and (4) an upper value for authigenic $\delta^{56}Fe$ of -0.4 ‰, which is the average value for the modern hydrothermal input (Beard et al., 2003; Bennett et al., 2009; Severmann et al., 2004; Sharma et al., 2001). The resulting mixing array (grey area in Fig. APPENDIX-III-1) explains most samples from KA-5 and HRM-3.

Calculations

Fe_T = Fe Total, Fe_D = Fe detrital, Fe_{Hy} = Fe hydrothermal

$Fe_T = Fe_D + Fe_{Hy}$

$Fe_{Hy} = x * Fe_D$ x: Proportion Fe_{Hy} an Fe_D: $x = Fe_{Hy} / Fe_D$

$Fe_T = Fe_D + x * Fe_D$

$Fe_T/Al = (Fe_D + x * Fe_D) /Al$

$Fe_T /Al = Fe_D/Al + (x * Fe_D)/Al$

$X = (Fe_T - Fe_D) / Fe_D$

$X = Fe_T/Fe_D - Fe_D /Fe_D$

$X = Fe_T /Fe_D – 1$ y: Proportion Fe_D to Fe_T: $y = Fe_D / Fe_T$

$X = 1/y – 1$ 1-y: Proportion Fe_{Hy} to Fe_T

$Fe_T = Fe_D + (1/y – 1) Fe_D$

$Fe_T/Al = Fe_D/Al + (1/y – 1) * Fe_D/Al$

$\delta^{56}Fe_T = y * \delta^{56}Fe_D + (1-y) \delta^{56}Fe_{Hy}$ (‰)

Given and decided parameters:

Fe_D/Al: 0.4 and 0.8, respectively

$\delta^{56}Fe_D$: 0.05 ‰

$\delta^{56}Fe_{Hy}$: -0.6 ‰ and -0.4 ‰ (modern hydrothermal average), respectively

Variable y: proportion of detrital Fe to total Fe

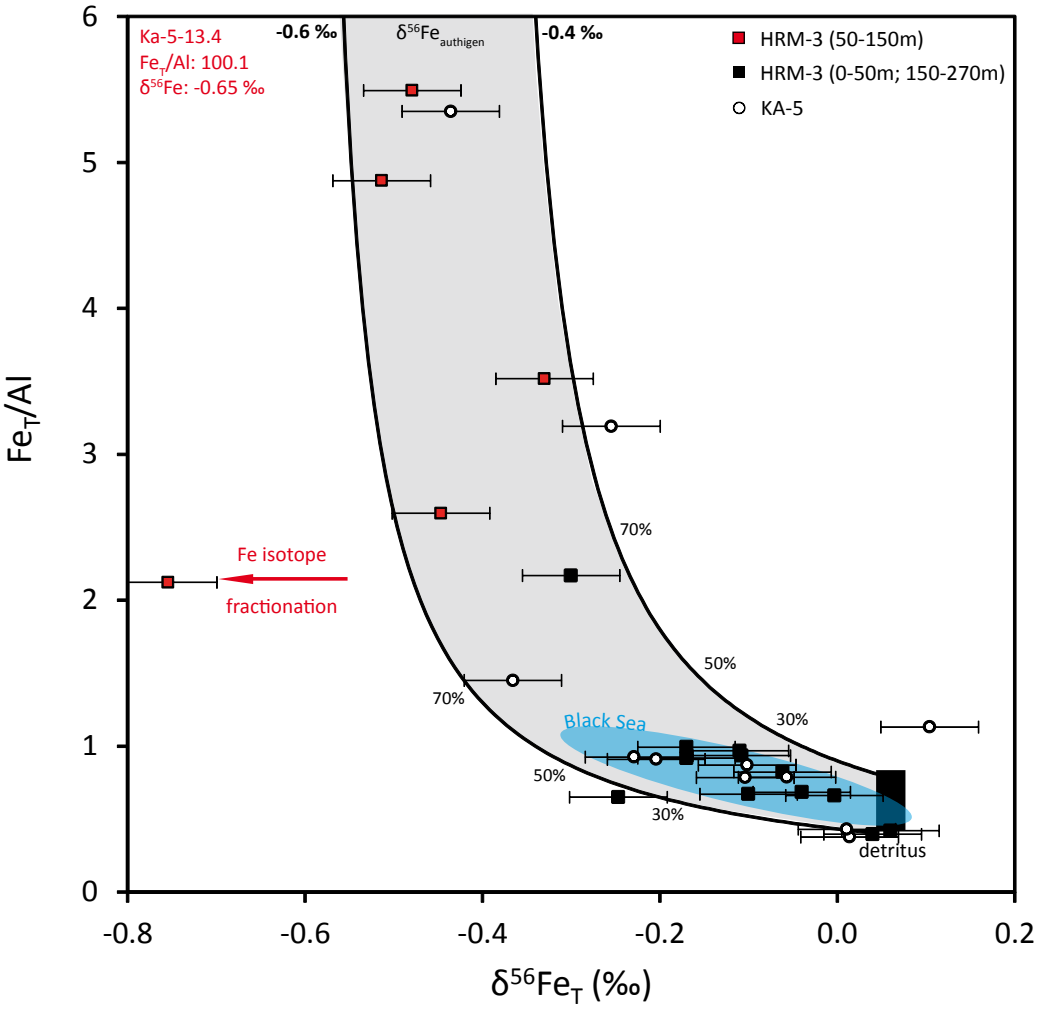

FIGURE APPENDIX-iii-1: Compilation of $\delta^{56}Fe$ against Fe_T/Al. The gray shaded area displays the mixing model with detrital $\delta^{56}Fe$ of 0.05 ‰ and a ratio of Fe_T/Al between 0.4 and 0.8 and authigenic iron (we assume no authigenic Al) that has a Fe isotopic composition between -0.6 to -0.4 ‰. Black numbers indicate the relative portion of authigenic Fe. Most samples are within the mixing area. Moreover, most HRM-3 samples with low authigenic Fe enrichment (black squares) follow a trend observed in modern Black Sea samples (blue area) (Severmann et al., 2008). Only one sample has a lower $\delta^{56}Fe$ than expected from the mixing model, indicating Fe isotope fractionation effects.

3. Additional figures and tables

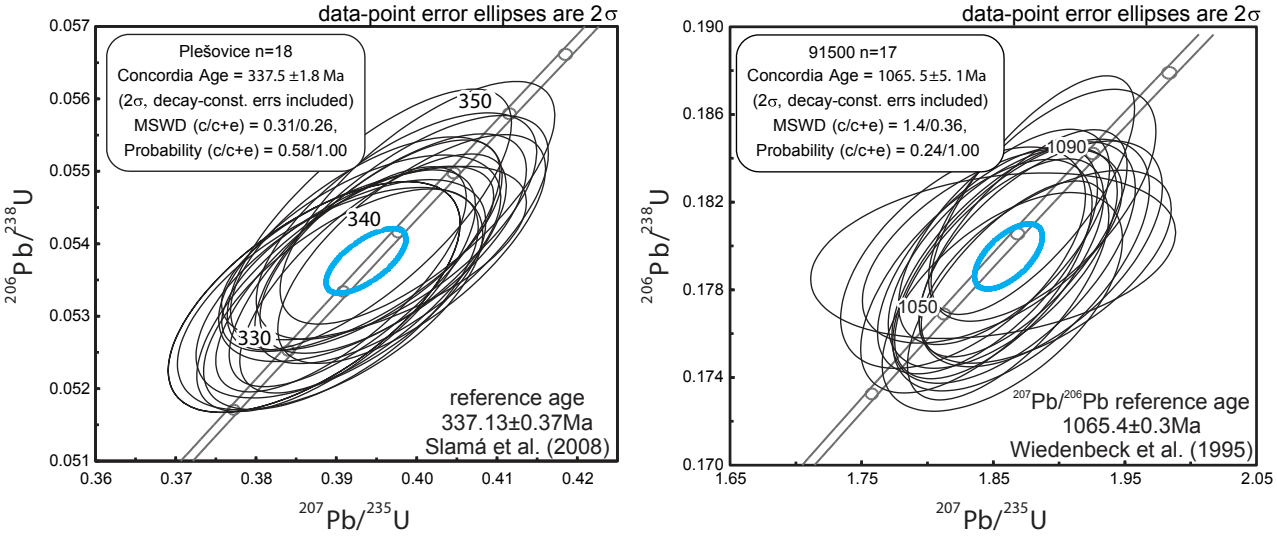

FIGURE APPENDIX-iii-2: Laser ablation ICP-MS U-Pb data of Plešovice and 91500 reference zircons used for quality control. Repeat analyses of the standard zircons during the analytical sessions yield concordia ages that are identical within error with the reference ages

Table III-1. SSB Fe isotope measurements

sample	depth	$\delta^{56}Fe_{av}$	$\delta^{56}Fe_1$	2SD[a]	$\delta^{56}Fe_2$	2SD[a]	$\delta^{57}Fe_1$	2SD[a]	$\delta^{57}Fe_2$	2SD[a]	$\delta^{58}Fe_1$	2SD[a]	$\delta^{58}Fe_2$	2SD[a]
	m	(‰)	(‰)		(‰)		(‰)		(‰)		(‰)		(‰)	
HRM-3-21	21	**-0.17**	-0.22	0.04	-0.12	0.03	-0.33	0.07	-0.15	0.07	-0.14	0.35	-0.12	0.39
HRM-3-27	27	**-0.10**	-0.12	0.04	-0.08	0.03	-0.16	0.07	-0.07	0.06	-1.22	0.96	0.00	0.37
HRM-3-33	33	**-0.04**	-0.08	0.03	-0.01	0.04	-0.10	0.06	0.00	0.05	0.16	0.33	0.09	0.36
HRM-3-48	48	**-0.11**	-0.11	0.04	-0.12	0.03	-0.15	0.06	-0.16	0.06	0.00	0.38	-0.13	0.36
HRM-3-55	55	**-0.75**	-0.75	0.03	-0.74	0.03	-1.12	0.06	-1.10	0.06	-0.92	0.36	-1.48	0.32
HRM-3-73	73													
HRM-3-85	85	**-0.52**	-0.51	0.03	-0.53	0.03	-0.78	0.06	-0.75	0.07	-0.58	0.41	-0.53	0.34
HRM-3-96	96	**-0.47**	-0.48	0.04	-0.47	0.03	-0.74	0.05	-0.69	0.07	-1.28	0.42	-0.96	0.36
HRM-3-119	119	**-0.41**	-0.45	0.03	-0.37	0.04	-0.67	0.06	-0.56	0.08	-0.68	0.33	-0.59	0.34
HRM-3-161	161	**0.04**	0.05	0.03	0.03	0.04	0.09	0.06	0.08	0.08	0.12	0.32	0.26	0.33
HRM-3-166	166	**-0.30**	-0.30	0.03	-0.31	0.04	-0.43	0.05	-0.44	0.06	-0.65	0.34	-0.39	0.34
HRM-3-190	190													
HRM-3-206	206													
HRM-3-216	216	**0.06**	0.05	0.03	0.08	0.03	0.07	0.07	0.15	0.07	0.01	0.34	0.36	0.37
HRM-3-240	240	**-0.17**	-0.19	0.04	-0.14	0.03	-0.25	0.08	-0.19	0.06	-0.37	0.32	-0.26	0.30
HRM-3-265	265	**-0.11**	-0.16	0.03	-0.06	0.03	-0.21	0.07	-0.14	0.06	-0.31	0.32	-0.06	0.34
HRM-3-268	268													

[a] 2 standard deviation of 20 cycles during the measurement on the ICP-MS

Table III-2. Thermo Scientific iCAP Qq Instrument settings and operating conditions

Instrument	Thermo Scientific iCAP Qc
Forward Power	1550 W
Coolant gas flow	14.0 l/min
Sample gas flow	0.85 l/min
Sampling depth	4.3 mm
Data acquisition protocol	Time-resolved analysis
Isotopes determined	^{202}Hg, ^{204}(Hg + Pb), ^{206}Pb, ^{207}Pb, ^{208}Pb, ^{232}Th, ^{235}U, ^{238}U
Acquisition mode	Peak jumping, one point per peak
Dwell time	10ms, except ^{207}Pb and ^{235}U: 20ms
Cones	Ni, skimmer with sensitivity insert
Laser-ablation system	Resonetics RESOlution M-50
Laser type/ wavelength	Excimer 193 nm
Pulse duration	20 ns
Energy density	2.6 J/cm^2
ThO^+/Th^+	< 1.0%
Nominal spot diameter	33 µm
Sampling strategy	spot
Laser repetition rate	4 Hz
He gas flow	600 ml/min
N_2 gas flow	3 ml/min

Table III-3. LA-ICP-MS detrital zircon data for grains younger than 700Ma.
Concordia ages in bold type were calculated from two analyses of the same grain.

	Pb	U	Th	Th/U	$^{206/204}$Pb	$^{208/206}$Pb	ratios	±		±		±		±		ages								concordia ages for analyses with probability of concordance >0.15, including decay constant errors			
							^{208}Pb/^{232}Th	1σ%	$^{207/206}$Pb	1σ%	^{207}Pb/^{235}U	1σ%	^{206}Pb/^{238}U	1σ%	rho	^{208}Pb/^{232}Th	±2σ	$^{207/206}$Pb	±2σ	^{207}Pb/^{235}U	±2σ	^{206}Pb/^{238}U	±2σ	concordia age	±2σ	MSWD	prob.
	[ppm]	[ppm]	[ppm]																							
greywacke from surface outcrop (n=71 analyses of which 59 are concordant)																										
HRM-3JP_01	59	582	378	0.69	679	0.21	0.032	4.7	0.064	1.5	0.909	2.0	0.103	1.3	0.67	629	58	739	62	656	19	633	16				
HRM-3JP_02	32	311	263	0.92	1021	0.28	0.030	4.3	0.059	4.1	0.804	4.3	0.098	1.3	0.30	604	51	576	177	599	39	605	15	605	15	0.11	0.74
HRM-3JP_04	27	272	151	0.66	3962	0.20	0.030	4.4	0.061	1.1	0.842	1.6	0.100	1.1	0.71	595	52	635	49	620	15	616	14	617	13	0.55	0.46
HRM-3JP_05	9	82	54	0.69	2116	0.22	0.032	4.4	0.061	1.7	0.868	2.1	0.103	1.3	0.60	638	55	635	73	635	20	634	15	634	15	0.00	0.99
HRM-3JP_06	31	330	187	0.59	3166	0.19	0.030	4.3	0.060	1.7	0.798	2.1	0.096	1.3	0.60	604	51	603	72	596	19	594	14	594	14	0.07	0.80
HRM-3JP_08	14	165	63	0.43		0.13	0.028	4.3	0.059	1.8	0.740	2.2	0.091	1.3	0.58	554	47	569	77	562	19	561	14	561	13	0.05	0.83
HRM-3JP_11	14	157	79	0.54		0.18	0.030	4.3	0.060	1.3	0.747	1.8	0.091	1.2	0.67	594	51	590	57	566	15	561	13	562	12	1.02	0.31
HRM-3JP_13	23	277	113	0.49	3183	0.15	0.027	4.4	0.060	1.6	0.724	2.0	0.088	1.1	0.58	534	47	593	70	553	17	544	12	545	12	1.91	0.17
HRM-3JP_14	19	189	151	0.88	2888	0.27	0.032	4.3	0.061	1.4	0.865	1.9	0.102	1.3	0.67	627	53	650	60	633	18	628	15	629	15	0.49	0.49
HRM-3JP_15	24	271	177	0.75	3037	0.22	0.028	4.3	0.062	1.5	0.823	1.9	0.096	1.2	0.64	565	48	686	63	610	18	589	14				
HRM-3JP_16	16	150	144	1.03	2511	0.31	0.032	4.3	0.061	1.8	0.879	2.1	0.105	1.1	0.53	638	54	629	76	641	20	644	14	643	13	0.14	0.71
HRM-3JP_18	65	785	439	0.60	5191	0.18	0.026	4.3	0.060	1.1	0.713	1.7	0.086	1.3	0.75	519	44	605	49	546	15	532	13				
HRM-3JP_20	45	444	171	0.51	1368	0.15	0.032	4.3	0.061	1.1	0.866	1.5	0.103	1.1	0.70	631	53	631	47	634	14	634	13	634	12	0.02	0.88
HRM-3JP_22	27	266	153	0.63	4869	0.20	0.031	4.3	0.060	1.5	0.823	2.0	0.099	1.3	0.65	613	52	621	65	610	18	607	15	608	15	0.18	0.67
HRM-3JP_25	24	227	178	0.83	5247	0.26	0.032	4.3	0.061	1.5	0.867	2.0	0.104	1.2	0.63	641	54	625	65	634	18	636	15	636	15	0.12	0.73
HRM-3JP_26	68	810	394	0.52	7356	0.16	0.028	4.3	0.059	1.1	0.735	1.7	0.090	1.2	0.75	565	48	571	48	560	14	557	13	558	13	0.30	0.59
HRM-3JP_29	44	560	256	0.51	2451	0.15	0.025	4.3	0.064	1.2	0.755	1.7	0.086	1.2	0.69	493	42	735	52	571	15	531	12				
HRM-3JP_31	8	82	64	0.86	1308	0.26	0.031	4.5	0.061	2.0	0.866	2.4	0.103	1.3	0.53	612	54	635	87	633	23	633	15	633	15	0.00	0.97
HRM-3JP_36	49	471	335	0.80	6375	0.25	0.032	4.3	0.062	1.2	0.880	1.7	0.104	1.2	0.69	641	54	661	53	641	16	635	14	637	14	0.84	0.36
HRM-3JP_40	25	285	158	0.59	2245	0.18	0.027	2.8	0.060	2.5	0.710	2.7	0.086	1.2	0.44	532	29	589	107	545	23	534	12	535	12	0.98	0.32
HRM-3JP_42	25	269	258	1.10	1993	0.25	0.021	4.1	0.062	1.6	0.775	2.0	0.091	1.2	0.60	423	34	657	69	583	18	564	13				
HRM-3JP_44	12	134	81	0.67	3444	0.20	0.027	2.9	0.059	1.8	0.741	2.1	0.091	1.1	0.53	541	31	567	78	563	18	562	12	562	12	0.01	0.91
HRM-3JP_47	22	224	124	0.58	3752	0.19	0.032	2.7	0.061	1.6	0.818	2.0	0.098	1.2	0.59	633	34	623	70	607	18	603	13	604	13	0.32	0.57
HRM-3JP_49	11	117	77	0.73	1691	0.23	0.031	3.1	0.060	1.9	0.814	2.5	0.099	1.6	0.63	614	37	593	83	605	23	608	18	607	18	0.13	0.72
HRM-3JP_50	31	343	240	0.74	5757	0.24	0.028	2.7	0.058	1.4	0.700	1.8	0.088	1.1	0.62	559	30	525	62	539	15	542	12	542	11	0.30	0.58
HRM-3JP_52	19	212	86	0.48	2464	0.14	0.027	2.7	0.059	1.8	0.734	2.1	0.091	1.1	0.51	541	29	550	80	559	18	561	12	561	12	0.07	0.79
HRM-3JP_53	16	177	113	0.70	2854	0.22	0.026	3.0	0.058	1.6	0.689	2.1	0.086	1.3	0.63	528	31	525	71	532	17	534	13	534	13	0.06	0.81
HRM-3JP_55	12	108	147	1.53	1138	0.38	0.022	3.1	0.065	2.0	0.789	2.3	0.088	1.2	0.52	442	27	764	83	591	21	547	12				
HRM-3JP_57	2	22	19	0.95	333	0.29	0.026	3.0	0.058	2.8	0.691	3.2	0.086	1.6	0.49	525	31	540	124	533	27	532	16	532	16	0.02	0.90
HRM-3JP_59a	17	175	136	0.88	1641	0.27	0.027	2.8	0.059	1.6	0.700	2.0	0.087	1.3	0.64	533	29	553	69	539	17	535	13	**533**	**8**	**2.20**	**0.14**
HRM-3JP_59b	17	189	126	0.72	2326	0.22	0.027	2.7	0.059	1.4	0.700	1.8	0.086	1.1	0.61	531	29	578	62	539	15	529	11				
HRM-3JP_60	21	223	121	0.63	3331	0.19	0.026	2.8	0.059	1.6	0.727	2.0	0.090	1.2	0.59	528	29	554	70	555	17	555	13	555	12	0.00	0.97
HRM-3JP_61	14	162	99	0.65	2796	0.20	0.028	2.8	0.057	1.4	0.729	1.8	0.093	1.2	0.64	567	31	494	62	556	16	571	13				
HRM-3JP_62	34	412	166	0.44	6497	0.14	0.027	2.8	0.059	1.2	0.689	1.7	0.085	1.2	0.68	534	29	550	55	532	14	528	12	529	11	0.60	0.44
HRM-3JP_65	16	175	125	0.78	1910	0.24	0.028	2.6	0.059	2.1	0.734	2.4	0.090	1.2	0.51	554	29	568	90	559	21	557	13	557	13	0.06	0.81
HRM-3JP_66	11	113	69	0.67	1510	0.20	0.030	2.8	0.060	1.4	0.827	1.9	0.100	1.2	0.64	602	34	608	62	612	17	613	14	613	14	0.03	0.87
HRM-3JP_67	20	244	72	0.35	2611	0.10	0.023	3.6	0.067	1.3	0.758	1.8	0.082	1.3	0.71	462	32	838	53	573	16	508	12				
HRM-3JP_69	41	451	361	0.89	5507	0.27	0.027	2.6	0.059	1.2	0.732	1.6	0.091	1.1	0.68	537	28	552	51	558	14	559	12	559	11	0.08	0.77
HRM-3JP_71	39	414	178	0.46		0.15	0.031	2.8	0.060	1.7	0.799	2.1	0.097	1.2	0.56	620	34	598	74	596	19	596	13	596	13	0.00	0.95
HRM-3JP_73	22	245	169	0.72	2334	0.23	0.029	2.7	0.059	1.6	0.724	2.1	0.090	1.3	0.63	577	31	550	70	553	18	554	14	553	14	0.01	0.92
HRM-3JP_74	15	175	78	0.47	1541	0.15	0.029	2.8	0.059	1.4	0.737	1.9	0.091	1.3	0.68	582	32	560	61	561	17	561	14	561	14	0.00	0.96

Table III-3. continued

Concordia ages in bold type were calculated from two analyses of the same grain.

						ratios										ages								concordia ages for analyses with probability of concordance >0.15, including decay constant errors			
	Pb	U	Th	Th/U	$^{206/204}$Pb	$^{208/206}$Pb	^{208}Pb/	±		±	^{207}Pb/	±	^{206}Pb/	±		^{208}Pb/		^{207}Pb/		^{206}Pb/						
	ppm	ppm	ppm				^{232}Th	1σ%	$^{207/206}$Pb	1σ%	^{235}U	1σ%	^{238}U	1σ%	rho	^{232}Th	±2σ	$^{207/206}$Pb	±2σ	^{235}U	±2σ	^{238}U	±2σ	concordia age	±2σ	MSWD	prob.
HRM-3JP_75	25	287	152	0.58	2017	0.18	0.028	2.8	0.059	1.6	0.732	2.0	0.090	1.3	0.62	565	31	555	70	557	18	558	13	558	13	0.01	0.92
HRM-3JP_77	16	152	118	0.82	1993	0.26	0.032	2.8	0.060	1.9	0.853	2.2	0.102	1.2	0.54	645	35	621	80	626	21	628	14	628	14	0.03	0.86
HRM-3JP_78	9	103	50	0.57	1650	0.17	0.026	3.0	0.058	1.8	0.685	2.2	0.086	1.2	0.55	518	31	526	80	530	18	530	12	530	12	0.01	0.92
HRM-3JP_79	15	146	102	0.77	2069	0.24	0.031	2.9	0.060	1.5	0.806	2.0	0.097	1.4	0.68	609	35	605	65	600	19	599	16	599	16	0.03	0.85
HRM-3JP_80	46	492	375	0.79	5793	0.25	0.028	2.7	0.059	1.4	0.709	1.8	0.087	1.2	0.65	561	30	574	60	544	15	537	12	539	12	1.40	0.24
HRM-3JP_84	19	210	104	0.53	3683	0.17	0.028	2.8	0.058	1.5	0.725	1.9	0.090	1.1	0.60	564	31	544	67	553	16	556	12	555	12	0.12	0.72
HRM-3JP_85	51	549	493	0.94	6698	0.28	0.027	2.7	0.058	1.2	0.725	1.6	0.090	1.1	0.69	533	29	547	51	553	14	555	12	554	11	0.08	0.77
HRM-3JP_86	18	193	129	0.71	3654	0.23	0.029	2.8	0.058	1.9	0.726	2.2	0.091	1.2	0.53	580	32	527	82	554	19	561	12	560	12	0.69	0.41
HRM-3JP_88	18	206	124	0.67	5459	0.21	0.028	2.8	0.058	1.4	0.733	1.8	0.091	1.1	0.63	562	32	543	62	558	16	562	12	561	12	0.36	0.55
HRM-3JP_89	25	241	135	0.69		0.19	0.027	2.8	0.060	1.4	0.817	1.9	0.099	1.2	0.67	539	30	602	60	606	17	608	14	607	14	0.04	0.85
HRM-3JP_90	20	201	99	0.56	2378	0.17	0.030	2.8	0.060	1.5	0.832	2.0	0.101	1.2	0.63	597	33	602	66	615	18	619	14	618	14	0.25	0.62
HRM-3JP_92	21	236	82	0.38	3424	0.12	0.031	2.9	0.060	1.3	0.802	1.9	0.098	1.5	0.76	619	35	589	55	598	18	600	17	599	16	0.15	0.70
HRM-3JP_93	28	320	154	0.56	4904	0.17	0.027	2.9	0.059	1.3	0.739	1.8	0.091	1.2	0.66	538	31	565	58	562	15	561	13	561	12	0.02	0.89
HRM-3JP_94	20	220	169	0.83	2073	0.26	0.027	2.7	0.061	1.7	0.729	2.2	0.086	1.3	0.60	530	29	646	74	556	19	534	13				
HRM-3JP_95	29	295	273	0.83	3161	0.26	0.032	2.9	0.061	1.5	0.863	1.9	0.102	1.2	0.62	646	37	645	63	632	18	628	14	629	14	0.28	0.59
HRM-3JP_96	31	311	182	0.70	5375	0.20	0.029	2.8	0.060	1.8	0.863	2.1	0.104	1.1	0.53	584	32	620	76	632	20	635	13	635	13	0.15	0.70
HRM-3JP_97	35	394	189	0.53	9079	0.16	0.028	2.7	0.060	1.2	0.759	1.7	0.092	1.1	0.69	565	30	588	52	573	15	570	12	571	12	0.44	0.51
HRM-3JP_101	13	151	78	0.59	3937	0.18	0.028	3.0	0.059	1.7	0.736	2.1	0.090	1.3	0.59	548	33	575	75	560	18	556	14	557	13	0.23	0.63
HRM-3JP_102	15	171	79	0.57	1648	0.14	0.021	3.2	0.058	1.5	0.683	2.1	0.085	1.4	0.69	426	27	530	66	528	17	528	14	528	14	0.00	0.95
HRM-3JP_103	13	150	98	0.73		0.22	0.026	2.7	0.058	1.4	0.696	1.8	0.087	1.1	0.62	520	28	541	63	536	15	535	12	536	11	0.03	0.86
HRM-3JP_107	17	189	127	0.71	2170	0.25	0.029	2.8	0.067	1.4	0.787	2.1	0.085	1.6	0.75	587	32	847	57	590	19	525	16				
HRM-3JP_108	26	267	130	0.53	4223	0.16	0.030	2.8	0.060	1.4	0.808	1.9	0.098	1.2	0.64	589	33	595	63	601	17	603	14	602	13	0.05	0.82
HRM-3JP_109a	34	344	360	1.19		0.34	0.026	3.7	0.059	1.4	0.742	1.8	0.091	1.1	0.63	524	38	571	60	564	15	562	12	**567**	**8**	**0.40**	**0.53**
HRM-3JP_109b	25	274	218	0.91	4004	0.26	0.026	3.7	0.058	1.3	0.748	1.7	0.093	1.1	0.65	522	38	540	56	567	15	574	12				
HRM-3JP_111	10	118	51	0.48	2595	0.15	0.027	3.8	0.058	1.7	0.709	2.1	0.089	1.2	0.57	538	40	528	75	544	18	548	12	547	12	0.28	0.60
HRM-3JP_112	15	160	65	0.45	2458	0.14	0.031	3.7	0.060	1.5	0.818	2.0	0.099	1.3	0.64	609	45	604	67	607	18	608	15	608	14	0.01	0.91
HRM-3JP_113	9	92	85	1.00		0.31	0.028	3.7	0.058	1.9	0.728	2.2	0.091	1.2	0.52	562	41	520	84	556	19	564	13	563	12	1.13	0.29
HRM-3JP_114	10	97	109	1.26	1655	0.38	0.027	3.8	0.058	2.1	0.726	2.4	0.090	1.2	0.51	544	41	548	91	554	21	555	13	555	13	0.03	0.87
sample from HRM-3 drill core at 249.5 to 250.1m (n=101 analyses of which 83 are concordant)																											
L_01	11	116	98	0.89	1667	0.28	0.029	4.5	0.060	1.9	0.767	2.2	0.093	1.2	0.54	582	52	598	82	578	20	573	13	**577**	**9**	**0.38**	**0.54**
L_01rep	8	88	55	0.66	1199	0.21	0.029	5.1	0.060	1.8	0.775	2.1	0.094	1.2	0.55	585	58	591	77	582	19	580	13				
L_02	25	267	106	0.40	4315	0.12	0.032	4.5	0.060	1.6	0.861	1.9	0.104	1.1	0.57	636	57	616	67	631	18	635	13	634	13	0.32	0.57
L_03	51	596	142	0.24	9136	0.07	0.030	4.5	0.059	1.3	0.801	1.7	0.098	1.2	0.68	604	54	581	55	597	16	602	13	600	13	0.54	0.46
L_05	20	216	110	0.63	1308	0.19	0.029	5.7	0.060	3.6	0.797	3.7	0.096	1.1	0.30	579	66	619	154	595	34	589	13	589	13	0.15	0.70
L_06	16	171	52	0.30	3338	0.09	0.032	4.7	0.061	1.2	0.867	1.7	0.104	1.3	0.73	631	59	622	51	634	16	637	15	636	15	0.34	0.56
L_08	4	41	30	0.76	808	0.23	0.032	4.8	0.061	1.9	0.867	2.4	0.103	1.4	0.60	629	60	632	82	634	23	634	17	634	17	0.00	0.96
L_09	12	133	76	0.58	2301	0.18	0.030	4.7	0.059	1.6	0.778	1.9	0.095	1.1	0.59	598	55	577	68	585	17	586	13	586	13	0.07	0.79
L_10	68	658	538	0.80	3127	0.25	0.030	4.6	0.060	1.7	0.813	2.2	0.098	1.4	0.64	603	54	612	72	604	20	602	16	602	16	0.07	0.79
L_11	25	244	170	0.72	4276	0.22	0.031	4.5	0.060	1.9	0.825	2.3	0.100	1.2	0.53	609	54	592	83	611	21	616	14	615	14	0.33	0.56
L_16	21	202	176	0.90	1702	0.27	0.031	4.5	0.061	1.6	0.863	2.0	0.103	1.2	0.61	614	55	631	67	632	19	632	15	632	14	0.00	0.97
L_20	26	258	119	0.46		0.14	0.033	4.5	0.061	1.5	0.896	1.9	0.106	1.2	0.62	655	58	652	64	650	18	649	15	649	14	0.01	0.94

Table III-3. continued

Concordia ages in bold type were calculated from two analyses of the same grain.

	Pb	U	Th	Th/U	$^{206/204}$Pb	$^{208/206}$Pb	ratios									ages								concordia ages for analyses with probability of concordance >0.15, including decay constant errors			
							^{208}Pb/	±		^{207}Pb/	±		^{206}Pb/	±		^{208}Pb/		^{207}Pb/		^{206}Pb/							
	[ppm]	[ppm]	[ppm]				^{232}Th	1σ%		$^{207/206}$Pb	1σ%	^{235}U	1σ%	^{238}U	1σ%	rho	^{232}Th	±2σ	$^{207/206}$Pb	±2σ	^{235}U	±2σ	^{238}U	±2σ	concordia age	±2σ	MSWD	prob.
L_21	70	653	460	0.83	1237	0.25	0.030	4.5	0.060	2.6	0.817	2.8	0.099	1.1	0.40	590	53	602	112	606	26	607	13	607	13	0.01	0.93
L_23	29	299	249	0.83		0.26	0.029	4.5	0.060	1.2	0.771	1.7	0.093	1.1	0.67	574	51	598	54	580	15	576	12	577	12	0.62	0.43
L_24	8	91	51	0.59		0.18	0.030	4.7	0.060	1.6	0.804	2.0	0.098	1.3	0.63	596	56	596	68	599	19	600	15	600	15	0.01	0.91
L_26	24	300	87	0.29	2778	0.09	0.030	4.6	0.061	1.6	0.786	1.9	0.094	1.1	0.56	601	54	626	68	589	17	579	12	580	12	1.80	0.18
L_27	10	112	43	0.39	1619	0.12	0.031	4.6	0.060	2.0	0.814	2.4	0.098	1.5	0.60	608	55	618	84	605	22	601	17	602	16	0.15	0.70
L_27	9	99	55	0.58	1033	0.18	0.032	4.6	0.061	1.7	0.876	2.1	0.104	1.2	0.58	633	58	646	74	639	20	637	15	637	15	0.06	0.80
L_28	50	479	368	0.78	11607	0.24	0.032	4.5	0.061	1.2	0.874	1.6	0.104	1.1	0.66	633	56	632	52	638	15	639	13	639	13	0.08	0.78
L_30	26	241	102	0.59	360	0.26	0.043	5.0	0.111	2.7	1.505	2.9	0.098	1.2	0.42	858	84	1820	97	932	36	603	14				
L_34	25	281	100	0.37	3765	0.11	0.029	1.8	0.060	1.3	0.810	1.7	0.097	0.9	0.64	586	20	614	57	602	16	600	13	599	10	0.24	0.62
L_36	35	404	95	0.25	5637	0.07	0.030	1.9	0.060	1.2	0.820	1.6	0.099	1.1	0.70	595	22	610	50	608	15	607	13	608	13	0.01	0.91
L_37	4	53	19	0.36	687	0.11	0.027	2.5	0.057	3.1	0.702	3.4	0.090	1.5	0.43	535	27	485	136	540	29	553	15	552	15	1.01	0.31
L_38	22	228	104	0.47	3041	0.15	0.032	1.9	0.061	1.5	0.867	1.9	0.104	1.1	0.58	634	23	629	67	634	18	635	13	635	13	0.03	0.86
L_39	14	138	90	0.67		0.21	0.030	1.9	0.060	1.7	0.809	2.0	0.097	1.1	0.56	598	22	611	72	602	18	599	13	600	13	0.09	0.76
L_40	7	67	37	0.56	898	0.17	0.031	2.6	0.058	2.4	0.826	2.7	0.104	1.2	0.46	624	32	518	104	612	25	637	15				
L_41	22	250	149	0.61	3143	0.18	0.028	1.9	0.059	1.5	0.743	1.8	0.092	1.1	0.58	549	21	560	65	564	16	565	12	565	11	0.03	0.86
L_42	40	454	147	0.34	3153	0.11	0.032	1.8	0.061	1.6	0.866	1.9	0.103	1.1	0.57	630	22	648	68	633	18	629	13	630	13	0.30	0.59
L_44	7	63	59	0.97	1690	0.29	0.032	1.9	0.061	2.2	0.894	2.6	0.105	1.3	0.49	633	23	656	95	648	25	646	15	647	15	0.04	0.84
L_45	21	244	56	0.24	3449	0.07	0.030	2.3	0.060	1.5	0.803	1.9	0.097	1.2	0.63	596	27	595	64	598	17	599	14	599	13	0.01	0.91
L_46	19	224	101	0.48	2309	0.15	0.028	1.8	0.061	1.6	0.761	2.0	0.091	1.2	0.60	549	19	630	68	575	17	561	13				
L_47	13	130	100	0.79		0.24	0.031	1.7	0.060	1.6	0.857	1.9	0.103	1.1	0.58	614	21	612	68	629	18	633	14	632	13	0.39	0.53
L_49	26	250	174	0.71	2284	0.22	0.032	1.9	0.061	1.4	0.871	1.8	0.103	1.1	0.60	631	23	642	62	636	17	634	13	635	13	0.06	0.80
L_50rep	26	300	132	0.45		0.14	0.028	5.0	0.059	1.5	0.738	2.0	0.091	1.3	0.65	559	56	564	66	561	17	561	14	**561**	**9**	**0.01**	**0.91**
L_50rep-r	136	1603	706	0.41		0.12	0.027	5.0	0.059	1.1	0.738	1.7	0.091	1.3	0.74	548	54	563	49	561	15	561	13				
L_51	9	93	67	0.74		0.22	0.031	2.1	0.061	1.6	0.859	2.0	0.102	1.2	0.59	609	25	633	70	630	19	629	14	**631**	**11**	**0.00**	**0.99**
L_51rep	9	91	60	0.69	3090	0.21	0.032	5.0	0.061	2.2	0.869	2.7	0.104	1.5	0.56	630	62	629	97	635	26	636	18				
L_52	15	165	92	0.57	2756	0.18	0.029	1.8	0.059	1.4	0.767	1.9	0.094	1.2	0.64	581	20	575	63	578	17	579	13	579	13	0.02	0.90
L_52rep	23	243	190	0.77	3474	0.25	0.029	5.0	0.060	1.4	0.730	1.9	0.089	1.2	0.63	576	57	587	63	556	16	549	12				
sm_02	36	418	205	0.49	4439	0.15	0.027	1.7	0.060	1.2	0.724	1.7	0.087	1.2	0.70	539	18	609	53	553	15	540	12				
sm_04	86	839	517	0.61	9897	0.19	0.032	1.7	0.061	1.1	0.857	1.7	0.103	1.3	0.76	635	21	627	48	629	16	629	16	629	15	0.00	0.94
sm_05	26	240	201	0.84		0.26	0.032	1.9	0.060	1.5	0.866	1.9	0.104	1.2	0.62	632	23	620	65	633	18	637	14	636	14	0.28	0.60
sm_13	19	213	74	0.35	4091	0.11	0.030	2.1	0.060	1.5	0.804	1.9	0.098	1.2	0.63	600	25	592	64	599	17	601	14	601	13	0.08	0.78
sm_14	10	99	67	0.72		0.21	0.031	2.0	0.061	2.0	0.871	2.3	0.104	1.2	0.54	611	24	624	85	636	22	640	15	639	15	0.13	0.72
sm_16	30	342	119	0.40	1272	0.13	0.031	1.9	0.070	1.7	0.932	2.1	0.097	1.1	0.53	623	23	914	72	669	20	598	13				
sm_17	7	69	43	0.63		0.19	0.031	3.0	0.061	2.1	0.869	2.5	0.103	1.3	0.53	612	36	641	91	635	24	633	16	633	16	0.03	0.87
sm_18	68	665	564	0.76		0.22	0.030	2.8	0.061	1.2	0.872	1.7	0.104	1.1	0.68	593	33	642	53	636	16	635	14	635	13	0.06	0.80
sm_19	26	231	268	1.20	3613	0.34	0.030	2.9	0.061	1.2	0.870	1.6	0.104	1.1	0.70	591	34	636	50	635	15	635	14	635	13	0.00	0.98
sm_20	22	219	111	0.51	4057	0.16	0.030	3.0	0.060	1.5	0.811	1.9	0.098	1.2	0.63	605	36	595	64	603	17	605	14	605	13	0.09	0.77
sm_27	12	124	93	0.74		0.24	0.030	3.0	0.060	1.9	0.764	2.3	0.092	1.3	0.56	599	35	603	82	577	20	570	14	571	14	0.60	0.44
sm_29	13	146	58	0.41	2316	0.13	0.030	3.1	0.059	1.9	0.791	2.4	0.097	1.5	0.62	598	36	578	82	592	22	595	17	594	17	0.17	0.68
sm_30	24	263	138	0.52	4125	0.16	0.028	2.9	0.059	1.5	0.737	1.9	0.091	1.2	0.62	558	32	565	65	561	17	560	13	560	13	0.03	0.86
sm_32	53	605	167	0.27	3885	0.08	0.030	2.8	0.060	1.2	0.800	1.7	0.097	1.2	0.70	595	33	588	51	597	15	599	13	599	13	0.18	0.67
sm_33	5	61	17	0.31	856	0.09	0.025	3.8	0.064	2.0	0.752	2.4	0.086	1.2	0.52	508	38	727	87	570	21	531	13				

Table III-3. continued
Concordia ages in bold type were calculated from two analyses of the same grain.

	Pb	U	Th	Th/U	$^{206/204}$Pb	$^{208/206}$Pb	ratios									ages								concordia ages for analyses with probability of concordance >0.15, including decay constant errors			
							^{208}Pb/	±		^{207}Pb/	±		^{206}Pb/	±		^{208}Pb/		^{207}Pb/		^{206}Pb/							
	[ppm]	[ppm]	[ppm]				^{232}Th	1σ%		$^{207/206}$Pb	1σ%	^{235}U	1σ%	^{238}U	1σ%	rho	^{232}Th	±2σ	$^{207/206}$Pb	±2σ	^{235}U	±2σ	^{238}U	±2σ	concordia age	±2σ	MSWD	prob.
sm_34	13	124	85	0.66		0.21	0.032	3.0	0.059	1.7	0.838	2.0	0.102	1.2	0.57	643	38	585	73	618	19	628	14	626	14	1.36	0.24
sm_35	36	399	143	0.37		0.11	0.030	2.9	0.060	1.1	0.806	1.6	0.098	1.1	0.71	602	34	598	48	600	14	601	13	601	13	0.01	0.92
sm_37	23	231	128	0.57	3115	0.17	0.030	3.0	0.060	1.5	0.845	1.9	0.103	1.2	0.63	606	35	586	64	622	18	632	14	630	14	1.96	0.16
sm_38	18	183	115	0.62	3135	0.19	0.030	2.9	0.059	1.6	0.805	2.0	0.098	1.2	0.60	591	34	580	68	600	18	605	14	604	13	0.53	0.47
sm_39	17	153	107	0.69	3466	0.22	0.034	2.9	0.062	1.4	0.905	1.9	0.107	1.2	0.64	669	38	659	61	655	18	653	15	654	14	0.03	0.87
sm_40	14	127	89	0.74	1838	0.22	0.031	2.9	0.062	1.6	0.879	1.9	0.103	1.1	0.58	617	35	665	67	641	18	634	13	635	13	0.83	0.36
sm_42	68	762	191	0.25	7923	0.08	0.030	2.9	0.060	1.1	0.804	1.7	0.097	1.2	0.74	599	34	609	49	599	15	597	14	598	14	0.23	0.63
sm_43	14	146	90	0.62	7051	0.20	0.031	2.9	0.061	1.7	0.826	2.0	0.099	1.1	0.55	615	35	623	72	611	18	608	13	608	13	0.17	0.68
sm_44	37	444	152	0.35		0.11	0.028	2.9	0.058	1.3	0.730	1.7	0.091	1.1	0.63	567	32	525	57	556	14	564	12	563	11	1.88	0.17
sm_45	24	296	68	0.24		0.07	0.028	3.0	0.059	1.5	0.734	1.9	0.091	1.2	0.63	558	33	557	65	559	17	559	13	559	13	0.00	0.95
sm_47	10	111	49	0.48	1126	0.14	0.028	3.1	0.059	2.0	0.764	2.3	0.094	1.2	0.51	558	34	572	86	576	20	578	13	577	13	0.02	0.90
sm_48	49	512	447	0.89	13006	0.27	0.028	2.8	0.059	1.2	0.758	1.7	0.094	1.2	0.69	556	31	555	53	573	15	577	13	576	12	0.65	0.42
sm_50	22	216	127	0.61	4666	0.18	0.031	3.0	0.061	1.3	0.871	1.8	0.104	1.3	0.73	615	37	630	55	636	18	638	16	637	16	0.06	0.80
sm_51	28	274	179	0.65		0.20	0.032	2.8	0.061	1.4	0.869	1.7	0.104	1.1	0.62	639	36	628	59	635	16	637	13	636	13	0.08	0.77
sm_53	21	193	116	0.61	3012	0.18	0.034	2.8	0.062	1.5	0.955	2.0	0.111	1.3	0.66	671	37	679	64	681	20	681	17	681	16	0.00	0.96
sm_54	25	275	98	0.36	5535	0.11	0.029	2.9	0.059	1.6	0.795	1.9	0.099	1.1	0.57	587	34	549	69	594	17	606	13				
sm_55	26	260	138	0.56	4753	0.16	0.030	2.9	0.060	1.3	0.861	1.7	0.103	1.0	0.61	595	34	620	58	631	16	634	12	633	12	0.22	0.64
sm_56	6	57	43	0.78	1045	0.23	0.032	2.9	0.061	2.1	0.892	2.5	0.105	1.2	0.50	628	36	657	92	647	24	645	15	645	15	0.07	0.80
sm_57	20	221	83	0.40		0.11	0.028	3.2	0.059	1.5	0.791	1.9	0.097	1.2	0.61	556	35	570	66	592	17	598	13	597	13	0.70	0.40
sm_59	13	154	52	0.35		0.11	0.030	2.9	0.059	2.1	0.792	2.4	0.097	1.1	0.48	588	34	577	92	592	22	596	13	596	13	0.18	0.67
sm_60	69	814	346	0.45	9919	0.12	0.024	2.8	0.061	1.2	0.714	1.7	0.085	1.2	0.69	470	26	631	53	547	14	527	12				
sm-b-02	30	339	108	0.32	7486	0.10	0.031	5.1	0.060	1.3	0.793	1.8	0.096	1.2	0.66	611	61	599	58	593	16	591	13	592	13	0.06	0.81
sm-b-03	31	295	212	0.73		0.22	0.032	5.0	0.062	1.8	0.906	2.1	0.106	1.1	0.51	642	63	667	79	655	21	651	14	652	14	0.16	0.69
sm-b-04	35	352	276	0.81	6652	0.25	0.032	5.0	0.061	1.3	0.864	1.7	0.103	1.1	0.63	637	62	625	57	632	16	635	13	634	13	0.11	0.74
sm-b-05	9	85	90	1.08	2235	0.34	0.032	5.0	0.061	2.0	0.866	2.4	0.103	1.4	0.58	642	63	639	84	634	23	632	17	632	17	0.03	0.87
sm-b-07	32	323	90	0.28	9628	0.08	0.031	5.0	0.061	1.2	0.866	1.7	0.104	1.2	0.69	620	61	622	53	633	16	636	14	635	14	0.25	0.62
sm-b-08	54	581	458	0.84	2122	0.27	0.028	5.0	0.060	2.1	0.736	2.4	0.089	1.1	0.46	564	55	596	92	560	21	551	11	552	11	0.91	0.34
sm-b-09	19	207	140	0.70	3004	0.23	0.029	5.0	0.061	1.4	0.753	1.8	0.090	1.1	0.63	577	57	628	60	570	16	555	12				
sm-b-10	7	74	65	0.86	944	0.27	0.030	5.1	0.059	1.7	0.766	2.1	0.095	1.3	0.60	593	59	558	73	578	18	583	14	582	14	0.46	0.50
sm-b-15	21	254	95	0.38		0.12	0.029	5.1	0.059	1.5	0.738	1.9	0.090	1.2	0.62	574	58	580	65	562	16	557	13	558	12	0.45	0.50
sm-b-16	23	230	152	0.66	4088	0.21	0.031	5.0	0.061	1.6	0.833	2.0	0.099	1.2	0.61	618	61	636	68	616	19	610	14	611	14	0.57	0.45
sm-b-17	56	552	386	0.73	3718	0.23	0.030	5.1	0.060	1.5	0.801	1.9	0.097	1.1	0.61	602	61	601	64	597	17	596	13	596	13	0.02	0.89
sm-b-19	9	95	74	0.85	1527	0.26	0.027	5.1	0.058	2.1	0.712	2.4	0.089	1.1	0.47	536	54	527	94	546	21	551	12	**557**	**9**	**0.18**	**0.67**
sm-b-19rep	16	166	155	0.95		0.29	0.028	5.0	0.059	1.6	0.739	2.0	0.091	1.2	0.57	560	55	556	72	562	17	563	12				
sm-b-24	13	131	71	0.53	1011	0.20	0.036	5.1	0.071	1.4	0.956	1.9	0.097	1.3	0.66	717	71	968	59	681	19	598	14				
sm-b-25	53	645	218	0.33	6748	0.11	0.030	5.0	0.059	1.1	0.737	1.6	0.091	1.2	0.75	592	58	565	47	561	14	560	13	560	12	0.04	0.84
sm-b-26	9	99	67	0.65	1137	0.21	0.028	5.1	0.060	1.7	0.710	2.0	0.086	1.1	0.54	563	56	601	75	545	17	531	11				
sm-b-28	64	494	1055	3.00	5119	0.55	0.018	5.4	0.061	1.5	0.837	1.9	0.100	1.2	0.60	365	39	634	67	618	18	613	14	614	13	0.38	0.54
sm-b-29	71	823	264	0.48		0.15	0.031	5.3	0.060	1.2	0.827	1.6	0.100	1.1	0.68	616	64	610	52	612	15	612	13	612	13	0.01	0.94
sm-b-30	52	576	147	0.26	8982	0.08	0.031	5.0	0.060	1.3	0.805	1.7	0.097	1.1	0.65	616	61	612	57	600	16	597	13	598	13	0.25	0.62
sm-b-34	36	390	124	0.34	7857	0.10	0.031	5.0	0.060	1.4	0.816	1.9	0.098	1.2	0.64	608	60	609	62	606	17	605	14	605	13	0.02	0.90

Table III-4: U-Pb data for reference materials treated as unknowns

	Pb [ppm]	U [ppm]	Th [ppm]	Th/U	$^{206}Pb/^{204}Pb$	$^{208}Pb/^{206}Pb$	ratios $^{208}Pb/^{232}Th$	±1σ%	$^{207}Pb/^{206}Pb$	±1σ%	$^{207}Pb/^{235}U$	±1σ%	$^{206}Pb/^{238}U$	±1σ%	rho
Ples	32	684	62	0.09	7250	0.03	0.017789	2.91	0.052728	1.48	0.387236	1.92	0.053264	1.22	0.64
Ples	35	750	65	0.09	7411	0.03	0.016978	2.97	0.053020	1.61	0.389221	2.00	0.053242	1.18	0.59
Ples	34	738	65	0.09	5896	0.03	0.016818	2.95	0.053015	1.29	0.389982	1.82	0.053351	1.28	0.70
Ples	35	749	65	0.10	9146	0.03	0.016930	3.87	0.053069	1.49	0.390573	1.89	0.053378	1.15	0.61
Ples	35	748	66	0.10	6983	0.03	0.016813	2.92	0.053212	1.36	0.390577	1.79	0.053234	1.17	0.65
Ples	36	774	73	0.09	9605	0.03	0.017806	4.66	0.052941	1.12	0.390591	1.63	0.053509	1.19	0.73
Ples	25	529	43	0.09	3357	0.03	0.017124	2.60	0.052945	1.29	0.392670	1.76	0.053790	0.97	0.68
Ples	37	780	69	0.10	9074	0.03	0.016016	4.37	0.052969	1.47	0.392912	1.83	0.053799	1.08	0.59
Ples	37	775	74	0.09	7534	0.03	0.018314	3.11	0.053119	1.18	0.393523	1.75	0.053730	1.30	0.74
Ples	38	796	72	0.09	15466	0.03	0.018000	5.11	0.052880	1.36	0.393739	1.75	0.054002	1.11	0.63
Ples	37	793	71	0.08	9650	0.03	0.019217	5.15	0.052607	1.24	0.394111	1.83	0.054334	1.35	0.74
Ples	36	781	75	0.10	8055	0.03	0.018142	4.80	0.053402	1.17	0.394581	1.72	0.053589	1.26	0.73
Ples	22	470	37	0.08	6086	0.02	0.016362	2.83	0.053137	1.59	0.394695	1.97	0.053872	0.91	0.58
Ples	35	752	66	0.09	9259	0.03	0.016657	4.36	0.053330	1.27	0.397082	1.71	0.054002	1.15	0.67
Ples	36	765	67	0.10	10299	0.03	0.016508	3.94	0.053147	1.36	0.397495	1.79	0.054244	1.18	0.66
Ples	37	797	71	0.09	6710	0.03	0.018484	5.02	0.053415	1.36	0.398133	1.87	0.054058	1.29	0.69
Ples	36	758	73	0.10	5135	0.03	0.017533	3.40	0.053714	1.22	0.399389	1.71	0.053927	1.20	0.70
Ples	37	784	70	0.10	4531	0.03	0.016799	3.14	0.053181	1.22	0.400102	1.75	0.054565	1.25	0.72
91500	16	93	30	0.35	3670	0.11	0.054202	3.00	0.073835	1.73	1.827044	2.08	0.179468	1.15	0.55
91500	16	93	30	0.35	3029	0.11	0.053914	2.91	0.074596	1.53	1.837169	1.95	0.178621	1.22	0.62
91500	16	96	32	0.36	1797	0.11	0.054095	2.85	0.074640	1.43	1.845673	1.85	0.179343	1.18	0.64
91500	17	101	35	0.35	3004	0.11	0.055180	2.02	0.074504	1.80	1.849242	2.18	0.180017	1.01	0.56
91500	15	89	31	0.33	2490	0.11	0.059507	5.07	0.075156	1.32	1.854494	1.75	0.178962	1.15	0.65
91500	13	77	25	0.36	2017	0.11	0.053427	4.08	0.075894	1.65	1.856889	2.01	0.177450	1.15	0.57
91500	16	91	31	0.34	2914	0.11	0.057262	5.18	0.075054	1.53	1.857182	1.91	0.179464	1.15	0.60
91500	17	99	34	0.35	2394	0.11	0.054358	4.70	0.074701	1.37	1.858231	1.76	0.180414	1.11	0.63
91500	17	104	36	0.34	2939	0.11	0.056213	2.94	0.075852	1.23	1.861316	1.68	0.177973	1.15	0.68
91500	17	101	35	0.36	2265	0.11	0.054006	4.71	0.075479	1.59	1.865404	2.03	0.179244	1.25	0.62
91500	17	101	34	0.35	3218	0.11	0.054410	3.01	0.075761	1.68	1.871169	2.13	0.179130	1.31	0.61
91500	16	92	30	0.35	2770	0.11	0.055266	4.53	0.075402	1.26	1.872670	1.72	0.180126	1.17	0.68
91500	17	97	34	0.34	2275	0.10	0.055942	2.92	0.074790	1.16	1.880096	1.68	0.182320	1.22	0.73
91500	13	76	25	0.36	1675	0.11	0.053793	3.88	0.076148	1.62	1.886104	2.00	0.179642	1.17	0.59
91500	16	94	31	0.35	3037	0.11	0.055789	4.41	0.075263	1.44	1.887197	1.87	0.181859	1.19	0.64
91500	17	100	35	0.36	1956	0.11	0.054278	2.16	0.076567	1.65	1.890258	2.05	0.179052	1.00	0.60
91500	17	93	32	0.52	788	0.15	0.052544	6.57	0.074683	2.94	1.849914	3.06	0.179554	0.86	0.28

Table III-4: continued

	ages								concordia age			
	$^{208}Pb/^{232}Th$	±2σ	$^{207}Pb/^{206}Pb$	±2σ	$^{207}Pb/^{235}U$	±2σ	$^{206}Pb/^{238}U$	±2σ	age	±2σ	MSWD	probability
Ples	356	21	317	67	332	11	335	8	334	8	0.27	0.61
Ples	340	20	330	73	334	11	334	8	334	8	0.02	0.90
Ples	337	20	329	59	334	10	335	8	335	8	0.04	0.85
Ples	339	26	332	68	335	11	335	8	335	7	0.01	0.92
Ples	337	20	338	62	335	10	334	8	334	8	0.01	0.91
Ples	357	33	326	51	335	9	336	8	336	8	0.14	0.71
Ples	343	18	326	59	336	10	338	8	338	6	0.15	0.70
Ples	321	28	327	67	336	10	338	7	338	7	0.09	0.76
Ples	367	23	334	53	337	10	337	9	337	8	0.02	0.90
Ples	361	37	324	62	337	10	339	7	339	7	0.25	0.62
Ples	385	39	312	56	337	11	341	9	340	9	1.05	0.30
Ples	363	35	346	53	338	10	337	8	337	8	0.12	0.73
Ples	328	18	335	72	338	11	338	8	338	6	0.01	0.92
Ples	334	29	343	57	340	10	339	8	339	8	0.02	0.90
Ples	331	26	335	62	340	10	341	8	340	8	0.03	0.86
Ples	370	37	346	61	340	11	339	9	340	8	0.05	0.82
Ples	351	24	359	55	341	10	339	8	339	8	0.54	0.46
Ples	337	21	337	55	342	10	342	8	342	8	0.05	0.83
91500	1067	62	1037	70	1055	27	1064	23	1061	21	0.55	0.46
91500	1061	60	1058	62	1059	26	1059	24	1059	22	0.00	0.96
91500	1065	59	1059	57	1062	25	1063	23	1063	21	0.02	0.88
91500	1086	43	1055	72	1063	29	1067	24	1067	20	0.11	0.74
91500	1168	115	1073	53	1065	23	1061	22	1063	21	0.15	0.69
91500	1052	84	1092	66	1066	27	1053	22	1057	21	1.24	0.26
91500	1125	114	1070	62	1066	25	1064	23	1065	21	0.03	0.86
91500	1070	98	1060	55	1066	23	1069	22	1068	20	0.09	0.77
91500	1105	63	1091	49	1067	22	1056	22	1062	20	1.68	0.19
91500	1063	98	1081	64	1069	27	1063	25	1065	23	0.29	0.59
91500	1071	63	1089	67	1071	28	1062	26	1065	24	0.54	0.46
91500	1087	96	1079	51	1071	23	1068	23	1070	21	0.17	0.68
91500	1100	63	1063	46	1074	22	1080	24	1076	21	0.40	0.52
91500	1059	80	1099	65	1076	27	1065	23	1069	22	0.95	0.33
91500	1097	94	1076	58	1077	25	1077	24	1077	22	0.00	0.96
91500	1068	45	1110	66	1078	27	1062	24	1064	19	2.02	0.16
91500	1035	133	1060	118	1063	41	1065	17	1064	17	0.00	0.95

4. References

Beard, B.L., Johnson, C.M., Von Damm, K.L., Poulson, R.L., 2003. Iron isotope constraints on Fe cycling and mass balance in oxygenated Earth oceans. Geology 31, 629-632.

Bennett, S.A., Rouxel, O., Schmidt, K., Garbe-Schönberg, D., Statham, P.J., German, C.R., 2009. Iron isotope fractionation in a buoyant hydrothermal plume, 5 S Mid-Atlantic Ridge. Geochimica et Cosmochimica Acta 73, 5619-5634.

Bigeleisen, J., Mayer, M.G., 1947. Calculation of equilibrium constants for isotopic exchange reactions. The Journal of Chemical Physics 15, 261-267.

Busigny, V., Planavsky, N.J., Jézéquel, D., Crowe, S., Louvat, P., Moureau, J., Viollier, E., Lyons, T.W., 2014. Iron isotopes in an Archean ocean analogue. Geochimica et Cosmochimica Acta 133, 443-462.

Butler, I.B., Archer, C., Vance, D., Oldroyd, A., Rickard, D., 2005. Fe isotope fractionation on FeS formation in ambient aqueous solution. Earth and Planetary Science Letters 236, 430-442.

Butler, I.B., Rickard, D., 2000. Framboidal pyrite formation via the oxidation of iron (II) monosulfide by hydrogen sulphide. Geochimica et Cosmochimica Acta 64, 2665-2672.

Dauphas, N., Rouxel, O., 2006. Mass spectrometry and natural variations of iron isotopes. Mass Spectrometry Reviews 25, 515-550.

Drost, K., 2008. Sources and geotectonic setting of Late Neoproterozoic, Early Palaeozoic volcano-sedimentary successions of the Teplá-Barrandian unit (Bohemian Massif): evidence from petrographical, geochemical, and isotope analyses. Geologica saxonica 54, 1-165.

Drost, K., Romer, R.L., Linnemann, U., Fatka, O., Kraft, P., Marek, J., 2007. Nd-Sr-Pb isotopic signatures of Neoproterozoic–Early Paleozoic siliciclastic rocks in response to changing geotectonic regimes: A case study from the Barrandian area (Bohemian Massif, Czech Republic). Geological Society of America Special Papers 423, 191-208.

Guilbaud, R., Butler, I.B., Ellam, R.M., 2011. Abiotic pyrite formation produces a large Fe isotope fractionation. Science 332, 1548-1551.

Guilbaud, R., Butler, I.B., Ellam, R.M., Rickard, D., 2010. Fe isotope exchange between Fe (II) aq and nanoparticulate mackinawite (FeS m) during nanoparticle growth. Earth and Planetary Science Letters 300, 174-183.

Pašava, J., Hladikova, J., Dobes, P., 1996. Origin of Proterozoic metal-rich black shales from the Bohemian Massif, Czech Republic. Economic Geology 91, 63-79.

Pašava, J., Sulovsky, P., Kovalova, M., 1993. Geochemistry and mineralogy of Proterozoic metal-rich black shales from the Bohemian Massif, Czech Republic, with a description of possible new molybdenum selenide and telluride phases. The Canadian Mineralogist 31, 745-754.

Pin, C., Waldhausrová, J., 2007. Sm-Nd isotope and trace element study of Late Proterozoic metabasalts ("spilites") from the Central Barrandian domain (Bohemian Massif, Czech Republic). Geological Society of America Special Papers 423, 231-247.

Polyakov, V., Clayton, R., Horita, J., Mineev, S., 2007. Equilibrium iron isotope fractionation factors of minerals: reevaluation from the data of nuclear inelastic resonant X-ray scattering and Mössbauer spectroscopy. Geochimica et Cosmochimica Acta 71, 3833-3846.

Rickard, D., Luther, G.W., 2007. Chemistry of iron sulfides. Chemical reviews 107, 514-562.

Rickard, D., Luther III, G.W., 1997. Kinetics of pyrite formation by the H2S oxidation of iron (II) monosulfide in aqueous solutions between 25 and 125° C: The mechanism. Geochimica et Cosmochimica Acta 61, 135-147.

Rouxel, O., Fouquet, Y., Ludden, J.N., 2004. Subsurface processes at the Lucky Strike hydrothermal field, Mid-Atlantic Ridge: evidence from sulfur, selenium, and iron isotopes. Geochimica et Cosmochimica Acta 68, 2295-2311.

Rouxel, O., Shanks III, W.C., Bach, W., Edwards, K.J., 2008. Integrated Fe-and S-isotope study of seafloor hydrothermal vents at East Pacific Rise 9–10 N. Chemical Geology 252, 214-227.

Rudnick, R., Gao, S., 2003. Composition of the continental crust. Treatise on geochemistry 3, 1-64.

Schauble, E., Rossman, G., Taylor, H., 2001. Theoretical estimates of equilibrium Fe-isotope fractionations from vibrational spectroscopy. Geochimica et Cosmochimica Acta 65, 2487-2497.

Schoenberg, R., von Blanckenburg, F., 2006. Modes of planetary-scale Fe isotope fractionation. Earth and Planetary Science Letters 252, 342-359.

Schoonen, M., Barnes, H., 1991. Reactions forming pyrite and marcasite from solution: II. Via FeS precursors below 100 C. Geochimica et Cosmochimica Acta 55, 1505-1514.

Severmann, S., Johnson, C., Beard, B., German, C., Edmonds, H., Chiba, H., Green, D., 2004. The effect of plume processes on the Fe isotope composition of hydrothermally derived Fe in the deep ocean as inferred from the Rainbow vent site, Mid-Atlantic Ridge, 36 14′ N. Earth and Planetary Science Letters 225, 63-76.

Severmann, S., Johnson, C.M., Beard, B.L., McManus, J., 2006. The effect of early diagenesis on the Fe isotope compositions of porewaters and authigenic minerals in continental margin sediments. Geochimica et Cosmochimica Acta 70, 2006-2022.

Severmann, S., Lyons, T.W., Anbar, A., McManus, J., Gordon, G., 2008. Modern iron isotope perspective on the benthic iron shuttle and the redox evolution of ancient oceans. Geology 36, 487-490.

Sharma, M., Polizzotto, M., Anbar, A., 2001. Iron isotopes in hot springs along the Juan de Fuca Ridge. Earth and Planetary Science Letters 194, 39-51.

Syverson, D.D., Borrok, D.M., Seyfried Jr, W.E., 2013. Experimental determination of equilibrium Fe isotopic fractionation between pyrite and dissolved Fe under hydrothermal conditions. Geochimica et Cosmochimica Acta 122, 170-183.

Wilkin, R., Barnes, H., 1997. Formation processes of framboidal pyrite. Geochimica et Cosmochimica Acta 61, 323-339.

Wu, L., Druschel, G., Findlay, A., Beard, B.L., Johnson, C.M., 2012. Experimental determination of iron isotope fractionations among–FeS aq–Mackinawite at low temperatures: Implications for the rock record.

Geochimica et Cosmochimica Acta 89, 46-61.

Selected contributions of co-authors

CHAPTER I

The modeling in chapter I based on calculations of Martin Wille (detailed description within the mentioned reference). The carbon isotopic composition was measured by Bernd Steinhilber. XRF measurements were performed by Daniel Schoekle.

CHAPTER II

The main element data was provided by Brian Philip Nel. The appropiate reference was mentioned in table 1.

Chapter III

The description of the geological setting was mainly written by Kerstin Drost. Furthermore, the U-PB age determination was done by Kerstin Drost. Figure 1 was designed by Kerstin Drost. Sulfur isotope data was measured by Bernd Steinhilber. XRF analyses were performed by Daniel Schoeckle.

Acknowledgment

Primarily, I want to thank Martin Wille for creating this PhD project and his excellent supervision. The numerous scientific discussions with Martin helped significantly to develop new ideas. He was always open-minded about new approaches in the data interpretation, but also very good in finding the weak point of a story, which required further reflection.

I want to thank Ronny Schoenberg for providing detailed insights into the analytical procedure of mass spectrometric measurements. His expertise and the way he communicates this expertise are remarkable. Moreover, the working conditions in general were excellent in Tuebinga, which was for the most part the merit of Ronny. In this regard special thanks also go to my two great roommates Sümeyya and Gülüm. Furthermore, strongly acknowledged are Elmar Reitter and Bernd Steinhilber for their helpfulness and patience in the lab.

Altogether, the atmosphere in the entire working group was always nice and friendly. Since the very beginning I felt very comfortable here in Tuebinga. Thank you!